

03 MAR 1998

# CLEMSON UNIVERSITY



## **THERMAL AND FLOW STRUCTURES IN ACCELERATED /DECELERATED TRANSITIONAL BOUNDARY LAYERS**

---

Final Report

By

Ting Wang  
Department of Mechanical Engineering

---

Program Managers

Dr. James M. McMichael  
Dr. Mark Glauser

---

Prepared Under the Financial Support of the  
Air Force Office of Scientific Research

Grant Numbers: F49620-94-1-0126

February 1998

*Quality Inspected*

19980310031

DISTRIBUTION STATEMENT A

Approved for public release;  
Distribution Unlimited

REPORT DOCUMENTATION PAGE			Form Approved OMB No. 0704-0188
<small>Public reporting burden for this collection of information is estimated to average 1 hour per response, including the time for reviewing instructions, searching existing data sources, gathering and maintaining the data needed, and completing and reviewing the collection of information. Send comments regarding this burden estimate or any other aspect of this collection of information, including suggestions for reducing this burden, to Washington Headquarters Services, Directorate for Information Operations and Reports, 1215 Jefferson Davis Highway, Suite 1204, Arlington, VA 22202-4302, and to the Office of Management and Budget, Paperwork Reduction Project (0704-0188), Washington, DC 20503.</small>			
1. AGENCY USE ONLY (Leave blank)	2. REPORT DATE	3. REPORT TYPE AND DATES COVERED	
	Feb. 15, 1998	Final Report	
4. TITLE AND SUBTITLE		5. FUNDING NUMBERS	
Thermal and Flow Structures in Accelerated/Decelerated Transitional Boundary Layers		F49620-94-1-0126	
6. AUTHOR(S)			
Ting Wang			
7. PERFORMING ORGANIZATION NAME(S) AND ADDRESS(ES)		8. PERFORMING ORGANIZATION REPORT NUMBER	
Department of Mechanical Engineering Clemson University Clemson, SC 29634-0921			
9. SPONSORING / MONITORING AGENCY NAME(S) AND ADDRESS(ES)		10. SPONSORING / MONITORING AGENCY REPORT NUMBER	
Air Force Office of Scientific Research/NA Bolling AFB, DC 20331-6448			
11. SUPPLEMENTARY NOTES Program Monitors: Dr. James M. McMichael and Dr. Mark Glauser			
12a. DISTRIBUTION/AVAILABILITY STATEMENT		12b. DISTRIBUTION CODE	
Unclassified-Unlimited			
13. ABSTRACT (Maximum 200 words)			
<p>The objective of this program is to experimentally investigate the flow and thermal structures in transitional boundary layers with both favorable and adverse pressure gradients at elevated free-stream turbulence (FSTI between 3% to 7%). The experiments were performed in a low-speed, open-circuit, blowing type wind tunnel. A uniformly heated wall was used as the test surface. The experimental parameters (FSTI, roughness, and streamwise pressure gradients) were then systematically varied to study their individual and combined effects on the thermal and flow structures in the laminar-turbulent transition process. A specially designed miniature three-wire probe was used to measure the flow and thermal structures in the boundary layer including the Reynolds stresses, Reynolds heat fluxes, turbulent Prandtl numbers, eddy diffusivities, and turbulent thermal diffusivities within the transitional and turbulent boundary layers. Conditional sampling techniques were applied to investigate the intermittent thermal and flow behaviors in the transitional boundary layers. Spectral analysis was conducted. The primary conclusions from each part of the investigation are summarized in this report. Corresponding papers are attached for detailed information.</p>			
14. SUBJECT TERMS			15. NUMBER OF PAGES
Boundary Layer Transition, Free-Stream Turbulence, Favorable and Adverse Pressure Gradients, Conditional Sampling, Vorticity-Temperature Sensor			
16. PRICE CODE			
17. SECURITY CLASSIFICATION OF REPORT	18. SECURITY CLASSIFICATION OF THIS PAGE	19. SECURITY CLASSIFICATION OF ABSTRACT	20. LIMITATION OF ABSTRACT
Unclassified	Unclassified	Unclassified	WL

# CLEMSON UNIVERSITY



## **THERMAL AND FLOW STRUCTURES IN ACCELERATED /DECELERATED TRANSITIONAL BOUNDARY LAYERS**

---

Final Report

By

Ting Wang  
Department of Mechanical Engineering

---

Program Managers

Dr. James M. McMichael  
Dr. Mark Glauser

---

Prepared Under the Financial Support of the  
Air Force Office of Scientific Research

Grant Numbers: F49620-94-1-0126

February 1998

## FINAL REPORT

### Thermal and Flow Structures in Accelerated/Decelerated Transitional Boundary Layers at Elevated Free-Stream Turbulence

**Grant No:** F49620-94-1-0126

**Reporting Period :** (August 1, 1994 - September 15, 1997)

**Principal Investigator:** Ting Wang, Professor  
Department of Mechanical Engineering  
Clemson University  
Clemson, SC 29634-0921

Phone: (864) 656-5630, Fax: (864) 656-4435  
E-mail: ting.wang@ces.clemson.edu

### ABSTRACT

The objective of this program is to experimentally investigate the flow and thermal structures in transitional boundary layers with both favorable and adverse pressure gradients at elevated free-stream turbulence (FSTI between 3% to 7%). The experiments were performed in a low-speed, open-circuit, blowing type wind tunnel. A uniformly heated wall was used as the test surface. The experimental parameters (FSTI, roughness, and streamwise pressure gradients) were then systematically varied to study their individual and combined effects on the thermal and flow structures in the laminar-turbulent transition process. A specially designed miniature three-wire probe was used to measure the flow and thermal structures in the boundary layer including the Reynolds stresses, Reynolds heat fluxes, turbulent Prandtl numbers, eddy diffusivities, and turbulent thermal diffusivities within the transitional and turbulent boundary layers. Conditional sampling techniques were applied to investigate the intermittent thermal and flow behaviors in the transitional boundary layers. Spectral analysis was conducted. The primary conclusions from each part of the investigation are summarized in this report. Corresponding papers are attached for detailed information.

### OBJECTIVE

The objective of this program is to experimentally investigate the flow and thermal structures in transitional boundary layers with both favorable and adverse pressure gradients at elevated free-stream turbulence (between 3% to 7%). This program focuses on the mechanisms of fluid dynamics and their relation to thermal transport in bypass transition, which is different from conventional studies in natural transition.

The results of this program are expected to be useful for improving modeling of laminar-turbulent transitional flow and heat transfer. The ultimate impact is to improve the prediction of

heat transfer on gas turbine blades and vanes such that the thermal performance of future aeroengines can be augmented, the reliability of hot-section components can be improved, and maintenance can be reduced.

## APPROACH

The experiments were conducted in an open-circuit, blowing type wind tunnel. The test section had an aspect ratio of six, so the flow can remain two dimensional in the centerspan. A pliable heated test wall was designed with 180 thermocouples. Various hot wire sensors were designed to measure Reynolds stresses, Reynolds heat fluxes, Turbulent Prandtl numbers, and vorticities. Coarse grids were used to generate various levels of free-stream turbulence intensities (FSTI) up to 7 %. One test wall was used to control the pressure gradients inside the test section. The baseline case was first conducted with zero pressure gradient and at low FSTI condition. The experimental parameters (FSTI, roughness, and streamwise pressure gradients) were then **systematically** varied to study their individual and combined effects on the thermal and flow structures in the laminar-turbulent transition process. Conditional sampling techniques were applied to investigate the intermittent thermal and flow behaviors in the transitional boundary layers. This systematic approach is summarized below.

<u>Subjects</u>	<u>Paper Reference No.</u>
Baseline cases	1
Elevated free-stream turbulence intensity (FSTI)	2
Favorable pressure gradient	3
Combined FSTI and favorable pressure gradient	4
Spectral analysis of transitional flow	5
Development of a conditional sampling technique	6
Conditionally sampled accelerating flow	7,8
New conditional sampling technique for high FSTI flow	9
Adverse pressure gradient (attached flow)	10,11
Surface roughness	12

The results of data taken through the upgraded equipment are beneficial to the users in the following aspects:

- a. Onset and end of transition in terms of  $Re_x$ ,  $Re_{\delta^*}$ , and  $Re_{\theta}$  under various free-stream turbulence levels.
- b. Turbulent spot production rates.
- c. Intermittency distributions in the boundary layer and in the streamwise direction.
- d. Conditionally-sampled flow and thermal structures from the non-turbulent and turbulent portions of the transitional flow. This includes mean velocity, mean temperature, Reynolds stresses ( $u'^2$ ,  $v'^2$ , and  $\bar{uv}$ ) and Reynolds heat fluxes ( $\bar{vt}$ ,  $\bar{ut}$ ).

- e. Experimental values for turbulent thermal diffusivity, eddy diffusivity, and turbulent Prandtl number ( $Pr_t$ ) in the transitional and turbulent heated boundary layers at various pressure gradients and free-stream turbulence levels.
- f. Heat-transfer coefficient (Stanton Number) and skin-friction coefficient ( $C_f$ ) in the transition region.
- g. Spectral information for both power spectrum and thermal energy spectrum in transitional flow including integral and dissipation lengths.

## **EXECUTIVE SUMMARY**

The flow and thermal structures of a two-dimensional heated boundary layer undergoing natural or bypass transition from laminar to turbulent flow were investigated in detail. The experiments were performed in a low-speed, open-circuit, blowing type wind tunnel. A uniformly heated wall was used as the test surface. 185 thermocouple wires were embedded in the test wall for measuring wall temperatures and Stanton numbers. A specially designed miniature three-wire probe was used to measure the flow and thermal structures in the boundary layer including the Reynolds stresses, Reynolds heat fluxes, turbulent Prandtl numbers, eddy diffusivities, and turbulent thermal diffusivities within the transitional and turbulent boundary layers. The primary conclusions from each part of the investigation are summarized below.

### **Summary of the Baseline Case**

The baseline case with low FSTI and zero pressure gradient on a smooth surface was conducted. The transition onset for the baseline case occurred at  $Re_X = 5.5 \times 10^5$  ( $Re_\theta = 492$ ) which is earlier than the transition onset for a free-stream turbulence intensity (FSTI) value of 0.5% predicted from correlations. Apparently, factors other than FSTI influence transition onset. Onset of transition was taken as the point of minimum skin friction (and/or Stanton number). Measurements of the Reynolds normal stress indicated that the flow in the transition region is much less isotropic than the flow in a fully turbulent boundary layer. The Reynolds shear stress was shown to be generated within the boundary layer ( $Y^+ = 70 \sim 100$ ) and imposed on the wall shear. Mean temperature profiles lagged in development compared to the mean velocity profiles and the values of the Reynolds analogy factor,  $2St/C_f$ , in the late-transition early-turbulent region were lower than the 1.2 value known to apply to the high-Reynolds-number turbulent flow. These results indicate a slower response of heat transport in this region compared to that of momentum transport.

The streamwise gradients of the streamwise Reynolds normal stress,  $\partial u'^2 / \partial x$ , and the streamwise Reynolds heat flux,  $\partial \bar{u}t / \partial x$ , were shown to be of significant magnitude in the transition region and should not be ignored in transitional flow models when computational

methods are used. The profiles of Reynolds cross-stream heat flux showed negative values in the near wall region. The region of negative  $\bar{v}t$  narrowed as the flow proceeded downstream. These negative values of  $\bar{v}t$  in a flow with a negative mean temperature gradient result in negative eddy thermal diffusivity and negative  $Pr_t$ , which are not physically appropriate. It is speculated that the negative values might be caused by the size of the sensor and the three-dimensional behavior of transition. The difference between eddy viscosity and eddy thermal diffusivity distributions reflected the apparent disparity between turbulent momentum and thermal transport mechanisms in the transitional boundary layer.

### Summary of the Streamwise Accelerating Cases

Streamwise acceleration was shown to delay the point of transition onset both in terms of physical distance,  $x$ , and Reynolds number based on  $x$ . The transition onset momentum Reynolds number,  $Re_{\theta s}$ , was relatively insensitive to acceleration. In general, the physical length of transition increased with increasing  $K$  ( $\equiv \frac{v}{U^2} \frac{dU}{dx}$ ). This was supported by the boundary layer

thickness and integral parameters which indicated that an increasing favorable pressure gradient suppresses boundary layer growth and development through the transition region. The Reynolds normal stresses were suppressed in the near-wall region ( $Y^+ < 50$ ) relative to the baseline case as  $K$  increased. This was believed to be caused by a thickening of the viscous sublayer relative to the boundary layer thickness. The lag that was observed between the mean temperature profiles and the mean velocity profiles for the baseline case became more pronounced with increasing  $K$ . Comparison of the evolution of RMS temperature fluctuations to the evolution of Reynolds normal stresses indicated a lag in the RMS temperature fluctuations. This supported the observation from the mean temperature and velocity profiles that the thermal transport lags behind the momentum transport in the transition region and that the effect is more pronounced as  $K$  increases.

### Summary of the Conditional Sampling Technique

Nine different criterion functions were investigated for conditional sampling technique. Criterion functions based on correlations schemes consistently resulted in intermittency values 0.14 to 0.38 lower in the outer boundary layer region ( $y/\delta^* > 4.0$ ) than the values found from single signal schemes. No differences were found using the temperature based criterion function to support the use of a separate thermal intermittency factor in accelerating flows. Inherent differences were shown to exist between each criterion function's turbulence recognition capabilities. Each criterion function weights different areas within a turbulent spot. As a result, different criterion functions may result in the same overall intermittency factor, but analysis of the turbulent and non-turbulent portions would not always yield the same result.

A criterion function based on Reynolds stress,  $(\partial \bar{u}v / \partial x)^2$ , resulted in the sharpest demarcation between turbulent and non-turbulent portions of the flow. This criterion function also had a negligible variation of threshold value throughout the transition region with the lowest sensitivity of the resultant intermittency to the variation of the threshold. These results indicate that using the Reynolds shear stress for turbulent/non-turbulent discrimination in a heated transitional boundary layer is superior to a single velocity or temperature scheme. The

intermittency across the boundary layer for the baseline and each accelerating case were obtained. Peak values in intermittency for the early to mid-transitional regions were found to occur away from the wall at approximately  $y/\delta = 0.3$  for the baseline case and three accelerating cases. To match the universal intermittency distribution of Dhawan and Narasimha (1958), the values of intermittency at the near-wall minimum  $y/\delta = 0.1$  should be used as the representative "near-wall" values.

### **Summary of the Conditional Sampling Results of Low Turbulence Cases**

The conditionally sampled distribution of the skin friction coefficients revealed that values for  $C_f$  in the non-turbulent and turbulent portions significantly deviated from the respective laminar and turbulent correlations. Reconstructing the local overall  $C_f$  value using the laminar and turbulent correlations consistently overestimates the experimentally determined unconditioned  $C_f$  values. The results indicate that a single representative near-wall intermittency value may not be the characteristic property for the transition region and that the intermittency variation across the boundary layer may play a more important role than previously thought. Evaluation of the conditionally sampled momentum thickness confirmed that the higher loss of momentum in the transition region is a direct result of the turbulent portion of the boundary layer. The mean velocity profiles from the turbulent portions had the appearance of a low-Reynolds-number turbulent boundary layer with a large wake region. In the late transition region, as  $K$  increased, the wake region in the turbulent portion was suppressed relative to the unconditioned result.

The increased magnitude of the streamwise Reynolds normal stress was discovered to be a direct result of the fluctuations in the turbulent portions and not a result of the "mean-step" contribution. The "mean-step" change indicated the step change between the turbulent and non-turbulent mean values. The peak intensity of the streamwise Reynolds normal stress in the non-turbulent portion was suppressed at an earlier stage as  $K$  increased. The Reynolds shear stress was normalized by the individual  $C_f$  values obtained for each portion. The peak magnitudes of Reynolds shear still exceeded the wall shear but not by the magnitudes previously seen. The results indicated that the turbulent shear was generated in the boundary layer at  $Y^+ \approx 100$  and imposed on the wall shear and that the "mean-step" contribution was negligible. As  $K$  increased,  $uv$  in the turbulent portion was more uniformly distributed through the inner boundary layer than the unconditioned results. The peak intensity in the RMS temperature fluctuations in the non-turbulent portions increased in magnitude relative to the unconditioned data and the values in the turbulent portion at  $Y \approx 100$ . These values eventually became greater than the turbulent and unconditioned values in the late transition region. The streamwise Reynolds heat flux in the turbulent portion increased in magnitude as  $K$  increased.

### **Conditionally Sampled Results of Elevated FSTI Cases**

In the elevated FSTI condition, the laminar flow is highly disturbed. The stage of linear instability amplification, triggered by infinitesimal disturbances, is bypassed. The nonlinear instability, triggered by finite-amplitude disturbance, dominates. This is called bypass transition. Due to the highly disturbed condition in the laminar part, the turbulent and nonturbulent parts of the transitional flow become difficult to discern. Because of this, the conventional sampling

technique of applying the "dual-slope" method to the distribution of the accumulative probability function encounters difficulty. A modified method, using one slope on the accumulative probability chart to determine the threshold, was made. This modified method was convenient to apply and was also theoretically verified. The results showed that using the Reynolds stress signal ( $uv$ ) instead of  $u'$  signal can enhance the certainty for demarcating the turbulent and nonturbulent signals. This implies that using the turbulence transport behavior ( $uv$ ) is much superior to using the turbulence energy ( $u'^2$ ) for separating the turbulent and nonturbulent signals.

As shown in Fig.3, the conditionally sampled results indicated that the both components of turbulence energy ( $u'$  and  $v'$ ),  $t'$ , and  $ut$  are high in the nonturbulent part --- this is contrary to the low FSTI cases; whereas, the Reynolds momentum and thermal transports ( $uv$  and  $vt$ ) are low in the nonturbulent part --- this is similar to the low FSTI cases. This implies that although the velocity trace of the non-turbulent part was hardly distinguishable from the turbulent part in high FSTI situations, the flow and thermal transport mechanisms of the non-turbulent part were distinctively different from the turbulent part.

### Spectral Analysis

A spectral analysis was conducted for both turbulence power spectra, as well as thermal power spectra, for heated transitional boundary layers at FSTI of 0.5% and 6.4%, respectively. The power spectra of  $u'$ ,  $v'$  and  $t'$  as well as their cospectra ( $uv$ ,  $ut$ ,  $vt$ ) were analyzed. The spectral analogy and the differences between the momentum and the thermal transports were investigated. The results showed that the location of maximum turbulence production ( $y/\delta \approx 0.1$ ) coincided with the peak location of  $u'$ ; whereas, the region of high turbulent shear ( $y/\delta \approx 0.35$ ) produced little turbulence energy. The power spectrum of  $t'$  was mostly correlated with  $u'$  in the early to middle transitional flow, but it was significantly correlated with  $v'$  in the late transitional and early turbulent flow regions. The dissipation power spectra for both  $u'$  and  $v'$  evolved faster than their turbulence power spectra.  $vt$  is transported by smaller eddies than is  $ut$ . A hypothetical energy transfer process during laminar-turbulent transition was proposed.

### Adverse Pressure Gradient (Decelerating) Cases at Low FSTI

The effects of adverse pressure gradients on the thermal and momentum characteristics of a heated transitional boundary layer were investigated with free-stream turbulence ranging from

0.3 to 0.6 percent. The acceleration parameter  $K$  ( $\equiv \frac{v}{U_\infty^2} \frac{dU_\infty}{dx}$ ) was kept constant along the test

section. Both surface heat transfer and boundary layer measurements were conducted. The boundary layer measurements were conducted with a three-wire probe (two velocity wires and one temperature wire) for two representative cases,  $K1 = -0.51 \times 10^{-6}$  and  $K2 = -1.05 \times 10^{-6}$ . The surface heat transfer measurements were conducted for  $K$  values ranging from  $-0.45 \times 10^{-6}$  to  $-1.44 \times 10^{-6}$  over five divergent wall angles. The Stanton numbers of the decelerating cases were greater than that of the zero-pressure-gradient turbulent correlation in the low-Reynolds-number turbulent flow, and the difference increased as the adverse pressure gradient was increased. The adverse pressure gradient caused earlier transition onset and shorter transition length based on

$Re_x$ ,  $Re_{\delta^*}$ , and  $Re_{\theta}$  in comparison to zero-pressure-gradient conditions. As expected, there was a reduction in skin friction as the adverse pressure gradient increased. In the  $U^+$ - $Y^+$  coordinates, the adverse pressure gradients had a significant effect on the mean velocity profiles in the near-wall region for the late-laminar and early transition stations. The mean temperature profile was observed to precede the velocity profile in starting and ending the transition process, opposite to what occurred in favorable pressure gradient cases in previous studies. A curve fit of the turbulent temperature profile in the long-linear region for the K2 case gave a conduction layer thickness of  $Y^+ = 9.8$  and an average  $Pr_t = 0.71$ . In addition, the wake region of the turbulent mean temperature profile was significantly suppressed.

The fluctuation quantities,  $u'$ ,  $v'$ , and  $t'$ , the Reynolds shear stress ( $\bar{uv}$ ), and the Reynolds heat fluxes ( $\bar{ut}$ ,  $\bar{vt}$ ) were measured. In general,  $u'/U_{\infty}$ ,  $v'/U_{\infty}$  and  $\bar{vt}$  have higher values across the boundary layer for the adverse pressure gradient cases than they do for the baseline case ( $K = 0$ ). The development of  $v'$  for the decelerating cases was more actively involved than that of the baseline case. In the early transition region, the Reynolds shear stress distribution for the K2 case showed a near-wall region of high turbulent shear generated at  $Y^+ = 7$ . At stations farther downstream, this near-wall shear reduced in magnitude, while a second region of high turbulent shear developed at  $Y^+ = 70$ . For the baseline case, however, the maximum turbulent shear in the transition region was generated at  $Y^+ = 70$ , and no near-wall high shear region was seen. Stronger adverse pressure gradients appear to produce more uniform and higher  $t'$  in the near-wall region ( $Y^+ < 20$ ) in both transitional and turbulent boundary layers. The instantaneous velocity signals did not show any clear turbulent/non-turbulent demarcations in the transition region. Increasingly stronger adverse pressure gradients seemed to produce large non-turbulent unsteadiness (or instability waves) at a similar magnitude as the turbulent fluctuations such that the production of turbulent spots was obscured. The turbulent spots could not be identified visually or through conventional conditional sampling schemes. In addition, the streamwise evolution of eddy viscosity, turbulent thermal diffusivity, and  $Pr_t$  were also measured.

#### Conditional Sampling for Adverse Pressure Gradient (Decelerating) Cases at Low FSTI

The amplification rate of instability under the influence of adverse pressure gradient is much larger than at the zero-pressure gradient condition. The instantaneous velocity traces do not indicate any visible turbulent wave packets. Several existing conditional sampling techniques have been tried. The results are not conclusive. Efforts are continuing in search of an appropriate conditional sampling technique for adverse pressure gradient cases.

#### Effect of Leading Edge Roughness

An experimental study was undertaken to gain insight into the physical mechanisms that affect the laminar-turbulent transition process downstream of the leading-edge roughness condition. In order to simulate the randomly distributed roughness located near the leading edge of the turbine blade, 1200, 180, and 40 GRIT sandpaper strips were adhered to the leading edge of the test surface. Similarly, 0.762, 1.59, and 2.31 mm diameter cylinders were chosen to simulate the relatively isolated peak nature of the roughness structure. A total of eight different leading-edge conditions and 56 test cases were examined. The roughness Reynolds number

ranged from 2 to 2840. Tests were also conducted by using a smooth strip of tape at the leading edge to determine the relative effects of the sandpaper backing and the actual roughness of the sandpaper. All of these leading-edge conditions were compared to the undisturbed leading edge.

Overall, greater maximum roughness height was observed to induce greater enhancement of the surface heat transfer than the undisturbed case. Depending on the free-stream velocity and the distance from the leading edge disturbance, the enhancement ranged from negligible to 200%. At low free-stream velocities ( $U_\infty = 5$  m/s), the maximum roughness height was the primary contributor to deviations observed from the undisturbed case, irrespective of the roughness geometry. At higher free-stream velocities, 5-7 m/s, the Stanton number versus  $Re_x$  correlation exhibited dual slope region between the typical laminar and turbulent correlations, also irrespective of the roughness geometry. Although the first slope was significantly different from the laminar correlation (as much as 88% higher), inspection of the mean velocity profiles, RMS fluctuations, Reynolds shear stress, and instantaneous velocity signals indicated that the boundary layer was pre-transitional in this region. The second segment of the dual-slope Stanton number distribution was steeper than the first and the junction between these two segments was determined to be the approximated onset of boundary layer transition.

### **Development of Various Three-Wire Sensors for Reynolds Heat Fluxes Measurements**

The equipment and instrumentation associated with this project was previously supported by a DEPSCoR Equipment program (Grant No. F49620-93-1-0533). This equipment program contributed the design and fabrication of the following sensors to be used in the present program:

- a. A special, custom-made, three-wire miniature sensor was designed and built to measure Reynolds stresses ( $\bar{uv}$ ) and Reynolds heat fluxes ( $\bar{ut}$  and  $\bar{vt}$ ) in transitional and turbulent boundary layers.
- b. A three-wire sensor was specially designed and custom made to measure spanwise Reynolds heat flux ( $\bar{wt}$ ) and spanwise Reynolds normal stress ( $w'$ ). The information obtained from  $\bar{wt}$  and  $w'$  is necessary to check turbulence energy and turbulent thermal energy closure of a transitional boundary layer flow.
- c. A rake of six wire sensors was designed and fabricated to measure the spatial correlation and coherent structures across the transitional boundary layers.

### **Development and Evaluation of the Six-Wire Vorticity-Temperature Sensor**

A complex six-wire vorticity-temperature sensor was fabricated with the support by a previous DEPSCoR Equipment program (Grant No. F49620-93-1-0533). The vorticity sensor part of this miniature six-wire sensor was designed based on the probe made by Eckelmann et al. (1977) but much smaller. The measurement volume of this probe is 2.03 mm x 1.19 mm x 2.25 mm. This six-wire probe can directly measure the three-dimensional mean and fluctuating quantities of velocity, temperature, Reynolds stresses and Reynolds heat Fluxes. Using Taylor's

Hypothesis, it can also measure the mean and fluctuating quantities of all three components of vorticity as well as the vorticity-temperature correlations.

Since no existing data can be used to qualify all the parameters, a data evaluation process was conducted in the wake behind a 2-D cylinder cross-flow. The results show that the six-wire probe successfully determined the trend of the flow past the cylinder. However, the interpretation of the measured values of the three components of vorticity required an extreme caution. A careful analysis of the vorticity results indicated that it is not necessarily good for spacing between the sensors to be too close. The inherent measurement uncertainty can be amplified by the closeness of the sensors and introduce false vorticity values. For a meaningful application of a six-wire vorticity-temperature probe, it is crucial that the vorticity and its fluctuation scales of the test flow field be created to match the probe size, or a probe size and sensor spacing be appropriately designed for measuring a given vorticity field.

### **PERSONNEL ASSOCIATED WITH THIS PROJECT**

Jeffery Keller (Ph.D., graduated, partially supported by an EPSCoR Fellowship Grant)  
Mark Pinson (a doctoral student, partially supported by an EPSCoR Fellowship Grant)  
Scott Mislevy (MS, graduated, partially supported by an EPSCoR Fellowship Grant)  
Soovo Sen (MS, graduated, partially supported by this AFOSR grant)  
Dadong Zhou (Ph.D., graduated, partially supported by a previous AFOSR Grant)

### **PUBLICATIONS**

#### **Technical Reports:**

Mislevy, S. and Wang, T., "The Effects of Adverse Pressure Gradients on the Momentum and Thermal Structures in Transitional Boundary Layers," Research Report, Air Force Office of Scientific Research, 1995. --- Submitted earlier to Dr. James McMichael.

Pinson, M. and Wang, T., "The effects of Leading Edge Roughness on Flow and Heat Transfer in Transitional Boundary Layers," Research Report, Air Force Office of Scientific Research, 1998 ---- submitted with this final report.

Sen, Soovo and Wang, T., "Development of a Miniture Six-Wire Vorticity-Temperature Sensor," Research Report, Air Force Office of Scientific Research, 1998 --- submitted with this final report.

#### **Journal Publications (Attached in Appendix)**

1. Wang, T., J. F. Keller, and Zhou, D. D., "Flow and Thermal Structures in a Transitional Boundary Layer," J. of Experimental Fluid and Thermal Science, Vol. 12, pp.352-363, 1996.
2. Zhou, D. and Wang, T, 1995, "Effects of Elevated Free-stream Turbulence on Flow and Thermal Structures in Transitional Boundary Layers," ASME Journal of Turbomachinery, Vol. 117, pp. 407-417.

3. Keller, F. J. and Wang, T., 1996, "Flow and Heat Transfer Behavior in Transitional Boundary Layers with Streamwise Acceleration," ASME Journal of Turbomachinery, Vol. 118, pp. 314-326.
4. Zhou, D. and Wang, T, "Combined Effects of Elevated Free-Stream Turbulence and Streamwise Acceleration on Flow and Thermal Structures in Transitional Boundary Layers," Journal of Experimental Fluid and Thermal Science, Vol.12, pp. 338-351, 1996.
5. Wang, T. and Zhou, D., "Spectral Analysis of Transitional Boundary Layer on a Heated Plate," International Journal of Heat and Fluid Flow, vol.17 pp.12-21, 1996.
6. Keller, F. J. and Wang, T., "Effects of Criterion Functions on Intermittency in Heated Transitional Boundary Layers with and without Streamwise Acceleration," ASME Journal of Turbomachinery, Vol. 117, No. 1, pp. 154-165, 1995.
7. Wang, T. and Keller, F.J., "Intermittent Flow and Thermal Structures of Accelerated Transitional Boundary Layers, Part 1:Mean Quantities" ASME paper GT-97-402, accepted for publication in the ASME Journal of Turbomachinery, 1997.
8. Wang, T. and Keller, F.J., "Intermittent Flow and Thermal Structures of Accelerated Transitional Boundary Layers, Part 2: Fluctuation Quantities" ASME paper GT-97-403, accepted for publication in the ASME Journal of Turbomachinery, 1997
9. Wang, T. and Zhou, D., "Conditionally Sampled Flow and Thermal Structures of Heated Transitional Boundary Layers at Elevated Free-Stream Turbulence," accepted for publication in the International Journal of Heat and Fluid Flows, 1998.
10. Mislevy, S. P. and Wang, T., "The Effects of Adverse Pressure Gradients on Momentum and Thermal Structures in Transitional Boundary Layers. Part 1: Mean Quantities," ASME Journal of Turbomachinery, Vol. 118, pp. 717-727, 1996.
11. Mislevy, S. P. and Wang, T., "The Effects of Adverse Pressure Gradients on Momentum and Thermal Structures in Transitional Boundary Layers. Part 2: Fluctuation Quantities," ASME Journal of Turbomachinery, Vol. 118, 728-736, 1996.
12. Pinson, M. and Wang, T., "Effects of Leading Edge Roughness on Flow and Heat Transfer in Transitional Boundary Layers," International J. of Heat and Mass Transfer, Vol.40, No.12, pp 2813-2823, 1997.

**Referred Conference Proceedings (not attached)**

13. Wang, T. and Zhou, D., "Spectral Analysis of Transitional Boundary Layer on a Heated Plate," Proceedings of the Sixth Asian Congress of Fluid Mechanics, Singapore, May 1995, pp. 1226-1229.

14. Mislevy, S. P. and Wang, T., "The Effects of Adverse Pressure Gradients on Momentum and Thermal Structures in Transitional Boundary Layers. Part 1: Mean Quantities," ASME paper 95-GT-4, presented at the 1995 ASME International Gas Turbine Congress, Houston, June, 1995.
15. Mislevy, S. P. and Wang, T., "The Effects of Adverse Pressure Gradients on Momentum and Thermal Structures in Transitional Boundary Layers. Part 2: Fluctuation Quantities," ASME paper 95-GT-5, presented at the 1995 ASME International Gas Turbine Congress, Houston, June, 1995.
16. Pinson, M. and Wang, T., "Effects of Leading Edge Roughness on Flow and Heat Transfer in Transitional Boundary Layers," ASME Paper 94-GT-326, Presented at the 1994 International Gas Turbine Congress, Netherlands, June 1994.
17. Keller, F. J. and Wang, T., "Flow and Heat Transfer Behavior in Transitional Boundary Layers with Streamwise Acceleration," ASME Paper 94-GT-24, Presented at the 1994 International Gas Turbine Congress, Netherlands, June 1994.
18. Wang, T. and Keller, F.J., "Intermittent Flow and Thermal Structures of Accelerated Transitional Boundary Layers, Part 1:Mean Quantities" ASME paper GT-97-402, presented at the ASME Turbo Expo'97, Orlando, Fl, 1997
19. Wang, T. and Keller, F.J., "Intermittent Flow and Thermal Structures of Accelerated Transitional Boundary Layers, Part 2: Fluctuation Quantities" ASME paper GT-97-403, presented at the ASME Turbo Expo'97, Orlando, Fl, 1997
20. Wang, T. and Zhou, D., "Conditionally Sampled Flow and Thermal Structures of Heated Transitional Boundary Layers at Elevated Free-Stream Turbulence," ASME paper FEDSM 97-3109, presented at the ASME Fluid Engineering Conference, Vancouver, Canada, 1997.

# **Appendix**

## **Publications**



# Flow and Thermal Structures in a Transitional Boundary Layer

Ting Wang

F. Jeffrey Keller

Dadong Zhou

Department of Mechanical Engineering,  
Clemson University,  
Clemson, South Carolina

■ A three-wire probe was specifically designed and fabricated to measure the flow structure and the thermal field in transitional and low Reynolds number turbulent flow. In addition to the skin friction coefficient and Stanton number on the surface, detailed measurements were made of the mean and fluctuation quantities of the flow and temperature fields in the boundary layer. The evolution of the  $\bar{u}v$  profiles indicates that turbulent shear is generated near  $Y^+ = 70-100$  and imposes itself on the wall within the boundary layer.  $\bar{u}t$ ,  $\bar{v}t$ ,  $\varepsilon_H$ ,  $\varepsilon_M$ , and  $Pr_t$  were measured near the end of transition and in the turbulent flow region.  $Pr_t$  is shown to be greater than the typical value of 0.9 in the near-wall region. The Reynolds analogy factor (2  $St/C_f$ ) in the early turbulent flow region is approximately 0.9, which is lower than the typical value of 1.2 for turbulent flow. The data presented in this paper serve as the baseline for a series of consecutive studies related to investigating various parameters that affect laminar-turbulent transition.

**Keywords:** *transitional flow, Reynolds stress, Reynolds heat flux, turbulent Prandtl number*

## INTRODUCTION

Boundary layer transition from laminar to turbulent flow has been recognized as an important feature in the through-flow of a gas turbine [1-3]. Recognizing and understanding the fundamental mechanisms involved in transitional convective heat transfer are the keys to improving heat transfer modeling and enhancing the accuracy of thermal load predictions for gas turbine blades.

In the turbulent boundary layer, thermal transport is treated as a passive process that is predominantly controlled by the mixing effect of the turbulent momentum transport. The near-unity value of 0.9 has often been assigned to the turbulent Prandtl number for calculating heat transfer in a turbulent boundary layer. However, this close correlation between momentum and thermal transport has not been verified and may well be invalid for a boundary layer undergoing laminar-turbulent transition. The objective of this study is to investigate detailed flow and thermal structures in the transitional boundary layer.

Many studies have been conducted to investigate the flow and thermal structures in heated transitional boundary layers. However, most of them are either limited to wall measurements of  $C_f$  and  $St$  or provide only partial information of mean velocity ( $\bar{U}$ ), mean temperature ( $\bar{T}$ ), and streamwise velocity fluctuations ( $u'$ ). An extensive literature search on the measurement of Reynolds shear stress ( $\bar{u}v$ ) and heat fluxes ( $\bar{v}t$  and  $\bar{u}t$ ) in the transitional

boundary layer yielded little information. Most of the documented work was performed with fully developed turbulent boundary layers or in turbulent jets. Among the few studies providing both flow and heat transfer data in the transitional boundary layers is that of Kim et al. [4], who performed measurements of Reynolds heat fluxes ( $\bar{v}t$  and  $\bar{u}t$ ) on a flat plate at two different levels of free-stream turbulence intensity, 0.32% and 1.79%. In their experiment on low free-stream turbulence intensity (FSTI), the transitional region was too short to obtain useful information for  $\bar{v}t$  measurements. In their high-FSTI experiment, they observed that the turbulent heat flux ( $\bar{v}t$ ) was greater than the wall heat flux in the transitional region. This was not seen in a fully developed turbulent boundary layer. They calculated  $Pr_t$  through the transitional region, which had not been previously documented. Sohn et al. [5] performed a similar study in which they measured Reynolds heat fluxes over a flat plate. Surprisingly, they measured strong negative values of  $\bar{v}t$  in the transitional boundary layer, which had not been observed by Kim et al. [4].

In view of the inconvenience of patching the partial information obtained from various laboratories and reports and the lack of more complete information, including Reynolds stresses and Reynolds heat fluxes, this paper intends to provide a more integrated picture of heated transitional boundary layers by presenting data from a

Address correspondence to Professor Ting Wang, Department of Mechanical Engineering, Clemson University, Box 340921, Clemson, SC 29634-0921.

single facility. The measurements include  $C_f$ ,  $St$ ,  $\bar{U}$ ,  $\bar{T}$ ,  $u'$ ,  $v'$ ,  $ut$ , and  $uv$  through the transition region. Additional measurements of  $\bar{v}$ ,  $\varepsilon_H$ ,  $\varepsilon_M$ , and  $Pr_t$  were taken in the late part of the transition region and in the low Reynolds number turbulent region, where the boundary layer was sufficiently thick for accurate measurement of these variables. In addition, the data presented in this paper serve as the baseline for a series of sequential studies at Clemson University investigating parameters that affect laminar-turbulent transition in an actual gas turbine environment, such as elevated free-stream turbulence [6], favorable pressure gradients [7], adverse pressure gradients [8], and roughness [9].

## EXPERIMENTAL PROGRAM

### Test Facility

The experiments were conducted in a two-dimensional open circuit, blowing-type wind tunnel (Fig. 1). Using an industrial fan, air was drawn through the filter box and then forced through two grids, a honeycomb, a heat exchanger, a screen pack, and a 9:1 contraction nozzle before entering the test section. The air speed could be adjusted continuously (without steps) by a constant-torque, variable-frequency motor controller. The maximum velocity was 35 m/s, uniform within 0.7% and steady within 1% in a 20-h period. The free-stream temperature, controlled by a heat exchanger and the air-conditioning system in the laboratory, could be maintained within 0.5°C over a 20-h period with uniformity within 0.1°C. Both velocity and temperature uniformity were measured by using a 2.54 × 2.54-cm grid across the cross section of the test section inlet. A suction fan and a low-pressure plenum were installed to provide boundary layer suction at the leading edge, at a rate of 1100 cfm. The leading edge bleed scoop was designed after that of Blair et al. [10].

The rectangular test section is 0.15 m wide, 2.4 m long, and 0.92 m high and has an aspect ratio of 6 to reduce the effects of three-dimensionality. The rectangular test wall (2.4 × 0.92 m) is composite in nature and was designed and constructed to be flexible so that it can be bent to varying degrees of streamwise curvature for future efforts. The support wall is a 4.68-mm-thick polycarbonate sheet. The back of this polycarbonate sheet is covered with 0.25-m-thick R-30 fiberglass wool to minimize back-conduction loss to the room. Attached to the inside of the polycarbonate support wall is a 1.5-mm-thick heater patch.

The heater patch was constructed of heater foil sandwiched between a glass cloth and a silicone rubber sheet. The advantages of using this heating patch are that it is flexible and has a well-protected heating foil. Moreover, the heating patch does not wrinkle but remains flat during the periodic heating and cooling processes. A 1.56-mm-thick aluminum sheet is bonded to the heater to distribute the heat uniformly. Covering the aluminum sheet is a 0.04-mm-thick, 3M-413 double-sided tape. Grooves were carved through the tape to accommodate the thermocouples. One hundred eighty-five 3-mil E-type thermocouples were strategically deployed (Fig. 2). Of these 185 thermocouples, 74 were placed on the centerline and the rest in off-centerline positions in the cross-span direction to capture the "footprints" of the 3-D transitional flow. The grooves were then filled with high-temperature RTV. This arrangement ensures that the thermocouple junctions are well protected and that they can sustain severe bending stress in future curvature studies. A 1.56-mm-thick polycarbonate sheet was then placed over the double-sided tape. This smooth polycarbonate sheet serves as the boundary layer test surface. Another side of the test section, parallel to the test surface, is made of a 6-mm-thick flexible polycarbonate sheet. Fourteen 2.54-cm-diameter measuring holes were drilled along the centerline, and eight measuring holes of the same size were drilled off-centerline in the cross-span direction. Plexiglas plugs, flush with the inner surface, were used to plug the holes. Measurements were made by traversing the probe through these holes into the test section. The first measuring hole is located 20 cm from the leading edge, and the remainder are spaced 15 cm from each other. A very smooth Masonite table surface serves as the bottom wall of the test section. The outer wall can be adjusted to vary the pressure gradient in the test section. A detailed description of each component of the wind tunnel and the test facility is documented by Shome [11].

### The Three-Wire Sensor

The three-wire sensor is designed similarly to that used by Sohn et al. [5]. Basically, two 1.0-mm-long, 2.5- $\mu$ m-diameter gold-plated tungsten wires arranged in an X-array were used for velocity measurement. The sensing length is 0.5 mm, etched in the center (Fig. 3). The spacing between the wires in the X-array is 0.35 mm. The temperature sensor is a 1.2- $\mu$ m unplated platinum wire placed in

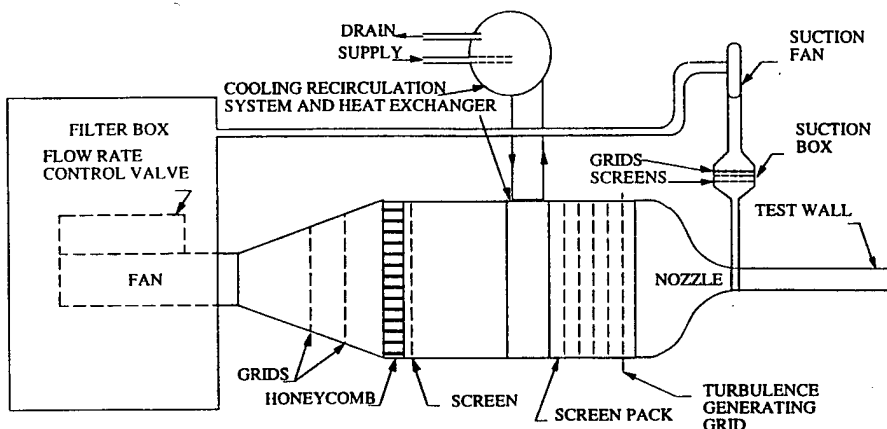


Figure 1. Schematic of the wind tunnel facility.

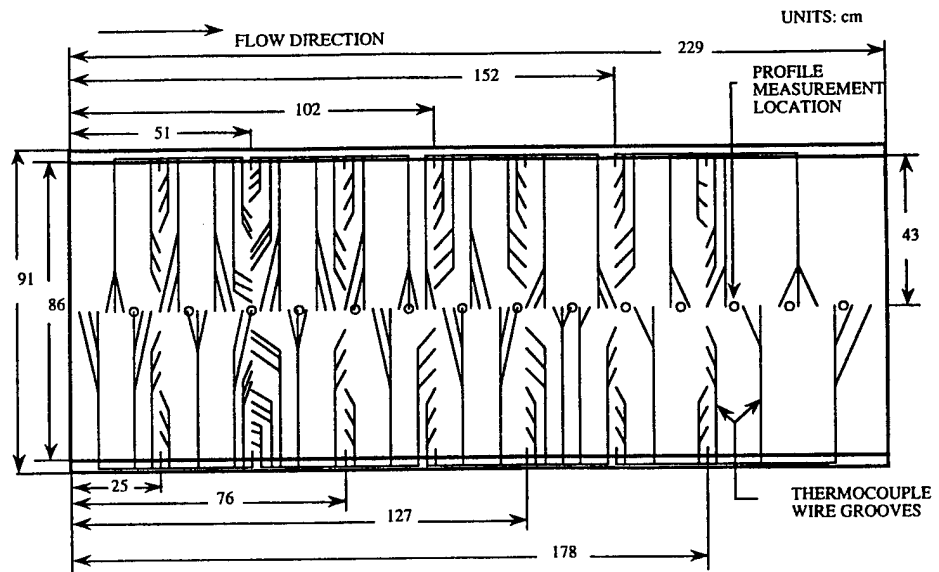


Figure 2. Schematic of test surface and thermocouple layout. (o) Locations for boundary layer measurements.

a plane parallel to that of the cross-wire and spaced 0.35 mm from the X-array. The typical prong configuration of a boundary layer probe is compromised, because bending three pairs of prongs to ensure the exact sensor arrangement is difficult from a fabrication point of view and is also costly. To allow near-wall measurement and to reduce probe interference, the probe support is bent at a 10°

angle from the wire axis (Fig. 3); this ensures that both of the X-wires can touch the wall simultaneously. This design, which doesn't involve bending the prongs, provides a 50% reduction in the manufacturing cost. Due to the 10° inclined angle, the cross-wires have respective slant angles of 35° and -55° relative to the probe axis, instead of the  $\pm 45^\circ$  of traditional X-wires. However, these X-wires are

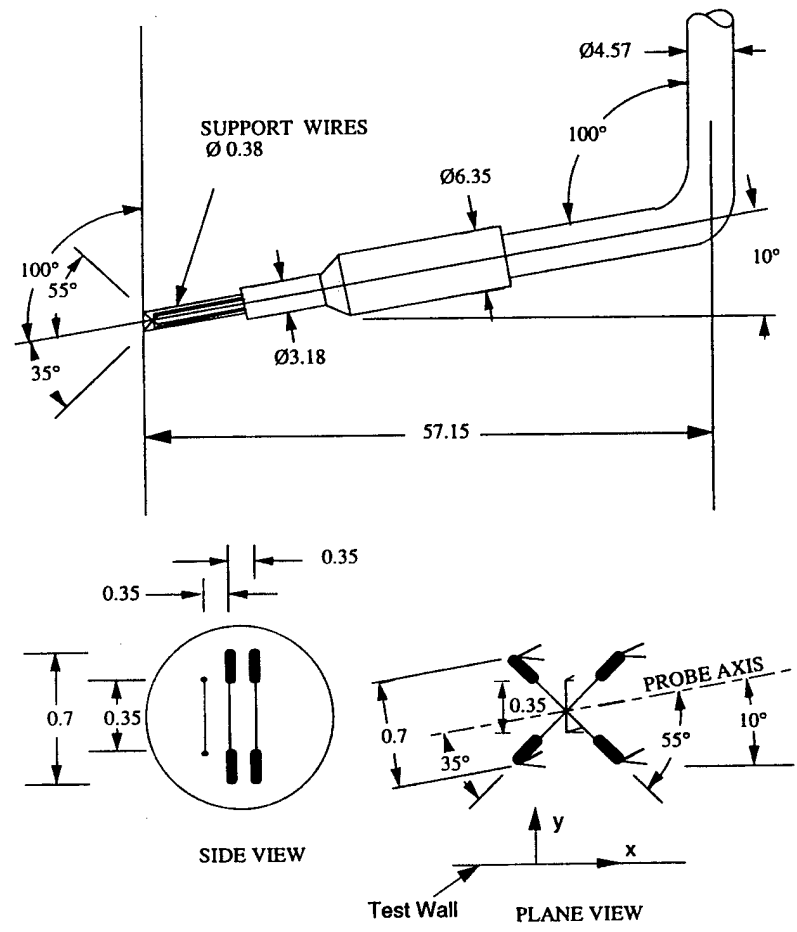


Figure 3. Three-wire boundary layer sensor for measuring Reynolds stresses and heat fluxes. Dimensions in millimeters.

DIMENSIONS IN mm

still perpendicular to each other. A detailed probe description is given by Shome [11] and Keller [12].

### Instrumentation and Measurements

A TSI IFA 100 intelligent flow analyzer system was used as a constant-temperature anemometer. A DISA M20 temperature bridge was used to operate the cold wire in the constant-current mode. The TSI Model 157 signal conditioner is used in the external mode for low-pass filtering of the cold-wire anemometer signals.

In order to simulate a zero pressure gradient flow condition, the  $C_{pr}$  distribution, with the reference temperature taken at the first station, was kept within  $\pm 1.0\%$  by adjusting the outer wall and measuring the static pressures at all 14 stations by a trial-and-error method.

The wind tunnel was started at least 12 h prior to the experimentation. The steadiness of the global wall temperature distribution was checked approximately every 2 h. Each time, an average of three different scans, with each scan made at a sample rate of 1 channel/s, was obtained. In addition, a local check of the steadiness of the wall temperature at each station was performed before, midway, and at the end of each measurement of the boundary layer temperature profile.

The X-wires of the three-wire sensor were operated at overheat ratios of 1.43 and 1.66 in the constant-temperature mode. The 1.2- $\mu\text{m}$  cold wire was operated at a very low overheat ratio in the constant-current mode by using the DISA M20 bridge. A probe current of 0.1 mA and an amplifier gain of 3500 were used. The frequency response of the temperature wire was found by Keller [12] to be approximately 3000 Hz. The data from all three sensors were sampled at 2 kHz for 20 s. A low-pass filter set at 1 kHz for each channel was also employed so that the data could be used later for power spectra and waveform analyses. To locate the wall, the smallest  $Y^+$  (near  $Y^+ = 7$ ) that could be achieved was specified, and the probe was traversed toward the wall until the mean streamwise velocity corresponding to the specified  $Y^+$  (as given by the near-wall region correlation,  $U^+ = Y^+$ ) was achieved. Measurements were made at 12 stations located at distances of 44.45–215.9 cm from the leading edge. No measurements were taken at the first two stations because of the thin boundary layer. Thirty points across the boundary layer were measured for each station.

Chua and Antonia's method [13] for correcting temperature contamination of the hot wires was used. The advantage of this method is that the hot-wire signal can be corrected by using instantaneous temperatures instead of instantaneous temperature fluctuations. Just as a hot wire responds to temperature fluctuations, a cold wire responds to velocity fluctuations. Analysis of the cold wire was performed in this study following the scheme presented by LaRue et al. [14]. For the 1.2- $\mu\text{m}$  cold wire, the velocity sensitivity coefficient at 20 m/s is  $1.75 \times 10^{-4} \text{ }^\circ\text{C}/(\text{m/s})$ . For a 5% change in velocity, the error in temperature measurement for the 1.25- $\mu\text{m}$  platinum wire is  $0.000175^\circ\text{C}$ . This estimate indicates that correction for velocity contamination is not required as long as a low heating current is used.

The three-wire sensor was qualified in a boundary layer undergoing laminar-turbulent transition. The standards used were mean velocity profile results, mean tempera-

tures, Reynolds normal and shear stresses, and the temperature fluctuations from a commercially available single hot wire, an X-wire, and a single cold wire. The results were satisfactory and were documented with detailed experimental procedures and data reduction techniques by Shome [11] and Keller [12].

### Stanton Number Measurement

The wall temperature was corrected for front polycarbonate wall conduction effects, radiation loss, back loss, streamwise conduction loss, compressibility, and recovery effect. The effect of relative humidity on obtaining the free-stream, dry-bulb temperature was also corrected. The detailed procedure was documented by Keller [12].

## RESULTS AND DISCUSSION

In this experiment, a boundary layer was allowed to undergo natural transition from laminar to fully turbulent flow. Three sets of Stanton number data were taken in one 22-h run. The first run was conducted after a 12-h stabilization period and followed by two runs conducted at 17 h and 22 h, respectively. The maximum variation in the Stanton numbers during the 10-h period was approximately  $\pm 3\%$ .

The free-stream turbulence intensity (FSTI), calculated from three components of velocity fluctuations, is shown in Fig. 4a to have a value of about 0.5% for a free-stream velocity of 13 m/s. The ratios of  $v'/u'$  and  $w'/u'$  in the free stream, also shown in Fig. 4a, are not isotropic; the values varied between 2.0 and 1.6 for  $v'/u'$  and between

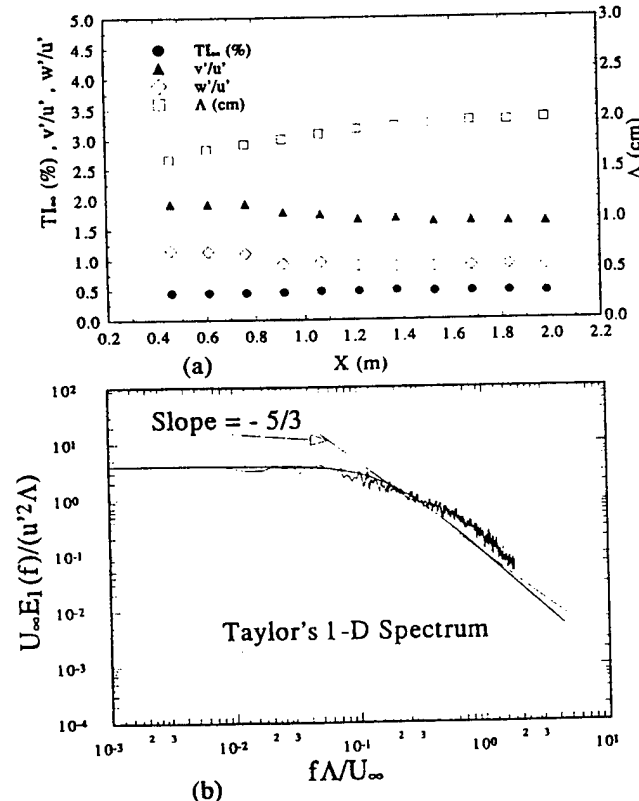
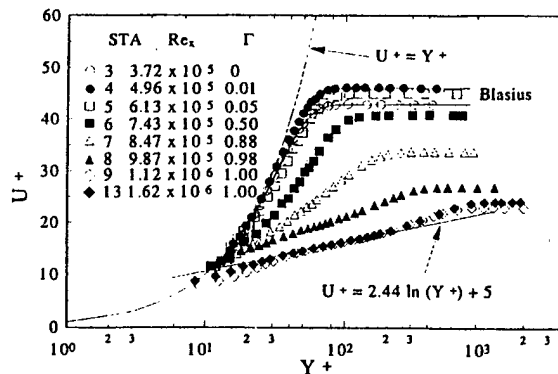


Figure 4. Free-stream turbulence. (a) Intensities and length scales; (b) spectral distribution.

Figure 5. Mean velocity profiles,  $U^+$  vs.  $Y^+$ .

0.9 and 1.1 for  $w'/u'$ . The free-stream turbulence integral length scales are also shown in this figure. The spectral distribution of the streamwise velocity fluctuations in the free stream for the baseline case is shown in Fig. 4b. The 1-D spectrum,  $E_1(f)$ , is normalized by  $u'^2$ , the integral length scale  $\Lambda$ , and the free-stream velocity  $U_\infty$ . The frequency  $f$  is normalized by  $\Lambda$  and  $U_\infty$ . For comparison, Taylor's 1-D energy spectrum [15] is also shown in this figure. The spectral distribution,  $E_1(f)$ , follows Taylor's 1-D energy spectrum in the low-frequency range and deviates from it in the high-frequency range. This is probably caused by the nonisotropy of the grid-generated free-stream turbulence structure in the present study.

### Mean Velocity Profiles

The results of the mean velocity profiles, plotted in wall units of  $U^+$  vs.  $Y^+$ , are shown in Fig. 5 and are consistent with those of Blair [16] and Kuan and Wang [17]. As seen in Fig. 5, the velocity profiles at stations 3 and 4 are Blasius flow. A set of single-wire data (not shown) was taken as a guide for determining the skin friction coefficients because the single wire could be positioned very close to the wall (about  $Y^+ = 2$ ). The skin friction coefficients for these two stations were determined by extrapolating the linear correlation ( $U^+ = Y^+$ ) to the wall. The profiles after  $Re_x = 1.12 \times 10^6$ , that is, stations 9–13, are clearly turbulent and preserve the “law of the wall” characteristics over a sufficient range of  $Y^+$ . This indicates that the Clauser technique is appropriate for determining the skin friction coefficient. The profiles from  $Re_x = 6.13 \times 10^5$  to  $9.87 \times 10^5$ , stations 5–8, are transitional, neither displaying the turbulent log-linear behavior nor matching the Blasius profile. Based on the assumption that the viscous sublayer within  $Y^+ < 10$  is not affected by the transition process, the  $C_f$  values for these transitional stations were determined by forcing the profile through the  $U^+ = Y^+$  correlation in the near-wall region ( $Y^+ < 10$ ).

### Skin Friction Coefficient and Stanton Number

The skin friction coefficient is shown in Fig. 6. In this study, the beginning of the transition is identified as the point of minimum skin friction coefficient, or lowest Stanton number, and the end of the transition as the point of maximum skin friction coefficient, or highest Stanton number, immediately following the rise. Based on these criteria, the onset of transition occurred at approximately

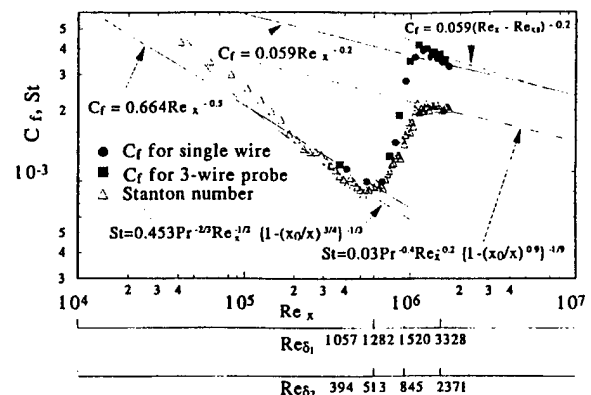


Figure 6. Skin friction coefficient and centerline Stanton number distributions. The correlations are from Kays and Crawford [27].

$Re_x = 5.5 \times 10^5$  ( $Re_{\delta_1} = 1294$ ,  $Re_{\delta_2} = 492$ ), and the end of transition occurred at approximately  $Re_x = 1.12 \times 10^6$  ( $Re_{\delta_1} = 1826$ ,  $Re_{\delta_2} = 1302$ ) (Table 1).  $C_f$  exceeds the turbulent correlation by 4% at  $Re_x = 1.12 \times 10^6$  (early turbulent flow).

The Stanton number measurements are overlaid in Fig. 6 with the skin friction coefficient. The Stanton number asymptotically approaches the turbulent correlation rather than “overshooting” the turbulent correlation, which, as is seen in the  $C_f$  values, results in a breakdown of the Reynolds analogy factor ( $2 St/C_f$ ) in the early turbulent region. As shown in Fig. 7, the value of  $2 St/C_f$  dips below the typical value for turbulent boundary layers in the late transition region ( $x = 120$  cm). The value for  $2 St/C_f$  is approximately 0.9 at station 9 and slowly approaches the fully turbulent value as the flow progresses downstream. This is consistent with the  $2 St/C_f$  value of 0.8 obtained by Wang [18] in the late transition and early turbulent regions.

The onset of transition was observed earlier than in previous studies, as shown in Fig. 8. For an FSTI value of 0.5%, the predicted  $Re_\theta$  for transition onset ranges between 615 from the Mayle [3] correlation to 771 from the

Table 1. Reynolds Numbers at Onset and End of Transition

FSTI at $X_s$	0.5%
$U_\infty$ (m/s)	12.24
Onset of transition	
$x$ (cm)	68
$Re_{xs}$	$5.5 \times 10^5$
$Re_{\delta_1}$	1294
$Re_{\delta_2}$	492
End of transition	
$x$ (cm)	137
$Re_{xe}$	$11.2 \times 10^6$
$Re_{\delta_1}$	1826
$Re_{\delta_2}$	1302
Length of transition	
$x$ (cm)	69
$Re_x$	$5.7 \times 10^5$
$Re_{\delta_1}$	532
$Re_{\delta_2}$	810

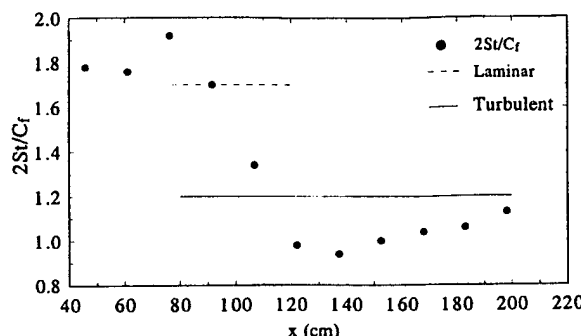


Figure 7. Reynolds analogy factor,  $2 St/C_f$ , distribution.

Abu-Ghannam and Shaw correlation [19]. The value obtained in this experiment,  $Re_{\theta_s} = 492$ , falls below this range. However, the results of Blair [20] for an FSTI of 0.17% and of Kim [21] for an FSTI of 0.3% also fall considerably below each of the prediction schemes. Since extensive efforts were made to minimize the possible effects of extraneous variables, factors other than FSTI must influence transition onset. This reinforces the similar conclusion made by Volino and Simon [22]. Abu-Ghannam and Shaw [19] proposed a correlation for the end of transition of the form  $Re_{\theta_E} = 2.667 Re_{\theta_s}$ . This correlation is also shown in Fig. 8. The  $Re_{\theta_E}$  value of 1302 determined for the baseline case is within 1% of the result calculated using the Abu-Ghannam and Shaw correlation. This earlier transition did not seem to affect the flow and thermal structures presented in this paper.

#### Boundary Layer Integral Parameters

The boundary layer thickness and integral parameters are shown in Fig. 9 along with the appropriate laminar and turbulent solutions. The turbulent solutions have been adjusted to account for the virtual origin of the turbulent boundary layer beginning at  $x_s$ . The boundary layer thickness observed in Fig. 9 can be explained using this approach. The boundary layer thickness follows the laminar boundary layer values up to the point of transition and

then follows the turbulent boundary layer values (beginning at  $x_s$ ) beyond this point. It is interesting to note that the boundary layer development of the transitional flow fits that of the turbulent flow after the effect of a virtual origin is incorporated. Dhawan and Narasimha [23] observed a similar result.

The displacement thickness, however, is seen to have a different development. It follows the laminar solution up through the end of transition, but when the flow becomes fully turbulent at station 9 ( $x = 137$  cm), the displacement thickness begins to increase and is approximately 5% higher than the turbulent values for stations 10–13. The shape factor  $H$  is observed to drop rapidly through the transition region and to reach a constant value of approximately 1.40 by station 9, which is 8.5% higher than the turbulent value of 1.29 predicted by the  $1/7$  power law.

#### Streamwise Velocity Fluctuations ( $u'^2$ )

The streamwise evolution of Reynolds normal stresses can be related to the evolution of  $u'$ , as shown in Fig. 10, which is comparable with those documented by Wang et al. [24], Kim et al. [25], and Kuan and Wang [17]. To avoid repeating lengthy discussions, a brief description is outlined below. Stations 3 and 4 are laminar. The peaks in the  $u'$  profiles indicate an amplifying sinusoidal instability wave that is not turbulence. The appearance of a near-wall peak at station 5 ( $Re_x = 6.13 \times 10^5$ ) indicates that the flow was undergoing transition. The peak value of  $u'/U_\infty$  within the boundary layer grew rapidly, and the location of the peak moved closer to the wall as the flow developed downstream in the transition region. The peak reached a maximum of 17.5% at  $y/\delta_1 = 0.05$  at station 7 ( $Re_x = 8.47 \times 10^5$ ). Beyond this point, the magnitude of the first peak diminished, but the location of the peak moved closer to the wall. A second peak can be observed at station 8 around  $y/\delta_1 = 2$ . For a more detailed discussion of streamwise Reynolds normal stress, see Kuan and Wang [17] or Kuan [26], where an in-depth analysis employing a conditional sampling technique was used to separate the intermittent effect from the real turbulence in the turbulent spots.

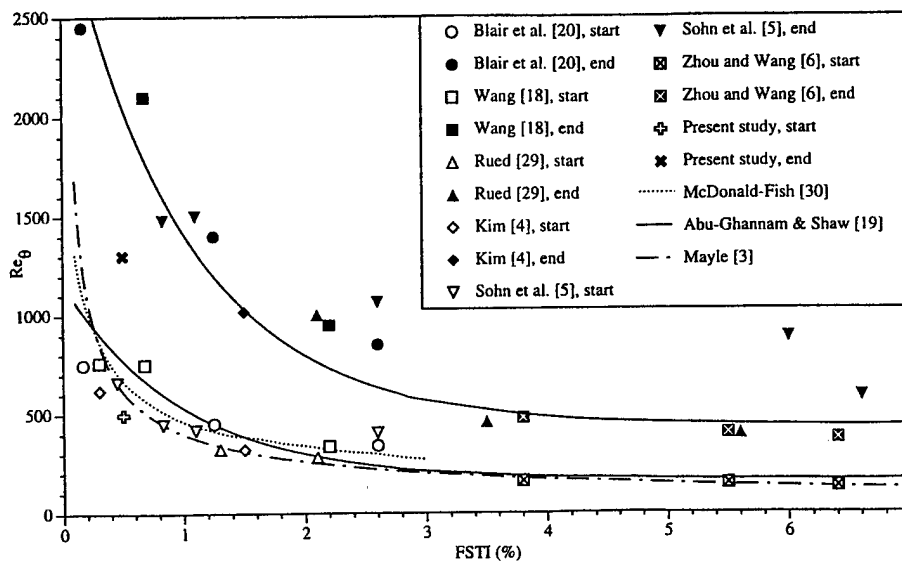


Figure 8. Comparison of start and end of transition versus FSTI.

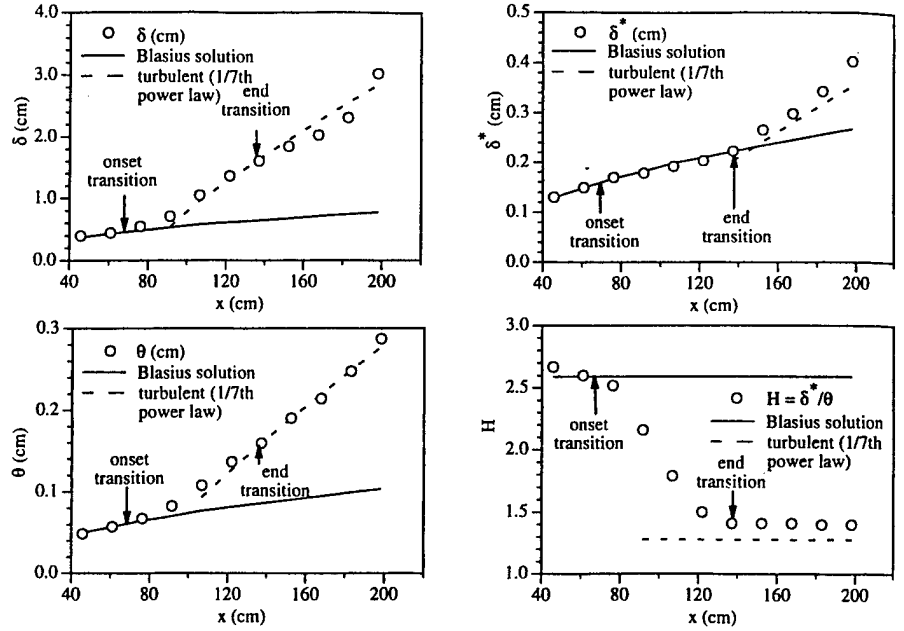


Figure 9. Boundary layer integral parameters.

#### Cross-Stream Velocity Fluctuations ( $\overline{v'^2}$ )

The evolution of  $v'$  in Fig. 11 was very similar to that of  $u'$  shown in Fig. 10. The near-wall peak reached a maximum of 4.5% at station 8, which is downstream of where the  $u'$  peak reached its maximum. The main difference between  $u'$  and  $v'$  is that  $u'$  decreased very quickly downstream from the maximum value, whereas the peak value of  $v'$  decreased only a small amount, to 4%, and maintained that value into the turbulent flow region. A second peak was also seen in the  $v'$  profile at station 7 at around  $y/\delta_1 = 1$ .

#### Reynolds Shear Stress ( $\overline{uv}$ )

As shown in Fig. 12, in the early transition at station 5 the peak of the turbulent shear ( $\overline{uv}$ ), which occurred at  $y/\delta = 0.2$ , was about 40% of the wall shear ( $u'^2$ ). At station 6, the peak of the turbulent shear moved outward

to  $y/\delta = 0.3$ , with a value larger than the wall shear. The peak of  $\overline{uv}$ , still staying at around  $y/\delta = 0.3$ , continued to grow to a maximum at station 7 of about twice the magnitude of the wall shear. The magnitude of  $\overline{uv}$  decayed after station 7 across the whole boundary layer and reached equilibrium between stations 9 and 13. In order to see more clearly the behavior of  $\overline{uv}$  near the wall, four selected  $\overline{uv}$  profiles at stations 4, 7, 8, and 13 have been replotted in wall coordinates ( $Y^+$ ) in Fig. 13. An almost constant turbulent shear stress appears in a region of  $Y^+ = 20-40$  at station 4. This indicates that the turbulent shear communicated well near the wall in the boundary layer in the early stage of the transition when the turbulence production was not high. Somehow, this communication could not keep up with the vigorous generation of turbulent shear stress that occurred around  $Y^+ = 70-100$  at station 7. The localized high shear, with a magnitude twice that of the wall shear, took a little while to communicate with the wall until a relatively uniform distribution

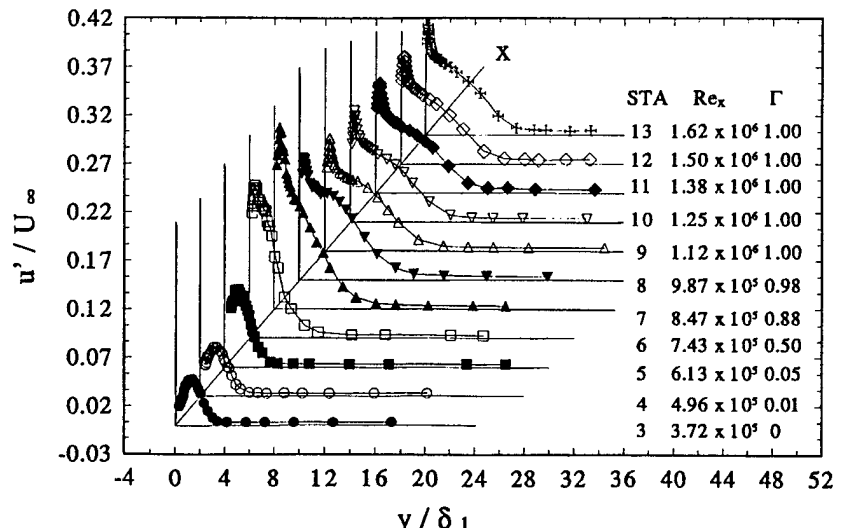


Figure 10. Streamwise velocity fluctuation profiles.

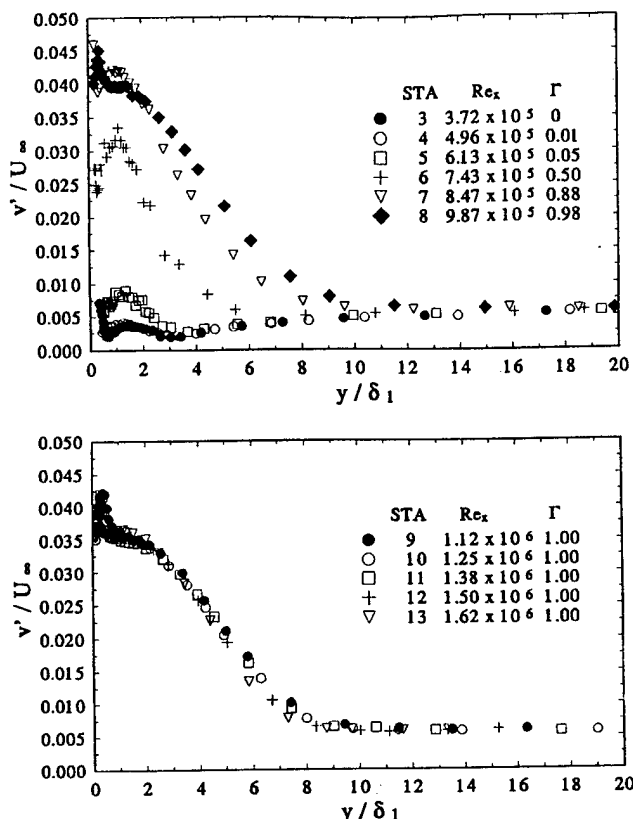


Figure 11. Cross-stream velocity fluctuation distributions.

of  $\bar{uv}$  in  $Y^+ = 70-100$  could be seen at station 8. This constant  $\bar{uv}$  region became more uniformly distributed and stretched to a wider region ( $Y^+ = 20-200$ ) at station 13. The magnitude of maximum  $\bar{uv}/u^{*2}$  decreased from 1.8 at station 7, through 1.2 at station 8, to finally about 0.9 at station 13. This whole sequence of turbulent shear development indicates that the turbulent shear actually imposes itself on the wall shear from a region away from the wall. Although locally the turbulent shear stress diminishes near the wall, the turbulent shear stress produced within the boundary layer is able to influence the mean velocity profile through the turbulence diffusion and local momentum balance such that the molecular shear at the wall is adjusted to be approximately equal to the turbulent shear. This is evidenced by the near-wall region of constant turbulent shear stress over the friction velocity ratio at about 0.9 at station 13 in Fig. 13.

The phenomena described above, which indicate that the boundary layer Reynolds shear stress in the transitional region is greater than the wall shear stress, can be further verified by integrating the mean flow governing equations. Assuming that the mean flow is two-dimensional in the transitional region at a zero pressure gradient, the mean flow governing equations are

$$\frac{\partial U}{\partial x} + \frac{\partial V}{\partial y} = 0 \quad (1)$$

and

$$\rho U \frac{\partial U}{\partial x} + \rho V \frac{\partial U}{\partial y} = \frac{\partial \tau}{\partial y} \quad (2)$$

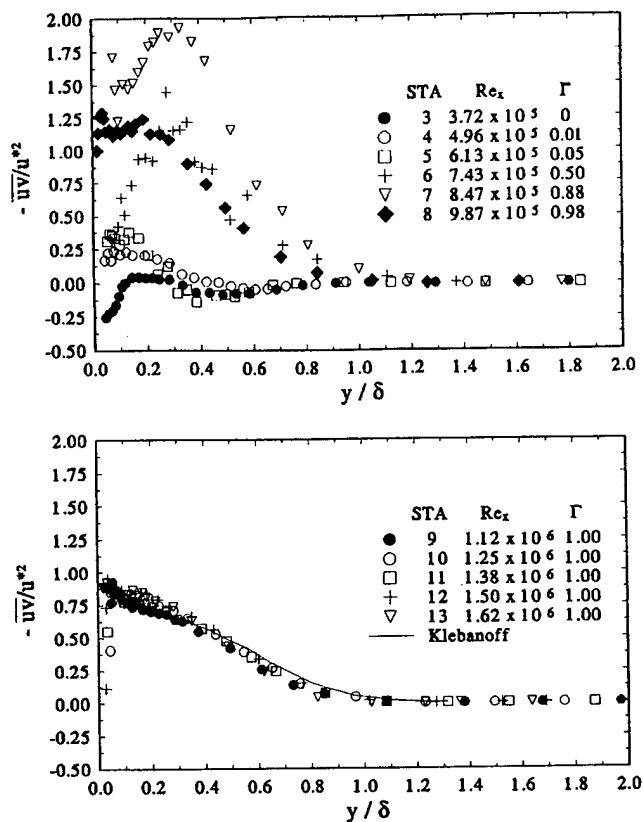


Figure 12. Reynolds shear stress distributions.

In these equations,  $U$  and  $V$  are the mean streamwise and cross-stream velocities and  $\tau$  is the total shear stress contributed by both the molecular shear stress and the Reynolds shear stress.

Equation (2)  $- \rho U \times$  Eq. (1) gives

$$\begin{aligned} \rho U \frac{\partial U}{\partial x} + \rho V \frac{\partial U}{\partial y} - \rho U \left( \frac{\partial U}{\partial x} + \frac{\partial V}{\partial y} \right) &= \frac{\partial \tau}{\partial y}, \\ \rho V \frac{\partial U}{\partial y} - \rho U \frac{\partial V}{\partial y} &= \frac{\partial \tau}{\partial y}, \quad (3) \\ \text{or } -\rho U^2 \frac{\partial(V/U)}{\partial y} &= \frac{\partial \tau}{\partial y}. \end{aligned}$$

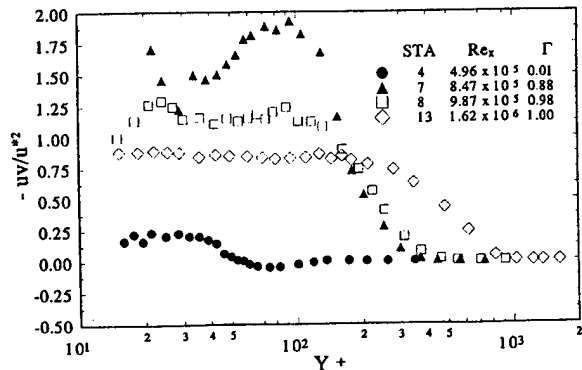


Figure 13. Reynolds shear stress distributions in wall coordinates.

Integration of Eq. (3) from zero to any  $y$  location gives

$$\tau(y) - \tau_w = \int_0^{V/U(y)} (-\rho U^2) d\left(\frac{V}{U}\right). \quad (4)$$

By applying l'Hospital's rule and the continuity equation, it can be shown that  $V/U \rightarrow 0$  as  $y \rightarrow 0$ .

In the transitional boundary layer region, the mean velocity profile changes from a laminar profile to a turbulent profile, so  $U$  increases in the near-wall region along the downstream direction (e.g.,  $\partial U / \partial x > 0$ ). Therefore, from the continuity equation,  $\partial V / \partial y < 0$ . Since  $V$  is zero at the wall, there is a negative  $V$  region close to the wall. Also,  $V/U$  approaches zero as it moves toward the wall, and  $U$  is positive in the boundary layer, so  $|V/U|$  decreases close to the wall. Furthermore, the integration in Eq. (4) is positive in this near-wall region because both  $-\rho U^2$  and  $V/U$  are negative. Therefore, the total shear stress  $\tau$  should increase away from the wall in the near-wall region of the boundary layer. With the fact that the molecular shear stress decreases away from the wall, the Reynolds shear stress increases away from the wall and can become larger than the wall shear stress.

### Mean Temperature

The mean temperature profiles are plotted in wall coordinates of  $T^+$  vs.  $Y^+$  in Fig. 14, along with three correlations: (1) the laminar solution for uniform heat flux with the effect of unheated starting length, (2) the conduction layer distribution  $T^+ = \text{Pr}_t Y^+$ , and (3) the turbulent temperature "law of the wall":

$$T^+ = Y_{cl}^+ \text{Pr}_t + \frac{\text{Pr}_t}{0.41} \ln\left(\frac{Y^+}{Y_{cl}^+}\right)$$

from Kays and Crawford [27]. The evolution of the mean temperature profile in a transitional flow is similar to the mean velocity profile, although subtle differences exist. In Fig. 5, the mean velocity profile becomes fully turbulent between stations 9 and 13, whereas the mean temperature profiles are still changing, as shown in Fig. 13. This indicates a lag in the development of the mean temperature compared to the mean velocity profiles. This would support the observation made earlier in Fig. 7 that a break-

down of the Reynolds analogy occurs in the late transition and early turbulent regions. Similar observations were made by Blair [20] and by Wang et al. [24].

### RMS Temperature Fluctuation ( $t'$ )

The evolution of the rms temperature fluctuation normalized by the temperature difference  $T_w - T_x$  is presented in Fig. 15. At about station 5 ( $\text{Re}_x = 6.13 \times 10^5$ ), the profile shows the appearance of a near-wall peak, indicating the onset of transition. The near-wall peak grew sharply as the transition proceeded, reached a maximum of about 0.11 at station 7, and then decayed. A secondary peak appeared at  $y/\delta = 0.5$  at station 6 ( $\text{Re}_x = 7.43 \times 10^5$ ). This secondary peak was also observed by Sohn et al. [5], although they did not observe the near-wall peak. The trend of  $t'$  is very similar to the  $u'$  profiles in the appearance of a near-wall peak and a secondary peak. As the transition proceeded further downstream, the location of the near-wall peak moved closer to the wall and the magnitude of the secondary peak was reduced. At the later stages of transition, the  $t'$  profile asymptotically attained some kind of similarity. This observation indicates a similarity between the  $t'$  and the  $u'$  profiles, except that the  $t'$  profiles have a less steep slope outward from the peak and show a broader plateau before the  $t'$  falls off in the outer boundary layer.

### Reynolds Heat Fluxes ( $\bar{vt}$ and $\bar{ut}$ )

One of the primary aims of this study was to measure the Reynolds heat fluxes,  $\bar{vt}$  and  $\bar{ut}$ . However, accurate  $\bar{vt}$  measurements in the transitional boundary layer are difficult. Due to the thin transitional boundary layer in the present experimental rig, the measurements of  $\bar{vt}$  are extremely uncertain and the results are under investigation (see detailed discussions in [11, 12, 28]). Therefore, only the results in the late transition and early turbulent boundary layer, normalized by the wall heat flux, are shown in Fig. 16. Unlike the  $\bar{uv}$  distribution, there is no region of constant heat flux across the boundary layers.

Despite the difficulty in accurately measuring  $\bar{vt}$  in the transitional boundary layer, the measurements of  $\bar{ut}$  are clean and without any ambiguities because the value of  $u$

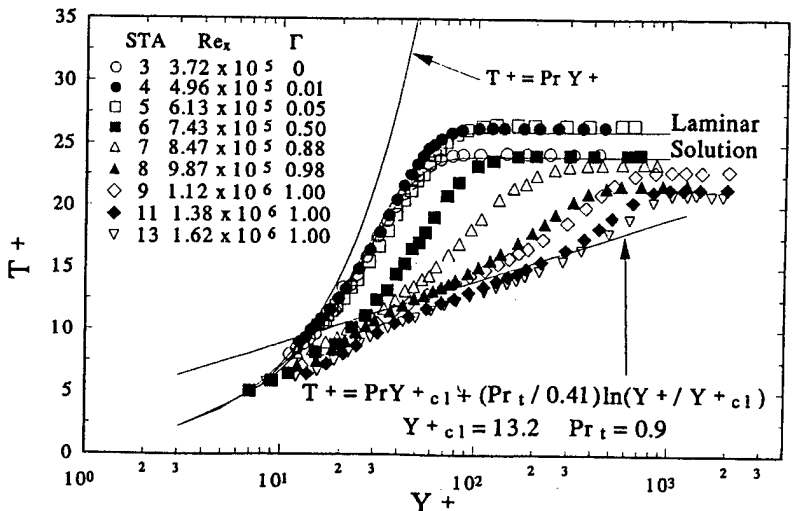


Figure 14. Mean temperature profiles,  $T^+$  vs.  $Y^+$ .

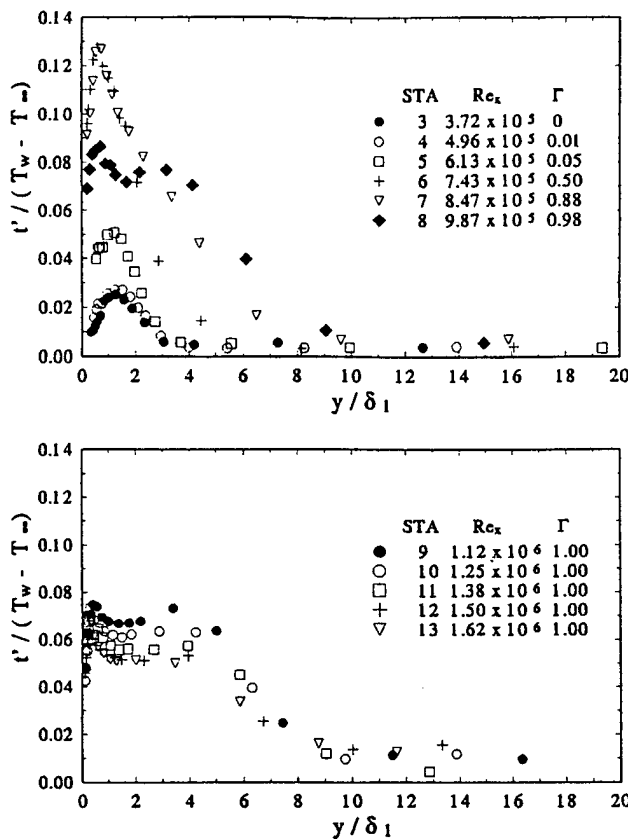


Figure 15. Streamwise evolution of rms temperature profiles.

is normally one order of magnitude larger than  $v$ . The results of the negative streamwise Reynolds heat flux,  $-\bar{u}t$ , normalized by the wall heat flux are shown in Fig. 17. In the late laminar flow (stations 3 and 4),  $-\bar{u}t$  had a maximum value in the magnitude of the wall heat flux at about  $y = 0.45\delta$ . This indicates that some turbulent transport of heat flux had occurred in the late laminar region. Once the flow entered the transitional region,  $-\bar{u}t$  increased dramatically to a maximum of about 17 times greater than the wall heat flux at stations 6 and 7 and then decreased at the outer boundary layer. A comparison between stations 6 and 7 shows that the near-wall peak maintained the same magnitude for both stations but that station 6 had a higher value of  $-\bar{u}t$  in the outer boundary

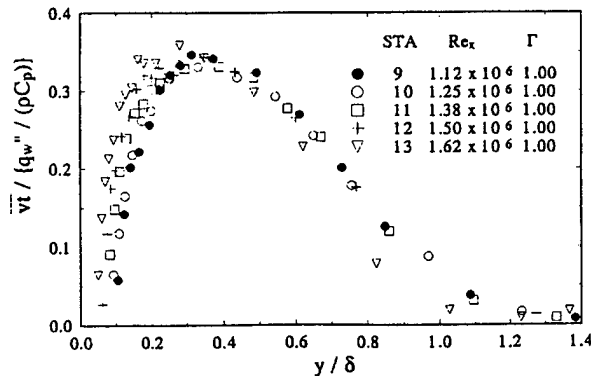


Figure 16. Cross-stream Reynolds heat flux distributions.

layer. Stations 8 and 9, in the late transitional region, both show a near-wall peak and a secondary peak at about  $y = 0.48$ , which is close to the local maximum of stations 3 and 4. From station 10 to station 13, the flow gradually reached equilibrium outward from the wall in the turbulent flow.

#### Eddy Diffusivities and Turbulent Prandtl Number

The eddy viscosity  $\varepsilon_M$  and the turbulent thermal diffusivity  $\varepsilon_H$  normalized by their molecular counterparts are shown in Fig. 18. Note that each station is plotted on a different scale. Both  $\varepsilon_M/\nu$  and  $\varepsilon_H/\alpha$  have finite values much beyond the boundary layer thickness. This indicates that the turbulent shear stress layer and the turbulent heat flux layer were thicker than the velocity and thermal boundary layers. After station 8,  $\varepsilon_M$  showed a distinctive peak near  $y/\delta = 0.3$ –0.4, and the peak remained at that location downstream. However,  $\varepsilon_H/\alpha$  did not show such a distinctive peak. The different distributions of  $\varepsilon_M/\nu$  and  $\varepsilon_H/\alpha$  reflect the disparity between the turbulent momentum and the thermal transport mechanism in the transitional boundary layer. The values for both  $\varepsilon_M/\nu$  and  $\varepsilon_H/\alpha$  increased continuously downstream, with  $\varepsilon_M/\nu$  having much higher values than  $\varepsilon_H/\alpha$ . The maximum values at station 13 for  $\varepsilon_M/\nu$  and  $\varepsilon_H/\alpha$  were about 50 and 20, respectively.

The value of  $Pr_t$  in the outer boundary layer ( $y/\delta > 0.2$ ) is greater than the value of 0.9 typically used in modeling transitional flow, although it is still of magnitude

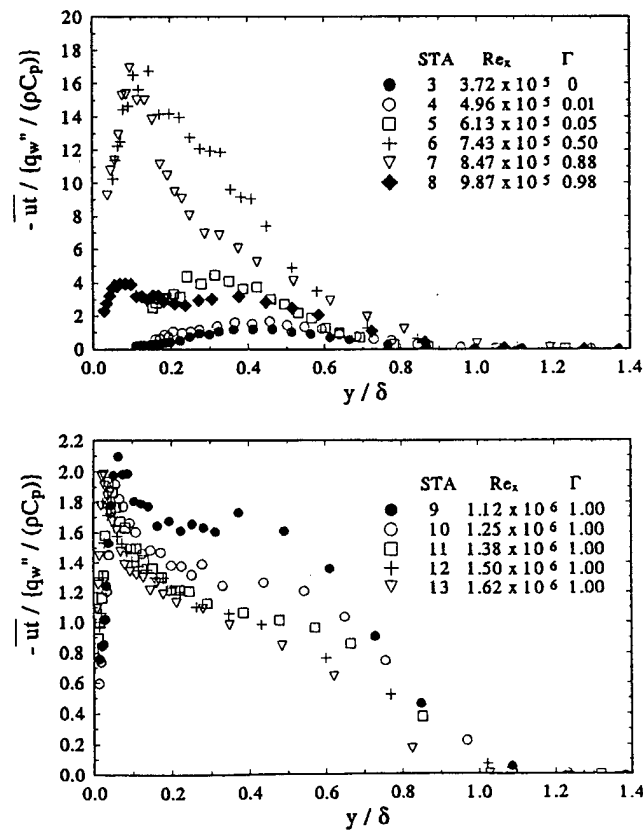


Figure 17. Streamwise Reynolds heat flux distributions.

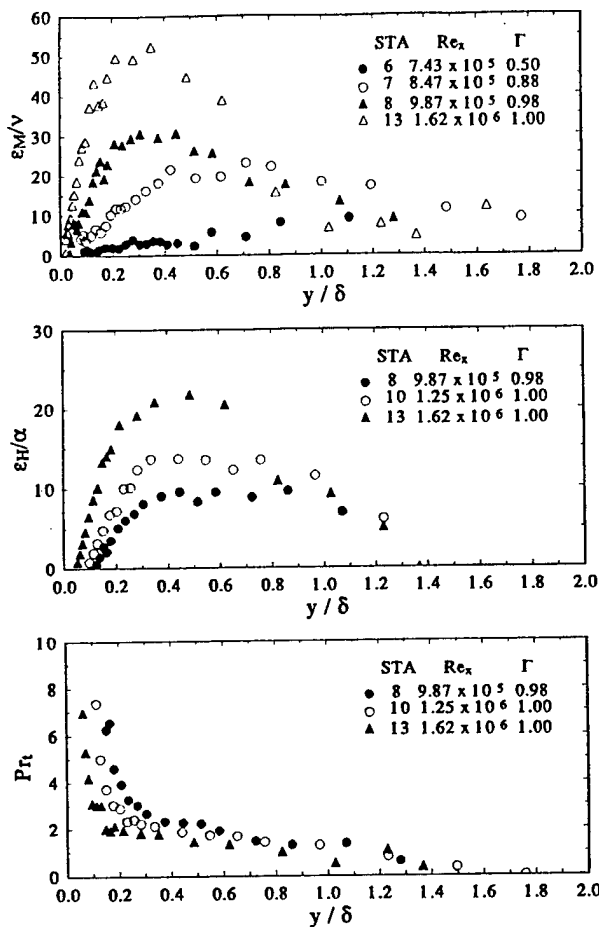


Figure 18. Streamwise evolution of eddy viscosity, diffusivity, and turbulent Prandtl number profiles.

unity. In the near wall region, the value of  $Pr_t$  is much higher than 1.

### UNCERTAINTY

The uncertainty analysis of the three-wire probe was performed by Keller [12]. The largest contribution to the uncertainty of  $\bar{u}v$  and  $u'$  was from the yaw factor. The total uncertainty was about 12% for  $\bar{u}v$  and 7% for  $u'$ . The uncertainty values for the other parameters are shown in Table 2.

### CONCLUSION

A three-wire probe was designed and custom made for the measurement of Reynolds stresses and heat fluxes in a transitional boundary layer. Two of the three wires, which were used for measuring velocities, were operated hot in a constant-temperature mode. The third wire, which measured temperature, was operated cold (low overheat) in a constant-current mode. In addition to the skin friction coefficient and Stanton number on the surface, detailed measurements were made of the mean and fluctuation

quantities of the flow and temperature fields in the boundary layer. The results show that the evolution of  $v'$  is faster than that of  $u'$ .  $v'$  reaches an asymptotic distribution across the boundary layer in the middle of the transition and maintains that value through the end of transition and into the turbulent region, whereas  $u'$  reaches a maximum in the middle of the transition region and decreases into the turbulent flow region. The evolution of the  $\bar{u}v$  profiles in the transitional flow indicates that turbulent shear was generated in the region of  $Y^+ = 70-100$  and gradually changed the mean velocity profile near the wall by imposing itself on the wall within the boundary layer.

The streamwise Reynolds heat flux,  $\bar{u}t$ , can be as high as 17 times greater than the wall heat flux in the transitional boundary layer.  $\bar{u}t$ ,  $\varepsilon_H$ ,  $\varepsilon_M$ , and  $Pr_t$  were measured near the end of transition and in the low Reynolds number turbulent flow region. Both the turbulent shear stress layer and the turbulent heat flux were measured to be much thicker than the velocity and thermal boundary layers.  $Pr_t$  is shown to increase beyond a typical value of 0.9 as the wall is approached. The Reynolds analogy factor ( $2 St/C_f$ ) in the early turbulent flow region is approximately 0.9, which is lower than the typical turbulent flow value 1.2.

The difference in the distribution of  $\varepsilon_M$  and  $\varepsilon_H$  reflects the apparent disparity between the turbulent momentum and the thermal transport mechanisms in the transitional boundary layer. The physics of this should be incorporated into transitional flow models when computational methods are used.

This program was sponsored by the Air Force Office of Scientific Research (grant No. AFOSR-89-0324) and the Office of Naval Research (grant No. N00014-89-J-3105). Part of the facility was previously constructed through support from the National Science Foundation (grant No. CBT-8708843). The U.S. government is authorized to reproduce and distribute reprints for governmental purposes notwithstanding any copyright notation thereon.

### NOMENCLATURE

$C_f$	skin friction coefficient [ $= \tau_w/(\rho U_\infty^2/2)$ ], dimensionless
$C_p$	specific heat, J/g-k
$C_{pr}$	static pressure coefficient [ $= (P - P_{ref})/\rho U_\infty^2$ ], dimensionless
FSTI	free-stream turbulence intensity ( $= [(u^2 + v^2 + w^2)/3]^{1/2}/U_\infty$ ), percent
$Pr_t$	turbulent Prandtl number ( $= [\bar{u}v/(\partial U/\partial y)]/[\bar{u}t/(\partial T/\partial y)]$ ), dimensionless
$q''$	heat flux, watt/m <sup>2</sup>
St	Stanton number [ $= q''/\rho C_p U_\infty (T_w - T_\infty)$ ], dimensionless
$t$	fluctuation in temperature, K
$T$	instantaneous temperature, K

Table 2. Uncertainties of  $\bar{U}$ ,  $\bar{T}$ ,  $u'$ ,  $v'$ ,  $t'$ ,  $\bar{u}v$ ,  $\bar{u}t$ , and  $\bar{v}t$  in the Transitional Region

Parameter	$\bar{U}$	$(\bar{T} - \bar{T}_\infty) / (\bar{T}_w - \bar{T}_\infty)$	$u'$	$v'$	$t' / (\bar{T}_w - \bar{T}_\infty)$	$\bar{u}v$	$\bar{u}t$	$\bar{v}t$
Uncertainty (%)	3.5	1.7	3.6	8.4	1.8	15.0	3.7	20.4

$\bar{T}$	mean temperature, K
$t'$	rms value of temperature fluctuations, K
$u, v$	instantaneous velocity fluctuations in streamwise and cross-stream directions, m/s
$u', v'$	rms values of velocity fluctuations, m/s
$u^*$	friction velocity ( $\equiv \sqrt{\tau_w/\rho}$ ), m/s
$\bar{ut}$	streamwise Reynolds heat flux, mK/s
$\bar{uv}$	Reynolds shear stress, $\text{m}^2/\text{s}^2$
$\bar{vt}$	cross-stream Reynolds heat flux mK/s
$U$	instantaneous velocity, m/s
$\bar{U}$	mean streamwise velocity, m/s
$U^+$	( $= U/u^*$ ), dimensionless
$X_0$	unheated starting length, m
$x_s$	onset of transition, m
$Y^+$	( $= yu^*/\nu$ ), dimensionless

#### Greek Symbols

$\delta$	boundary layer thickness at $0.995U_\infty$ , m
$\delta_1$	displacement layer thickness, m
$\delta_2$	momentum layer thickness, m
$\varepsilon_H$	turbulent (or eddy) thermal diffusivity, $\text{m}^2/\text{s}$
$\varepsilon_M$	turbulent (or eddy) viscosity, $\text{m}^2/\text{s}$
$\rho$	density, $\text{kg}/\text{m}^3$
$\tau_w$	shear stress on the wall, $\text{N}/\text{m}^2$
$\Lambda$	integral length scale ( $= U_0^\infty \bar{u}(t)u(t+\tau)/\bar{u}^2 d\tau$ ), m
$\Gamma$	intermittency, dimensionless

#### Subscripts

w	at the wall
$\infty$	in the free stream

#### REFERENCES

1. Graham, R. W., Fundamental Mechanisms that Influence the Estimate of Heat Transfer to Gas Turbine Blades, 79-HT-43, ASME, New York, 1979.
2. Graham, R. W. (Ed.), *Transition in Turbines*, Symposium Proceedings, NASA CP-2386, 1984.
3. Mayle, R. E., The Role of Laminar-Turbulent Transition in Gas Turbine Engines, *J. Turbomach.* **113**, 509-537, 1991.
4. Kim, J., Simon, T. W., and Kestoras, M., Fluid Mechanics and Heat Transfer Measurements in Transitional Boundary Layers Conditionally Sampled on Intermittency, *ASME J. Turbomach.* **116**, 405-416, 1994.
5. Sohn, K. H., Reshotko, E., and Zaman, K. B. M. Q., Experimental Study of Boundary Layer Transition on a Heated Flat Plate, FED-114, ASME, New York, 167-172, 1991.
6. Zhou, D., and Wang, T., Effects of Elevated Free-Stream Turbulence on Flow and Thermal Structures in Transitional Boundary Layers, 93-GT-66, ASME, New York, 1993; also in *ASME J. Turbomach.* **117**, 407-417, 1995.
7. Keller, F. J., and Wang, T. W., Flow and Heat Transfer Behavior in Transitional Boundary Layers with Streamwise Acceleration, 94-GT-24, ASME, New York, 1994; also to appear in *ASME J. Turbomach.* 1996.
8. Mislevy, S. P., and Wang, T., The Effects of Adverse Pressure Gradients on Momentum and Thermal Structures in Transitional Boundary Layers: Part 1: Mean Quantities; Part 2: Fluctuation Quantities, 95-GT-4 and 95-GT-5, ASME, New York, 1995.
9. Pinson, M., and Wang, T., Effects of Leading-Edge Roughness on Fluid Flow and Heat Transfer in the Transitional Boundary Layer over a Flat Plate, 94-GT-326, ASME, New York, 1994.
10. Blair, M. F., Bailey, D. A., and Schlinker, R. H., Development of a Large-Scale Wind Tunnel for the Simulation of Turbomachinery Airfoil Boundary Layers, *Trans. ASME* **103**, 678-687, 1981.
11. Shome, B., Development of a Three-Wire Probe for the Measurement of Reynolds Stresses and Heat Fluxes in Transitional Boundary Layers, M.S. Thesis, Dept. Mech. Eng., Clemson Univ., Clemson, SC, 1991.
12. Keller, F. J., Flow and Thermal Structures in Heated Transitional Boundary Layers With and Without Streamwise Acceleration, Ph.D. Dissertation, Dept. Mech. Eng., Clemson Univ., Clemson, S.C., 1993.
13. Chua, L. P., and Antonia, R. A., Turbulent Prandtl Number in a Circular Jet, *Int. J. Heat Mass Transfer* **33**(2), 331-339, 1990.
14. LaRue, J. C., Deaton, T., and Gibson, C. H., Measurement of High-Frequency Temperature, *Rev. Sci. Instrum.* **46**(6), 757-764, 1975.
15. Taylor, G. I., The Spectrum of Turbulence, *Proc. Roy. Soc.*, 1937, Series A151, page 421.
16. Blair, M. F., Influence of Free-Stream Turbulence on Turbulent Boundary Layer Heat Transfer and Mean Profile Development, Part I: Experimental Data, *J. Heat Transfer* **105**, 33-47, 1983.
17. Kuan, C. L., and Wang, T., Investigation of the Intermittent Behavior of a Transitional Boundary Layer Using a Conditional Averaging Technique, *Exp. Thermal Fluid Sci.* **3**, 157-170, 1990.
18. Wang, T., An Experimental Investigation of Curvature and Free-Stream Turbulence Effects on Heat Transfer and Fluid Mechanics in Transitional Boundary Layers, Ph.D. Dissertation, Dept. Mech. Eng., Univ. Minnesota, Minneapolis, MN, 1984.
19. Abu-Ghannam, B. J., and Shaw, R., Natural Transition of Boundary Layers—The Effect of Turbulence, Pressure Gradient and Flow History, *J. Mech. Eng. Sci.* **22**, 213-228, 1980.
20. Blair, M. F., Influence of Free-Stream Turbulence on Boundary Layer Transition in Favorable Pressure Gradients, *J. Eng. Power* **104**, 743-750, 1982.
21. Kim, J., Free-Stream Turbulence and Concave Curvature Effects on Heated, Transitional Boundary Layers, Ph.D. Dissertation, Dept. Mech. Eng., Univ. Minnesota, Minneapolis, MN, 1990.
22. Volino, R. J., and Simon, T. W., Bypass Transition in Boundary Layers Including Curvature and Favorable Pressure Gradient Effects, *ASME J. Turbomach.* **117**, 166-174, 1995.
23. Dhawan, S., and Narasimha, P., Some Properties of Boundary Layer Flow during the Transition from Laminar to Turbulent Motion, *J. Fluid Mech.* **3**, 418-436, 1958.
24. Wang, T., Simon, T. W., and Buddhavarapu, J., Heat Transfer and Fluid Mechanics Measurements in Transitional Boundary Layer Flows, *ASME J. Turbomach.* **109**(3), 443-452, 1987.
25. Kim, J., Simon, T. W., and Kestoras, M., Fluid Mechanics and Heat Transfer Measurements in Transitional Boundary Layers Conditionally Sampled on Intermittency, *Int. J. Heat Mass Transfer* **3**, 133-154, 1989.
26. Kuan, C. L., An Experimental Investigation of Intermittent Behavior in the Transitional Boundary Layer, M.S. Thesis, Dept. Mech. Eng., Clemson Univ., Clemson, SC, 1987.
27. Kays, W. M., and Crawford, M. E., *Convective Heat and Mass Transfer*, McGraw-Hill, New York, 1993.
28. Wang, T., Keller, F. J., and Zhou, D., Experimental Investigation of Reynolds Shear Stresses and Heat Fluxes in a Transitional Boundary Layer, *Fundamental and Applied Heat Transfer Research for Gas Turbine Engines* (ASME HTD 226) pp. 61-70, 1992.
29. Rued, K., and Wittig, S., Free-Stream Turbulence and Pressure Gradient Effects on Heat Transfer and Boundary Layer Development on Highly Cooled Surfaces, *J. Turbomach.* **107**, 1007-1015, 1985.
30. McDonald, H., and Fish, R. W., Practical Calculations of Transitional Boundary Layers, *Int. J. Heat Mass Transfer* **16**, 1729-1744.

D. Zhou  
J. Wang

Department of Mechanical Engineering,  
Clemson University,  
Clemson, SC 29634-0921

# Effects of Elevated Free-Stream Turbulence on Flow and Thermal Structures in Transitional Boundary Layers

*The effects of elevated free-stream turbulence on flow and thermal structures in transitional boundary layers were investigated experimentally on a heated flat plate. Detailed boundary layer measurements using a three-wire probe and wall heat transfer were made with free-stream turbulence intensities of 0.5, 3.8, 5.5, and 6.4 percent, respectively. The onset of transition, transition length, and the turbulent spot formation rate were determined. The statistical results of the streamwise and cross-stream velocity fluctuations, temperature fluctuation, Reynolds stresses, and Reynolds heat fluxes were presented. The eddy viscosity, turbulent thermal diffusivity, and the turbulent Prandtl number were calculated and related physical mechanisms are discussed.*

## Introduction

One of the key factors in improving the prediction of the thermal load on gas turbine blades is to improve the understanding of the momentum and thermal transports during the laminar-turbulent transition process (Graham, 1979, 1984; Mayle, 1991). As much as 50–80 percent of the surface of a typical turbine blade is commonly covered by flow undergoing transition (Turner, 1971). Transition from laminar to turbulent boundary layer flow significantly increases the local wall shear stresses and the convective heat transfer rates. These increases must be appropriately factored into the design of gas turbine blades. Unsatisfactory prediction of the location and streamwise coverage of transition on gas turbine blades can result in either reduced longevity and reliability of the blade or engine performance below design objectives. In gas turbine environments, one of the most important factors controlling the transition process is elevated free-stream turbulence intensity (FSTI). Measurements of FSTI at the inlet of the turbine show values of 5 to 10 percent due to the disturbances from the upstream conditions. Turbulence in the wakes following the trailing edges of the vanes can be as high as 15 to 20 percent (Mayle, 1991). Very few experiments have been conducted to examine transition at such FSTI levels.

At low FSTI levels, boundary layer transition begins with a weak instability in the laminar boundary layer and proceeds, through various stages of amplified instability, to fully turbulent flow (Schubauer and Skramstad, 1948; Klebanoff et al., 1962). The critical Reynolds number, above which the selec-

tive amplification of the two-dimensional infinitesimal disturbances may occur, and the growth rates of the amplified disturbances, can be predicted by linear instability theory. At high free-stream turbulence, the amplification of linear instability waves is bypassed in such a manner that turbulent spots are directly produced within the boundary layer by the influence of the finite perturbations, which provide a nonlinear transition mechanism (Morkovin, 1969). Since linear instability theory is irrelevant in this case, this bypass transition is much more difficult to analyze and is poorly understood. Even the conventional view of a laminar boundary layer must be modified or redefined in such high FSTI levels. Dyban et al. (1980) investigated the structure of laminar boundary layers that developed under elevated FSTI of from 0.3 to 25.2 percent. They found a peak in the rms streamwise velocity fluctuation ( $u'$ ) in the late-laminar boundary layers. The entire  $u'$  profiles were elevated due to the penetration of the high FSTI. The maximum penetration occurred for the 4.5 percent FSTI case. They called the laminar boundary layers generated at very high FSTI "pseudo-laminar" to distinguish them from both the purely laminar layer and the fully turbulent layer that develops at low turbulence. Their results, though interesting, were limited to the distribution of disturbances within the laminar boundary layer. The onset and end of transition for a flat plate was investigated by Abu-Ghannam and Shaw (1980) in a low-speed wind tunnel with FSTI ranging from 0.3 to 5 percent. Their results showed that the higher values of FSTI result in an earlier transition and a shorter transition length. Suder et al. (1988) investigated the effects of FSTI ranging from 0.3 to 5 percent on boundary layer transition. They observed linear growth of the Tollmien-Schlichting (T-S) waves with an FSTI of 0.3 percent and the bypass transition mechanism for an FSTI of 0.65 percent and higher. Their results indicated that there

Contributed by the International Gas Turbine Institute and presented at the 38th International Gas Turbine and Aeroengine Congress and Exposition, Cincinnati, Ohio, May 24–27, 1993. Manuscript received at ASME Headquarters February 18, 1993. Paper No. 93-GT-66. Associate Technical Editor: H. Lukas.

exists a critical value of the peak rms of the velocity fluctuations within the boundary layer of approximately 3 to 3.5 percent of the free-stream velocity. Once the unsteadiness within the boundary layer reached this critical value, turbulent bursting was initiated, regardless of the transition mechanism. More information on transition, especially the bypass transition, can be found in the discussion of instability and transition predictability by Morkovin (1978). Many other reviews of boundary layer instability and transition can be found in the literature, e.g., Reshotko (1976), Tani (1981), and Narasimha (1985). Recently, Volino and Simon (1995) reviewed published experimental data related to the bypass transition in boundary layers including curvature and favorable pressure gradient effects. An extreme wealth of information on the role of laminar-turbulent transition in gas turbine engines can be found in Mayle (1991).

Studies of elevated free-stream turbulence effects on heat transfer in transitional boundary layer flows are limited and are much less numerous than those treating fluid mechanics. Blair (1982) conducted several tests with a uniformly heated flat wall in accelerated transitional boundary layers with FSTI ranging from approximately 0.7 to 5 percent. He concluded that the transition Reynolds number is relatively insensitive to acceleration at even moderate turbulence levels (around 4 percent). The results of Blair's tests showed the combined effects of FSTI and pressure gradients; however, the isolated effects of the elevated FSTI alone were not available. Wang et al. (1987) investigated the heat transfer and fluid mechanics in transitional boundary layers with 0.68 and 2.0 percent FSTI. They observed that average turbulent Prandtl number values in the early turbulent flow are 20 percent higher than 0.9, a value known to apply to fully turbulent flow. This average Prandtl number is reduced as FSTI increases. Temperature profiles in the late transitional and early turbulent flows have a thicker conduction layer than those in fully turbulent flow. This conduction thickness decreases as the FSTI level increases. They also pointed out that the effect of elevated FSTI penetrates to very near the

wall in the profiles of Reynolds streamwise normal stress ( $u'$ ). However, the effect of elevated FSTI on the Reynolds shear stress ( $-\bar{uv}$ ) and the mean velocity profiles is seen, predominantly, in the outer portion of the boundary layer. Kim et al. (1989) performed fluid mechanics and heat transfer measurements in transitional boundary layers, which were conditionally sampled on intermittency for two different values of FSTI, 0.32 and 1.79 percent. The turbulent heat flux was measured by using a triple-wire probe. The results showed that a large increase in turbulent heat flux above the wall heat flux value occurs within the turbulent spot, and the turbulent Prandtl numbers in the turbulent core region of the transitional flow are smaller than unity. Contrary to the results of Kim et al., the most recent experimental results of Sohn and Reshotko (1991), Shome (1991), and Wang et al. (1992) showed that the cross-stream heat fluxes ( $\bar{vT}$ ) are highly negative values in the middle transitional region. The layer of negative  $\bar{vT}$  becomes thinner and moves toward the wall as the flow proceeds downstream. Also, Sohn and Reshotko reported that the velocity profiles were observed to lag the temperature profiles during the transitional process to turbulent flow, which is the opposite of the observations of Blair (1982), Wang et al. (1987), and Kim et al. (1989). The boundary layer spectra in Sohn and Reshotko's report indicated selected amplification of T-S waves for 0.4 percent FSTI as predicted by linear instability. For 0.8 percent and 1.1 percent FSTI, T-S waves are localized very near the wall and do not play a dominant role in the transition process.

The present experimental study investigates boundary layer transition over a heated flat plate with a free-stream turbulence range of from 0.5 to 7 percent. A miniature three-wire probe was employed to measure both the instantaneous streamwise, cross-stream velocity components and the temperature simultaneously. The onset and end of transition were obtained both from the wall Stanton number measurements and from boundary layer flow and thermal structure measurements. The emphasis of this paper is on the study of the evolution of Reynolds shear stresses and heat fluxes.

## Nomenclature

$C_f$  = skin friction coefficient =  $\tau_w / (\rho U_\infty^2 / 2)$   
 $C_p$  = specific heat  
 $E_1(f)$  = one-dimensional spectrum of  $u'$   
 $f$  = frequency  
FSTI = free-stream turbulence intensity  
 $= \sqrt{(u^2 + v^2 + w^2) / 3} / U_\infty$   
 $n$  = turbulent spot production rate,  
No./s · m  
 $\hat{n}$  = dimensionless turbulent spot production  
rate =  $n v^2 / U_\infty^2$   
 $Pr_t$  = turbulent Prandtl number =  $\epsilon_M / \epsilon_H$   
 $q''$  = heat flux  
 $Re_x$ ,  $Re_{\delta}$ ,  $Re_\theta$  = Reynolds numbers based on  $x$ ,  $\delta^*$ , and  
 $\theta$ , respectively  
 $St$  = Stanton number =  $q'' / \rho C_p U_\infty (T_w - T_\infty)$   
 $t$  = instantaneous temperature fluctuation  
 $t'$  = rms value of  $t$   
 $T$  = mean temperature  
 $T^+$  = mean temperature in wall units  
 $= (T_w - T) \rho C_p u^* / q''$   
 $u$ ,  $v$  = instantaneous streamwise and cross-  
stream velocity fluctuations  
 $u'$ ,  $v'$  = rms values of  $u$  and  $v$   
 $u^*$  =  $\sqrt{\tau_w / \rho}$  = friction velocity  
 $U$  = mean streamwise velocity

$U^+$  = mean streamwise velocity in wall units  
 $= U / u^*$   
 $x$  = streamwise distance from leading edge  
 $y$  = distance away from the wall  
 $Y^+$  =  $yu^* / v$   
 $\alpha$  = thermal diffusivity  
 $\delta$  = boundary layer thickness at  $0.995 U_\infty$   
 $\delta^*$  = displacement boundary layer thickness  
 $\epsilon_H$  = turbulent thermal diffusivity  
 $= -\bar{vT} / (\partial T / \partial y)$   
 $\epsilon_M$  = turbulent viscosity =  $-\bar{uv} / (\partial U / \partial y)$   
 $\theta$  = momentum boundary layer thickness  
 $\Lambda_f$  = integral length scale  
 $= U / \int_0^\infty u(t) u(t + \tau) / u^2 d\tau$   
 $\nu$  = kinematic viscosity  
 $\rho$  = density  
 $\sigma$  = turbulent spot propagation parameter  
 $\tau$  = shear stress

## Subscripts

$e$  = at transition end  
 $s$  = at transition start  
 $w$  = at the wall  
 $\infty$  = in the free stream

eddy viscosity, turbulent thermal diffusivity, and turbulent Prandtl number under the influences of elevated FSTI during the process of laminar-turbulent transition.

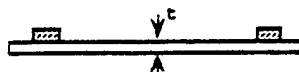
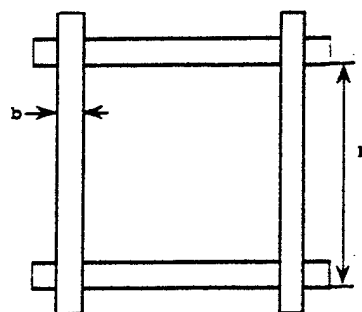
### Experimental Program

**Wind Tunnel.** The present research employed a two-dimensional, open-circuit, blowing type wind tunnel. The detailed description of the design considerations and construction specifications was documented by Kuan (1987) and Kuan and Wang (1990). Air is drawn through a filter box, then forced through two grids, a honeycomb, a heat exchanger, a screen pack, and a contraction nozzle before entering the test section. The flow rate can be adjusted steplessly from 0.5 m/s to 35 m/s by a combination use of an inlet damper and a constant-torque, variable frequency motor controller. The steadiness of the free-stream velocity and temperature can be maintained within 1 percent and 0.5°C for a 24-hour period, and the uniformity is within 0.7 percent and 0.1°C, respectively.

**Test Section.** The rectangular test section is 0.15 m wide, 2.4 m long, and 0.92 m high with an aspect ratio of 6. The large aspect ratio reduces edge effects and ensures the two dimensionality of the boundary layer flow. One of the test section walls served as the test wall. The heat patch inside the test wall was constructed of a serpentine heater foil sandwiched between glass cloth and silicon rubber sheets. A 1.56 mm thick aluminum sheet was vulcanized to the front surface of the heater pad to ensure uniformity of the heat flux. A 1.56 mm polycarbonate sheet was placed on the aluminum surface to provide a smooth test surface on which the air flows and measurements were taken. The surface temperature was measured by 184 3 mil E-type thermocouples, which were embedded strategically inside the test wall to capture the spanwise variation of wall heat transfer in a transitional boundary layer. Fourteen measuring holes were drilled along the outer observation wall centerline in the test section and measurements were obtained by traversing the probe through these holes into the test section. Boundary layer suction was applied at the leading edge of the test section so that a near zero thickness boundary layer can be achieved at the leading edge. The detailed construction consideration and description of the heated test wall are contained in Wang et al. (1992) and Zhou (1993).

**Turbulence Generating Grids.** The background FSTI of this wind tunnel was about 0.5 percent. The higher turbulence levels required for this study were generated by inserting various turbulence generating grids into the wind tunnel. The turbulence generating grids consisted of biplane rectangular bar arrays with approximately a 69 percent open area (Fig 1). The grids were designed based on the recommendation of Baines and Peterson (1951) to produce test section turbulence levels ranging from approximately 3 to 7 percent. Grid-generated turbulence decays with distance from the grid. The decaying rate becomes smaller when the distance from the grid increases. In order to generate homogeneous and slowly decaying turbulence, the turbulence generating grids were inserted at the entrance to the main tunnel contraction instead of placing them at the inlet of the test section. The grids are referred to as grids 1, 2, and 3, corresponding to mesh widths,  $M$ , of 19.05, 24.13, and 33.02 cm, respectively. The test case with only background turbulence (no grid) served as the baseline case.

**Instrumentation and Data Reduction.** A three-wire sensor was specifically designed to measure the instantaneous longitudinal velocity, cross-stream velocity, and temperature simultaneously. The development and qualification of this three-wire sensor was described by Shome (1991) and Wang et al. (1992). Basically, an "X" array, consisting of gold-plated



Grid Number	$b$ (cm)	$M$ (cm)	$t$ (cm)	% Open Area
1	3.81	19.05	0.32	69
2	5.08	24.13	0.32	69
3	7.62	33.02	0.32	69

Fig. 1 Grid configuration

tungsten wires 1.0 mm long and 2.5  $\mu\text{m}$  in diameter, is used for velocity measurement. The sensing length is 0.5 mm, and is etched in the center. The spacing between the "X" array is 0.35 mm. The temperature sensor is a 0.35 mm long (with a sensing length of 0.35 mm) and a 1.2  $\mu\text{m}$  diameter unplated platinum wire placed in a plane parallel to the plane of the crossed wires and spaced 0.35 mm from the "X" array. To allow for near-wall measurement and to reduce probe interference, the probe support was bent at an angle of 10 deg from the wire axis. However, the  $x$  wires are still perpendicular to each other.

Two  $x$  wires were operated at an overheat ratio of about 1.2 (hot wires) in the constant temperature mode. The 1.2  $\mu\text{m}$  platinum wire was operated at a very low current of 0.1 mA (cold wire) in the constant current mode. In order to have a sufficiently extended length of transition for detailed measurements on the test wall, extremely low speed flows were provided for elevated FSTI cases. The unsteadiness, which commonly occurs in low speed operations, was overcome by a combined use of the inlet fan damper and the frequency controller. The typical overheat ratio of 1.5 for a standard 4.5  $\mu\text{m}$  tungsten wire was found to significantly contaminate the cold temperature wire. The temperature wire reading had an error of 10°C when the  $x$  wires were turned "on" compared with that when the  $x$  wires were turned "off" in the near-wall region in a boundary layer with the wall temperature 20°C above the free-stream temperature and at the free-stream velocity about 1 m/s. Therefore, relatively low overheat ratios for the  $x$  wires were required in order to minimize the "cross-talk" between the  $x$  wires and the temperature sensor. However, better velocity sensitivities for the  $x$  wires required higher overheat ratios. For compromise, an overheat ratio of about 1.2 was chosen. The method of Chua and Antonia (1990) was used for correcting temperature contamination of the hot wires. Based on this method, the hot-wire signals were corrected by using instantaneous temperatures instead of instantaneous temperature fluctuations. At low free-stream velocities, it was found that if the flow direction deviates a very small angle, from  $\pm 45$  deg to the  $x$  wires, a significant change of the results of the Reynolds shear stress ( $uv$ ) and the cross-stream Reynolds heat flux ( $vt$ ) would occur. This small flow angle was found by assuming

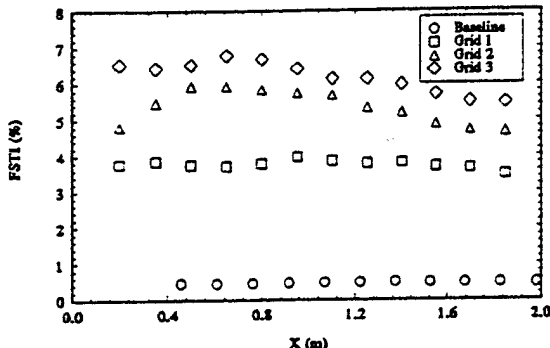


Fig. 2 FSTI distribution in the test section

that the mean cross-stream velocity ( $V$ ) is zero in the free stream. A typical flow angle of 3 deg can result in a 50 percent error in the  $uv$  and  $vw$  measurements at free-stream velocity of 2 m/s. A TSI Model IFA 100 Intelligent Flow Analyzer system was used as a coolant temperature anemometer. The IFA 100 allows simultaneous operation of up to four channels. A DISA M20 temperature bridge was used for operating the cold wire in the constant current mode. Three TSI Model 157 signal conditioners were used in the external mode for low pass filtering of all anemometer signals including that from the DISA M20. An 80386 microprocessor based, 20 MHz personal computer was used as the data acquisition controller. A MetraByte DAS-20 multifunction high-speed A/D data acquisition board was internally installed in the PC. A high-speed data acquisition software routine, STREAMER, was used to stream digital input data from DAS-20 directly into the hard disk. The sampling rate was 2 kHz and the sampling duration was 20 seconds.

The wall temperature measurements were performed through a FLUKE Model 8842A 5 1/2 digital multimeter with a built-in A/D converter and a FLUKE 2205A 100-channel switch controller, which allowed scanning/acquisition of wall thermocouple emf at various switching rates up to 5 channels/second.

Wall Stanton number was calculated from the power supplied to the heated test wall and the wall temperature measurement. The heat flux was corrected for the radiation loss, back, and streamwise conduction loss. The wall temperature was corrected for front polycarbonate wall conduction effects, the radiation loss, back and streamwise conduction loss, compressibility, recover effect, and relative humidity.

The detailed instrumentation description is contained in Shome (1991) and Wang et al. (1992).

## Results and Discussion

In this experiment, three different sizes of grid were used to produce different free-stream turbulence levels in the test section. The case with no grid served as the baseline case. The results of the baseline case were reported in a previous paper by Wang et al. (1992). The FSTI distributions along the streamwise direction in the test section, based on the three components of the velocity fluctuation, are shown in Fig. 2. For the baseline case and the grid 1 case, as shown in this figure, the FSTI remains almost constant through the test section. For the grid 2 and grid 3 cases, the FSTI increases at first, to station 4, and then starts to decay. The ratios of  $v'/u'$  and  $w'/u'$  in the freestream, as shown in Fig. 3, are not isotropic for the baseline and grid 2 cases, but they are near isotropic for the grid 1 and 3 cases. The three components of the velocity fluctuation and their length scales in the free stream were documented in detail by Zhou (1993).

The spectral distributions of  $u'$  in the free stream for all three elevated FSTI cases are similar. One representative

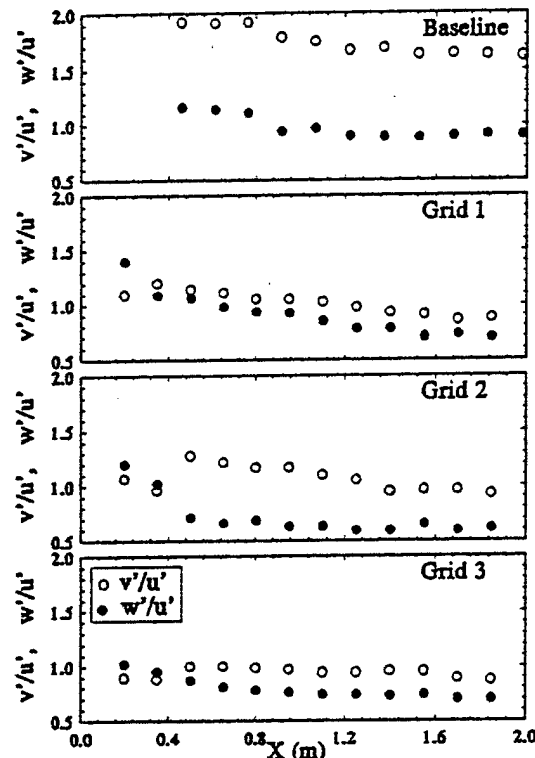


Fig. 3  $v'/u'$ ,  $w'/u'$  in the free stream

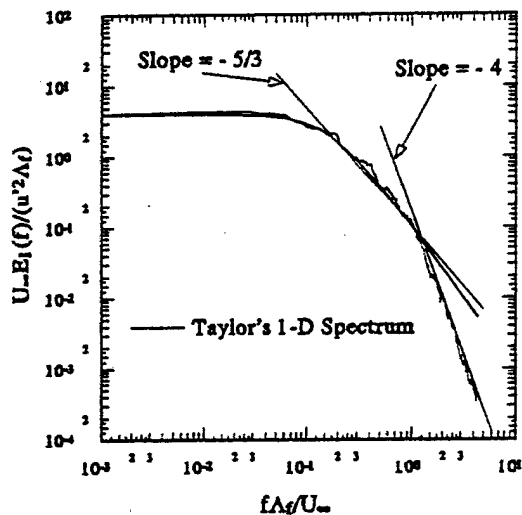


Fig. 4 Free-stream turbulence spectrum

case of grid 2 is shown in Fig. 4. The one-dimensional spectrum  $E_1(f)$  is normalized by the  $u'^2$ , the integral length scale  $A_f$ , and the free-stream velocity  $U_e$ . The frequency  $f$  is normalized by  $A_f$  and  $U_e$ . Also shown in this figure is Taylor's one-dimensional energy spectrum (Hinze, 1975). The spectral distribution  $E_1(f)$  follows Taylor's one-dimensional energy spectrum in the low-frequency range and deviates from it in the high-frequency range. In the high-frequency range, the spectrum  $E_1(f)$  has a distinctive slope of  $-4$ . This is consistent with the typical spectrum of grid generated turbulence (Kistler and Vrebalovich, 1966).

**Heat Transfer.** Three sets of Stanton number data were taken for each case in each 22-hour run. The first set was obtained after a 12-hour stabilization period followed by two sets obtained at 17 hours and 22 hours, respectively. Between these measurements of wall temperatures, boundary layer measurements were conducted. The maximum variation in

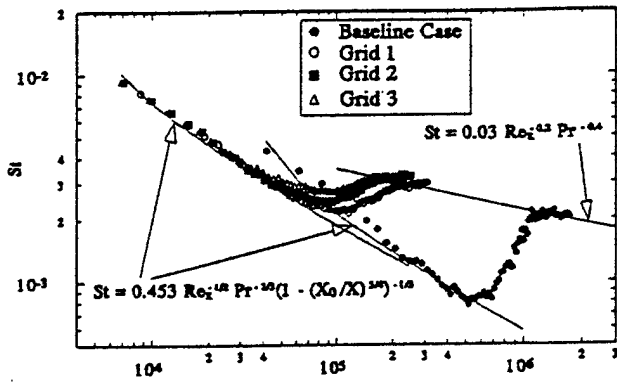


Fig. 5 Stanton number distribution

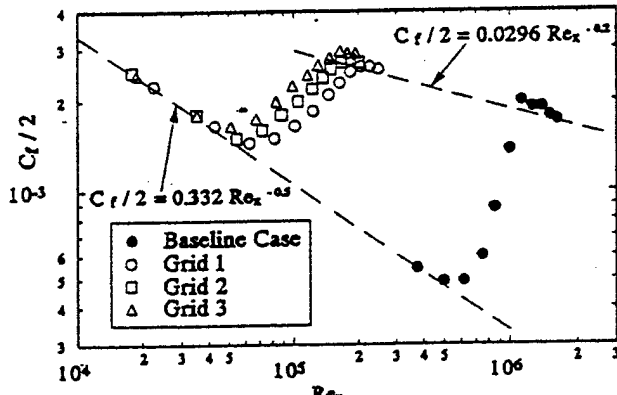


Fig. 6 Friction coefficient distribution

Stanton numbers during a 10-hour period was approximately  $\pm 3$  percent. An uncertainty analysis of the Stanton number measurement, following the procedure documented by Wang and Simon (1989), was conducted. The uncertainty was  $\pm 3$  percent in the laminar and turbulent regions and  $\pm 5$  percent in the transitional region. The centerline Stanton number distributions for the four cases are shown in Fig. 5. The unheated starting length effects for the laminar correlation has been included. It should be noted that the laminar correlation with unheated starting length appears different for different free-stream velocities when plotted in Fig. 5. To maintain clarity, it is plotted only for the baseline and the grid 2 cases. In the laminar portion, the Stanton number distributions follow the laminar correlation for the elevated FSTI cases. The onset of transition is defined as the location where the Stanton number reaches a minimum and starts to deviate from the laminar correlation, and the end of transition is defined as the location where the Stanton number merges with the turbulent correlation. As expected, higher FSTI leads to an earlier onset and an earlier end of transition. The effect of elevated FSTI on the heat transfer is negligible in the laminar region; however, in the turbulent region, the heat transfer is increased as can be seen from Fig. 5.

**Skin Friction.** The skin friction coefficients in the laminar region and transitional region were determined by extrapolating the linear correlation to the wall. The Clauser technique was employed for determining the skin friction coefficients in the turbulent region by best fitting the data points to the logarithmic law-of-the-wall profile. The development of the skin friction coefficients, shown in Fig. 6, is similar to that of the Stanton number (Fig. 5). The effect of the elevated FSTI on the skin friction in the laminar region is negligible. The effect in the turbulent region is not conclusive

Table 1 Reynolds numbers at onset and end of transition

		Baseline	Grid 1	Grid 2	Grid 3
FSTI at $X_s$		0.5%	3.8%	5.5%	6.4%
$U_\infty$ (m/s)		13.0	2.10	1.75	1.70
Onset of Transition	$X$ (cm)	61	45	45	42
	$Re_x$	$5.0 \times 10^4$	$6.0 \times 10^4$	$5.0 \times 10^4$	$4.5 \times 10^4$
	$Re_s$	1183	386	355	314
End of Transition	$Re_x$	434	161	148	131
	$X$ (cm)	136	150	144	139
	$Re_x$	$1.1 \times 10^6$	$2.0 \times 10^5$	$1.6 \times 10^5$	$1.5 \times 10^5$
	$Re_s$	1947	735	659	608
	$Re_s$	1327	480	404	375

due to limited data points and the typical overshooting behavior of  $C_f$  in the early turbulent flow region.

**Transition Start and Turbulent Spot Formation Rate.** In the present study, the onset and end of transition were primarily judged by the Stanton number and cross checked with the skin friction distributions and the evolution of the mean velocity and temperature profiles. The corresponding values of  $x$ ,  $Re_x$ ,  $Re_{s_s}$ , and  $Re_s$  at onset and at the end of transition for each case are listed in Table 1. The results indicate that elevated FSTI affects an early onset of transition and reduced extent of transition length based on  $Re_x$ , as well as on  $Re_{s_s}$  and  $Re_s$ .

The key characteristic in laminar-turbulent transition flow is the randomly intermittent laminar-turbulent behavior. The fraction of time the flow is turbulent is defined as the intermittency. Emmons (1951) presented a statistical theory for transition and provided an expression for the intermittency. Later, the theory was extended by Dhawan and Narasimha (1958) who showed, for time-averaged two-dimensional flows, that turbulent spots originate within a narrow region on the surface at some distance,  $x_s$ , from the leading edge, and that the turbulent spot production could be represented by a Dirac delta function. Based on this intermittency theory, once the location of the transition onset and the turbulent spot formation rate are known, the location of the end of transition and the intermittency distribution within the transition region can be predicted. The present calculation of the turbulent spot formation rate is based on the equation,  $\hat{n}\sigma = 4.6/(Re_{x_s} - Re_{x_s})^2$  (Mayle, 1991), in which the effect of FSTI is implicitly embedded in the  $Re_{x_s}$  and  $Re_{x_s}$ .

The onset of transition, based on the momentum thickness Reynolds number, and the calculated turbulent spot formation rate,  $\hat{n}\sigma$ , are plotted in Fig. 7. Also shown are the empirical correlations,  $Re_{s_s} = 400 (FSTI)^{-5/8}$  and  $\hat{n}\sigma = 1.5 \times 10^{-11} (FSTI)^{7/4}$ , given by Mayle (1991), which were formulated based on flat-wall, nonaccelerated flow data. For the elevated FSTI cases, the present data agree with Mayle's correlation. For the baseline case, the onset of transition is earlier and the calculated  $\hat{n}\sigma$  is larger than that predicted by Mayle's correlation. This indicates that some other factors, which were not incorporated into Mayle's correlations, influence the transition process in low FSTI environment. For a well-controlled experiment of a low-FSTI transitional flow study, typical factors that influence the onset of transition are related to inherent characteristics of the test facility and the uncontrollable disturbances in operating conditions. Some possible factors are the initial flow conditions at the leading edge, the free-stream integral length scale, floor vibration frequency, smoothness and flatness of the test surface, and precision of streamwise pressure gradient control.

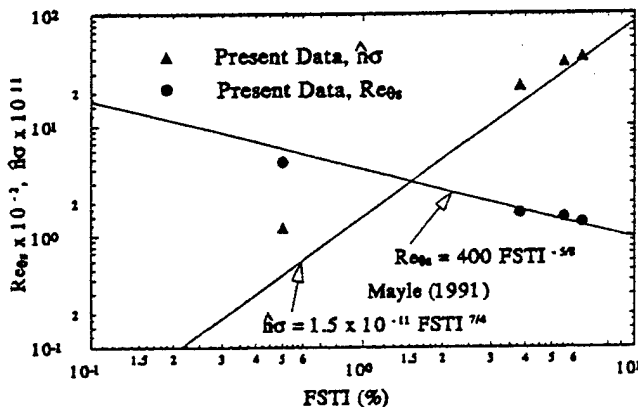


Fig. 7 Transition onset and turbulent spot formation rate

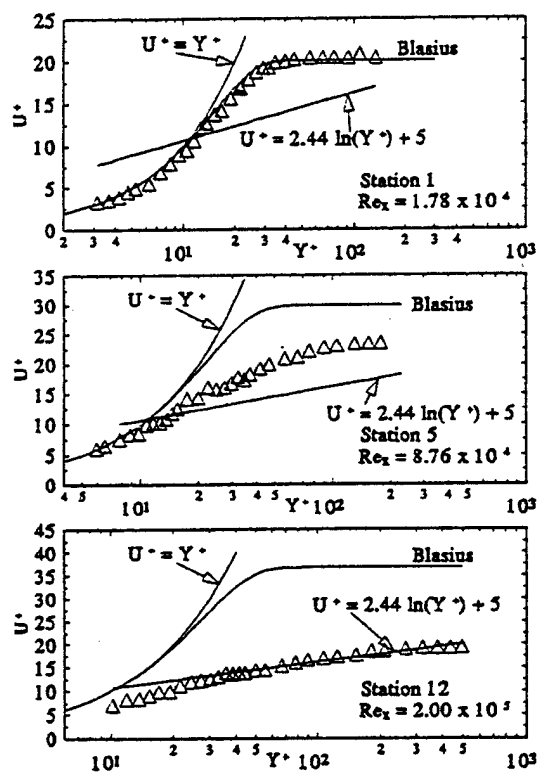


Fig. 8 Mean velocity profiles,  $U^+$  versus  $Y^+$

**Mean Velocity and Temperature Profiles.** Mean velocity and temperature profiles are plotted in wall units in Figs. 8 and 9, respectively. Since their overall evolution during the transition process is similar to that of the 2 percent FSTI case previously reported by Wang et al. (1987), only three profiles of each are shown as representative of the mean profile characteristics in the laminar, transitional, and turbulent flow region, respectively. In the laminar region, even at the elevated values of FSTI, the mean profiles are consistent with the laminar flow solution, as in the baseline case. In the turbulent region, both the mean velocity and temperature profiles preserve the logarithmic "law of the wall" characteristics over a sufficient range of  $Y^+$  (from 30 ~ 300), but the wake regions are completely depressed beyond  $Y^+ = 300$  due to the high FSTI, which is consistent with the previous results of Blair (1983a, b) and Wang et al. (1987). In the transition region, the mean profiles deviate from the typical laminar and turbulent profiles. No established method has been developed to compare them to those of the low-FSTI cases.

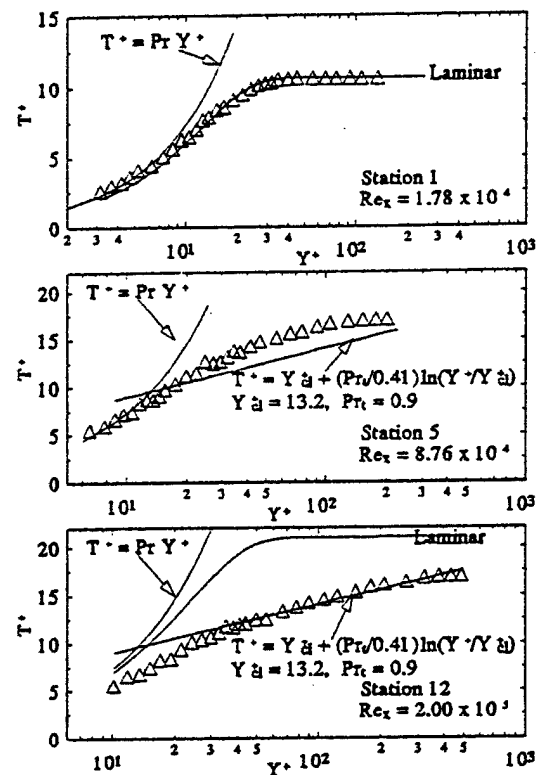


Fig. 9 Mean temperature profiles,  $T^+$  versus  $Y^+$

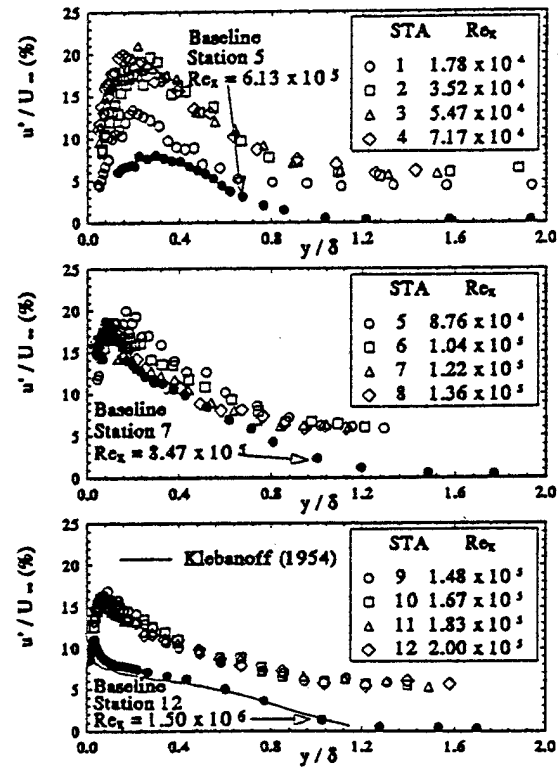


Fig. 10 Streamwise velocity fluctuation profiles

**Streamwise Velocity Fluctuation ( $u'$ ).** The normalized streamwise evolution of velocity fluctuation,  $u'/U_\infty$ , is shown in Fig. 10 for the grid 2 case. For comparison, three profiles of the baseline case, one near the onset of transition (station 5), one in the transition region with maximum  $u'$  (station 7), and one in the fully turbulent region (station 12), have also been incorporated into Fig. 10. The onset of transition for

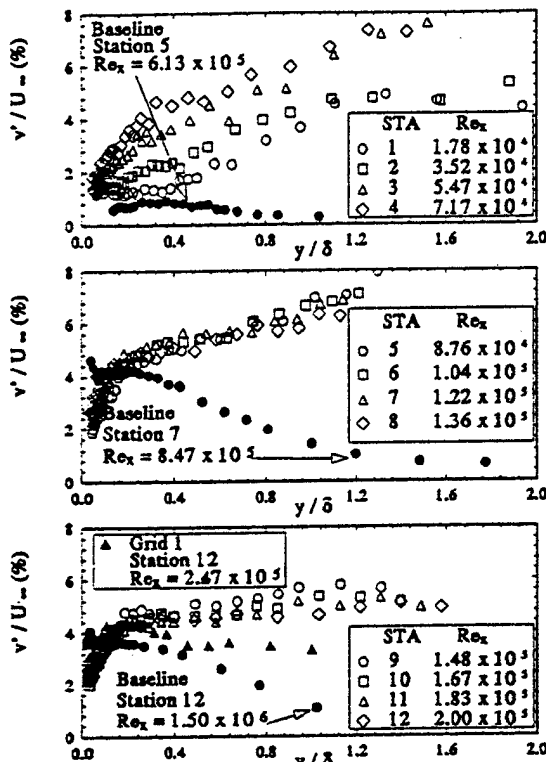


Fig. 11 Cross-stream velocity fluctuation profiles

grid 2, based on Stanton number distribution, is at  $Re_x = 5 \times 10^4$ . Therefore, stations 1 and 2 for the grid 2 case are in the laminar flow region. Comparison between the stations 1 and 2 for grid 2 case and station 5 for the baseline case indicates that the  $u'$  in the laminar flow was significantly elevated due to the higher FSTI. This is consistent with the results reported by Dyban et al. (1980). It is especially interesting to observe that the elevated  $u'/U_\infty$  distribution reaches 20 percent in the late laminar region (station 2) and remains at such high levels throughout the early half of the transition region until station 6. It is also to be noted that in the transitional flow, the maximum values of  $u'/U_\infty$  at stations 4 and 5 in the grid 2 case are only slightly higher than the maximum value at station 7 for the baseline case. This implies that even at elevated FSTI, the maximum Reynolds normal stresses due to the bursting activities are limited to around  $u'/U_\infty = 20$  percent. This may also imply that the penetration of the turbulence energy from the free stream into the boundary layer results in a uniform redistribution of turbulence energy across the boundary layer rather than in providing more bursting energy. This second implication can be further verified by examining the  $u'$  distribution in the turbulent flow region as shown by the  $u'/U_\infty$  profiles of stations 10, 11, and 12 in Fig. 10. This deep penetration of elevated free-stream turbulence to near the wall is consistent with the results of Wang et al. (1987). This is inconsistent with the results reported by Sohn and Reshotko (1991).

**Cross-Stream Velocity Fluctuation ( $u'$ ).** The evolution of  $u'/U_\infty$  for grid 2 case, as shown in Fig. 11, is very different from the baseline case in Wang et al. (1992) or other low FSTI cases in Kuan and Wang (1990) and Sohn et al. (1991). Three representative  $u'/U_\infty$  distribution curves, as mentioned in Fig. 10, are superimposed for comparison. It is obvious that the effect of elevated FSTI on  $u'$  is more predominant in the outer boundary layer than in the inner boundary layer. It appears that  $u'$ , in the boundary layer, is affected by FSTI through an energy diffusion process rather than through a

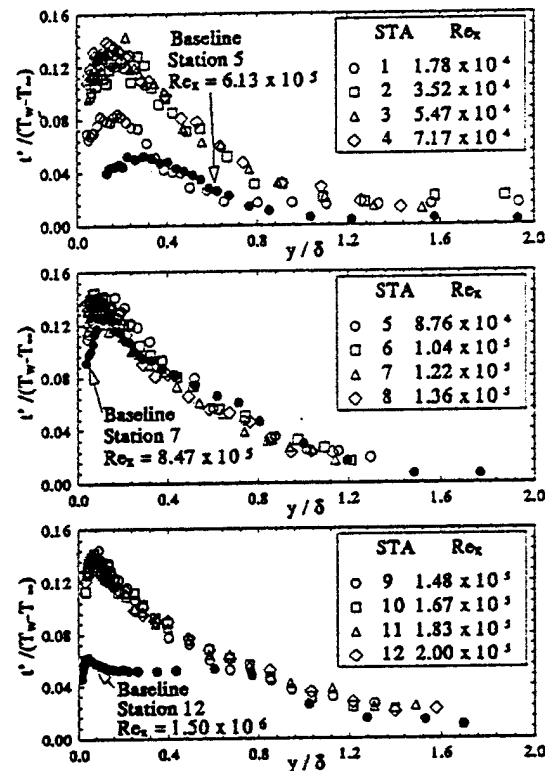


Fig. 12 rms temperature profiles

convective motion, or through a correlation with pressure fluctuations (return-to-isotropy). This speculation arises from by observing that the magnitude of  $u'$  in the free stream seems to control the  $u'$  distribution in the outer boundary layer since the data points for each curve, for all flow regions, indicate a smooth curve, which asymptotically approaches the free-stream value of  $u'$ . A typical near-wall peak of  $u'$ , which appears in the transition region for the baseline case (e.g., at station 7), is not observed in the elevated FSTI cases. Apparently, the elevated turbulence in the free stream does not promote the cross-stream component of the near-wall turbulence energy production, which produces large magnitudes of energy in the streamwise component. The  $u'/U_\infty$  distribution in the turbulent flow region at station 12 for the grid 1 case, which has lower FSTI than the grid 2 case, is superimposed in Fig. 11. A peak in  $u'$  can be clearly seen near  $y/\delta = 0.2$ . The mechanism involved in producing this round peak can be very different from the near-wall sharp peak prevailing in the low-FSTI cases. However, it is not clear how the near-wall production of the  $u'$ -component turbulence energy is suppressed in the elevated FSTI cases and why the highest  $u'$  value occurs away from the wall. Also shown in this figure are the varying values of  $u'/U_\infty$  in the free stream along the streamwise direction in the test section. The value of  $u'/U_\infty$ , which can be read from values beyond  $y/\delta = 1.6$  from Fig. 11, shows a variation from about 4.5 percent at stations 1 and 2 to 7 percent at stations 3 to 5 and back down to 4.5 percent at stations 10 to 12. This trend can also be seen from  $u'/u'$  in Fig. 3 since  $u'$  remains nearly constant along the streamwise direction.

**rms Temperature Fluctuation ( $t'$ ).** The evolution of the rms temperature fluctuation for the grid 2 case,  $t'/(T_w - T_\infty)$ , as presented in Fig. 12, is very similar to  $u'$ , with an elevated value across most of the boundary layer except in the outer boundary layer ( $y/\delta > 0.8$ ), where the elevated FSTI does not enhance  $t'$  as would be expected in a nearly isothermal region.

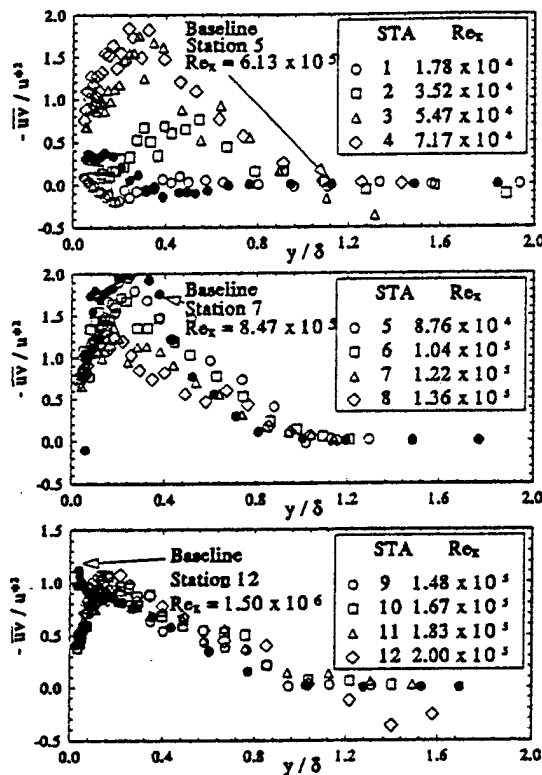


Fig. 13 Reynolds shear stress distribution

**Reynolds Shear Stress ( $\bar{u}\bar{v}$ ).** The evolution of the normalized Reynolds shear stress,  $-\bar{u}\bar{v}/\bar{u}^2$ , for the grid 2 case, and also the comparison with the baseline case, are shown in Fig. 13. For the grid 2 case, the normalized Reynolds shear stress reaches a maximum value of about 1.9 at stations 4 and 5. The peak value in the boundary layer then decreases and the peak location moves closer to the wall. This evolution of  $\bar{u}\bar{v}$  indicates that the turbulent shear is not generated near the wall as is that for  $\bar{u}'$ , but is produced away from the wall, at about  $y/\delta = 0.3$ , and progresses toward the wall to eventually affect the wall shear. This progression is similar to that for the baseline case. The detailed description was provided by Wang et al. (1992). The peak location for the baseline case in the turbulent region at station 12 is closer to the wall than that for the grid 2 case. The effect of elevated FSTI on  $\bar{u}\bar{v}$  seems smaller than on  $\bar{u}'$  and  $\bar{v}'$ .

**Reynolds Heat Fluxes ( $\bar{u}\bar{t}$  and  $\bar{v}\bar{t}$ ).** The results of  $-\bar{u}\bar{t}$  and  $\bar{v}\bar{t}$ , normalized by wall heat flux, for the grid 2 case are presented in Figs. 14 and 15. For the grid 2 case,  $-\bar{u}\bar{t}/(q_w''/\rho C_p)$  reaches its maximum value of almost 10 near stations 4 and 5. Then the peak value in the boundary layer decreases and the peak location moves closer to the wall. The peak value in the turbulent flow region is about 7. For the baseline case at station 12, the peak value is only about 2, much lower than that for the grid 2 case. The locations of these peaks closely correspond to those of the peaks for  $\bar{u}'$  (Fig. 10) and  $\bar{v}'$  (Fig. 12). As shown in Figs. 10 and 12,  $\bar{u}'$  and  $\bar{v}'$  are much higher in the laminar and turbulent regions for the grid 2 case than for the baseline case, but are about the same in the transition region as in the baseline case. The lower value of  $-\bar{u}\bar{t}/(q_w''/\rho C_p)$  in the transition region for the grid 2 case compared to that in the baseline case is unexpected. This is then identified as the low Reynolds number effect.

As shown in Fig. 15 for the grid 2 case, the normalized

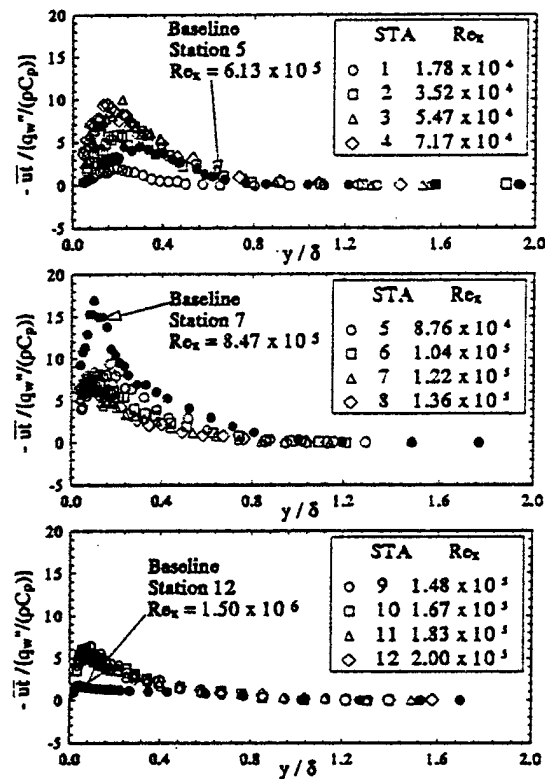


Fig. 14 Streamwise Reynolds heat flux distribution

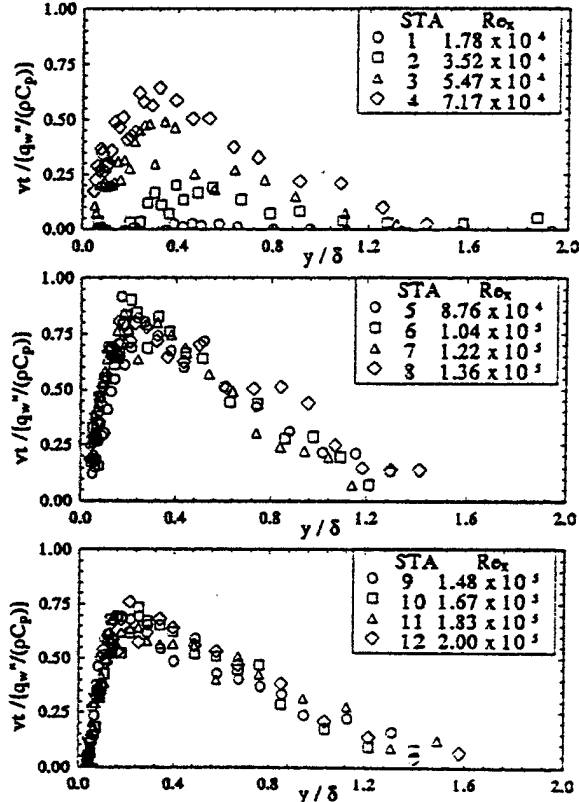


Fig. 15 Cross-stream Reynolds heat flux distribution

cross-stream Reynolds heat flux,  $\bar{v}\bar{t}/(q_w''/\rho C_p)$ , reaches its maximum value of about 0.9 at stations 5 and 7 in the transition region. This is later than  $\bar{u}\bar{t}$ , which reaches its maximum value at station 4. The peak value of  $\bar{v}\bar{t}/(q_w''/\rho C_p)$  then decreases with the peak value in the turbulent region to

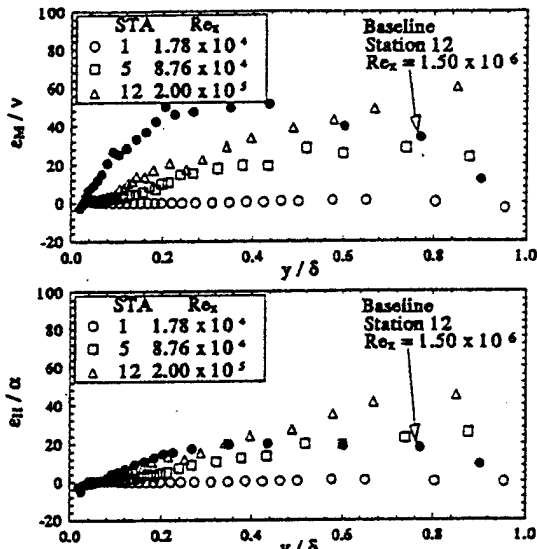


Fig. 16 Streamwise evolution of eddy viscosity and turbulent thermal diffusivity profiles

about 0.7. The baseline case at station 7 is also shown in Fig. 15 for comparison. Negative  $\bar{u}t$  occurs in the inner boundary layer for the baseline case but no negative  $\bar{u}t$  is observed in the elevated FSTI cases. The possible explanations of this negative value were discussed by Wang et al. (1992). The spatial resolution of the probe is of special concern near the wall because of the decreasing eddy size as the wall is approached and the thin boundary layer in the baseline case. For the higher FSTI cases, the free-stream velocity ( $\sim 2$  m/s) was much lower than that for the baseline case ( $\sim 12$  m/s), so that the boundary layer was much thicker. In the turbulent boundary layer the magnitude of  $\bar{u}t$  is elevated across the entire boundary layer for the grid 2 case, as compared to the baseline case at station 12 in Fig. 15.

**Eddy Diffusivities and Turbulent Prandtl Number.** The eddy viscosity,  $\epsilon_M$ , and the turbulent thermal diffusivity,  $\epsilon_H$ , normalized by their molecular counterparts at three stations for the grid 2 case, are shown in Fig. 16. The results for the baseline case at station 12 are also shown for comparison. For the grid 2 case, at station 1, where the flow behaves as laminar, the turbulent transport is low compared with the molecular transport, as expected, whereas for transitional flow (station 5) and turbulent flow (station 12), the turbulent transport is much higher than the molecular transport except in the very near-wall region. For the baseline case,  $\epsilon_M/v$  shows a peak near  $y/\delta = 0.3 \sim 0.4$  and gradually decreases in the outer boundary layer.  $\epsilon_H/\alpha$  shows a similar behavior except that the peak is not so obvious. For the grid 2 case, which is very different from the baseline case, a peak of  $\epsilon_M/v$  appears near  $y/\delta = 0.7$  at station 5 in the transitional flow region and  $y/\delta = 0.55$  at station 12 in the turbulent flow region.  $\epsilon_H/\alpha$  is similar to  $\epsilon_M/v$  in the turbulent flow region; however, in the transitional flow region, the maximum value of  $\epsilon_H/\alpha$  occurs in the outer boundary layer ( $y/\delta \approx 0.85$ ).

The turbulent Prandtl number,  $Pr_t$ , the ratio of the eddy viscosity over the turbulent thermal diffusivity, is shown in Fig. 17 for the grid 2 case. The data points are scattered in the early transition region (stations 4 to 6) but stabilized in the turbulent region (stations 10 to 12). In the region between  $y/\delta = 0.2$  to 0.8, the  $Pr_t$  values are close to 1.2 to 1.6, which are higher than 0.9, a value commonly applied to fully turbulent flow for low FSTI cases. In the near-wall region ( $y/\delta < 0.2$ ),  $Pr_t$  values are larger than 2. The validity of these values needs further verification due to the limits in spatial

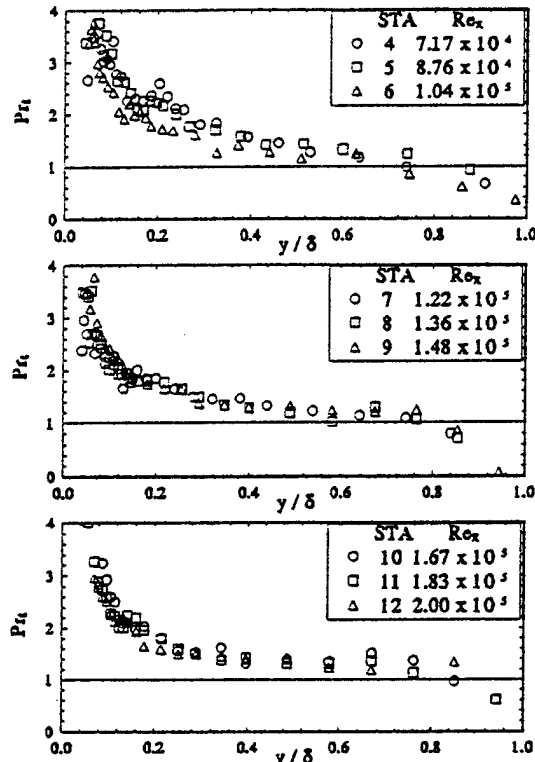


Fig. 17 Turbulent Prandtl number distribution

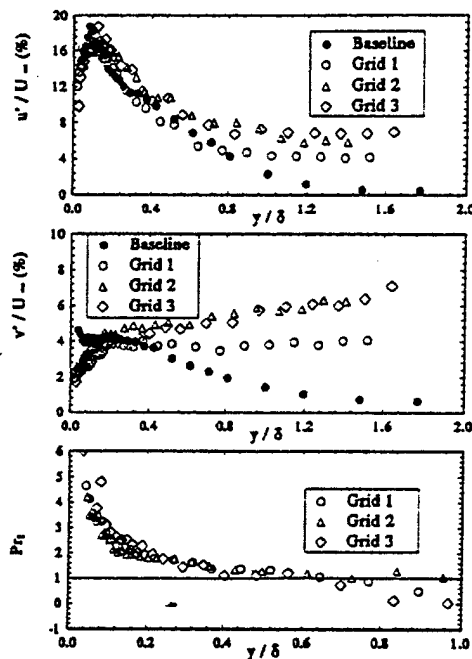
resolution in the near-wall region. However, values of  $Pr_t$  in the region of  $y/\delta \geq 0.2$  are believable. Based on these results, the higher turbulent Prandtl number (1.2 ~ 1.6) in the transitional and low-Reynolds-number turbulent flow should be considered in the modeling of transition.

The previous discussion is based on the comparison between the results of the baseline case and those of the grid 2 case. The comparisons among the grid 1, grid 2, and grid 3 cases are shown in Fig. 18. At maximum  $u'$  station in the transition region (Fig. 18a), the effects of the different grids on the  $u'/U_\infty$  and  $v'/U_\infty$  are confined in the outer region of the boundary layer ( $y/\delta > 0.4$ ), which are influenced by the different FSTI levels. In the fully turbulent region, the peak value of  $u'/U_\infty$  is slightly elevated due to a higher FSTI level (e.g., higher grid number). A peak of  $v'/U_\infty$  in the boundary layer is evident for grid 1 case, but is not observed for grids 2 and 3 cases due to the higher FSTI levels. Since the streamwise evolutions of  $uv$ ,  $ut$ ,  $vt$ , and  $Pr_t$  for these three grids are similar during the transition process, only the comparisons of the  $Pr_t$  distributions are presented. As shown in this figure, the  $Pr_t$  distributions for these three grids are very similar at maximum  $u'$  station and in the fully turbulent region.

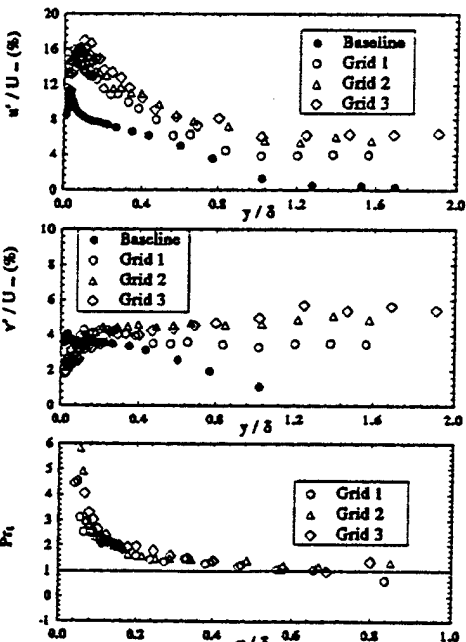
## Conclusion

Experiments were performed to investigate the effects of elevated FSTI (3 ~ 7 percent) on flow and thermal structures in heated transitional boundary layers. Wall heat transfer measurements indicated that elevated FSTI values result in an earlier onset of transition and reduced length of transition in terms of  $Re_\infty$ ,  $Re_\delta$ , and  $Re_\theta$ . The calculated turbulent spot formation rates at elevated FSTI cases agree with Mayle's correlation. In the turbulent region, the mean velocity and temperature profiles demonstrate the logarithmic "law of the wall" characteristics over a sufficient range of  $Y^+$  (30 ~ 300). The wake regions are completely depressed.

The  $u'$  distribution is significantly elevated across the entire boundary layer in the laminar and turbulent regions



(a) at stations with maximum  $u'$



(b) at station 12

Fig. 18 Comparison among different grids

due to elevated FSTI. The  $u'/U_{\infty}$  distribution reaches 20 percent in the late laminar region and remains at such high levels throughout the early half of the transition region. In the transitional region, the maximum Reynolds normal stresses of bursting activities are only slightly higher than the baseline case but are limited to approximately  $u'/U_{\infty} = 20$  percent. The evolution of the rms temperature fluctuation is very similar to  $u'$  with elevated values across 80 percent of the boundary layer.

The  $v'$  distribution in the outer boundary layer is controlled by the magnitude of  $v'$  in the free stream. The typical near-wall peak of  $v'$ , which appears in the transition region at low FSTI, is not observed. In the turbulent region, the very

near-wall peak of  $v'$  is suppressed and the maximum  $v'$  value occurs away from the wall in elevated FSTI cases.

The evolution of the  $\bar{u}v$  distribution at elevated FSTI is similar to that at low FSTI. In the transition region, Reynolds shear stress is produced not in the near-wall region where the vigorous turbulence production of  $u'$  occurs but away from the wall, at about  $y/\delta = 0.3$ . This high turbulent shear progresses toward the wall and eventually affects the wall shear.

The  $-\bar{u}t/(q_w/\rho C_p)$  distributions are elevated in the laminar and turbulent regions but reduced in the transitional region at higher FSTI. This is caused by the low Reynolds effect.

The  $\bar{v}t$  distributions reach maximum values in the transition region slower than the evolution of  $\bar{u}t$ . The regions of negative values of  $\bar{v}t$ , occurring in the transition region in the baseline case, are not observed in the elevated FSTI cases.

In the near-wall region ( $y/\delta < 0.2$ ), the  $Pr$  values are very large ( $> 2$ ); further verification of these high values is needed. In the region of  $y/\delta = 0.2 \sim 0.8$ , the  $Pr$  values are close to  $1.2 \sim 1.6$ . These higher  $Pr$ , in the transitional and low-Reynolds-number turbulent flow should be considered in the numerical modeling of transitional boundary layers.

### Acknowledgments

This program was sponsored by the Office of Naval Research (Grant No. N00014-89-J-3105) and the Air Force Office of Scientific Research (Grant No. AFOSR-89-0324). The program monitors are Dr. Gabriel Roy and Major Dan Fant, respectively. Part of the facility was constructed under a support from the National Science Foundation (Grant No. CBT-8708843).

### References

- Abu-Ghannam, J. B., and Shaw, R., 1980, "Natural Transition of Boundary Layers—the Effects of Turbulence, Pressure Gradient, and Flow History," *J. Mech. Eng. Sci.*, Vol. 22, pp. 213-228.
- Baines, W. D., and Peterson, E. G., 1951, "An Investigation of Flow Through Screens," *Trans. ASME*, Vol. 73, pp. 467-480.
- Blair, M. F., 1982, "Influence of Free-Stream Turbulence on Boundary Layer Transition in Favorable Pressure Gradients," *ASME Journal of Engineering for Power*, Vol. 104, pp. 743-750.
- Blair, M. F., 1983a, "Influence of Free-Stream Turbulence on Turbulent Boundary Layer Heat Transfer and Mean Profile Development, Part I—Experimental Data," *ASME Journal of Heat Transfer*, Vol. 105, pp. 33-40.
- Blair, M. F., 1983b, "Influence of Free-Stream Turbulence on Turbulent Boundary Layer Heat Transfer and Mean Profile Development, Part II—Analysis of Results," *ASME Journal of Heat Transfer*, Vol. 105, pp. 41-47.
- Chua, L. P., and Antonia, R. A., 1990, "Turbulent Prandtl Number in a Circular Jet," *International Journal of Heat and Mass Transfer*, Vol. 33, No. 2, pp. 331-339.
- Dhawan, S., and Narasimha, R., 1958, "Some Properties of Boundary Layer Flow During Transition From Laminar to Turbulent Motion," *Fluid Mech.*, Vol. 3, pp. 418-436.
- Dyban, Y. P., Epik, E. Y., and Suprun, T. T., 1980, "Characteristics of the Laminar Boundary Layer in the Presence of Elevated Free-Stream Turbulence," *Fluid Mechanics—Soviet Research* [in English], Vol. 22, No. 5, pp. 213-228.
- Emmons, H. W., 1951, "The Laminar-Turbulent Transition in a Boundary Layer—Part I," *J. Aero. Sci.*, Vol. 18, pp. 490-498.
- Graham, R. W., 1979, "Fundamental Mechanisms That Influence the Estimate of Heat Transfer to Gas Turbine Blades," *ASME Paper No. 79-HT-43*.
- Graham, R. W., ed., 1984, *Transition in Turbines*, NASA TM-79128.
- Hinze, J. O., 1975, *Turbulence*, 2nd ed., McGraw-Hill, New York.
- Kim, J., Simon, T. W., and Kestoros, M., 1989, "Fluid Mechanics and Heat Transfer Measurements in Transitional Boundary Layers Conditionally Sampled on Intermittency," presented at the 1989 ASME National Heat Transfer Conference, ASME HTD-Vol. 107, pp. 69-81.
- Kistler, A. L., and Vrebalovich, T., 1966, "Grid Turbulence at Large Reynolds Numbers," *J. Fluid Mech.*, Vol. 26, pp. 37-44.
- Klebanoff, P. S., Tidstrom, K. D., and Sargent, L. M., 1962, "The Three-Dimensional Nature of Boundary-Layer Instability," *J. Fluid Mech.*, Vol. 12, pp. 1-34.

Kuan, C. L., 1987, "An Experimental Investigation of Intermittent Behavior in the Transitional Boundary Layer," M.S. Thesis, Clemson University, Clemson, SC.

Kuan, C. L., and Wang, T., 1990, "Investigation of Intermittent Behavior of Transitional Boundary Layer Using a Conditional Averaging Technique," *Experimental Thermal and Fluid Science*, Vol. 3, pp. 157-170; also presented in 1989 at AIAA 20th Fluid Dynamics Plasma Dynamics and Lasers Conference, AIAA 89-1890.

Mayle, R. E., 1991, "The Role of Laminar-Turbulent Transition in Gas Transition Engines," *ASME JOURNAL OF TURBOMACHINERY*, Vol. 113, pp. 509-537.

Morkovin, M. V., 1969, "On the Many Faces of Transition," *Viscous Drag Reduction*, C. S. Wells, ed., Plenum Press, New York, pp. 1-31.

Morkovin, M. V., 1978, "Instability, Transition to Turbulence and Predictability," AGARDograph 236.

Narasimha, R., 1985, "The Laminar-Turbulent Transition Zone in the Boundary Layer," *Prog. Aerospace Sci.*, Vol. 22, pp. 29-80.

Reshotko, E., 1976, "Boundary Layer Stability and Transition," *Ann. Rev. Fl. Mech.*, Vol. 8, p. 311-350.

Schubauer, G. B., and Skramstad, H. K., 1948, "Laminar Boundary-Layer Oscillations and Transition on a Flat Plate," NACA Report 909.

Shome, B., 1991, "Development of a Three-Wire Probe for the Measurement of Reynolds Stresses and Heat Fluxes in Transitional Boundary Layers," MS Thesis, Dept. of Mech. Engr., Clemson University, Clemson, SC.

Sohn, K. H., and Reshotko, E., 1991, "Experimental Study of Boundary Layer Transition With Elevated Freestream Turbulence on a Heated Flat Plate," NASA CR-187068.

Sohn, K. H., Reshotko, E., and Zaman, K. B. M. Q., 1991, "Experimental Study of Boundary Layer Transition on a Heated Flat Plate," *ASME FED-Vol. 114*, pp. 163-171.

Suder, K. L., O'Brien, J. E., and Reshotko, E., 1988, "Experimental Study of Bypass Transition in a Boundary Layer," *NASA TM-100913*.

Tani, I., 1981, "Three-Dimensional Aspects of Boundary Layer Transition," *Proc. Indian Acad. Sci.*, Vol. 4, Part 2, pp. 219-238.

Turner, A. B., 1971, "Local Heat Transfer Measurements on a Gas Turbine Blade," *J. Mech. Eng. Sci.*, Vol. 13, pp. 1-12.

Volino, R. J., and Simon, T. W., 1995, "Bypass Transition in Boundary Layers Including Curvature and Favorable Pressure Gradient Effects," *ASME JOURNAL OF TURBOMACHINERY*, Vol. 117, No. 1, pp. 166-174.

Wang, T., and Simon, T. W., 1989, "Development of a Special-Purpose Test Surface Guided by Uncertainty Analysis," *Journal of Thermophysics*, Vol. 3, No. 1, pp. 19-26.

Wang, T., Simon, T. W., and Buddhavarapu, J., 1987, "Heat Transfer and Fluid Mechanics Measurements in Transitional Boundary Layer Flows," *ASME JOURNAL OF TURBOMACHINERY*, Vol. 109, No. 3, pp. 443-450.

Wang, T., Keller, F. J., and Zhou, D., 1992, "Experimental Investigation of Reynolds Shear Stresses and Heat Fluxes in a Transitional Boundary Layer," *Fundamental and Applied Heat Transfer Research for Gas Turbine Engines*, ASME HTD-Vol. 226, pp. 61-70.

Zhou, D., 1993, "Effects of Elevated Free-Stream Turbulence and Favorable Pressure Gradient on Flow and Thermal Structures in Transitional Boundary Layers," Ph.D. Dissertation, Dept. of Mech. Engr., Clemson University, Clemson, SC.



The American Society of  
Mechanical Engineers

## ASME COUPON BOOKS

Use coupons to purchase all ASME publications — including special publications, codes and standards, and technical papers (preprints). Use coupons to save money. Technical papers cost less when you purchase them with coupons! One coupon may be redeemed for one technical paper. That's a savings of \$.50 for members, \$1.00 for non-members (off the regular price for preprints).

### TECHNICAL PAPERS (PREPRINTS) COUPON BOOK

CONTAINS 10 COUPONS

ORDER No. CB0001

\$40 (ASME MEMBERS) / \$80 (NON-MEMBERS)

### PUBLICATIONS COUPON BOOK

CONTAINS 10 COUPONS (\$10 EACH)

ORDER No. CB0002

\$100 (MEMBER & NON-MEMBER)

#### TELEPHONE

800-THE-ASME (USA & CANADA) 201-882-1717 OR  
(800-843-2763)

95 800-843-2763 (MEXICO)

201-882-1167 (OUTSIDE NO. AMERICA)

#### FAX

201-882-5157 OR  
201-882-5155

#### E-MAIL

infocentral@asme.org

#### MAIL

ASME  
22 LAW DRIVE  
P.O. Box 2300  
FAIRFIELD, NEW JERSEY 07007-2300

# Flow and Heat Transfer Behavior in Transitional Boundary Layers With Streamwise Acceleration

F. J. Keller

T. Wang

Department of Mechanical Engineering,  
Clemson University,  
Clemson, SC

*The effects of streamwise acceleration on a two-dimensional heated boundary layer undergoing natural laminar-turbulent transition were investigated with detailed measurements of momentum and thermal transport phenomena. Tests were conducted over a heated flat wall with zero pressure-gradient and three levels of streamwise acceleration:  $K \equiv (\nu/U_\infty^2) (dU_\infty/dx) = 0.07, 0.16, \text{ and } 0.25 \times 10^{-6}$ . Free-stream turbulence intensities were maintained at approximately 0.5 percent for the baseline case and 0.4 percent for the accelerating cases. A miniature three-wire probe was used to measure mean velocity and temperature profiles, Reynolds stresses, and Reynolds heat fluxes. Transition onset and end were inferred from Stanton numbers and skin-friction coefficients. The results indicate that mild acceleration delays transition onset and increases transition length both in terms of distance,  $x$ , and Reynolds number based on  $x$ . Transition onset and length are relatively insensitive to acceleration in terms of momentum thickness Reynolds number. This is supported by the boundary layer thickness and integral parameters, which indicate that a favorable pressure gradient suppresses boundary layer growth and development in the transition region. Heat transfer rates and temperature profiles in the late-transition and early-turbulent regions lag behind the development of wall shear stress and velocity profiles. This lag increases as  $K$  increases, indicating that the evolution of the heat transport is slower than that of the momentum transport. Comparison of the evolution of rms temperature fluctuations to the evolution of Reynolds normal stresses indicates a similar lag in the rms temperature fluctuations.*

## Introduction

Knowledge of the physics involved in momentum and thermal transport in the transitional boundary layer can be applied to the external flow over gas turbine vanes and blades. For a commercial gas turbine engine, it is common for as much as 50 to 80 percent of the turbine blade surface to be covered with flow undergoing transition (Turner, 1971). Most modeling codes for heat transfer rely on some form of Reynolds analogy to predict thermal loading, i.e., inferring the thermal transport directly from the momentum transport. Recent experimental investigations indicate a breakdown in this analogy in the transitional flow process (Blair, 1982, 1992; Wang et al. 1985; Sharma, 1987; Volino and Simon, 1991). Therefore, the conventional technique of basing heat transfer modeling on a constant value or a multiple-layer model of the turbulent Prandtl number may be inadequate. Since turbine blades are exposed to a wide range of pressure gradients (Mayle, 1991), the reported discrepancy between fluid mechanics and heat transfer is especially important. Recognition and understanding of the underlying mechanisms involved in this discrepancy between momentum and thermal transport are essential to improving the accuracy of thermal load predictions. The purpose of this research program is to investigate the effects of streamwise acceleration on a two-dimensional boundary layer undergoing natural transition. The transport mechanisms within the boundary layer must be explored to determine what discrepancies exist between the momentum and thermal transport, thereby addressing the validity of Reynolds analogy for use in the transition process. The results of this study have served as a valuable reference for

comparison with the results of streamwise acceleration in elevated free-stream turbulence conditions (Zhou and Wang, 1993).

Most correlations for transition onset incorporate the combined effects of free-stream turbulence intensity (FSTI) and pressure gradient. In flows with low free-stream turbulence, large discrepancies exist between these methods in predicting transition onset, especially for favorable pressure gradients (Arnal, 1984). For flows with low FSTI, the pressure gradient significantly affects the transition onset. As FSTI increases, the pressure gradient has less of an effect (Abu-Ghannam and Shaw, 1980). The experimental results of many researchers, for example, Turner (1971), Abu-Ghannam and Shaw (1980), Blair (1982, 1992), Narasimha (1985), and Rued and Wittig (1985, 1986), showed that a favorable pressure gradient increases the length of transition. These results can be used to predict the fluid mechanics and momentum transport in transitional boundary layers and to predict heat transfer, provided that some form of Reynolds analogy holds. However, for favorable pressure gradient flow, experimental evidence indicates a breakdown of Reynolds analogy. Blair (1982, 1992), Sharma (1987), and Volino and Simon (1991) determined that the length of transition for accelerating flows is longer for the thermal than the momentum boundary layer. By comparing the Stanton numbers and temperature profiles to the shape factor and velocity profiles, Blair (1992) determined that the physical length of transition is one-third longer for heat transfer than it is for flow with  $K = 0.20 \times 10^{-6}$ . Blair reasoned that the difference between the velocity and the temperature profiles is produced by the streamwise pressure distribution. The boundary layer velocity distribution depends directly on mainstream acceleration, as shown by the equations of motion. The temperature distribution is only indirectly linked to the pressure gradient through the effect of acceleration on the turbulent transport of heat. These results indicate that inferring transition information

Contributed by the International Gas Turbine Institute and presented at the 39th International Gas Turbine and Aeroengine Congress and Exposition, The Hague, The Netherlands, June 13-16, 1994. Manuscript received by the International Gas Turbine Institute February 4, 1994. Paper No. 94-GT-24. Associate Technical Editor: E. M. Greitzer.

from the heat transfer measurements alone is unreliable for accelerating flow and that transition prediction based on fluid mechanics measurements will not accurately predict the heat transfer in transition.

Information regarding the mean flow structure within the transitional boundary layer for a zero-pressure gradient is well documented. Most of the results isolate the effects of FSTI on heat transfer and flow structure. Typical parameters investigated are mean velocity and temperature profiles, fluctuating turbulent velocity and Reynolds shear stresses ( $u'^2$ ,  $v'^2$ ,  $\bar{u}\bar{v}$ ), and Reynolds heat fluxes ( $\bar{u}\bar{t}$ ,  $\bar{v}\bar{t}$ ). The highlights of these results are listed below.

- 1 The streamwise fluctuating turbulent velocity ( $u'$ ) reaches a peak value of approximately 18 percent of  $U_\infty$ , regardless of the level of FSTI (Schubauer and Klebanoff, 1956; Wang et al., 1985; Kim et al., 1989; Kuan and Wang, 1990). This value is greater than the value for fully turbulent flow.
- 2 The  $u'$  profiles in the transition region are characterized by two peaks, one near-wall peak and a second peak midway through the boundary layer (Wang et al., 1985; Sohn et al., 1989; Kuan and Wang, 1990). The cause of the second peak is still the subject of controversy.
- 3 The cross-stream fluctuating turbulent velocity ( $v'$ ) reaches a constant value much earlier than  $u'$ , indicating that the flow in a transitional boundary layer is less isotropic than the flow of a fully turbulent boundary layer. The location of the peak in  $v'$  in the streamwise direction coincides with the location of the peak in  $u'$  in the streamwise direction (Kuan and Wang, 1990).
- 4 Measurements of the average Reynolds cross-stream heat flux ( $\bar{u}\bar{t}$ ) have resulted in negative values near the wall for some researchers (Sohn et al., 1989; Wang et al., 1992), while they remain positive for others (Kim et al., 1989). The reasons for this are as yet unknown.

Current documentation of the mean flow structure within transitional flows with favorable pressure gradients is extremely limited. Blair (1992) presented velocity and temperature profiles through the transition region for boundary layer flow with  $K = 0.20 \times 10^{-6}$  and FSTI = 2 percent (high FSTI transition). The results showed that the development of the temperature profiles lags behind those of the respective velocity profiles. This strongly indicates that acceleration affects heat transfer differently than it does flow structure. The cause of these differences remains to be determined. To the knowledge of these authors, no further information is available regarding detailed flow and thermal structure within the transitional boundary layer with a favorable pressure gradient.

## Nomenclature

$C_f$  = skin-friction coefficient =  $\tau_w/(\rho U_\infty^2(x)/2)$   
 $C_p$  = pressure coefficient =  $(P - P_\infty)/(\frac{1}{2}\rho U_\infty^2)$   
 $c_p$  = specific heat  
 $K$  = pressure gradient parameter =  $(\nu/U_\infty^2(x))(dU_\infty(x)/dx)$   
 $P$  = static pressure  
 $q''$  = wall heat flux  
 $Re$  = Reynolds number =  $U_\infty(x)x/\nu$   
 $t$  = instantaneous fluctuation in temperature  
 $t'$  = rms value of temperature fluctuation  
 $T$  = instantaneous temperature  
 $T$  = mean temperature

$u$ ,  $v$  = instantaneous velocity fluctuations in streamwise and cross-stream directions  
 $u'$ ,  $v'$  = rms values of velocity fluctuations  
 $u_r$  = friction velocity =  $\sqrt{\tau_w/\rho}$   
 $U$ ,  $V$  = instantaneous velocities  
 $\bar{U}$  = mean velocity  
 $U^+ = \bar{U}/u_r$   
 $\bar{u}\bar{v}$  = mean Reynolds shear stress  
 $\bar{u}\bar{t}$  = mean Reynolds streamwise heat flux  
 $\bar{v}\bar{t}$  = mean Reynolds cross-stream heat flux  
 $x$  = coordinate in streamwise direction  
 $y$  = coordinate normal to the surface

$Y^+ = yu_r/\nu$   
 $\Gamma$  = intermittency factor

$\delta$  = boundary layer thickness at 0.995  $U_\infty$

$\delta^*$  = displacement thickness

$\theta$  = momentum thickness

$\nu$  = kinematic viscosity

$\rho$  = density

$\tau_w$  = shear stress on the wall

## Subscripts

end = end of transition  
ref = reference location at  $x = 20$  cm  
 $s$  = onset of transition  
 $w$  = at the wall  
 $\infty$  = free-stream value

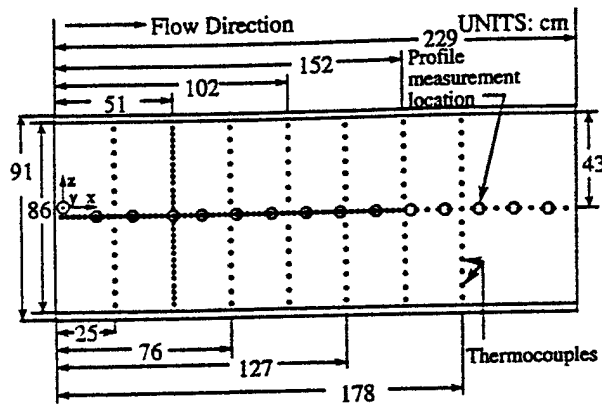


Fig. 1 Thermocouple layout on heated test wall

## Experimental Program

**Test Facility.** The experiments were conducted in a two-dimensional, open circuit, blowing-type wind tunnel capable of a maximum air speed of 35 m/s, uniform within 0.7 percent and steady within 1 percent over a 20-hour period. Rayon-viscous felt capable of filtering out particles larger than 5  $\mu\text{m}$  was used to filter the inlet airflow. The free-stream air temperature, controlled by the heat exchanger and the air-conditioning system in the laboratory, could be maintained within 0.5  $^\circ\text{C}$  over a period of 20 hours and uniformly within 0.1  $^\circ\text{C}$ . To ensure that the boundary layer began at the leading edge of the test wall, a suction fan and low-pressure plenum were installed to provide suction. A detailed description of the wind tunnel is provided by Kuan (1987) and Kuan and Wang (1990).

The test section was designed with a large aspect ratio of 6, which provided the two-dimensional flow required in this investigation. The test section was 0.15 m wide, 2.4 m long, and 0.92 m high. A composite construction was utilized for the rectangular 2.4  $\times$  0.92-m heated test wall. This design allows for flexibility, so that the test wall can be bent to varying degrees of streamwise curvature for future studies. The back surface was insulated with 25.4 cm of R30 fiberglass to minimize backplane conduction losses. The heating pad consisted of a heater foil sandwiched between glass cloth and silicon rubber sheets. A 1.56-mm-thick aluminum sheet was vulcanized to the front surface of the heater pad to improve the uniformity of the heat flux. A 1.56-mm polycarbonate sheet was placed on the front surface to provide a smooth test surface on which the air flows and from which measurements were taken. One hundred eight-

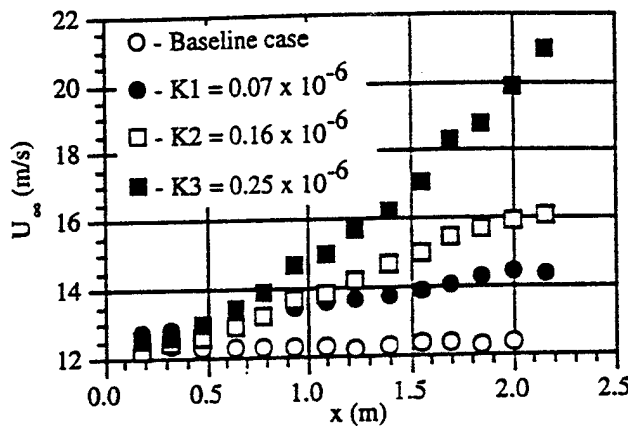


Fig. 2 Free-stream velocity for each case

five 3-mil E-type thermocouples were embedded beneath the test surface and were strategically placed along the test surface to capture the spanwise and streamwise evolution of the wall heat transfer during the transitional flow process (Fig. 1).

Fourteen measuring holes of 2.54-cm diameter were drilled along the centerline axis in the outer observation wall. The first centerline measuring hole (station 1) was located 20 cm from the leading edge, with the remaining measuring holes placed every 15 cm (labeled sequentially station 2 through 14). When the probe was placed through the measuring hole into the test section, the length of the probe extended 2 cm upstream of the hole location. Plexiglas plugs, flush with the inner surface, were used to plug the holes when measurements were not being taken. Slots cut into the bottom wall and the top wall provided for adjustment of the outer observation wall in order to vary the pressure gradient in the test section. A detailed description of the test section and heated test wall was documented by Wang et al. (1992).

**Geometry of the Test Section.** The geometry of the test section used in this investigation was first described by Keller and Wang (1993), and is repeated here for clarity. For the baseline case, with no acceleration, the outer wall of the test section was adjusted to account for the growth of the boundary layer and to maintain a near-zero pressure distribution inside the test section with a variation of pressure coefficient,  $C_p$ , within 1 percent. Three different favorable pressure gradients were utilized in this investigation. A constant pressure gradient parameter,  $K$ , was maintained during each case. One of the advantages of using a constant  $K$  over other pressure gradient parameters is that a constant  $K$  can be conveniently obtained by linearly decreasing the width of the test section from the

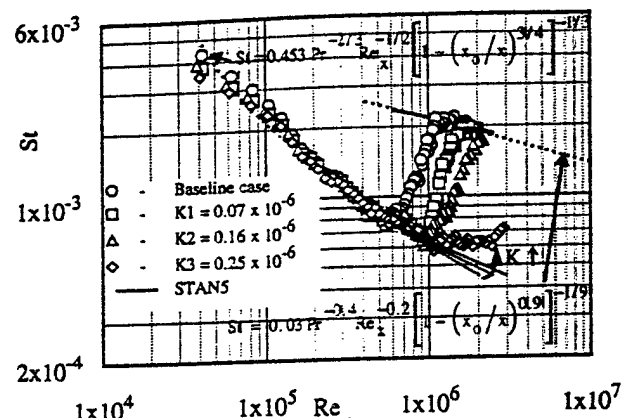


Fig. 4 Centerline Stanton number distribution for all cases

inlet to the exit. Fine tuning of the local width of the test section removed the effect of boundary layer growth on the pressure gradient. For each acceleration case, the width of the test section inlet was maintained at 15.24 cm, and the downstream width was arranged to decrease linearly to the exit plane. An exit width of 14.6 cm was used for the lowest acceleration case of  $K = 0.07 \times 10^{-6}$ , while an exit width of 8.9 cm was used for the highest acceleration case of  $K = 0.25 \times 10^{-6}$ . It should be noted that a constant  $K$  flow is inherently different from a Falkner-Skan flow, which has a constant  $\Lambda (= (\delta^2/\nu) (dU_x(x)/dx))$  value. Detailed explanations concerning the physical meaning of flow and thermal features of accelerated boundary layers with constant  $K$  values and the differences between a constant  $K$  and a constant  $\Lambda$  flow were made by Zhou and Wang (1992).

**Three-Wire Sensor.** A specially designed, miniature three-wire probe was used to measure the boundary layer velocity and temperature data. An "X" array, consisting of two 1.0-mm-long and 2.5-μm-dia Wollaston-type platinum-coated tungsten wires was used as the velocity sensor. An active sensing length of 0.5 mm was etched in the center. The "X" wires were placed orthogonal to each other with a spacing of 0.35 mm. The temperature sensor is a 0.35-mm-long unplated platinum wire 1.2 μm in diameter placed normal to the mean flow direction, in a plane parallel to the plane of the cross wire and spaced 0.35 mm from the "X" array. A complete description of the probe design and qualification, specifically in a heated transitional boundary layer, can be found in Shome (1991).

Table 1 Reynolds numbers at onset and end of transition for all test cases (note: \*\*\*\* indicates that no end of transition was observed in the test facility)

	Baseline	$K_1 = 0.07 \times 10^{-6}$	$K_2 = 0.16 \times 10^{-6}$	$K_3 = 0.25 \times 10^{-6}$
FSTI at $x_0$	0.5	0.4	0.4	0.4
$U_{\infty}$ (m/s)				
Sta01	12.24	12.68	12.20	12.45
$x = 18$ cm				
Onset of transition	$x(cm)$ 5.8	$x(cm)$ 107	$x(cm)$ 115	$x(cm)$ 122
	$Re_x$ $5.50 \times 10^5$	$Re_x$ $9.46 \times 10^5$	$Re_x$ $10.3 \times 10^5$	$Re_x$ $12.5 \times 10^5$
	$Re_{\theta}$ 1294	$Re_{\theta}$ 1322	$Re_{\theta}$ 1233	$Re_{\theta}$ 1233
	$Re_{\eta}$ 492	$Re_{\eta}$ 541	$Re_{\eta}$ 544	$Re_{\eta}$ 552
End of transition	$x(cm)$ 137	$x(cm)$ 168	$x(cm)$ 213	****
	$Re_x$ $11.2 \times 10^5$	$Re_x$ $15.7 \times 10^5$	$Re_x$ $21.7 \times 10^5$	****
	$Re_{\theta}$ 1826	$Re_{\theta}$ 1874	$Re_{\theta}$ 1880	****
	$Re_{\eta}$ 1302	$Re_{\eta}$ 1282	$Re_{\eta}$ 1235	****
Length of transition	$x(cm)$ 69	$x(cm)$ 91	$x(cm)$ 98	****
	$Re_x$ $5.70 \times 10^5$	$Re_x$ $6.24 \times 10^5$	$Re_x$ $11.4 \times 10^5$	****
	$Re_{\theta}$ 532	$Re_{\theta}$ 552	$Re_{\theta}$ 647	****
	$Re_{\eta}$ 810	$Re_{\eta}$ 741	$Re_{\eta}$ 691	****

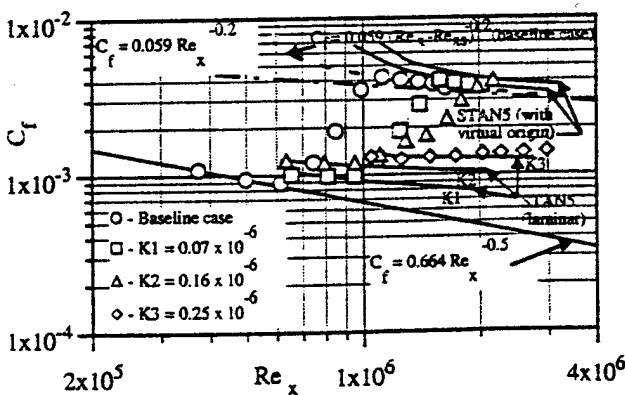


Fig. 3 Skin friction coefficient versus Reynolds number for each case

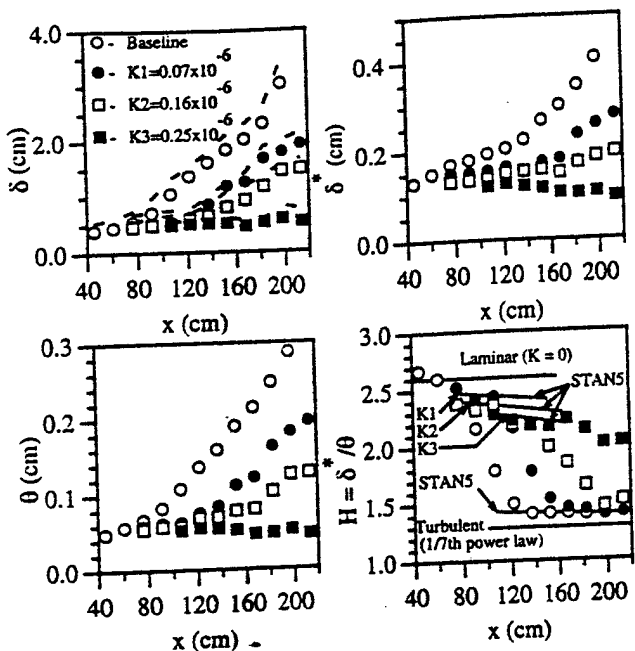


Fig. 5 Boundary layer integral parameters for all cases (--- thermal boundary layer thickness)

**Measurements and Instrumentation.** The velocity sensors were operated in a constant-temperature mode, using a TSI model IFA 100 Intelligent Flow Analyzer. A DISA M20 TSI model IFA 100 Intelligent Flow Analyzer. A DISA M20

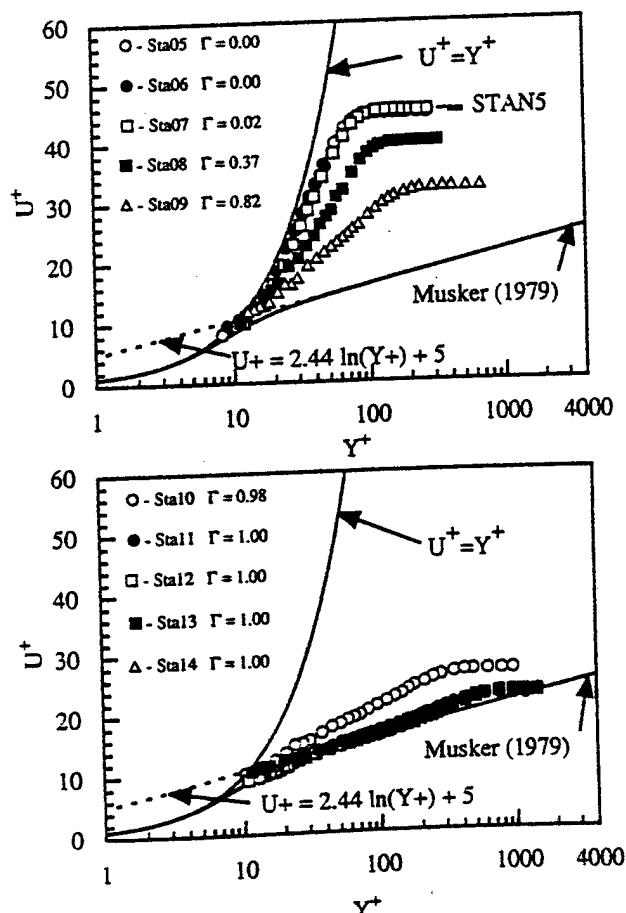


Fig. 6 Mean velocity profiles for  $K1 = 0.07 \times 10^{-6}$  in wall units

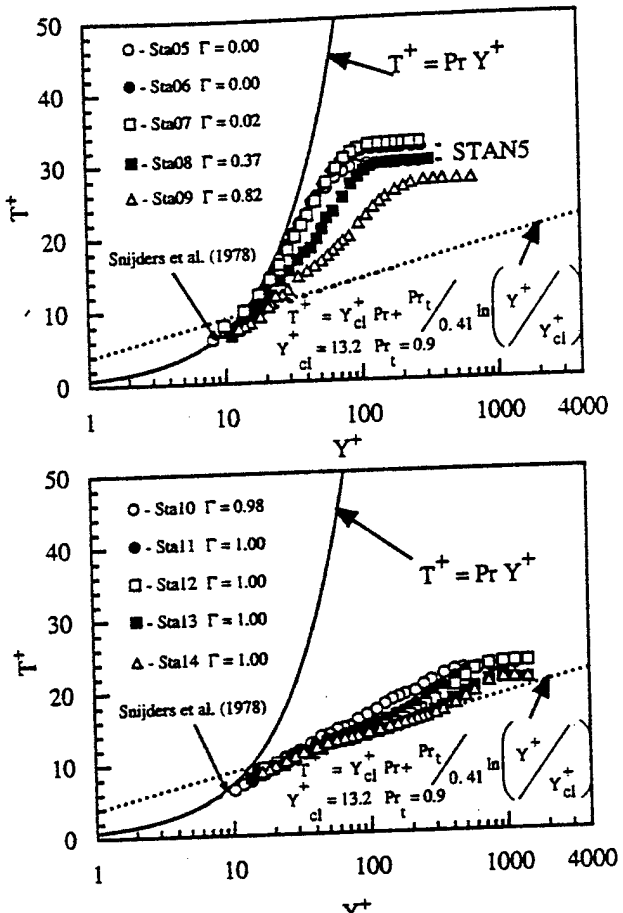


Fig. 7 Mean temperature profiles for  $K1 = 0.07 \times 10^{-6}$  in wall units

temperature bridge was used to operate the temperature sensor in the constant current mode. For future turbulent power and thermal power spectral analyses, TSI Model 157 signal conditioners were used to low-pass filter signals from all three sensors. The "X" wires of the three-wire sensor were operated at overheat ratios of 1.43 and 1.66. The temperature sensor was operated with a very low overheat ratio. The probe current was set at 0.1 mA, and an amplifier gain of 3500 was used. For convenience, the velocity wires are referred to as hot wires, and the temperature wire is referred to as a cold wire in this study. The optimum frequency response found for each velocity wire was approximately 200 kHz. The frequency response of the temperature sensor was experimentally determined to range from 4800 to 6400 Hz, depending on the velocity, by using the DISA M20 constant current bridge (see Wang et al., 1992, and Keller, 1993, for details). In addition to the three-wire sensor, a single hot wire was used to cross-check the results obtained from the three-wire sensor and to provide guidance for calculating the skin-friction coefficient in the near-wall region. The data from all of the sensors were subsequently sampled at 2 kHz for 20 seconds with the low-pass filter set at 1 kHz.

The wind tunnel, the test wall power supply, and the cooling water supply were started at least 12 hours prior to the experiment. A global measurement for wall temperature distribution was performed by scanning the temperature approximately every two hours. Each time, an average of three different scans, each made at a sample rate of 1 channel/second, was obtained. The local wall temperature was checked before, midway through, and after each measurement of the boundary layer temperature profile to ensure that it remained steady. Both the global and local check served to monitor the steadiness and the

free-stream temperature as well as the wall temperature. The thermocouple measurements were made through a Fluke 8842A 5-1/2 digit digital multimeter and a Fluke 2205A switch controller. For each case, a uniform heat flux of  $335 \text{ W/m}^2$  was applied to the test wall, and the free-stream temperature was maintained at approximately  $15^\circ\text{C}$ . The resulting wall temperatures ranged from  $24^\circ\text{C}$  to  $41^\circ\text{C}$ . All fluid properties were evaluated at atmospheric pressure and free-stream temperature.

## Results and Discussion

In the following discussion, the results of the baseline case are used for comparison with the accelerating cases. Please refer to Keller (1993) or Wang et al. (1992) for detailed documentation of the baseline case. After the sampled data were reduced, the intermittency function was obtained. The value of this function is 1 if the flow is turbulent, and 0 otherwise. The total percentage of time that the intermittency function is 1 determines the intermittency factor,  $\Gamma$ . For a complete description of the method used to determine the intermittency factor, refer to Keller and Wang (1993). The free-stream velocities for each of the three accelerating cases, along with the velocity of the baseline case, are shown in Fig. 2. For each accelerating case, the free-stream velocity at station 1 (the reference station for the  $C_p$  measurements) was maintained as close to the value used during the baseline case as possible. The  $K$  values obtained were  $K = 0.07 \times 10^{-6}$ ,  $K = 0.16 \times 10^{-6}$ , and  $K = 0.25 \times 10^{-6}$ . These values are termed  $K1$ ,  $K2$ , and  $K3$  for the remainder of the discussion.

**Skin Friction, Stanton Number, and Integral Parameters.** Station numbers are used when referencing all measurement locations. The variation of skin-friction coefficient for each case

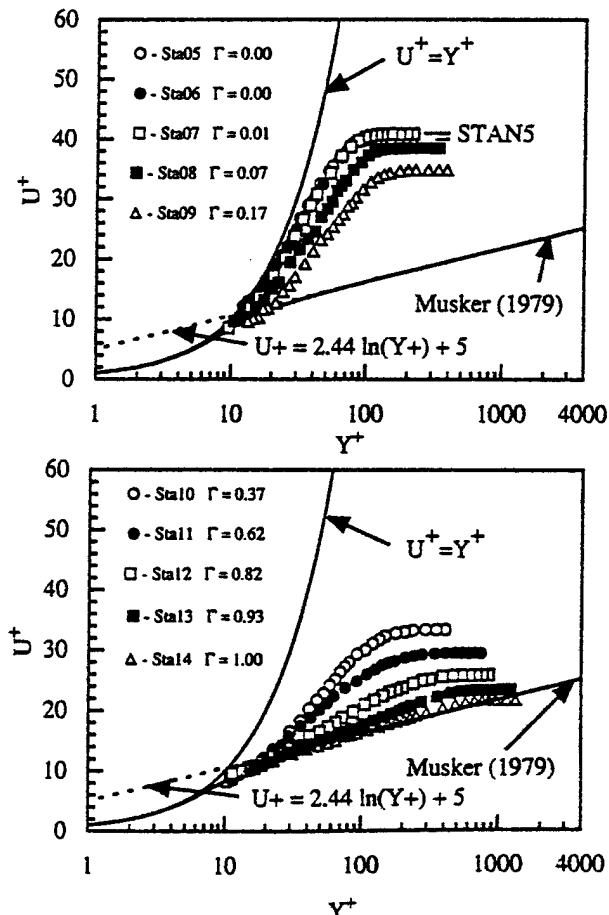


Fig. 8 Mean velocity profiles for  $K2 = 0.16 \times 10^{-6}$  in wall units

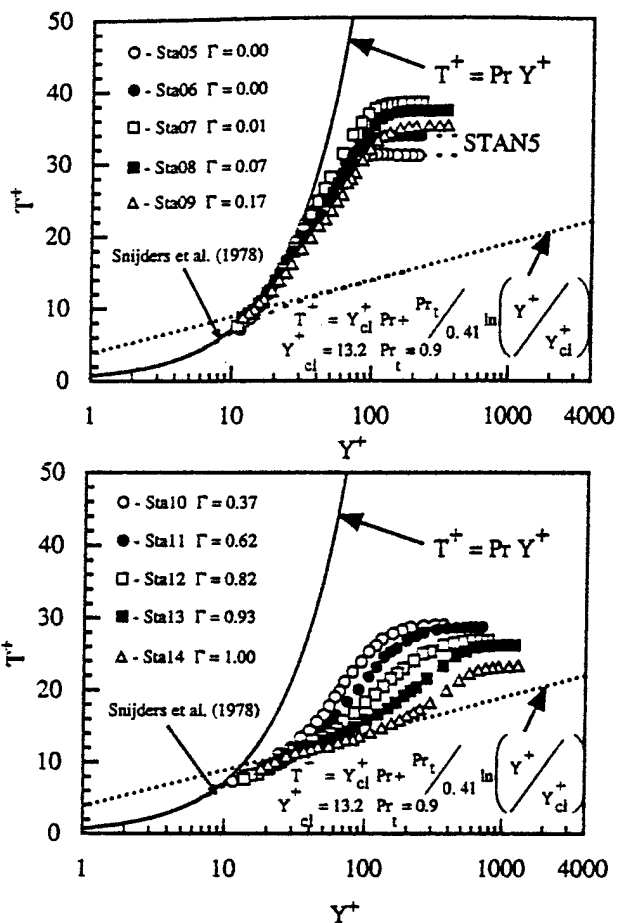


Fig. 9 Mean temperature profiles for  $K2 = 0.16 \times 10^{-6}$  in wall units

is shown in Fig. 3. All skin-friction values were obtained from the mean velocity profiles, including single hot-wire measurements for use as a guide. Mean velocity profile outputs from the STANS code (NASA/Lewis version, expanded from the original version from Crawford and Kays, 1976) were used to compare the laminar stations. The skin-friction values for laminar and turbulent flow from the STANS solutions are also shown in Fig. 3. For the laminar region, an increasing  $K$  makes the mean velocity profiles fuller, and thus increases the skin-friction coefficient. The same effect occurs in fully turbulent flow. From Fig. 3, it is observed that a higher  $K$  value delays the onset of transition and increases the length of transition. These observations are consistent with the experimental results of Turner (1971), Abu-Ghannam and Shaw (1980), Blair (1982, 1992), Narasimha (1985), and Rued and Wittig (1985, 1986).

The distribution of centerline Stanton numbers for each case is shown in Fig. 4. The Stanton numbers for all three accelerating cases follow their corresponding laminar correlations for zero pressure gradient up to the point of transition, and then approach the fully turbulent correlation at the end of transition. This is consistent with the experimental results of Blair (1982), which indicated no significant deviation from the laminar or turbulent correlations for flows with  $K$  values of  $0.2 \times 10^{-6}$  and  $0.75 \times 10^{-6}$ . For a strongly accelerating flow, such as  $K = 3.2 \times 10^{-6}$ , Rued and Wittig (1985) observed a 20 percent increase in Stanton number over their zero pressure gradient case for the early laminar region, followed by a slight decrease below the zero pressure gradient laminar correlation as the Reynolds number increases. The effects of streamwise acceleration on Stanton number in the laminar and turbulent boundary layer are not significant until a relatively large value of  $K$  is obtained.

In this investigation, transition onset was defined by the location,  $L$ , where the skin-friction coefficient (and/or Stanton number) deviates from the laminar correlation, and the end of transition was defined as the point of maximum skin friction (and/or Stanton number) immediately following the rise of  $C_f$ . The onset and end of transition were inferred from Figs. 3 and 4, and are listed in Table 1. As  $K$  increases, the location of transition onset is delayed both in terms of physical distance,  $x$ , and Reynolds number based on  $x$ . For the three accelerating cases,  $Re_x$  appears insensitive to the point of transition, which is consistent with the observations of Blair (1992). This is also consistent with the observation made by Abu-Ghannam and Shaw (1980), that a favorable pressure gradient has an insignificant effect on the onset of transition in terms of  $Re_x$ . The physical length of transition, in terms of  $x$ , for the  $K1$  case is actually shorter than that of the baseline case by approximately 12 percent (7 cm). This is attributed to the spacing of the measuring stations and the difficulty in obtaining an exact transition start and end point. Determination of the onset and end of transition was limited to a measuring station location or a point midway between two stations. If the point was determined to be midway between two stations, then the free-stream velocity and integral parameters were estimated by linearly interpolating between the values at the adjoining stations. For the  $K2$  case, the physical length of the transition region is much longer (42 percent) than the baseline case or the  $K1$  case. The length of transition in terms of  $Re_x$  and  $Re_x^*$  increases as  $K$  increases, whereas the length of transition decreases in terms of  $Re_x$  as  $K$  increases. For the  $K3$  case, the length of the test section was insufficient to obtain fully turbulent conditions.

The momentum boundary layer thickness, thermal boundary layer thickness, and integral parameters for each case are shown

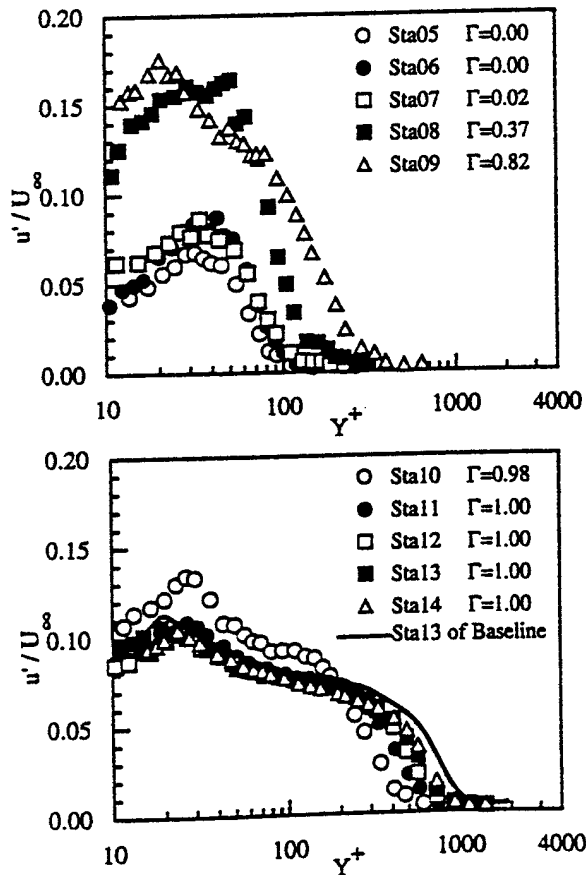


Fig. 10 Streamwise fluctuating turbulent velocity distributions for  $K1 = 0.07 \times 10^{-6}$  in wall units

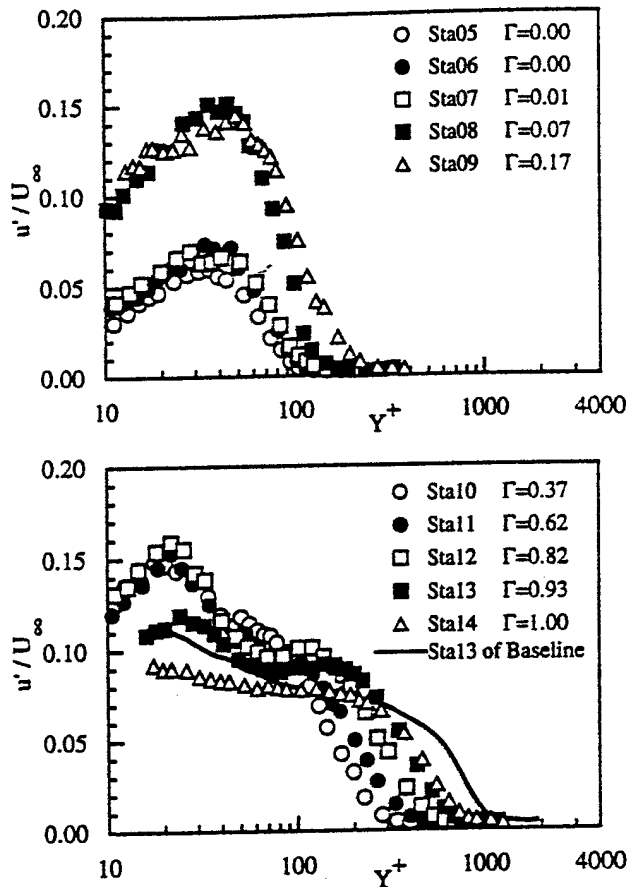


Fig. 11 Streamwise fluctuating turbulent velocity distributions for  $K2 = 0.18 \times 10^{-6}$  in wall units

in Fig. 5. Increasing the pressure gradient suppresses boundary layer growth and development through the transition region. For the strongest accelerating case,  $K3$ , the boundary layer displacement thickness and the momentum thickness actually decrease in the downstream direction. This is consistent with the analytical results of Zhou and Wang (1992) for laminar flows with constant  $K$  values.

**Mean Velocity and Mean Temperature Profiles.** The mean velocity and temperature profiles for cases  $K1$  and  $K2$  are shown in wall units in Figs. 6–9. The results of the  $K3$  case are omitted from further discussion since the flow for this case never reached beyond the early transition region, and no additional information was obtained. For the lowest accelerating case,  $K1$ , the mean velocity profiles followed the laminar solution up through station 7. The flow was transitional from stations 8 through 10 and matched the fully turbulent correlation for a zero pressure gradient flow from station 11 to station 14 (Fig. 6). Blair (1982, 1992) reported that the velocity profiles for fully turbulent flow with  $K = 0.2 \times 10^{-6}$  also matched the zero pressure gradient correlation. However, Julien et al. (1969) reported that for  $K$  values greater than  $0.57 \times 10^{-6}$ , the fully turbulent velocity profiles slightly "overshoot" the log-linear region of the zero pressure gradient turbulent correlation. Apparently, low  $K$  values, although sufficient to affect the onset of transition, are insufficient to cause significant deviation from the zero-pressure gradient turbulent correlation. The mean temperature profiles for the  $K1$  case are shown in Fig. 7. The mean temperature profiles begin to deviate from the laminar solution at the same location as the mean velocity profiles; however, comparison of the transitional profiles reveals that the streamwise evolution of temperature lags behind the velocity distribu-

tions. This lag is evident at stations 11 and 12, where the velocity profiles are in close agreement with the law of the wall, but the temperature profiles exhibit a much shorter logarithmic region and are still approaching the fully turbulent profile. A similar observation was made by Blair (1982, 1992). For the  $K2$  case, the same observation is made in Figs. 8 and 9. The mean velocity profiles in the turbulent region have a slightly steeper slope in the linear-log region than does the zero pressure gradient turbulent correlation. No obvious wake region is observed. This is similar to the "overshoot" in the log-linear region observed by Julien et al. (1969). For the transitional process, the lag of the temperature profiles behind the velocity profiles is more clear in the  $K2$  case. These results indicate that the development of momentum transport in accelerating transitional flows leads the development of thermal transport. Sharma (1987) showed that current transition modeling schemes predict the momentum boundary layer in accelerating flows well, but fail to predict the thermal boundary layer. This failure was determined to be due to the different paces of development of the momentum and thermal transport. Sharma stressed the need to model this discrepancy correctly so that accurate predictions can be obtained. These authors believe that an improved understanding of the physical mechanisms can be obtained by investigating the Reynolds stresses and heat fluxes inside the boundary layer, as shown in the following sections.

**Streamwise and Cross-Stream Turbulent Fluctuating Velocities ( $u'$  and  $v'$ ).** The streamwise evolution of turbulent fluctuating velocity,  $u'$ , for  $K1$  and  $K2$  is shown in Figs. 10 and 11, respectively. The turbulent fluctuating velocities ( $u'$  and  $v'$ ) are related to the Reynolds stresses as  $\rho u'^2$  and  $\rho v'^2$ . The laminar stations exhibit a peak in  $u'$  at approximately  $Y^- =$

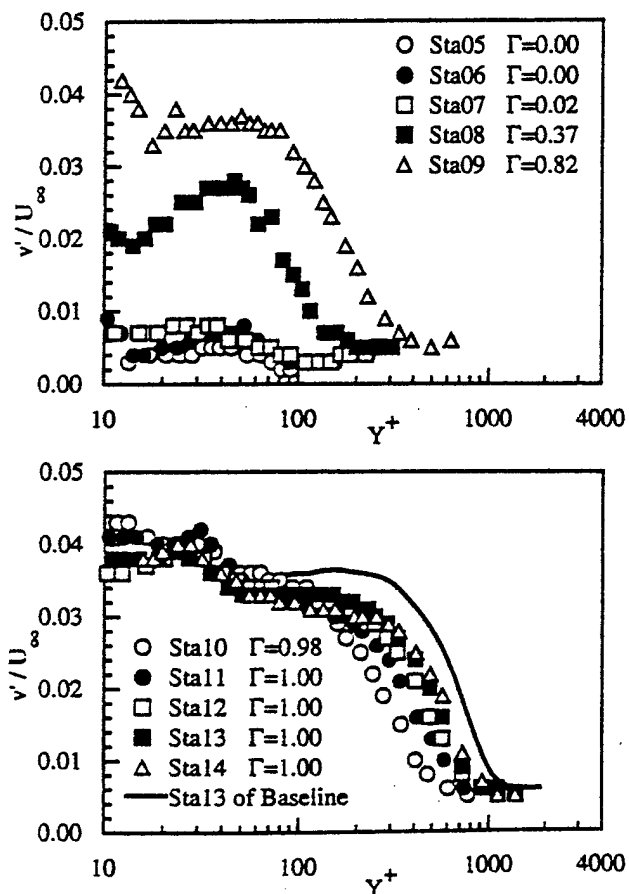


Fig. 12 Cross-stream fluctuating turbulent velocity distributions for  $K1 = 0.07 \times 10^{-4}$  in wall units

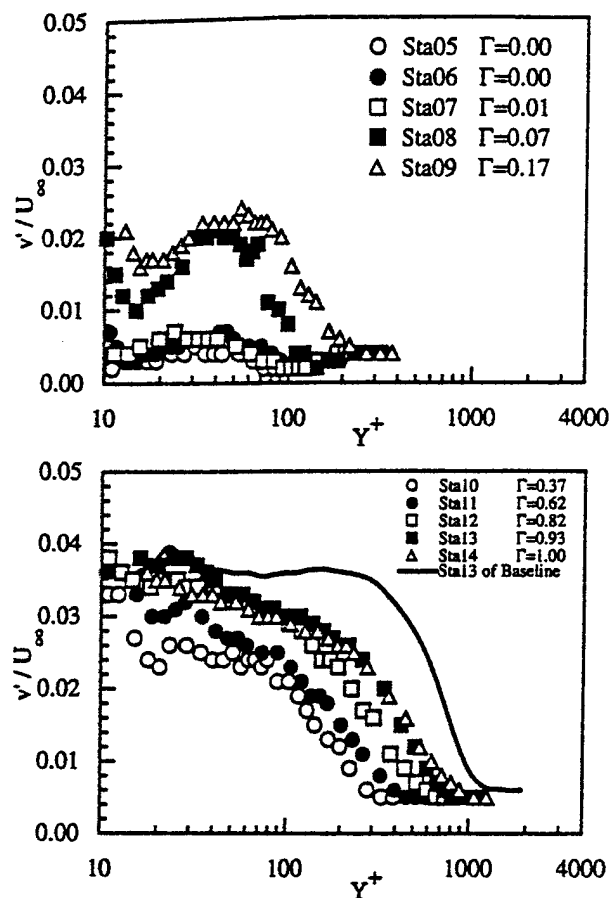


Fig. 13 Cross-stream fluctuating turbulent velocity distributions for  $K2 = 0.16 \times 10^{-4}$  in wall units

40. The magnitude of the peak intensity in the baseline case is approximately 5 percent of the free-stream velocity. The magnitudes of the peak intensities for the pressure gradient cases range from 7 to 9 percent of the free-stream velocity. These values are similar in magnitude to the intensities observed at the onset of transition for the baseline case. This indicates that in the presence of a favorable pressure gradient, a laminar boundary can tolerate a higher  $u'$  without undergoing transition than it can in the zero pressure gradient case. Within the transition region, the peak intensity observed in  $u'/U_s$  decreases as  $K$  increases. For the baseline case, the maximum  $u'$  in the transition region was 19 percent of the free-stream velocity. This maximum value slightly decreased to 18 percent for  $K1$  and to 16 percent for  $K2$ . For all three cases, the peak intensity in  $u'$  occurred in the transition region at approximately  $Y^+ = 30$ , near the beginning of the velocity log-linear region. For the fully turbulent region, as  $K$  increases, the peak intensity in  $u'$  is suppressed in the near-wall region between  $10 < Y^+ < 50$ , but it remains at the same level at the end of the log-linear region,  $200 < Y^+ < 300$ . This decrease is most likely due to a thickening of the viscous sublayer relative to the boundary layer thickness. It should be noted that the growth of both the viscous sublayer and the boundary layer is suppressed by a favorable pressure gradient; however, the viscous sublayer is suppressed less than the boundary layer.

The cross-stream turbulent fluctuating velocities,  $v'$ , for  $K1$  and  $K2$  are shown in Figs. 12 and 13, respectively. The trend in the development of  $v'$  for the accelerating cases is similar to that observed in the baseline case, but with less magnitude in the transition region as  $K$  increases. However, one distinct difference is observed in the fully turbulent region. For the

baseline case, the value of  $v'$  in the velocity log-linear region ( $40 < Y^+ < 200$ ) is fairly constant with a value of about 3.7 percent of the free-stream velocity. As  $K$  increases, this value is suppressed, and does not extend as far out into the boundary layer. For the  $K2$  case,  $v'$  never maintains a constant value, but progressively decreases from the near-wall maximum. It appears that pressure gradient affects  $v'$  more in the outer boundary layer than in the near-wall region.

The evolution of the maximum  $u'$  and  $v'$  for  $K1$  and  $K2$  is compared to the baseline case in Fig. 14. The streamwise locations are aligned with the onset and the end of transition. The results are similar to those observed from the baseline case, i.e., that  $u'$  increases to a maximum value in the early stage of transition and reduces in the late transition region. However,  $v'$  reaches the maximum value at about the same location that  $u'$  reaches the maximum, but it maintains this maximum value up through the turbulent flow region (see Kuan and Wang, 1989). The location of the peak value of  $u'$  migrates closer to the wall as the flow progresses downstream. Compared to the values of  $u'$  and  $v'$ , the flow in the transition region is much less isotropic than the flow in a fully turbulent boundary layer.

**Reynolds Shear Stress ( $\bar{uv}$ ).** Figures 15 and 16 show the evolution of Reynolds shear stress for cases  $K1$  and  $K2$ , respectively. As the  $K$  value is increased, the ratio of the turbulent shear to the wall shear is reduced at each corresponding  $\Gamma$  value. For example, the values of  $\bar{uv}/u_r$  at station 8 ( $\Gamma = 0.37$ ) for the  $K1$  case in Fig. 15 are higher than those at station 10 ( $\Gamma = 0.37$ ) for the  $K2$  case in Fig. 16 (note: the large scatter observed for station 8 is due to the low intermittency in the early transition region). This is due to the increased pressure gradient, which acts to make the velocity profiles fuller, thus increasing the viscous shear near the wall. In the pretransitional region, negative values occur for  $30 < Y^+ < 80$ . The cause of these negative values is not clear. In the transition region of the  $K1$  case, the peak values of  $\bar{uv}$  at station 9 are approximately 50 percent

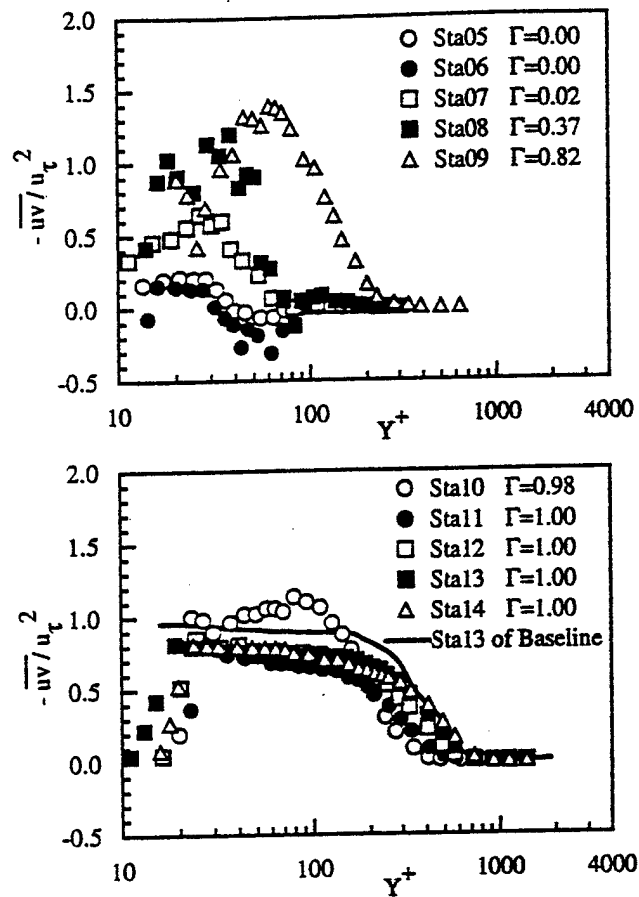


Fig. 15 Reynolds shear stress distributions for  $K1 = 0.07 \times 10^{-4}$  case in wall units

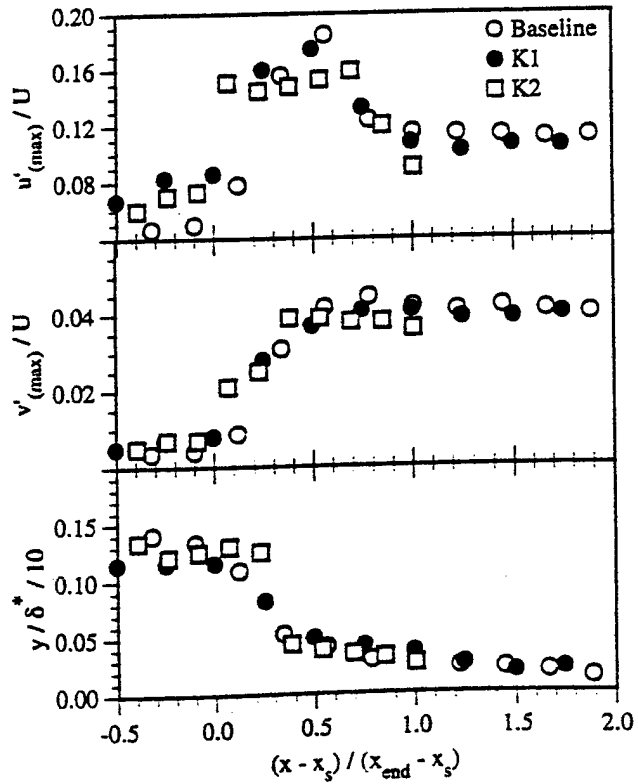


Fig. 14 Distributions of maximum fluctuating turbulent velocity and the corresponding  $y$  positions in the streamwise direction

larger than the wall shear. This indicates that the turbulent shear is generated within the boundary layer and imposes itself on the wall shear, as in the baseline case (see Wang et al., 1992). For the  $K2$  case, the turbulent shear never exceeds the wall shear. At station 12, shown in Fig. 16, the turbulent shear reaches a maximum value of approximately 90 percent of the wall shear. This value is only 30 percent greater than the fully turbulent value of station 14. This may be due to the applied pressure gradient suppressing the local turbulent shear generation at  $Y^+ \approx 100$ . This might also be explained as follows: The applied pressure gradient results in an effective communication between local high turbulent shear, generated around  $Y^+ \approx 100$ , and the wall, such that the wall shear is quickly adjusted to the produced shear away from the wall. Also, a comparison of the Reynolds shear stress shown in Figs. 15 and 16 and the  $u'$  shown in Figs. 10–13 reveals that the amplification process of the Reynolds shear stress near the onset of transition between stations 6 and 7 is faster than that of the Reynolds normal stress.

**The rms Temperature Fluctuation.** The evolution of the rms temperature fluctuations normalized by the temperature difference ( $T_w - T_s$ ) is shown in Figs. 17 and 18. In the laminar region, the  $t'$  profiles are similar to the  $u'$  profiles. A peak occurs at approximately  $Y^+ = 40$ , which is greater in magnitude than the corresponding profiles for the baseline case. In this region, a favorable pressure gradient has similar effects on  $t'$  and  $u'$ . As in the evolution of  $u'$ , shown in Figs. 10 and 11, there is little change in  $t'$  between stations 6 and 7.

As transition proceeds, the peak of  $t'$  rapidly increases in magnitude, similar to the increase observed in  $u'$ . Direct comparison of the evolution of  $t'$ , shown in Figs. 17 and 18, to the evolution of  $u'$  and  $v'$ , shown in Figs. 10–13, indicates a lag

in the evolution of the rms temperature fluctuations relative to the fluctuating velocities. For the  $K1$  case, the  $t'$  profiles continue to develop up through station 13, while  $u'$  in Fig. 10 reaches an equilibrium state by station 11. This lag of  $t'$  behind  $u'$  in reaching equilibrium is more pronounced for the  $K2$  case, as a comparison of Figs. 11 and 18 reveals. In Fig. 17, station 13 has two distinctive peaks at  $Y^+ = 40$  and 200, respectively; station 14 has a constant value on the region of  $20 < Y^+ < 100$  and a peak value at  $Y^+ = 300$ . This supports the observation drawn from the mean temperature and velocity profiles that the thermal transport lags behind the momentum transport in the transition region.

There are secondary  $t'$  peaks occurring at the outer portion of the log-linear region in the late-transitional and early-turbulent stations (stations 12–14 in Fig. 17 and stations 11–13 in Fig. 18). The magnitude of this second peak (located at approximately  $Y^+ = 200$ ) increases as  $K$  increases, and actually exceeds the near-wall peak (located at approximately  $Y^+ = 30$ ). This effect was not present in the fluctuating velocities, which indicates that an applied pressure gradient affects the thermal structures differently in this region than it does the flow structure. This may be a result of the differences between the transport mechanisms of momentum and heat.

**Reynolds Heat Fluxes ( $\bar{v}t$ ) and ( $\bar{u}t$ ).** Measurement of the cross-stream Reynolds heat flux,  $\bar{v}t$ , for the baseline case was discussed in detail by Wang et al. (1992) and Keller (1993). The results for station 5 are not shown since the flow was pretransitional and  $\bar{v}t$  and  $\bar{u}t$  are near zero. Large negative values of  $\bar{v}t$  were obtained in the inner boundary layer. The magnitude and boundary layer penetration of these negative values were the greatest in the midtransition region. As the transition process

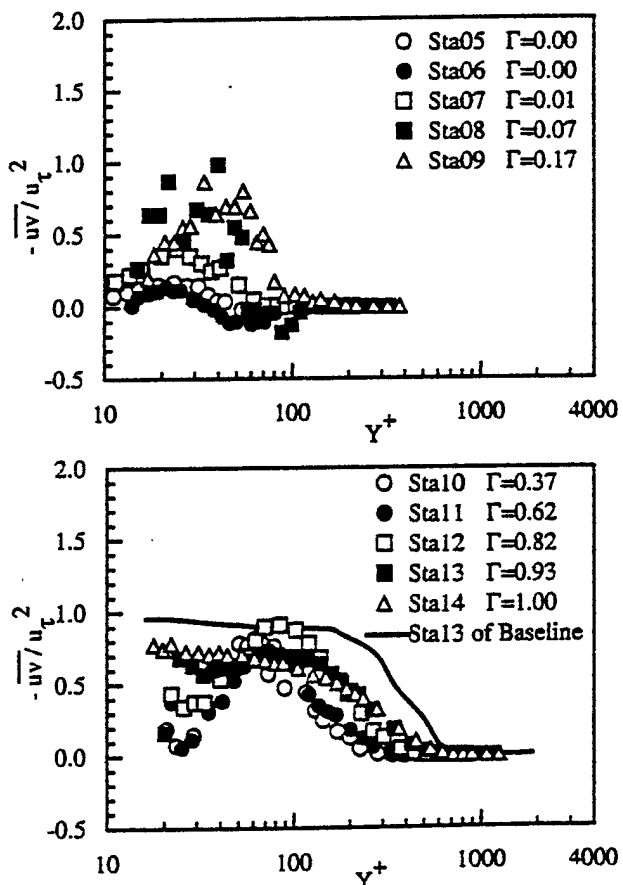


Fig. 16 Reynolds shear stress distributions for  $K2 = 0.16 \times 10^{-4}$  case in wall units

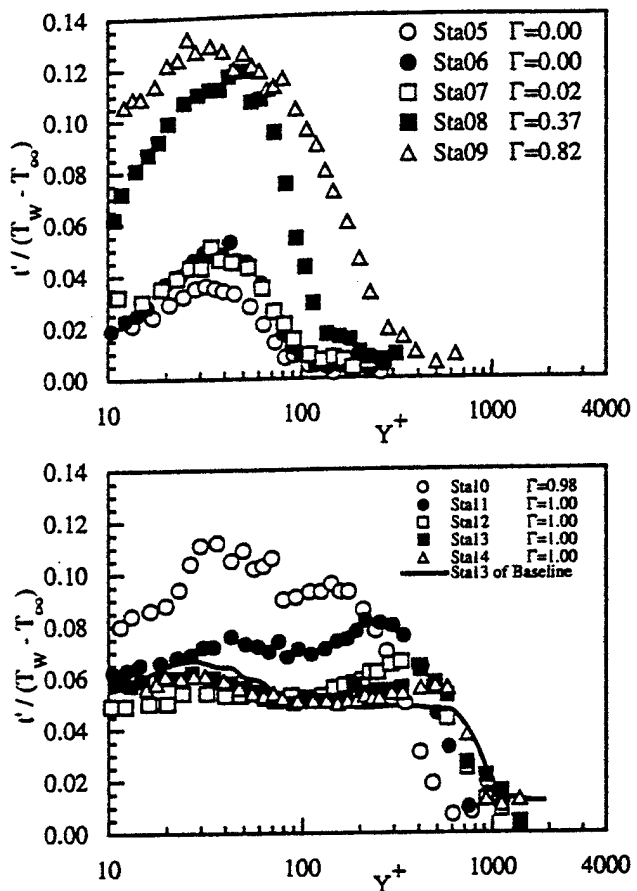


Fig. 17 The rms temperature fluctuations for  $K1 = 0.07 \times 10^{-4}$  in wall units

advanced, the near-wall region of negative  $\bar{v}t$  became narrower, finally occupying the inner 5–10 percent of the boundary layer. A negative time-averaged  $\bar{v}t$  in a thermal field of negative mean-temperature gradient results in a negative eddy thermal diffusivity, which is physically inappropriate. To explore this issue more fully and to attempt to determine whether the occurrence of a negative  $\bar{v}t$  within the boundary layer was a real physical phenomenon or an induced measurement error, several possible explanations were investigated: (1) insufficient frequency response of the cold wire (thermal lag), (2) thermal cross-talk between the hot and cold wires, (3) spatial resolution of the three-wire probe, and (4) three dimensionality of the transitional flow.

The issues of frequency response and thermal cross-talk were investigated experimentally and determined not to contribute to the negative  $\bar{v}t$  measurements (see Keller, 1993).

The issue of spatial resolution of the probe is of special concern near the wall since the eddy size decreases as the wall is approached, which may result in the two crossed wires sensing different velocities. This subject was investigated by Ligrani and Bradshaw (1987), who recommended that the spanwise distance between the sensors be  $S^* < 20 \sim 25$ , where  $S^*$  is the spacing between the wires in the wall coordinates. For the baseline case,  $S^*$  ranged from 12 to 23, which satisfied the recommended spacing. Sohn et al. (1989) also observed negative  $\bar{v}t$  in the transitional boundary layer and discussed the issue of spatial resolution. They believe that the negative  $\bar{v}t$  values may be due to sensor spacing; they have outlined a plan to investigate the effects of  $S^*$ , but no results have been published to date. To reduce the impact of spatial resolution, the flow speed was reduced to 8 m/s, so that a relatively thicker boundary

layer could be obtained. Similar large negative values of  $\bar{u}$  were again measured. A further reduction of the flow speed below 8 m/s resulted in total laminar flow in the present facility, so the effect of spatial resolution is not resolved.

The issue of three-dimensional effect is also of special concern for two reasons: (a) the uncertainty of the yaw angle can significantly contribute to the overall measurement uncertainty, and (b) the spanwise Reynolds heat flux,  $\bar{w}$ , would be important for transferring thermal energy. An uncertainty analysis showed that a  $\pm 2^\circ$  uncertainty in the flow angle relative to the wire can contribute to  $\pm 20$  percent uncertainty in  $\bar{w}$  measurement. Although 20 percent uncertainty may seem large, it does not alter the sign from a negative to a positive value. If the effect of three dimensionality is significant, the negative  $\bar{w}$  might be valid, because the downwash flow surrounding the turbulent spot brings in cooler flow from the mainstream toward the wall. This implies that further study is needed to measure  $\bar{w}$  and to verify that the measured energy transport is conserved in a control volume in the transitional boundary layer. The effect of fluid convection due to thermal gradients in the heated boundary layer was estimated by comparing the ratio of Grashof number to the Reynolds number squared. The ratio was below 0.1; therefore thermal gradients were determined to be insignificant, and were not considered to be a contributor to the effect of three dimensionality.

The evolution of normalized  $\bar{w}$  for the accelerating cases is shown in Figs. 19 and 20. The results are very similar to the results of the baseline case, with the following exception. As  $K$  increases, the negative values of normalized  $\bar{w}$  in the transition region increase in magnitude (i.e., become more negative), extend further into the boundary layer, and remain longer down-

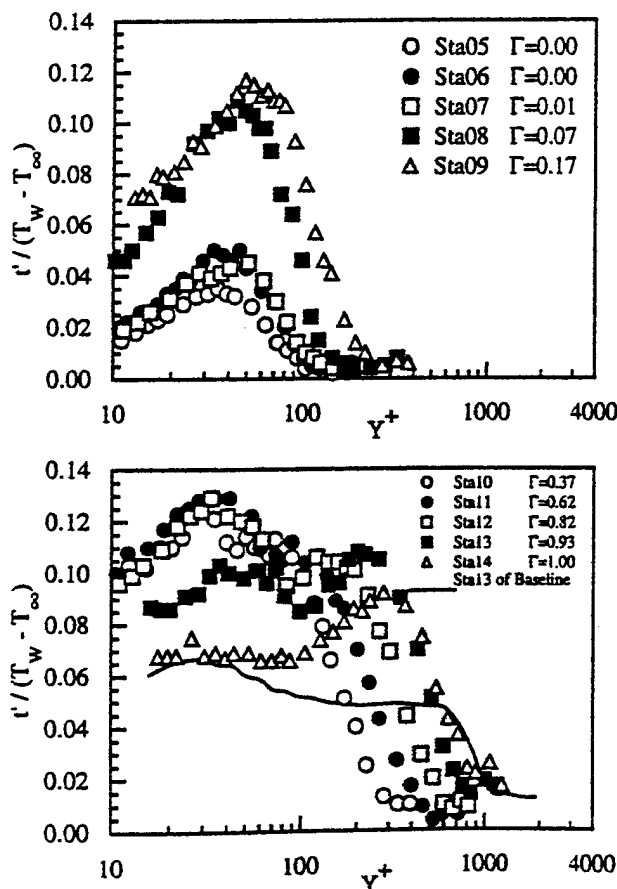


Fig. 18 The rms temperature fluctuations for  $K2 = 0.16 \times 10^{-4}$  in wall units

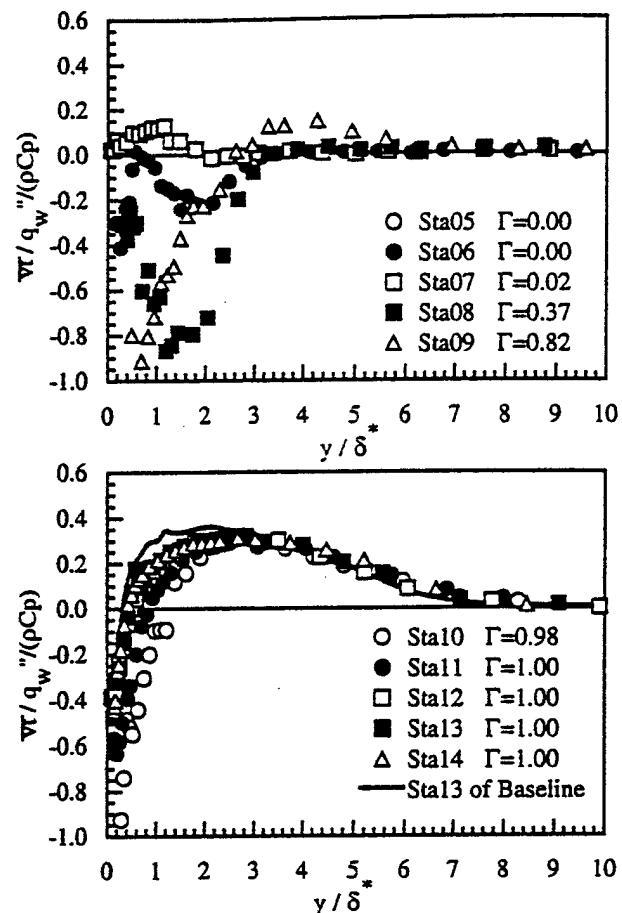


Fig. 19 Cross-stream Reynolds heat flux distributions for  $K1 = 0.07 \times 10^{-4}$  case

stream. As the velocity increases under the influence of a favorable pressure gradient, the spanwise distance between the sensors (in terms of  $S^+$ ) increases, although  $S^+$  for the accelerating cases met the criteria recommended by Ligrani and Bradshaw (1987),  $S^+ < 20 \sim 25$ . If spatial resolution of the sensor is the cause of the negative  $\bar{w}$  measurements, then the thinning of the boundary layer as  $K$  increases might explain the increase in the magnitude and the boundary layer penetration of the negative  $\bar{w}$  values. This topic is discussed in detail by Keller (1993).

The streamwise Reynolds heat flux,  $\bar{w}$ , normalized by the wall heat flux, is shown in Figs. 21 and 22. For the baseline case, the magnitude of the peak value of normalized  $\bar{w}$  in the transition region was approximately 17 times that of the wall heat flux. For the accelerating cases, this magnitude increased to approximately 20 times the wall heat flux. The location of this peak value moves away from the wall as  $K$  increases. For the baseline case, the peak intensity occurs at approximately  $Y^+ = 30$ , while for the  $K2$  case, the peak has moved to about  $Y^+ = 50$ . This may be caused by a thickening of the conduction layer relative to the boundary layer. The second peak at  $Y^+ = 200$  that was observed to occur in  $t'$  is also seen in the normalized  $\bar{w}$  profiles. The magnitude of this second peak, relative to the magnitude of the near-wall peak, also increases as  $K$  increases. This indicates that a favorable pressure gradient has a similar impact on the streamwise Reynolds heat flux as it has on  $t'$ .

The observations made from the Reynolds stresses, Reynolds heat fluxes, and rms temperature fluctuations within the boundary layer indicate that a favorable pressure gradient affects thermal structures differently than it affects flow structures in the

transitional boundary layer. Conditional sampling must be used to investigate further the intermittent flow and thermal structures in separate nonturbulent and turbulent portions to determine the causes of the differences observed and to address the impact of the large-scale eddy motion on these structures in transitional boundary layers.

**Eddy Viscosity ( $\epsilon_M$ ).** Since the issue of negative  $\bar{v}$  measurements was not resolved, eddy diffusivities and turbulent Prandtl numbers for the accelerating cases are not presented. The evolution of the eddy viscosities for the accelerating cases normalized by their viscous counterparts is shown in Figs. 23 and 24. In the early transition region,  $\epsilon_M$  is approximately zero. As transition progresses,  $\epsilon_M$  grows rapidly, reaching a peak magnitude at  $y/\delta = 0.4$  for both the  $K1$  and  $K2$  cases, similar to that observed in the baseline case. While the  $y/\delta$  location of this maximum value does not change as the flow moves downstream, the magnitude of the maximum value continues to increase. As  $K$  increases, the peak magnitude of the eddy viscosity is reduced. This supports the observation from Figs. 15 and 16 that the ratio of turbulent shear to the wall shear is suppressed as  $K$  increases.

### Uncertainty Analysis

Uncertainty analyses were conducted for the surface measurements,  $C_f$  and  $St$ , the boundary layer measurements,  $\bar{U}$ ,  $T$ ,  $u'$ ,  $\bar{u}\bar{v}$ , and  $\bar{v}$ , and the integral parameters,  $\delta^*$ ,  $\theta$ , and  $H$ . The propagation of the individual uncertainties into the final results was determined using the procedure set forth by Kline and McClintock (1953). The resultant uncertainties are listed in

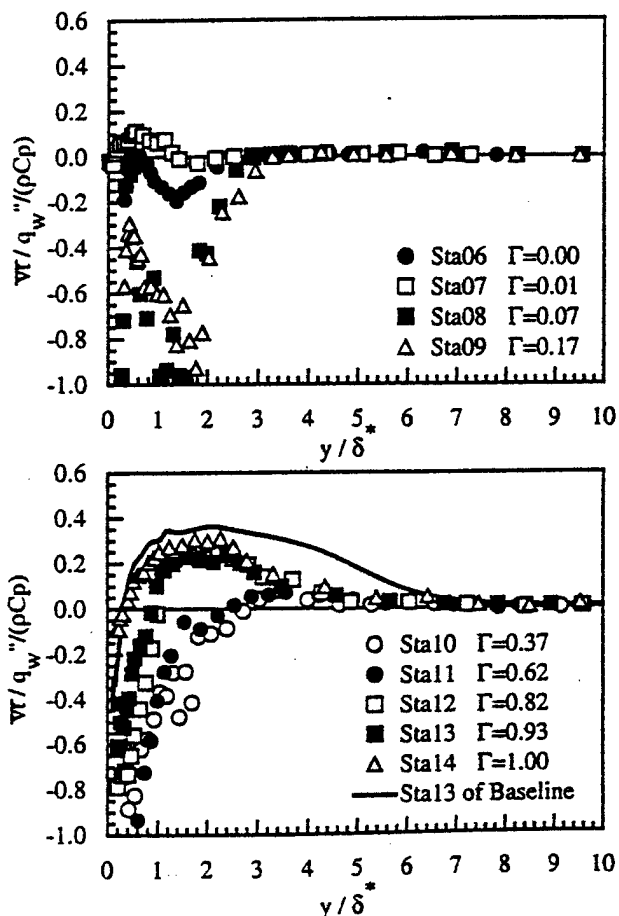


Fig. 20 Cross-stream Reynolds heat flux distributions for  $K2 = 0.16 \times 10^{-6}$  case

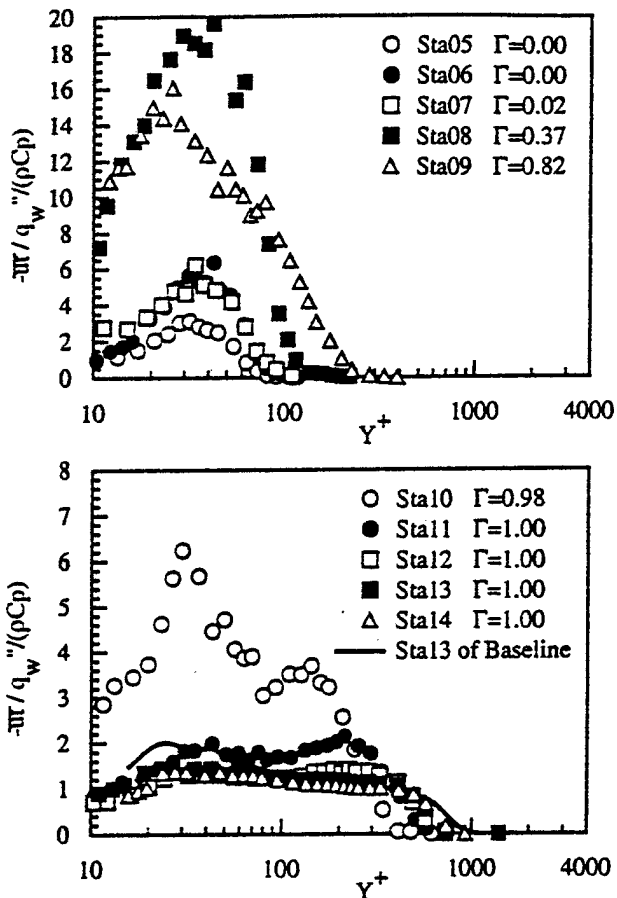


Fig. 21 Streamwise Reynolds heat flux distributions for  $K1 = 0.07 \times 10^{-6}$  in wall units

Table 2. A complete listing of the uncertainties and details of the methods used are documented by Keller (1993).

### Conclusions

The effects of streamwise acceleration on the flow and thermal structures of a two-dimensional heated boundary layer undergoing natural transition from laminar to turbulent flow were investigated in detail. A specially designed, miniature three-wire probe was used to measure the Reynolds stresses and

Table 2 Resultant uncertainties

Parameter	Uncertainty magnitude (%)
$C_f$	5
$C_f$ (transition)	13
$St$	4
$\bar{U}$	2.8
$T$	-0
$u'$	7.1
$\bar{u}\bar{v}$	11.9
$\bar{v}$	21.0
$\delta^*$	3.6
$\theta$	7.5
$H$	5.9
$y^+$	4.7
$U^+$	4.7
$T^+$	3.2

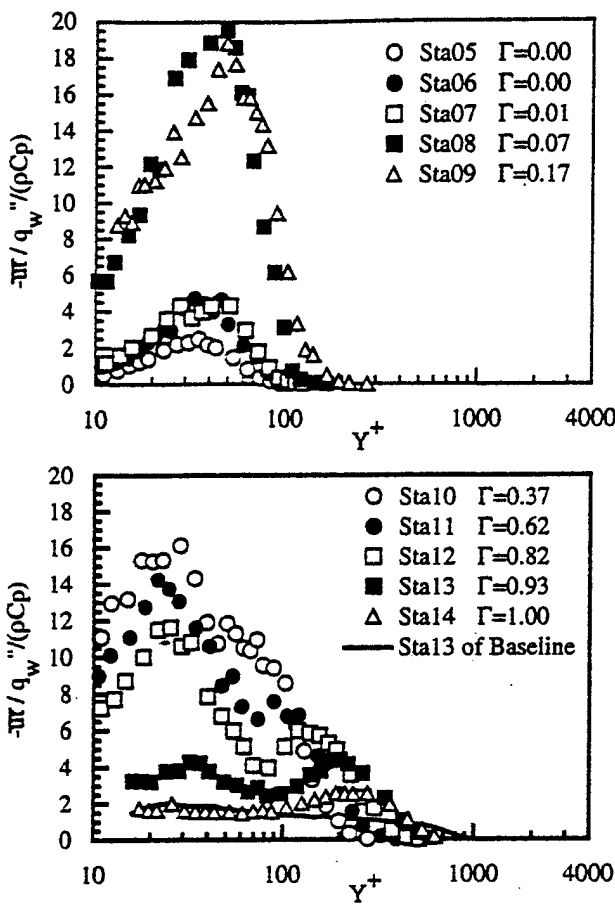


Fig. 22 Streamwise Reynolds heat flux distributions for  $K_2 = 0.16 \times 10^{-6}$  in wall units

heat fluxes within the transitional boundary layer. The primary conclusions are summarized below.

Streamwise acceleration was shown to delay the point of transition onset both in terms of physical distance,  $x$ , and Reynolds number based on  $x$ . The transition onset momentum Reynolds number,  $Re_{\theta}$ , was relatively insensitive to acceleration. In general, the physical length of transition increased with increasing  $K$ . However, the transition length in terms of  $Re_{\theta}$  was relatively constant with increasing  $K$ . This was supported by the boundary layer thickness and integral parameters, which indicated that an increasing pressure gradient suppresses boundary layer growth and development through the transition region. The streamwise fluctuating turbulent velocities were suppressed in the near-wall region ( $Y^+ < 50$ ) relative to the baseline case as  $K$  increased. This was believed to be caused by an increased viscous dampening resulted from a thickening of the viscous sublayer relative to the boundary layer thickness. The lag that was observed between the mean temperature profiles and the mean velocity profiles for the baseline case became more pronounced with increasing  $K$ . Comparison of the evolution of rms temperature fluctuations to the evolution of  $u'$  indicated a lag in the rms temperature fluctuations. This supports the observation drawn from the mean temperature and velocity profiles that the thermal transport lags behind the momentum transport in the transitional process and that the effect is more pronounced as  $K$  increases.

These results suggest that in performing numerical analyses of transitional boundary layers, the thermal transport should not be directly inferred from the momentum transport by a simple extension of Reynolds analogy.

#### Acknowledgments

This program was primarily sponsored by the Air Force Office of Scientific Research (Grant No. AFOSR-89-0324). The program monitors were Major Daniel Fant and Dr. James M. McMichael. Partial funding was provided by The Office of Naval Research (Grant No. N00014-89-J-3105). The program monitor was Dr. Gabriel Roy.

#### References

- Abu-Ghannam, B. J., and Shaw, R., 1980, "Natural Transition of Boundary Layers—The Effects of Turbulence, Pressure Gradient and Flow History," *J. Mech. Engr. Sci.*, Vol. 22, pp. 213-228.
- Arnal, D., 1984, "Description and Prediction of Transition in Two-Dimensional Incompressible Flow," AGARD-R-709, Vol. 2-1.
- Blair, M. F., 1982, "Influence of Free-Stream Turbulence on Boundary Layer Transition in Favorable Pressure Gradients," *ASME Journal of Engineering for Power*, Vol. 104, pp. 743-750.
- Blair, M. F., 1992, "Boundary Layer Transition in Accelerating Flows With Intense Free-Stream Turbulence: Part 1—Disturbances Upstream of Transition Onset; Part 2—The Zone of Intermittent Turbulence," *ASME Journal of Fluids Engineering*, Vol. 114, pp. 313-332.
- Crawford, M. E., and Kays, W. M., 1976, "STAN5—A Program for Numerical Computations of Two-Dimensional Internal and External Boundary-Layer Flows," NASA CR-2742.
- Julien, H. L., Kays, W. M., and Moffat, R. J., 1969, "The Turbulent Boundary Layer on a Porous Plate: An Experimental Study of the Effects of a Favorable Pressure Gradient," Report No. HMT-4, Thermosciences Division, Dept. of Mech. Engr., Stanford University, Stanford, CA.
- Keller, F. J., 1993, "Flow and Thermal Structures in Heated Transitional Boundary Layers With and Without Streamwise Acceleration," Ph.D. Dissertation, Dept. of Mech. Engr., Clemson University, Clemson, SC.

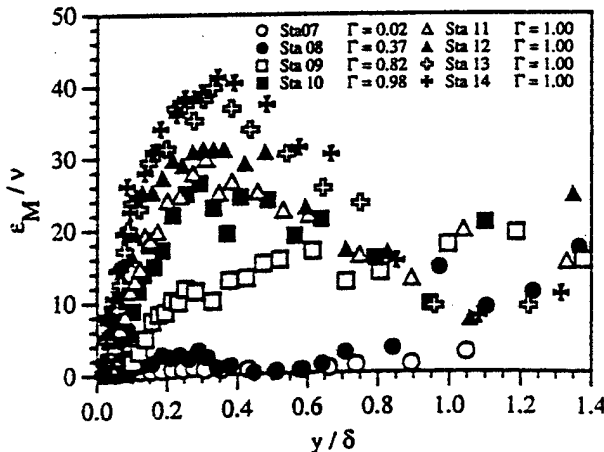


Fig. 23 Distribution of eddy viscosity for  $K_1 = 0.07 \times 10^{-6}$

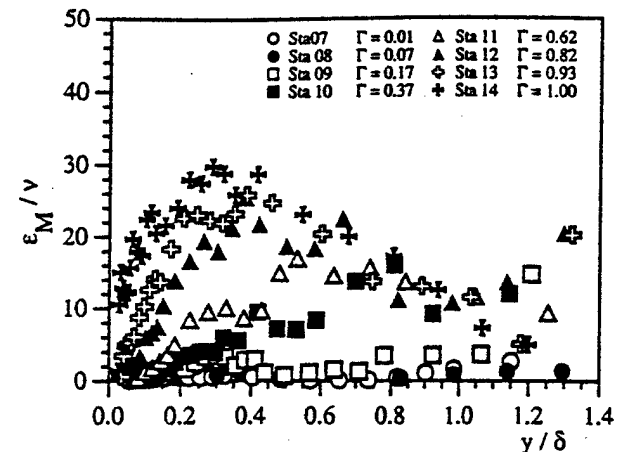


Fig. 24 Distribution of eddy viscosity for  $K_2 = 0.16 \times 10^{-6}$

Keller, F. J., and Wang, T., 1993, "Effects of Criterion Functions on Intermittency in Heated Transitional Boundary Layers With and Without Streamwise Acceleration," ASME Paper 93-GT-67; also ASME JOURNAL OF TURBOMACHINERY, Vol. 117, 1995, pp. 154-165.

Kim, J., Simon, T. W., and Kestoras, M., 1989, "Fluid Mechanics and Heat Transfer Measurements in Transitional Boundary Layers Conditionally Sampled on Intermittency," *Heat Transfer in Convective Flows*, ASME HTD-Vol. 107, pp. 69-81.

Kuan, C. L., 1987, "An Experimental Investigation of Intermittent Behavior in the Transitional Boundary Layer," M.S. Thesis, Dept. of Mech. Engr., Clemson University, Clemson, SC.

Kuan, C. L., and Wang, T., 1989, "Some Intermittent Behavior of Transitional Boundary Layers," AIAA Paper No. 89-1890.

Kuan, C. L., and Wang, T., 1990, "Investigation of Intermittent Behavior of Transitional Boundary Layers Using a Conditional Averaging," *Exp. Thermal and Fluid Sci.*, Vol. 3, pp. 157-170.

Ligrani, P. M., and Bradshaw, P., 1987, "Spatial Resolution and Measurement of Turbulence in the Viscous Sublayer Using Subminiature Hot-Wire Probes," *Experiments in Fluids*, Vol. 5, pp. 407-417.

Mayle, R. E., 1991, "The Role of Laminar-Turbulent Transition in Gas Turbine Engines," ASME JOURNAL OF TURBOMACHINERY, Vol. 113, pp. 509-537.

Musker, A. J., 1979, "Explicit Expression for the Smooth Wall Velocity Distribution in a Turbulent Boundary Layer," *AIAA Journal*, Vol. 17, No. 6, pp. 655-657.

Narasimha, R., 1985, "The Laminar-Turbulent Transition Zone in the Boundary Layer," *Prog. Aerospace Sci.*, Vol. 22, pp. 29-80.

Rued, K., and Wirtig, S., 1985, "Free-Stream Turbulence and Pressure Gradient Effects on Heat Transfer and Boundary Layer Development on Highly Cooled Surfaces," *ASME Journal of Engineering for Gas Turbines and Power*, Vol. 107, pp. 54-59.

Rued, K., and Wirtig, S., 1986, "Laminar and Transitional Boundary Layer Structures in Accelerating Flow With Heat Transfer," ASME JOURNAL OF TURBOMACHINERY, Vol. 108, pp. 116-123.

Schubauer, G. B., and Klebanoff, P. S., 1956, "Contributions on the Mechanics of Boundary-Layer Transition," NACA Technical Note #1289, supersedes NACA TN #3489.

Sharma, O. P., 1987, "Momentum and Thermal Boundary Layer Development on Turbine Airfoil Suction Surfaces," AIAA Paper No. 87-1918.

Shome, B., 1991, "Development of a Three-Wire Probe for the Measurement of Reynolds Stresses and Heat Fluxes in Transitional Boundary Layers," M.S. Thesis, Dept. of Mech. Engr., Clemson University, Clemson, SC.

Sohn, K. H., O'Brien, J. E., and Reshotko, E., 1989, "Some Characteristics of Bypass Transition in a Heated Boundary Layer," NASA TM102126.

Turner, A. B., 1971, "Local Heat Transfer Measurements on a Gas Turbine Blade," *J. of Mech. Engr. Sci.*, Vol. 13, No. 1, pp. 1-12.

Volino, R. J., and Simon, T. W., 1991, "A Review of Bypass Transition in Boundary Layers," NASA CR-187187.

Wang, T., Simon, T. W., and Buddhavarapu, J., 1985, "Heat Transfer and Fluid Mechanics Measurements in Transitional Boundary Layer Flows," ASME *Journal of Engineering for Gas Turbines and Power*, Vol. 107, pp. 1007-1015.

Wang, T., Keiler, F. J., and Zhou, D., 1992, "Experimental Investigation of Reynolds Shear Stresses and Heat Fluxes in a Transitional Boundary Layer," *Fundamental and Applied Heat Transfer Research for Gas Turbine Engines*, ASME HTD-Vol. 226, pp. 61-70.

Zhou, D., 1993, "Flow and Thermal Structures in Heated Transitional Boundary Layers With Elevated Free-Stream Turbulence and Pressure Gradients," Ph.D. Dissertation, Dept. of Mech. Engr., Clemson University, Clemson, SC.

Zhou, D., and Wang, T., 1992, "Laminar Boundary Layer Flow and Heat Transfer With Favorable Pressure Gradient at Constant  $K$  Values," ASME paper 92-GT-246.

Zhou, D., and Wang, T., 1993, "Combined Effects of Elevated Free-Stream Turbulence and Streamwise Acceleration on Flow and Thermal Structures in Transitional Boundary Layers," *Gas Turbine Heat Transfer*, ASME HTD-Vol. 242, pp. 41-52; also to appear in *Experimental Thermal and Fluid Science*, 1996.



# Combined Effects of Elevated Free-Stream Turbulence and Streamwise Acceleration on Flow and Thermal Structures in Transitional Boundary Layers

Dadong Zhou

Ting Wang

Department of Mechanical Engineering,  
Clemson University, Clemson, South Carolina

The combined effects of elevated free-stream turbulence intensity (FSTI) and streamwise acceleration on flow and thermal structures in transitional boundary layers were investigated experimentally on a heated flat plate with elevated FSTI levels ranging from 3 to 7%. The acceleration strength, based on the parameter  $K [= (\nu/\bar{U}_x^2) d\bar{U}_x/dx]$ , ranged from  $0.39 \times 10^{-6}$  to  $4.1 \times 10^{-6}$ . A three-wire probe was used to measure detailed momentum and thermal boundary layer structures, including the streamwise and cross-stream velocity fluctuations, temperature fluctuation, Reynolds stresses, Reynolds heat fluxes, eddy viscosity, turbulent thermal diffusivity, and turbulent Prandtl number. The results show that FSTI has a greater effect than streamwise acceleration on flow and thermal structures in transitional boundary layers. However, the effect of streamwise acceleration on increasing the transition length is significant. Furthermore, streamwise acceleration suppresses the magnitude of  $\bar{u}w$  and slows down the  $uw$  transition process relative to  $u'$  even when elevated FSTI seems to have a dominant effect. Acceleration is also shown to suppress  $\varepsilon_H$  more than  $\varepsilon_M$  in the transitional region.

**Keywords:** *transitional flow, free-stream turbulence, acceleration flow, favorable pressure gradient, Reynolds heat flux, turbulent Prandtl number*

## INTRODUCTION

A better understanding of momentum and thermal transport during the laminar-turbulent transition process is one of the key factors in attempts to improve predictions of the thermal load on gas turbine blades [1-3]. The transition from laminar to turbulent boundary layer flow significantly increases the local wall shear stresses and the convective heat transfer rates. These increases must be appropriately factored into the design of gas turbine blades, since as much as 50-80% of the surface of a typical turbine blade is commonly covered by flow undergoing transition [4]. The heat transfer problem of laminar-turbulent transition is especially important in the low-pressure turbines found in most aircraft engines. In the newest heavy-frame industrial H-type advanced gas turbine systems [5], the adoption of closed-loop steam

cooling eliminates the need for conventional air-film cooling in the first two stages; therefore correct prediction of the laminar-turbulent transition becomes more essential. An unsatisfactory prediction of the location and streamwise coverage of transition on gas turbine blades can result in either a reduction in the longevity and reliability of the blade or a reduction in engine performance [4] below design objectives.

In gas turbine environments, two of the most important factors affecting the transition process are elevated free-stream turbulence intensity (FSTI) and streamwise acceleration. Disturbances from the upstream combustors may cause background FSTI ranging from 2 to 10% at the inlet of the turbine. In addition, very high FSTI ranging from 10 to 20% is imposed periodically on the blades by the wakes following the trailing edges of the vanes. This elevated FSTI can expedite the onset of transition and

Address correspondence to Professor Ting Wang, Department of Mechanical Engineering, Clemson University, Box 340921, Clemson, SC 29634-0921.

Experimental Thermal and Fluid Science 1996: 12:338-351  
© Elsevier Science Inc., 1996  
655 Avenue of the Americas, New York, NY 10010

0894-1777/96/\$15.00  
SSDI 0894-1777(95)00125-5

shorten the length of transition. On the other hand, streamwise acceleration tends to be generally high on the suction side of the turbine airfoils near the leading edge, in the exit ducts of combustors, and on the pressure side of most airfoils near the trailing edge. The strong stabilizing effect of the favorable pressure gradient can retard transition and sometimes cause reverse transition (e.g., relaminarization) [3]. Understanding the combined effects of these two parameters on transition is important for designing high-performance gas turbines.

Little experimental work has been found in the literature on the effect of free-stream turbulence combined with the presence of streamwise acceleration (or favorable pressure gradients) on boundary layer transition in heated flows. In Blair's [6] experimental work, two constants  $K$  values of  $0.20 \times 10^{-6}$  and  $0.75 \times 10^{-6}$  were investigated with FSTIs ranging from approximately 0.7 to 5%. The onset and the end of transition for the various flow conditions were determined from both the wall heat transfer and the velocity profile data. For two test cases ( $K = 0.20 \times 10^{-6}$ , FSTI = 2%;  $K = 0.75 \times 10^{-6}$ , FSTI = 4%), in which turbulence intensity had a more pronounced effect than flow acceleration, the results for the onset and the end of transition from the mean velocity profile and the wall heat transfer distribution measurements agreed closely. However, for the other two cases ( $K = 0.2 \times 10^{-6}$ , FSTI = 1%;  $K = 0.75 \times 10^{-6}$ , FSTI = 2%), in which flow acceleration was more dominant than turbulence intensity, Blair claims that the lengths of the transitional flows, as determined from the wall heat transfer distributions, became at least one-third longer than those indicated by the shape factor distributions. The velocity and temperature profile data showed that the development of the transitional temperature profiles lagged behind that of the velocity profiles. These results indicated that the fully turbulent momentum boundary layer was established in a shorter distance than was required for the thermal boundary layer under the favorable pressure gradient at FSTI  $< 2\%$ . Blair's data also showed that the measured location of the onset of transition agreed closely with the theoretical prediction of van Driest and Blumer [7].

Rued and Wittig [8] investigated the effects of free-stream turbulence and streamwise pressure gradient on heat transfer and boundary layer development on highly cooled surfaces. The free-stream turbulence levels ranged from 1.6 to 11%, and two streamwise pressure gradient distributions with a maximum  $K$  value of  $6 \times 10^{-6}$  (not a constant  $K$  value) were considered. Heat transfer was systematically compared with and without acceleration. Comparing the results with those of zero pressure gradient flows at FSTI of 1.6 and 2.3%, they observed that delayed transition caused by a favorable pressure gradient reduces the Stanton numbers in the downstream part of the plate. In the leading edge region, however, the laminar heat transfer coefficients increased by approximately 20% because of the streamwise acceleration. At a high FSTI (8–11% at the leading edge), transition occurred immediately behind the leading edge. A strong acceleration ( $K = 3.2 \times 10^{-6}$ ) did not affect the onset of transition in such high FSTI cases but rather resulted in lower local Stanton numbers. When the acceleration parameter  $K$  was increased ( $K = 5.7 \times 10^{-6}$ ) by reducing the free-stream velocity, the results showed that even at the highest FSTI (11%) the transition was delayed. Furthermore,

for lower turbulence levels (up to 4%), no transition occurred during acceleration. For the strongest acceleration case ( $K = 5.7 \times 10^{-6}$ ), the Stanton numbers near the leading edge increased with raised turbulence levels of 7–11%, although the slopes of the Stanton number distributions (St. vs.  $Re_x$ ) near the leading edge were parallel to those of a laminar flow. All of the information provided for the acceleration cases was based only on the heat transfer of the test surface. No detailed measurements in the boundary layers were presented.

Mayle [3] reviewed the pressure gradient effect on boundary layer transition and discussed the effects of acceleration on both the spot production rate and the onset of transition. The momentum thickness Reynolds number at the onset of transition increases with an increase in acceleration or a decrease in the free-stream turbulence level. According to Mayle's review, the effect of acceleration is significant for low turbulence levels, whereas it is negligible for the turbulence levels found in gas turbines.

In addition to the onset and the end of transition, understanding the evolution of flow and thermal structures during laminar–turbulent transition is extremely important in improving computational modeling for predicting transitional flow and heat transfer. This paper emphasizes the study of the development of flow and thermal structures in boundary layers under the combined influences of elevated FSTI and streamwise acceleration during laminar–turbulent transition.

## EXPERIMENTAL PROGRAM

The detailed experimental facility, instrumentation, data acquisition and reduction, and experimental procedures have been demonstrated by Kuan and Wang [9] and Wang et al. [10]. Therefore, only a brief description of the experimental program is provided here.

### Wind Tunnel

The present study employs a 2-D, open-circuit, blowing type wind tunnel. The flow rate can be adjusted from 0.5 to 35 m/s. The steadiness of the free-stream velocity and temperature can be maintained within 1% and 0.5°C, respectively, for a 24-h period; the uniformity is within 0.7% and 0.1°C.

### Test Section

The rectangular test section is 0.15 m wide, 2.4 m long, and 0.92 m high with an aspect ratio of 6. This large aspect ratio reduces edge effects and ensures two-dimensionality of the boundary layer flow. One of the test section walls serves as the test wall. The heat patch inside the test wall is constructed of a serpentine heater foil sandwiched between glass cloth and silicone rubber sheets. The surface temperature is measured by 184 75- $\mu$ m (3-mil) E-type thermocouples. Fourteen measuring holes have been drilled along the outer observation wall centerline in the test section, and measurements are obtained by traversing probes through these holes into the test section. The spacing between the centerline thermocouples is

2.54 cm (1 in.), and the spacing between the measuring holes is 15.24 cm (6 in.). Boundary layer suction is applied at the leading edge of the test section.

### Flow Acceleration

In this experiment, the streamwise acceleration parameter  $K$  is kept constant in the test section simply by setting the test section into a wedge shape and then fine-tuning the test section wall to accommodate the growth of the boundary layer. It should be noted that a constant  $K$  flow is inherently different from a Falkner-Skan flow, which has a constant  $\Lambda$  [ $\equiv (\delta^2/\nu)d\bar{U}_x/dx$ ] value (see the discussion in Zhou and Wang [11]). Since no boundary layer thickness needs to be measured, a constant  $K$  flow can be more conveniently obtained in a bounded test section than can a Falkner-Skan flow.

### Turbulence-Generating Grids

The background FSTI of this wind tunnel is about 0.5%. The higher turbulence levels required for this study are generated by inserting various turbulence-generating grids into the wind tunnel. The turbulence-generating grids consist of biplanar rectangular bar arrays with approximately 69% open area (Fig. 1). Based on the recommendation of Baines and Peterson [12], the grids are designed to produce turbulence levels ranging from approximately 3 to 7% in the test section. Grid-generated turbulence decays with distance from the grid. The rate of decay be-

comes smaller as the distance from the grid increases. In order to generate homogeneous and slowly decaying turbulence, the turbulence-generating grids are inserted at the entrance of the main tunnel contraction instead of at the inlet of the test section. The grids are referred to as grids 1, 2, and 3 and have corresponding mesh widths,  $M$ , of 19.05, 24.13, and 33.02 cm, respectively. The test case with only background turbulence (no grid) serves as the baseline case.

### Instrumentation and Data Reduction

A three-wire sensor was specifically designed to simultaneously measure the instantaneous longitudinal velocity, the cross-stream velocity, and the temperature. The development and qualification of this three-wire sensor have been described by Shome [13] and are not repeated here. Only new experiences in obtaining measurements encountered in this study are described below.

Basically, the three-wire sensor consists of an X-array of gold-plated tungsten wires for measuring velocities and a 1.2- $\mu\text{m}$  platinum wire for measuring temperature. To allow near-wall measurement and to reduce probe interference, the probe support was bent at an angle of 10° from the wire axis. Due to this 10° inclined angle, the cross-wires have 35° and -55° slant angles, respectively, relative to the probe axis instead of the  $\pm 45^\circ$  angles used for traditional X-wires. However, the X-wires are still orthogonal to each other. The two X-wires are operated in the constant-temperature mode. The method of Chua and Antonia [14] is used for correcting temperature contamination of the hot wires.

The 1.2- $\mu\text{m}$  platinum wire is operated at a very low current of 0.1 mA (cold wire) in the constant-current mode. To sufficiently extend the length of transition for detailed measurements on the test wall, extremely low speed flows, down to 1.7 m/s, are provided for the elevated FSTI cases. At this low speed, relatively low overheat ratios for the X-wires are required to minimize the "cross-talk" between the X-wires and the temperature sensor. This cross-talk is primarily caused by the fluctuating radiation emanating from the hot wires to the cold wires. The X-wires generally have better velocity sensitivity at higher overheat ratios. As a compromise, an overheat ratio of about 1.2 is chosen for the X-wires, which makes the reading error of the temperature wire caused by the adjacent hot wires negligible. The overheat ratio of 1.2 was obtained by gradually reducing the overheat ratio from 1.6 to a value at which the cold wire reading did not vary, even when the hot wires were switched on and off.

At low free-stream velocities, it is found that if the flow direction deviates by a small angle from  $\pm 45^\circ$  to the X-wires, a significant change in the results for the Reynolds shear stress ( $\bar{uv}$ ) and the cross-stream Reynolds heat flux ( $\bar{vt}$ ) would occur. A typical flow angle of 1° can result in a 15% error in the  $\bar{uv}$  and  $\bar{vt}$  measurements at a free-stream velocity of 2 m/s. This small flow angle, which can be found by assuming that the mean cross-stream velocity ( $V$ ) is zero in the free stream, is added to the data reduction process. The frequency response of the platinum wire was tested to be from 4000 to 6000 Hz for a velocity range of 2–15 m/s. Therefore, frequency compensation was deemed unnecessary. The detailed fre-

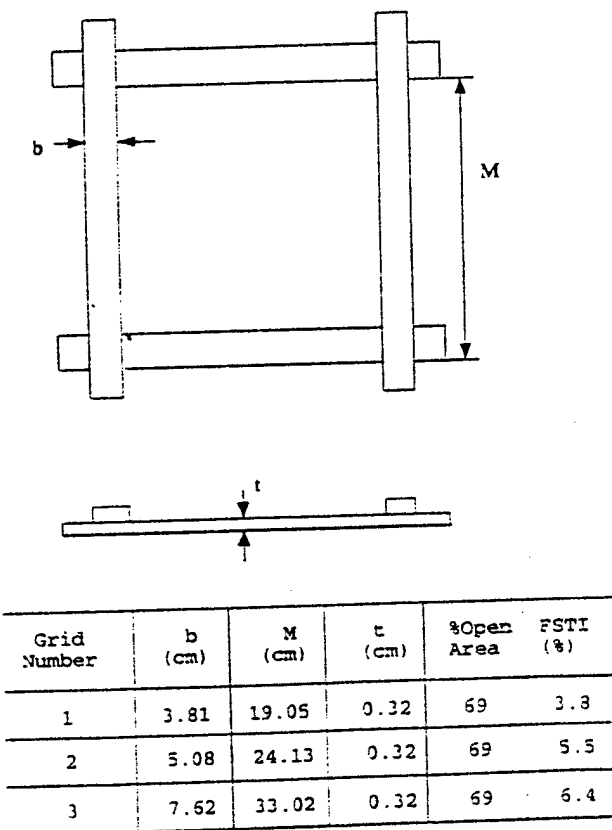


Figure 1. Grid configuration and FSTI produced.

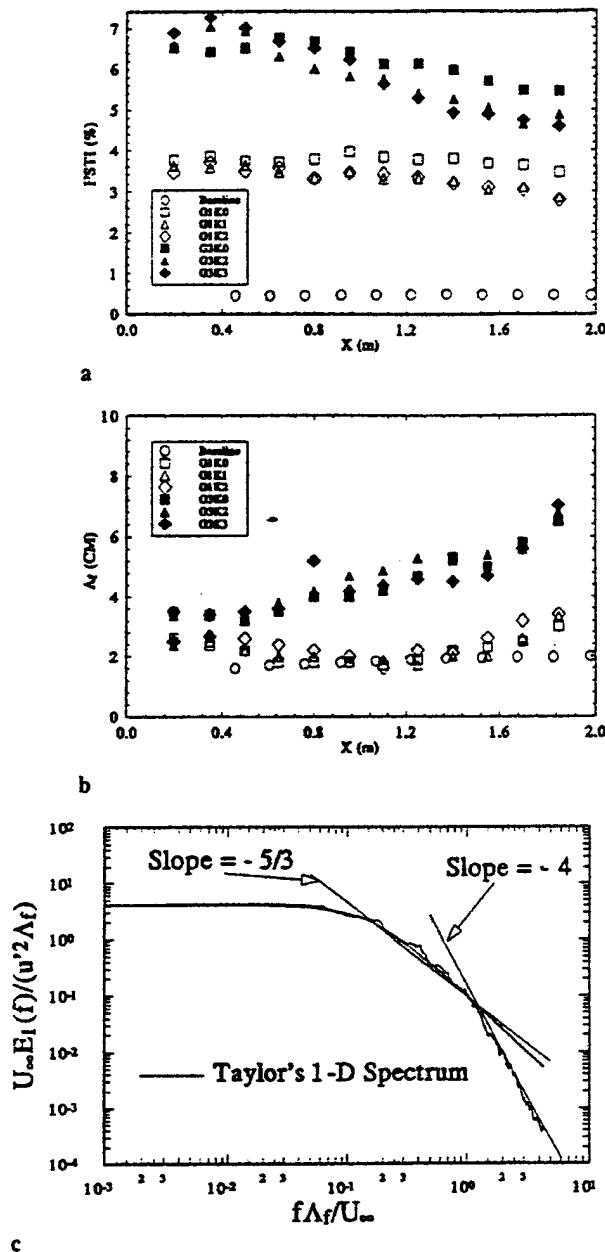


Figure 2. Free-stream turbulence. (a) Intensity distributions; (b) integral length scale distributions; (c) spectral distribution.

quency response test procedure and qualification are discussed in Keller [15].

A TSI Model IFA 100 intelligent flow analyzer system is used as a constant-temperature anemometer. A DISA M20 temperature bridge is used for operating the cold wire in the constant-current mode. An 80386 PC is used

as the data acquisition controller. A MetraByte DAS-20 A/D data acquisition board and high-speed data acquisition software, STREAMER, are used to acquire data. The sampling rate is 2 kHz, and the sampling duration is 20 s.

The wall temperature measurements are performed through a FLUKE Model 8842A digital multimeter with a built-in A/D converter and a FLUKE 2205A 100-channel switch controller.

The wall Stanton number is calculated from the power supplied to the heated test wall and the wall temperature measurement. The heat flux is corrected for the radiation loss, back loss, and streamwise conduction loss. The wall temperature is corrected for the temperature gradient in the front polycarbonate wall, compressibility, and recovery effect. The detailed data reduction process and uncertainty analysis are documented in Zhou [16]. The uncertainty of the Stanton number is 3% in the laminar and turbulent regions and 5% in the transitional region. The uncertainties of  $\bar{U}$ ,  $\bar{T}$ ,  $u'$ ,  $v'$ ,  $t'$ ,  $\bar{uv}$ ,  $\bar{ut}$ , and  $\bar{vt}$  near the wall in the transitional region are shown in Table 1.

## RESULTS AND DISCUSSION

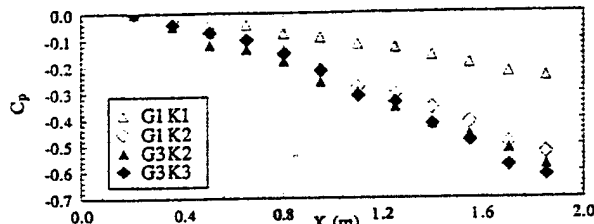
Wall heat transfer measurements for 16 accelerating cases were made first. The strongest acceleration was at  $K = 1.4 \times 10^{-6}$ . Then four accelerating cases were chosen for detailed measurements of flow and thermal structures in the boundary layers. For convenience, these four cases are referred to as G1K1 (grid 1,  $K = 0.39 \times 10^{-6}$ ), G1K2 (grid 1,  $K = 0.83 \times 10^{-6}$ ), G3K2 (grid 3,  $K = 0.83 \times 10^{-6}$ ), and G3K3 (grid 3,  $K = 1.0 \times 10^{-6}$ ). The zero pressure gradient cases are referred to as G1K0 and G3K0, respectively. The results of the baseline case were reported in a previous paper by Wang et al. [10]. The results of the elevated FSTI cases without streamwise acceleration were reported by Zhou and Wang [17], and the results of the effect of acceleration at low FSTI were reported by Keller [15] and Keller and Wang [18].

The FSTI distributions along the streamwise direction in the test section are based on the three components of the velocity fluctuation and are shown in Fig. 2a. As shown in this figure, the FSTI remains almost constant through the test section for the baseline case and the grid 1 case. For the grid 3 case, the FSTI decays in the test section. The FSTI decays faster in the presence of streamwise acceleration than it does in the zero pressure gradient case. The integral length scales, based on the streamwise velocity fluctuation, are shown in Fig. 2b. It is expected that the integral length scales downstream of the grids will be controlled by the grid sizes. Generally,  $v'/u'$  is close to unity and  $w'/u'$  is less than unity.

The spectral distributions of  $u'$  in the free stream for all three elevated FSTI cases with and without streamwise acceleration are similar. One representative case is shown in Fig. 2c. The 1-D spectrum,  $E_1(f)$ , is normalized by  $u'^2$ , the integral length scale  $\Lambda_f$ , and the free-stream velocity

Table 1. Uncertainties of  $\bar{U}$ ,  $\bar{T}$ ,  $u'$ ,  $v'$ ,  $t'$ ,  $\bar{uv}$ ,  $\bar{ut}$ , and  $\bar{vt}$  in the Transitional Region

Parameter	$\bar{U}$	$(\bar{T} - T_\infty) / (\bar{T}_w - \bar{T}_\infty)$	$u'$	$v'$	$t' / (\bar{T}_w - \bar{T}_\infty)$	$\bar{uv}$	$\bar{ut}$	$\bar{vt}$
Uncertainty (%)	3.5	1.7	3.6	8.4	1.8	15.0	3.7	20.4

Figure 3.  $C_p$  distributions in the test section.

$\bar{U}_\infty$ . The frequency  $f$  is normalized by  $\Lambda_f$  and  $\bar{U}_\infty$ . Also shown in this figure is Taylor's 1-D energy spectrum [19]. The spectral distribution  $E_1(f)$  follows Taylor's 1-D energy spectrum in the low-frequency range and deviates from it in the high-frequency range. In the high-frequency range, the spectrum  $E_1(f)$  has a distinctive slope of  $-4$ . This is consistent with the typical spectrum of grid-generated equilibrium turbulence [20]. The  $C_p$  distributions in the test section are shown in Fig. 3 for the four acceleration cases. The reference pressure was taken at station 1.

#### Heat Transfer

Three sets of Stanton number data are taken for each case in each 22-h run. Between these wall temperature measurements, boundary layer measurements are conducted.

The centerline Stanton number distributions for the grid 1 and grid 3 cases are shown in Figs. 4 and 5, respectively. The unheated starting-length effect is included in the laminar correlation. It should be noted that the laminar correlation with unheated starting length, when it is plotted in  $St$  vs.  $Re_x$ , appears differently for various free-stream velocities. In the laminar portion, the effects of acceleration on the Stanton number distributions for the grid 1 cases are negligible (Fig. 4); however, for the grid 3 cases (Fig. 5), the Stanton numbers for the zero pressure gradient case (G3K0) are about 5% higher than for the accelerated cases (G3K2 and G3K3). This indicates that a mild acceleration can effectively counteract the enhanced heat transfer due to elevated FSTI. A further increase in acceleration does not result in any additional effect on Stanton numbers in the laminar re-

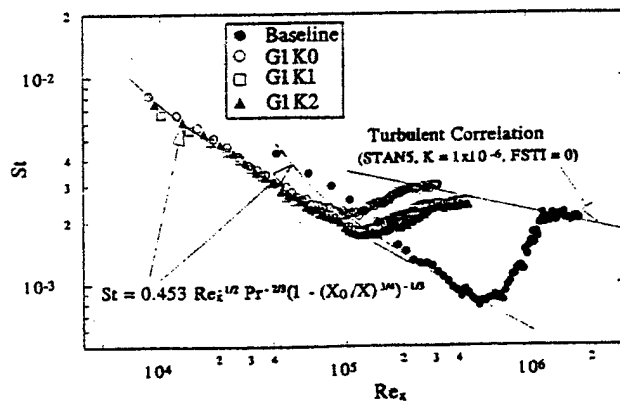


Figure 4. Stanton number distributions for grid 1 (FSTI = 3.8%).

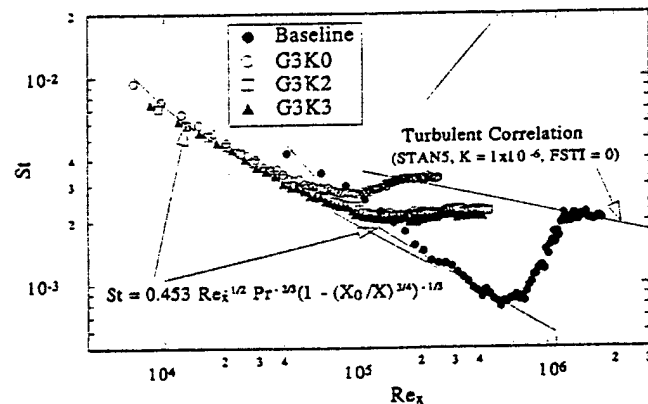


Figure 5. Stanton number distributions for grid 3 (FSTI = 6.4%).

gion. However, for the streamwise acceleration cases, the Stanton number distributions do not reach the turbulent correlation. The turbulent correlation, including the effects of both FSTI and the pressure gradients, is not available to the authors. The STAN5 code was then used to generate a turbulent curve for the effect of acceleration at zero FSTI. The mixing length model was used with an empirical correction for the pressure gradient effect. Since the effect of acceleration on  $St$  is not significant, correlation with only one  $K$  value is shown.

In Figs. 4 and 5, the onset of transition is defined as the location where the Stanton number starts to deviate from the laminar correlation, and the end of transition is defined as the location where the Stanton number merges with the turbulent correlation. As expected, higher FSTI leads to an earlier onset and an earlier end of transition, and the streamwise accelerations delay the onset of transition. It appears that elevated FSTI has a more pronounced effect on the onset of transition than the favorable pressure gradient does, while the end of transition is greatly affected by the pressure gradient. It is known that transition onset promoted by FSTI is often accompanied by a shortened transition length [3, 17, 21]; however, it is clear that the length of transition for each of the accelerating cases in Figs. 4 and 5 is increased by the effect of favorable pressure gradients. It is especially unexpected to see that the effect of the pressure gradient on the transition length is more pronounced at higher FSTI cases, as shown by comparing the almost horizontal slopes of the Stanton number distributions for the G3K2 and G3K3 cases in Fig. 5 with the steeper slopes for the grid 1 cases in Fig. 4. It can be seen in Fig. 5 that neither the G3K2 nor the G3K3 cases complete the transition process in the present facility.

Without acceleration, a typical relation between the onset and the end of transition Reynolds number is  $Re_{x,e} = 1.8 - 2.2 Re_{x,s}$ . In an attempt to reach the end of transition for the G3K2 and G3K3 cases,  $\bar{U}_\infty$  was increased; this increase caused the  $K$  values to decline. The related physical parameters at the onset and the end of transition are listed in Table 2. For both elevated FSTI conditions, mild accelerations (cases G1K1 and G3K2) delay the onset of transition by about 50% in  $Re_x$ , whereas a further increase of acceleration (cases G1K2 and G3K3) does not affect the onset of transition much, even, as

Table 2. Reynolds Numbers at Onset and End of Transition

	Baseline	G1K0	G2K0	G3K0	G1K1	G1K2	G3K2	G3K3
FSTI at $X_s$	0.5%	3.8%	5.5%	6.4%	3.8%	3.8%	6.4%	6.4%
$K \times 10^6$	0	0	0	0	0.39	0.83	0.83	1.00
Onset of transition								
$X$ (cm)	68	45	45	42	62	77	47	62
$Re_x$	$5.5 \times 10^5$	$6.0 \times 10^4$	$5.0 \times 10^4$	$4.5 \times 10^4$	$0.9 \times 10^5$	$1.2 \times 10^5$	$0.7 \times 10^5$	$0.8 \times 10^5$
$Re_{\theta}$	1294	386	355	314	489	505	414	425
$Re_g$	492	161	148	131	196	210	169	175
End of transition								
$X$ (cm)	137	150	144	139				
$Re_x$	$11.2 \times 10^5$	$2.0 \times 10^5$	$1.6 \times 10^5$	$1.5 \times 10^5$				
$Re_{\theta}$	1826	735	659	608				
$Re_g$	1302	480	404	375				
Length of transition								
$X$ (cm)	69	105	99	97				
$Re_x$	$5.7 \times 10^5$	$1.4 \times 10^5$	$1.1 \times 10^5$	$1.0 \times 10^5$				
$Re_{\theta}$	532	349	304	294				
$Re_g$	810	319	256	244				

*Not available*  
(Transition is not completed  
at the end of the test section)

shown in Fig. 6, with stronger  $K$  values up to as high as  $4.1 \times 10^{-6}$ .

### Skin Friction

The skin friction coefficients in the laminar and transitional regions are determined by extrapolating the linear viscous layer velocity correlation to the wall. The Clauser technique is employed for determining the skin friction coefficients in the turbulent region by best fitting the data points to the logarithmic law-of-the-wall profile. The development of the skin friction coefficients, shown in Fig. 7a, is similar to that of the Stanton numbers. Based on the analysis from Zhou and Wang [11], stronger accelerations (or larger  $K$  values) results in higher  $C_f$  values in the laminar boundary layer, as can be seen in Fig. 7a. For different streamwise accelerations, the laminar solutions

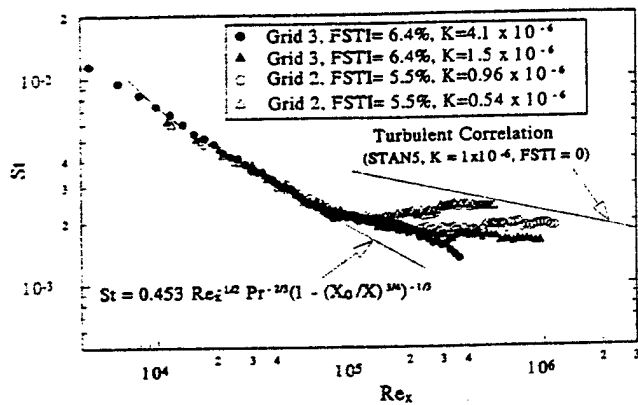
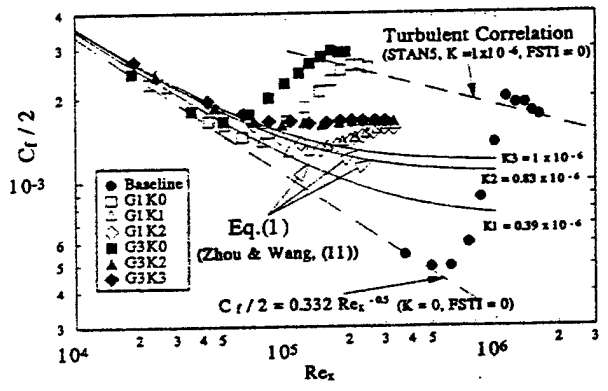


Figure 6. Stanton number distributions for grids 2 and 3.



a

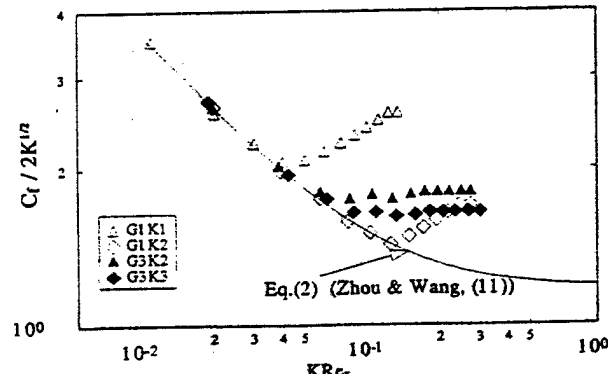


Figure 7. (a) Skin friction coefficient distributions. (b) Skin friction coefficient distributions for accelerated cases using the scaling parameters suggested by Zhou and Wang [11].

of  $C_f/2$  vs.  $Re_x$  have different curves:

$$C_f = 4\sqrt{\frac{K}{\Lambda}} + \frac{1}{3}\sqrt{K\Lambda} = \frac{4}{Re_s} \left(1 + \frac{\Lambda}{12}\right), \quad (1)$$

where [11]

$$\Lambda = \frac{1260}{158} \left[1 - (1 + K Re_x)^{-158/37}\right].$$

The effect of acceleration on heat transfer in the laminar boundary layer is very mild, so only the correlation curves for  $K = 0$  are plotted in Figs. 6 and 7 in order to keep both figures clear. The  $C_f$  distributions for various  $K$  values can be collapsed into one curve in the laminar region, as shown in Fig. 7b, by using the nondimensional parameters suggested by Zhou and Wang [11]:

$$\frac{C_f}{\sqrt{K}} = 4\sqrt{\frac{1}{\Lambda}} + \frac{1}{3}\sqrt{\Lambda}. \quad (2)$$

The effect of acceleration on the onset of transition, which can be seen more clearly in Fig. 7b than in Fig. 7a, shows that the effect of acceleration on the onset of transition is more pronounced for lower FSTI cases (grid 1) than it is for higher FSTI cases (grid 3). It is more convenient to use  $K Re_x$  values for accelerating flows than  $Re_x$ .

### Onset and End of Transition

In the present study, the onset and the end of transition are primarily determined from the Stanton number. Furthermore, they are cross-checked with the skin friction distributions, the evolution of the mean velocity and temperature profiles, and the intermittency distribution. For accelerating cases, the end of transition is obtained by extrapolating the Stanton number distribution to the turbulent correlation. The corresponding values of  $x$ ,  $Re_x$ ,  $Re_g$ , and  $Re_g^*$  at the onset and at the end of transition for each case are listed in Table 2. The results indicate that elevated FSTI results in an early onset of transition and a reduced extent of transition length based on  $Re_x$  as well as  $Re_g^*$  and  $Re_g$ . Although the end of transition does not occur in the test section for the accelerating cases, it can be seen by comparing the Stanton number distributions with the turbulent correlations in Figs. 4-6 that streamwise acceleration delays the onset of transition even at elevated FSTI and significantly increases the length of the transition region.

From the onset and the end of transition Reynolds numbers, the turbulent spot formation rate can be calculated based on the equation [3]

$$\hat{n}\sigma = \frac{4.6 \bar{U} v^2}{(x_e - x_s)^2 U_s^3},$$

where  $\bar{U}$  is an average free-stream velocity for the transition region. The onset of transition, based on the momentum thickness Reynolds number, and the calculated turbulent spot formation rate  $\hat{n}\sigma$  are plotted in Fig. 8. Also shown are the empirical correlations,  $Re_g = 400(FSTI)^{-5/8}$  and  $\hat{n}\sigma = 1.5 \times 10^{-11}(FSTI)^{7/4}$ , given by Mayle [3], which were formulated on the basis of flat-wall, nonaccelerated flow data. For the elevated FSTI cases at

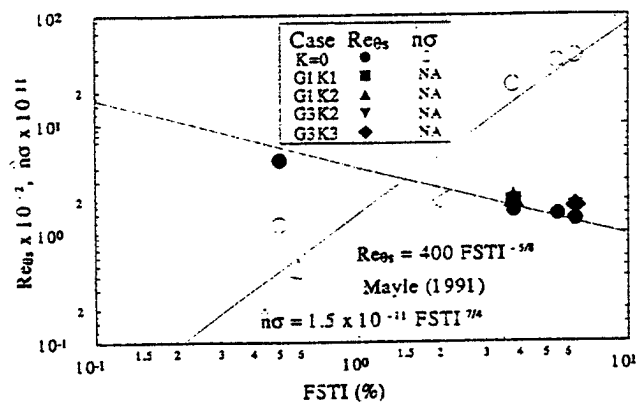


Figure 8. Transition onset and turbulent spot formation rate. NA = not available.

zero pressure gradient, the present data agree with Mayle's correlation. For the baseline case, the onset of transition is earlier, and the calculated  $\hat{n}\sigma$  is larger than that predicted by Mayle's correlation. For accelerating cases, the onset of transition momentum Reynolds numbers are slightly higher than Mayle's correlation. Since the end-of-transition locations for the accelerated cases are not known, the turbulent spot formation rates are not shown in Fig. 8.

### Mean Velocity and Temperature Profiles

With abundant information and data collected in the boundary layers in this study, only the G3K3 case is chosen as the representative to be compared with the baseline and G3K0 cases in order to investigate the combined effects of elevated FSTI and streamwise acceleration on the transitional flow and thermal structures in the boundary layer. The mean velocity and temperature profiles for the G3K0 case are plotted in wall units in Figs. 9 and 10, respectively. Since their overall evolution during the transition process is similar to that of the 2% FSTI case previously reported by Wang et al. [21], only three profiles of each are shown as representative of the mean profile characteristics in the laminar, transitional, and turbulent flow regions, respectively. The mean velocity and temperature profiles for the G3K3 case are plotted in

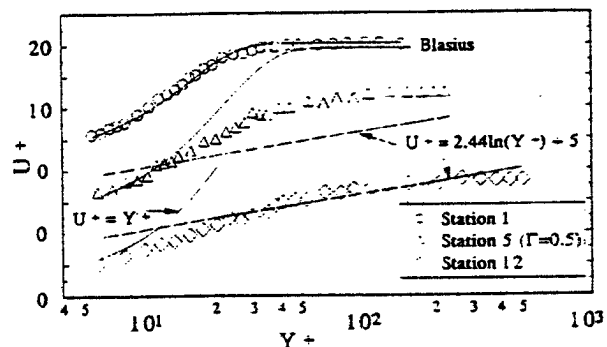


Figure 9. Mean velocity profiles for the G3K0 case.

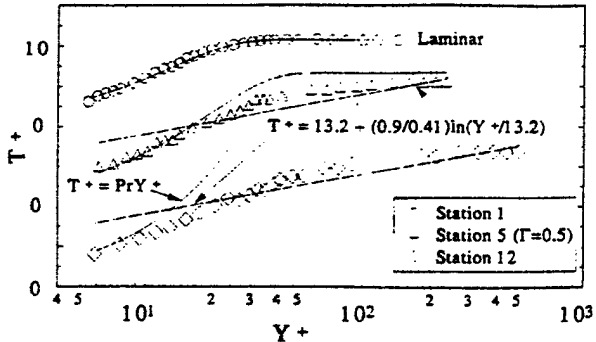


Figure 10. Mean temperature profiles for the G3K0 case.

wall units in Figs. 11 and 12, respectively. In the laminar region, even at elevated values of FSTI, the mean profiles are consistent with the laminar flow solutions. The Blasius solution is used for nonaccelerated cases, and solutions from Zhou and Wang [17] are used for accelerated cases. In the turbulent region (station 12), the mean velocity profile for the G3K0 case (Fig. 9) preserves the logarithmic law-of-the-wall characteristics over a sufficient range of  $Y^+$  (30–300), but the wake region is completely depressed beyond  $Y^+ = 300$  due to the high FSTI, which is consistent with the previous results of Blair [22] and Wang et al. [21]. However, the mean temperature at station 12 in Fig. 10 has not conformed to a typical turbulent profile. This indicates that the mean temperature lags behind the mean velocity in completing transition in high-FSTI cases. This tendency for temperatures to lag behind velocity in completing transition in low FSTI cases (< 2%) was first seen by Blair [22] and was confirmed by Wang et al. [21].

The effect of acceleration on the mean velocity profile can be seen by comparing stations 5 and 12 for the G3K3 (Fig. 11) and G3K0 (Fig. 9) cases. Station 5 happens to have  $\Gamma = 0.5$  for both G3K3 and G3K0; however, the  $U^+$  of G3K3 has a thicker, more viscous sublayer (about  $Y^+ = 18$ ) than does G3K0. In addition, the  $U^+$  profile of G3K3 is close to the laminar profile, whereas the G3K0 velocity profile is close to the turbulent profile. The same trend can be seen at station 12.

### Streamwise Velocity Fluctuations ( $u'$ )

The streamwise evolution of normalized velocity fluctuations,  $u'/\bar{U}_\infty$ , is shown in Fig. 13 for the G3K3 case. For

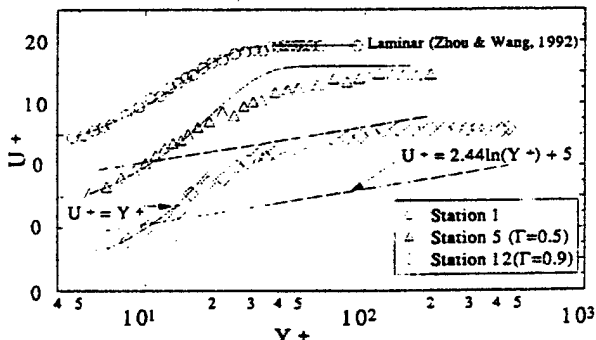


Figure 11. Mean velocity profiles for the G3K3 case.

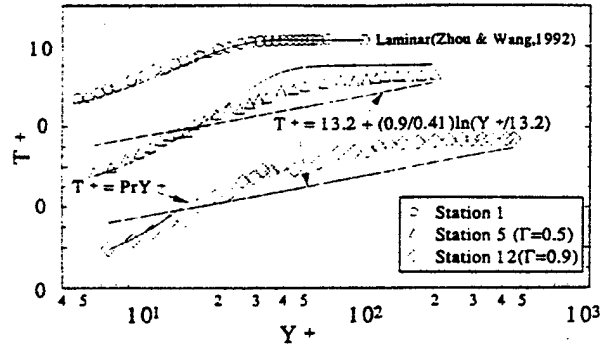


Figure 12. Mean temperature profiles for the G3K3 case.

comparison, three profiles—one near the onset of transition, one in the transition region with maximum  $u'$ , and one in the fully turbulent region—are incorporated into Fig. 13 for both the baseline and G3K0 cases. The intermittency for each station is shown in this figure. The criterion function based on Reynolds shear stress,  $[d(uv)/dt]^2$ , was used for turbulent/nonturbulent discrimination. The technique for determining the intermittency was detailed by Keller and Wang [23]. The intermittency value is 1 for a fully turbulent flow and 0 for a laminar flow. Based on the Stanton number distribution and the mean velocity and temperature profiles, stations 1, 2, and 3 for the G3K3 case are in the laminar flow region. Comparison among stations 1, 2, and 3 for the G3K3 case,

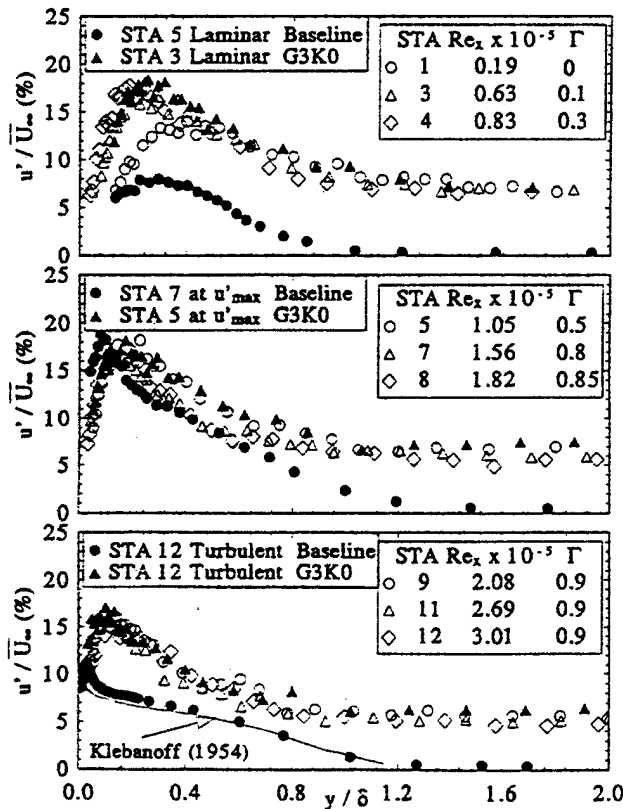


Figure 13. Streamwise Reynolds normal stress profiles for the G3K3 case.

station 3 for the G3K0 case, and station 5 for the baseline case indicates that the  $u'$  in the laminar flow is significantly raised due to the elevated FSTI; the favorable pressure gradient does not seem to affect the  $u'$  distribution. This is consistent with the results reported by Dyban et al. [24].

It is especially interesting to observe that the  $u'/\bar{U}_x$  distribution in the late laminar region (station 3 for the G3K0 case and station 4 for the G3K3 case) reaches a peak of about 18% and remains at such high levels throughout the early half of the transition region. It is also to be noted that in the transitional flow, the maximum values of  $u'/\bar{U}_x$  for the G3K0 and G3K3 cases are about the same as the maximum value at station 7 for the baseline case. It therefore appears that even at elevated FSTI up to 7%, the maximum Reynolds normal stresses due to the near-wall bursting activities are limited to around  $u'/\bar{U}_x = 20\%$ . Also, this observation may imply that the penetration of the turbulence energy from the free stream into the boundary layer results in a relatively uniform redistribution of turbulence energy across the boundary layer rather than an increase in bursting energy. Furthermore, it may be implied that *once the turbulent spot production rate is established in the beginning of transition, it does not change downstream, and the turbulent spots are the reluctant receptors of bounding turbulence energy imposed from the free stream*. It may be that the near-wall turbulence is dominated by the turbulence production and that the penetration of FSTI into the near-wall region is overshadowed by the bursting activities. This explanation can be verified by examining the overall elevated  $u'$  distributions of stations 9, 11, and 12 across the boundary layer in comparison with the baseline case in Fig. 13. This deep penetration of elevated free-stream turbulence to near the wall is consistent with the results of Wang et al. [21] but is inconsistent with the results reported by Sohn and Reshotko [25]. The discrepancy might be caused by the low free-stream velocity ( $\sim 2$  m/s) employed by the present study. The free-stream velocity in Sohn and Reshotko's study was approximately 33 m/s. In order to investigate the effect of low velocity or low Reynolds number, a single hot wire was used to measure the turbulent  $u'/\bar{U}_x$  profiles for different free-stream velocities and different Reynolds numbers. The results are shown in Fig. 14. As shown in this figure, the peak values of  $u'/\bar{U}_x$  in the boundary layer generally increase as the free-stream velocities decrease. However, for the two cases with different free-stream velocities but similar magnitudes of Reynolds numbers ( $\bar{U}_x = 3.9$  m/s,  $Re_x = 3.18 \times 10^5$  and  $\bar{U}_x = 7.8$  m/s,  $Re_x = 3.25 \times 10^5$ ), the  $u'/\bar{U}_x$  profiles overlap each other. In addition, for another two cases with the same free-stream velocity at 7.8 m/s but with different Reynolds numbers ( $Re_x = 3.25 \times 10^5$  and  $Re_x = 6.31 \times 10^5$ , respectively), the  $u'/\bar{U}_x$  profile of the lower Reynolds number has a higher value. From these observations it is clear that it is the effect of the low Reynolds number, not the free-stream velocity, that is important. However, when the Reynolds number is large ( $Re_x > 6.31 \times 10^5$ ), the effect of the Reynolds number on the near-wall peak value of the  $u'/\bar{U}_x$  is negligible, although the effect of Reynolds number on the outer boundary layer ( $y/\delta > 0.3$ ) is still obvious. This can be seen from the comparison among cases for  $\bar{U}_x = 15.6$  m/s,  $Re_x = 6.42 \times 10^5$ ,  $Re_x = 1.26 \times 10^6$ , and the baseline. The peak value of the  $u'/\bar{U}_x$

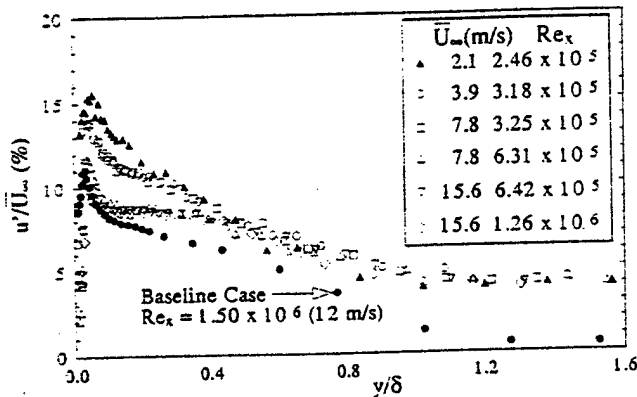


Figure 14. Effect of low Reynolds number on  $u'/\bar{U}_x$ .

with a high Reynolds number at elevated FSTI is about the same as that at low FSTI.

It should be noted that the transition is not completed at station 12 for the G3K3 case; however, the  $u'/\bar{U}_x$  distributions of stations 9, 11, and 12 do not show any change, and all of them coincide with the turbulent distribution of G3K0. A comparison between the G3K0 and G3K3 cases, as shown in Fig. 13, indicates that the streamwise acceleration for the elevated FSTI case has a negligible effect on the evolution of streamwise Reynolds normal stress; however, an extensive region with intermittency at 0.9 from stations 9 to 12 reflects the influence of acceleration.

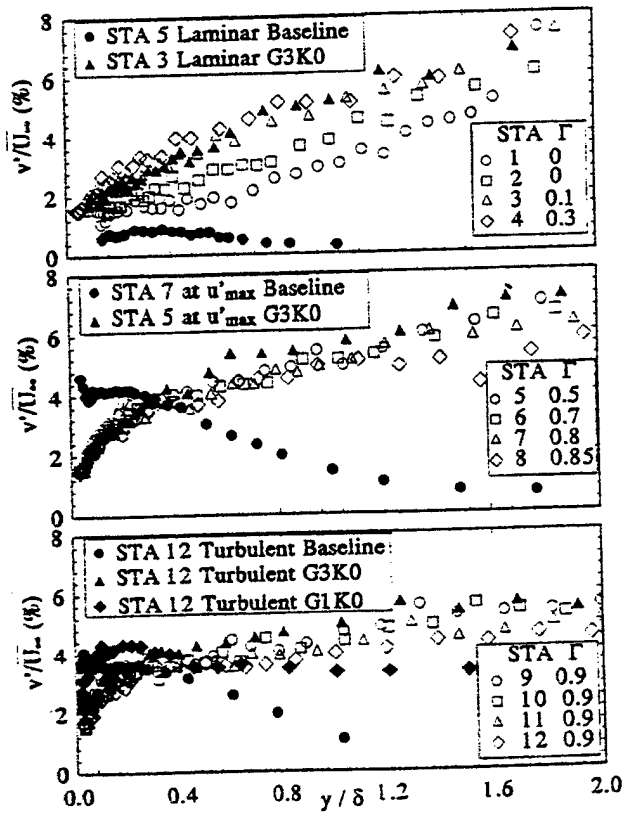


Figure 15. Cross-stream Reynolds normal stress profiles for the G3K3 case.

### Cross-Stream Velocity Fluctuations ( $v'$ )

The evolution of  $v'/\bar{U}_x$  for the G3K3 case, as shown in Fig. 15, is similar to that for the elevated FSTI cases without acceleration in Zhou and Wang [17], but it is very different from the baseline case in Wang et al. [10]. Three representative  $v'/\bar{U}_x$  distribution curves for both the baseline and G3K0 cases, at the same locations as mentioned in Fig. 13, are superimposed in the figure for comparison. The effect of the streamwise acceleration at elevated FSTI on the evolution of  $v'/\bar{U}_x$ , similar to that on  $u'/\bar{U}_x$ , is negligible, whereas the effect of elevated FSTI is significant. It is obvious that the effect of elevated FSTI on  $v'$  is more dominant in the outer boundary layer than in the inner boundary layer. Without much information to reveal the detailed mechanism involved in the transport of  $v'$ , it seems that  $v'$  in the boundary layer is affected by FSTI through an energy diffusion process rather than through convective motion or through a correlation with pressure fluctuations (return to isotropy). This speculation arises from the observation that the magnitude of  $v'$  in the free stream seems to control the  $v'$  distribution in the outer boundary layer. The data points for each curve, for all flow regions, show a smooth curve that asymptotically approaches the free-stream value of  $v'$ , while a typical near-wall peak of  $v'$ , which appears in the transition region (middle figure in Fig. 15) for the baseline case, is not observed in the elevated FSTI cases. Apparently, the elevated turbulence in the free stream does not promote energy production in the cross-stream

component of the near-wall turbulence, whereas elevated FSTI produces a large magnitude of turbulence energy in the streamwise component, as shown in Fig. 13.

The  $v'/\bar{U}_x$  distributions at stations 9–12 for the G3K3 case show a constant  $v'$  region between  $y/\delta = 0.2$  and 0.6. The  $v'/\bar{U}_x$  distribution in the turbulent flow region at station 12 for the G1K0 case, which has a lower FSTI than the G3K0 case, is superimposed in Fig. 15. In this  $v'$  distribution, a peak can be clearly seen near  $y/\delta = 0.2$ . This peak value may result in the constant  $v'/\bar{U}_x$  distribution for the G3K3 case mentioned above. The mechanism involved in producing this round peak, although not well understood, can be very different from the near-wall sharp peak prevailing in the low FSTI cases.

### RMS Temperature Fluctuation ( $t'$ )

The evolution of the rms temperature fluctuation for the G3K3 case,  $t'/(T_w - \bar{T}_x)$ , as presented in Fig. 16, is similar to  $u'$  in that it has an elevated value across most of the boundary layer except in the outer boundary layer ( $y/\delta > 0.8$ ), where the elevated FSTI does not enhance  $t'$  as would be expected in a nearly isothermal region. The effect of the streamwise acceleration at elevated FSTI on  $t'$ , similar to effects on  $u'$  and  $v'$ , is negligible. The  $t'$  distribution of stations 9, 11, and 12 are still changing and approaching the turbulent  $t'$  distribution of the G3K0 case. This indicates that  $t'$  lags behind  $u'$  in reaching the turbulent profile. This also supports the earlier discovery

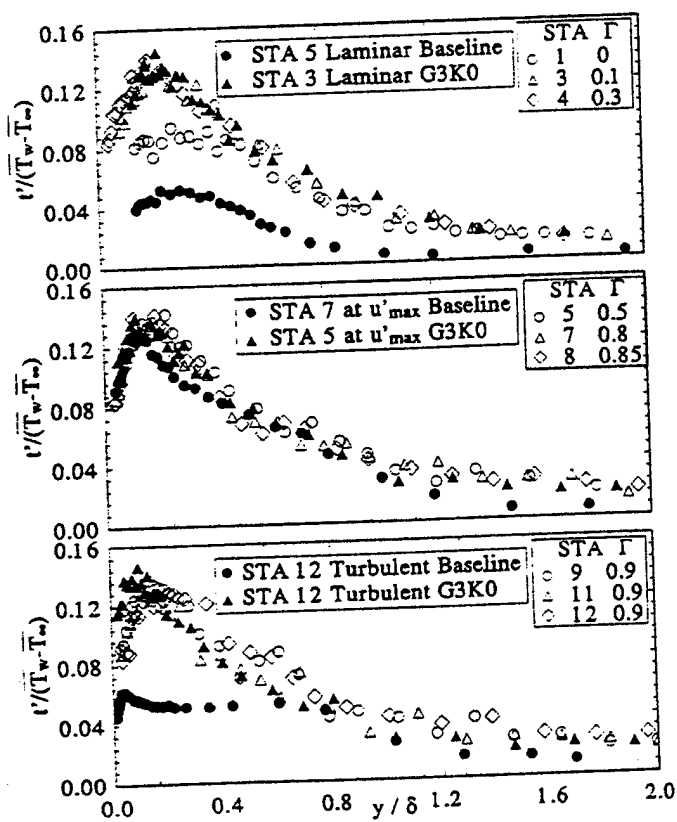


Figure 16. Streamwise evolution of  $t'$  profiles for the G3K3 case.

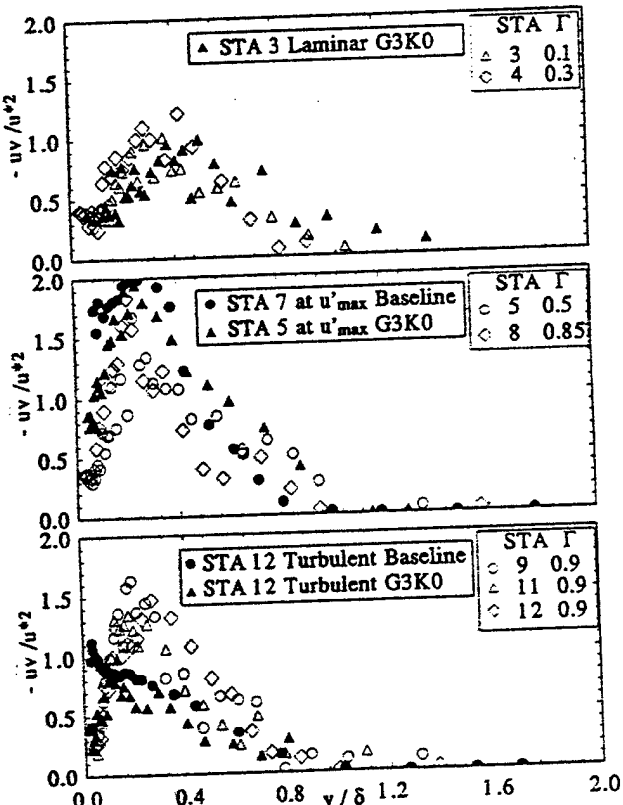


Figure 17. Reynolds shear stress distributions for the G3K3 case.

that the mean temperature lags behind the mean velocity in completing transition.

### Reynolds Shear Stress ( $\bar{u}\bar{v}$ )

For the elevated FSTI cases (G3K0 and G3K3), the normalized Reynolds shear stress produces a region of high shear around  $y/\delta = 0.4$  in the early transition region (stations 3 and 4) in Fig. 17. It reaches a maximum value of about 1.9 at station 8 and moves toward the wall to about  $y/\delta = 0.3$ . This evolution of  $\bar{u}v$  indicates that the turbulent shear stress is not generated near the wall, as is the turbulent normal stress  $u'$ , but is produced away from the wall, at about  $y/\delta = 0.3$ , and progresses toward the wall to eventually affect the wall shear. This progression is similar to that for the baseline case and is documented in more detail by Wang *et al.* [10]. The effect of the streamwise acceleration on  $\bar{u}v$  can be seen in two aspects: (1) at station 8, which has the maximum  $-\bar{u}v/u^{*2}$  value, the overall distribution is lower than it is for those without acceleration (baseline and G3K0) and (2) at the last station (12), the  $-\bar{u}v/u^{*2}$  distribution is still in a transitional status with the maximum value staying at approximately 1.5, although  $u'/\bar{U}_\infty$  in Fig. 13 reaches turbulent distribution.

### Reynolds Heat Fluxes ( $\overline{ut}$ and $\overline{vt}$ )

Normalized cross-stream Reynolds heat flux,  $\bar{v}t/(q_w^* / \rho C_p)$ , indicates the effectiveness of local turbulence in

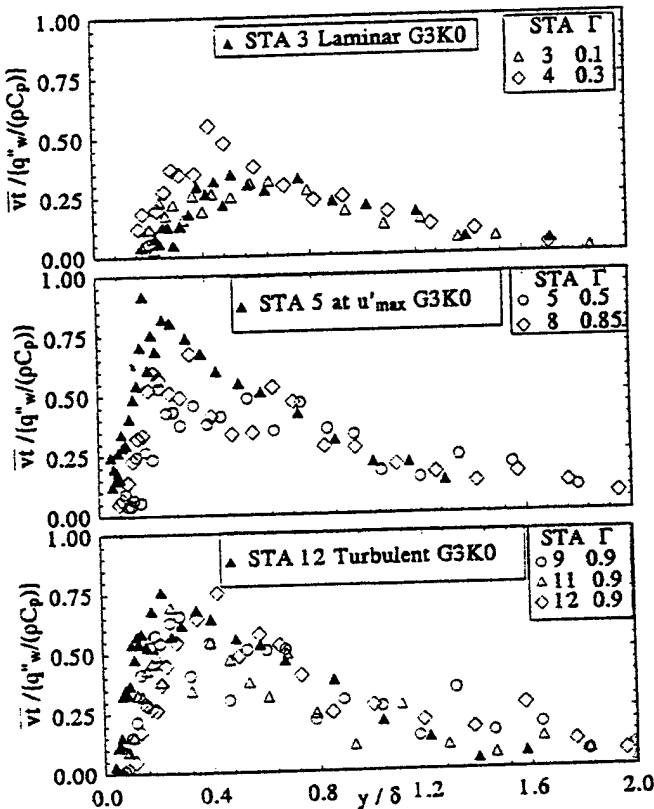


**Figure 18.** Cross-stream Reynolds heat flux distributions for the G3K3 case.

transferring heat from the surface, whereas normalized streamwise Reynolds heat flux,  $\bar{u}T / (q''_w / \rho C_p)$ , indicates the effectiveness of local turbulence in transferring accumulated thermal energy downstream. Unlike the turbulent shear stress, which can be produced away from the wall, the turbulent heat flux,  $\bar{u}T$ , can transfer only heat originated from a wall in a heated wall situation.

As shown in Fig. 18 for the G3K3 case,  $\bar{v}t/(q''_w/\rho C_s)$  reaches its maximum value of about 0.75 in the middle of the transition region. The peak value then maintains itself in the late transition region at about 0.7. The G3K0 case has a higher maximum value of  $\bar{v}t$  (about 0.9) in the middle of the transitional region than does the G3K3 case. The suppressed peak  $\bar{v}t$  value is evidence of a mild effect of acceleration on  $\bar{v}t$ . In the late transitional and early turbulent boundary layers in Fig. 18, the magnitude of  $\bar{v}t$  is elevated above the baseline case at station 12 across the entire boundary layer for the elevated FSTI cases (G3K0 and G3K3).

For both the G3K0 and G3K3 cases, as shown in Fig. 19,  $-\bar{u}t/(q_w^2/\rho C_p)$  reaches a maximum value of almost 9 in the transition region. Then the peak value for the G3K0 case in the boundary layer decreases, and the peak location moves closer to the wall at downstream stations. The peak value for the G3K0 case in the turbulent flow region is about 6. However, for the accelerating G3K3 case, similar to  $\bar{u}t$ , the peak value of  $-\bar{u}t/(q_w^2/\rho C_p)$  stays at about 8, and the peak location stays at about  $y/\delta = 0.2$ . For the baseline case at station 12, the peak

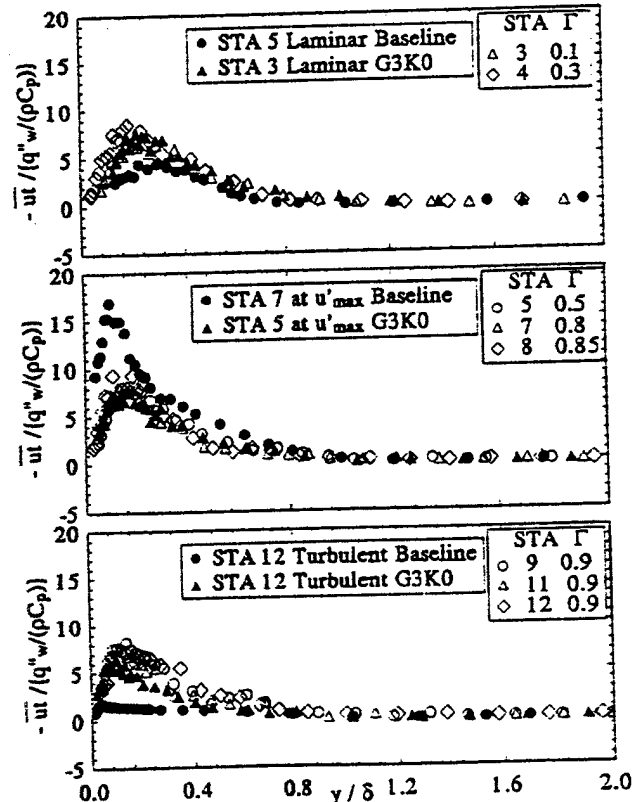


Figure 19. Streamwise Reynolds heat flux distributions for the G3K3 case.

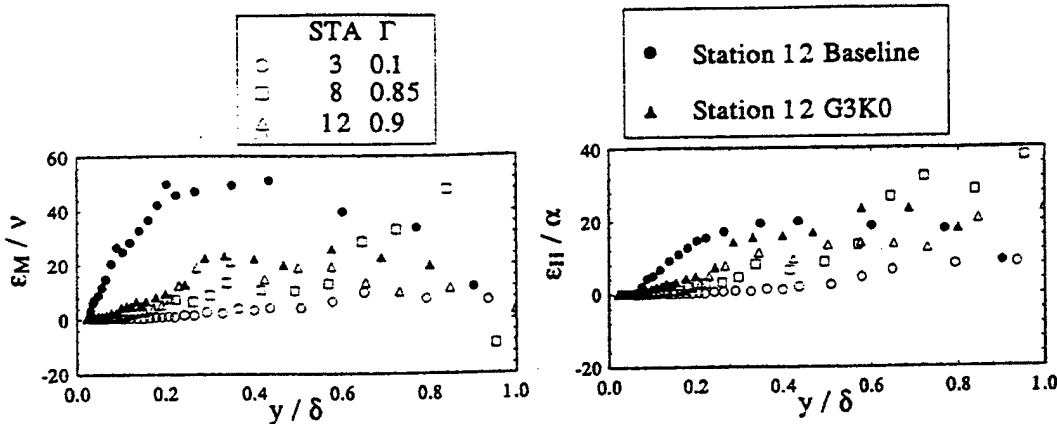


Figure 20. Streamwise evolution of the eddy viscosity and the turbulent thermal diffusivity profiles for the G3K3 case.

value is only about 2, which is much lower than the peak values for the elevated FSTI cases. It is therefore unexpected to see that the peak value of  $-\bar{u}t/(q_w''/\rho C_p)$  in the transition region for the baseline case reaches about 18, which is much higher than the transition region peak values for the elevated FSTI cases. Looking back at Figs. 13 and 16, individual  $u'$  and  $t'$  values are much higher in the laminar and turbulent regions for the elevated FSTI cases than they are for the baseline case, whereas in the transition region they are about the same as in the baseline case. It was first speculated that the lower value of  $-\bar{u}t/(q_w''/\rho C_p)$  in the transitional region for elevated FSTI cases is caused by the relatively poor correlation between  $u$  and  $t$ ; however, detailed analysis revealed that the lower value of  $-\bar{u}t/(q_w''/\rho C_p)$  is caused by the fact that the Stanton numbers in the transitional region of the elevated FSTI cases are higher than those in the baseline case. Actually, a further examination of the data indicated that the correlation between  $u$  and  $t$  in cases with a lower FSTI is about the same as that for elevated FSTI cases with and without streamwise acceleration.

#### $\epsilon_M$ , $\epsilon_H$ , and $Pr_t$

The eddy viscosity  $\epsilon_M$  and the turbulent thermal diffusivity  $\epsilon_H$ , normalized by their molecular counterparts at three stations for the G3K3 case, are shown in Fig. 20. The results for the baseline and G3K0 cases in the turbulent flow at station 12 are shown for comparison. For the G3K3 case,  $\epsilon_M/\nu$  for stations 3 and 8 has a maximum value of about  $y/\delta = 0.8$ , while for station 12 a region of relative constant value of  $\epsilon_M/\nu = 20$  stretches from  $y/\delta = 0.3$  to 0.6. For the G3K0 case, the constant  $\epsilon_M/\nu$  area is wider,  $y/\delta = 0.5$ –0.8. There is no such constant  $\epsilon_M/\nu$  region for the baseline case. The maximum of  $\epsilon_M/\nu$  for the baseline is reached at about  $y/\delta = 0.4$  at station 12. Although  $\epsilon_H/\alpha$  is different from  $\epsilon_M/\nu$  in the baseline case, their distributions are similar in the accelerated boundary layer at elevated FSTI.

For all cases,  $Pr_t$  values, as shown in Fig. 21, are large near the wall and decrease gradually away from the wall. In about 70–80% of the boundary layer, the  $Pr_t$  values are much higher than 0.9, a value commonly applied to fully turbulent flow for low FSTI cases. This figure also shows that the elevated FSTI case has a lower  $Pr_t$  distribution in

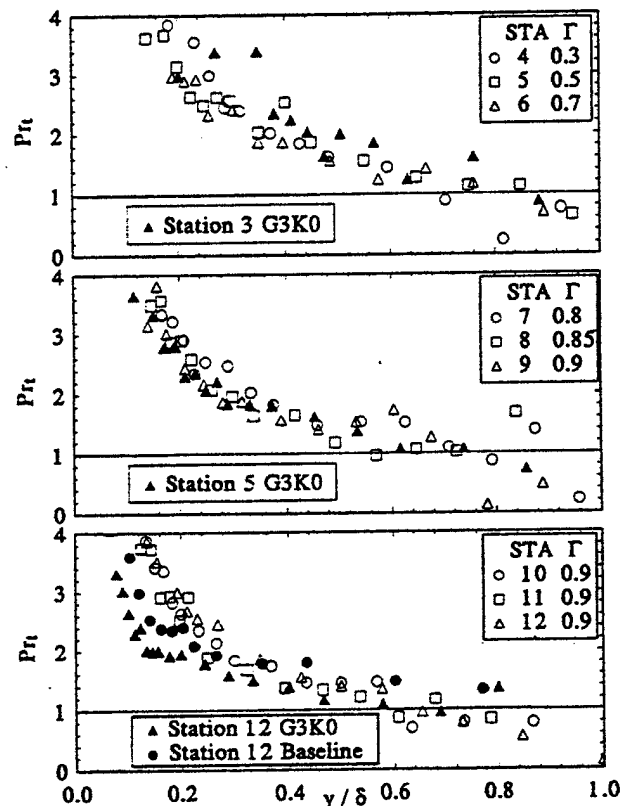


Figure 21. Turbulent Prandtl number distributions for the G3K3 case.

the turbulent region (G3K0 vs. baseline). The effect of favorable pressure gradient on  $Pr_t$  in the transition region is not significant, as indicated by the middle figure of Fig. 21. Since the transition is not complete in the accelerated cases, the effect of acceleration on  $Pr_t$  in turbulent regions is not ascertainable.

#### CONCLUSION

Experiments were performed to investigate the combined effects of elevated FSTI (3–7%) and streamwise accelera-

tion on flow and thermal structures in heated transitional boundary layers. Wall heat transfer measurements indicated that elevated FSTI values result in an earlier onset of transition and a reduced length of transition, whereas streamwise acceleration generally delays the onset of transition and lengthens the transition region, even at elevated FSTI. A mild acceleration has a significant effect on the onset and end of transition. However, at elevated FSTI, further increasing the acceleration to as high as  $K = 4.1 \times 10^{-6}$  does not affect the onset of transition.

At elevated FSTI, the streamwise acceleration has a negligible effect on  $\bar{T}$ ,  $u'$ ,  $v'$ ,  $\bar{v}$ ,  $\bar{U}$ , and  $\Pr_t$  distributions and has a mild effect on  $uv$  distributions across the boundary layers. A noticeable effect of acceleration on the flow structure can be seen in both the  $\bar{U}$  and the  $\bar{uv}$  distributions. Overall, in the range of FSTI tested by this study (3–7%), the effect of FSTI is more pronounced than is the effect of acceleration on the onset of transition. However, the effect of acceleration on the length of transition cannot be ignored, especially at a higher FSTI.

With respect to its impact on flow and thermal structure in transitional and turbulent boundary layers, FSTI is clearly more dominant than acceleration (or favorable pressure gradient). Because of the dominant role of FSTI, some of the results of this paper are similar to those reported by Zhou and Wang [17], who investigated the effect of elevated FSTI on laminar-turbulent transition without streamwise acceleration.

## FUTURE RESEARCH NEEDS

Future research is needed to transfer the physical mechanisms revealed in the present study to flow and heat transfer modeling in transitional boundary layers. Conditionally sampled results obtained by separating nonturbulent and turbulent parts of the transitional flow will be important for transitional flow calculations performed by using an intermittency model. With regard to predicting heat transfer on turbine blades, combinations of many other factors such as roughness, surface curvatures, adverse pressure gradients, separation, and unsteady wakes should be considered.

This program was sponsored by the Office of Naval Research (grant No. N00014-89-J-3105) and the Air Force Office of Scientific Research (grant No. AFOSR-89-0324). The program monitors were Dr. Gabriel D. Roy and Major Daniel B. Fant, USAF, respectively. Part of the facility was constructed through the support of the National Science Foundation (grant No. CBT-8708843).

## NOMENCLATURE

$C_f$	skin friction coefficient [ $= \tau_w / (\rho \bar{U}_x^2 / 2)$ ], dimensionless
$C_p$	pressure coefficient [ $= (P - P_{ref}) / (\rho \bar{U}_x^2 / 2)_{ref}$ ], dimensionless
$c_p$	specific heat, J/(kg K)
FSTI	free-stream turbulence intensity ( $= [(u^2 + v^2 + w^2)/3]^{1/2} / \bar{U}_x$ ), percent
$K$	streamwise acceleration parameter [ $= (\nu / \bar{U}_x^2) d\bar{U}_x / dx$ ], dimensionless
$n$	turbulent spot production rate, $m^{-1} s^{-1}$
$\hat{n}$	turbulent spot production rate ( $= n \nu^2 / \bar{U}_x^3$ ), dimensionless

$\Pr_t$	turbulent Prandtl number ( $= \varepsilon_M / \varepsilon_H$ ), dimensionless
$q''$	heat flux, $W/m^2$
Re	Reynolds number, dimensionless
St	Stanton number ( $= q''_w / [\rho c_p \bar{U}_x (\bar{T}_w - \bar{T}_x)]$ ), dimensionless
$t$	instantaneous temperature fluctuation or time k or s
$t'$	rms value of $t$ , k
$\bar{T}$	mean temperature, K
$\bar{T}^+$	mean temperature, [ $= (\bar{T}_w - \bar{T}) \rho c_p u^* / q''_w$ ], wall units, dimensionless
$u, v$	instantaneous streamwise and cross-stream velocity fluctuations, $m/s$
$u', v'$	rms values of $u$ and $v$ , $m/s$
$u^*$	friction velocity ( $= \sqrt{\tau_w / \rho}$ ), $m/s$
$\bar{U}$	mean streamwise velocity, $m/s$
$U^+$	mean streamwise velocity, wall units, dimensionless
$x$	streamwise distance from leading edge, m
$x_0$	unheated starting length, m
$y$	distance from the wall, mm
$Y^+$	( $= yu^* / \nu$ ), dimensionless

## Greek Symbols

$\alpha$	thermal diffusivity, $m^2/s$
$\delta$	boundary layer thickness, mm
$\delta^*$	displacement, mm
$\theta$	momentum thicknesses, mm
$\varepsilon_H$	turbulent thermal diffusivity [ $= - \bar{v}t / (\partial \bar{T} / \partial y)$ ], $m^2/s$
$\varepsilon_M$	turbulent viscosity [ $= - \bar{uv} / (\partial \bar{U} / \partial y)$ ], $m^2/s$
$\Gamma$	intermittency, dimensionless
$\Lambda$	( $\delta^2 / \nu$ ) $d\bar{U}_x / dx$ , dimensionless
$\Lambda_f$	integral length scale [ $= \bar{U} \int_0^\infty u(t)u(t+\tau) / u^2 d\tau$ ], m
$\nu$	kinematic viscosity, $m^2/s$
$\rho$	density, $kg/m^3$
$\sigma$	turbulent spot propagation parameter, dimensionless
$\tau$	shear stress, $N/m^2$

## Subscripts

e	end of the transition
s	start of the transition
w	wall
$\infty$	free stream
ref	reference location at $x = 20$ cm

## REFERENCES

1. Graham, R. W., Fundamental Mechanisms That Influence the Estimate of Heat Transfer to Gas Turbine Blades, 79-HT-43, ASME, New York, 1979.
2. Graham, R. W. (Ed.), *Transition in Turbines*, Symposium Proceedings, NASA CP-2386, 1984.
3. Mayle, R. E., The Role of Laminar-Turbulent Transition in Gas Turbine Engines, *J. Turbomach.* 113, 509–537, 1991.
4. Turner, A. B., Local Heat Transfer Measurements on a Gas Turbine Blade, *J. Mech. Eng. Sci.* 13(1), 1–12, 1971.
5. Farmer, R., and Fulton, K., Design 60% Net Efficiency in Frame 7.9 H Steam-Cooled CCGT, *Gas Turbine World* May-June, 12–22, 1995.
6. Blair, M. F., Influence of Free-Stream Turbulence on Boundary Layer Transition in Favorable Pressure Gradients, *J. Eng. Power* 104, 743–750, 1982.

7. van Driest, E. R., and Blumer, C. B., Boundary Layer Transition, Free-Stream Turbulence and Pressure Gradient Effects, *AIAA J.* 1(6), 1303-1306, 1963.
8. Rued, K., and Wittig, S., Free Stream Turbulence and Pressure Gradient Effects on Heat Transfer and Boundary Layer Development on Highly Cooled Surfaces, *J. Turbomach.* 107, 1007-1015, 1985.
9. Kuan, C. L., and Wang, T., Investigation of the Intermittent Behavior of a Transitional Boundary Layer Using a Conditional Averaging Technique, *Exp. Thermal Fluid Sci.* 3, 157-170, 1990.
10. Wang, T., Keller, F. J., and Zhou, D., Experimental Investigation of Reynolds Shear Stresses and Heat Fluxes in a Transitional Boundary Layer, *Fundamental and Applied Heat Transfer Research for Gas Turbine Engines*, HTD 226, ASME, New York, pp. 61-70, 1992.
11. Zhou, D., and Wang, T., Laminar Boundary Layer Flow and Heat Transfer with Favorable Pressure Gradient and Constant  $K$  Values, 92-GT-246, ASME, New York, 1992.
12. Baines, W. D., and Peterson, E. G., An Investigation of Flow Through Screens, *Trans. ASME* 73, 467-480, 1951.
13. Shome, B., Development of a Three-Wire Probe for the Measurement of Reynolds Stresses and Heat Fluxes in Transitional Boundary Layers, M.S. Thesis, Dept. Mech. Eng., Clemson Univ., Clemson, SC, 1991.
14. Chua, L. P., and Antonia, R. A., Turbulent Prandtl Number in a Circular Jet, *Int. J. Heat Mass Transfer* 33(2), 331-339, 1990.
15. Keller, F. J., Flow and Thermal Structures in Heated Transitional Boundary Layers With and Without Streamwise Acceleration, Ph.D. Dissertation, Dept. Mech. Eng., Clemson Univ., Clemson, SC, 1993.
16. Zhou, D., Effects of Elevated Free-Stream Turbulence and Streamwise Acceleration on Flow and Thermal Structures in Transitional Boundary Layers, Ph.D. Dissertation, Dept. Mech. Eng., Clemson Univ., Clemson, SC, 1993.
17. Zhou, D., and Wang, T., Effects of Elevated Free-Stream Turbulence on Flow and Thermal Structures in Transitional Boundary Layers, 93-GT-66, ASME, New York, 1993; also in *ASME J. Turbomach.*, 117(3), 407-417, 1995.
18. Keller, F. J., and Wang, T. W., Flow and Heat Transfer Behavior in Transitional Boundary Layers with Streamwise Acceleration, 94-GT-24, ASME, New York, 1994; also to appear in *ASME J. Turbomach.*, 1996.
19. Hinze, J. O., *Turbulence*, 2nd ed., p. 60, McGraw-Hill, New York, 1975.
20. Kistler, A. L., and Vrebalovich, T., Grid Turbulence at Large Reynolds Numbers, *J. Fluid Mech.*, 26, 37-44, 1966.
21. Wang, T., Simon, T. W., and Buddhavarapu, J., Heat Transfer and Fluid Mechanics Measurements in Transitional Boundary Layer Flows, *ASME J. Turbomach.* 109(3), 443-452, 1987.
22. Blair, M. F., Influence of Free-Stream Turbulence on Turbulent Boundary Layer Heat Transfer and Mean Profile Development, Part I: Experimental Data, *J. Heat Transfer* 105, 33-47, 1983.
23. Keller, F. J., and Wang, T., Effects of Criterion Functions on Intermittency in Heated Transitional Boundary Layers With and Without Streamwise Acceleration, 93-GT-67, ASME, New York, 1993; also in *ASME J. Turbomach.* 117(1), 154-165, 1995.
24. Dyban, Y. P., Epik, E. Y., and Suprun, T. T., Characteristics of the Laminar Boundary Layer in the Presence of Elevated Free-Stream Turbulence, *Fluid Mech.—Sov. Res.* 22(5), 213-228, 1980.
25. Sohn, K. H., and Reshotko, E., Experimental Study of Boundary Layer Transition with Elevated Free-Stream Turbulence on a Heated Plate, NASA CR-187068, 1991.

---

Received July 9, 1994; revised October 5, 1995



# Spectral analysis of boundary-layer transition on a heated flat plate

Ting Wang and Dadong Zhou

Department of Mechanical Engineering, Clemson University, Clemson, SC, USA

A spectral analysis was made for a boundary layer undergoing laminar-turbulent transition over a heated flat plate with free-stream turbulence intensities of 0.5% and 6.4%. Detailed boundary-layer measurements were made with a three-wire probe that simultaneously measured two velocity components and the temperature. The power spectra of  $u'$ ,  $v'$ , and  $t'$ , as well as their co-spectra, were analyzed. The spectral analogy and the differences between the momentum and thermal transports were investigated. The results showed that the location of maximum turbulence production ( $y/d \approx 0.1$ ) coincided with the peak location of  $u'$ ; whereas, the region of high turbulent shear ( $y/d \approx 0.35$ ) produced little turbulence energy. The power spectrum of  $t'$  was mostly correlated with  $u'$  in the early to middle transitional flow, but it was significantly correlated with  $v'$  in the late transitional and early turbulent flow regions. The dissipation power spectra for both  $u'$  and  $v'$  evolved faster than their turbulence power spectra.  $\bar{v}t$  seems to be transported by smaller eddies than  $\bar{u}t$ . A hypothetical energy transfer process during laminar-turbulent transition was then proposed.

**Keywords:** turbulent transition; spectral analysis; heat transfer; boundary layer

## Introduction

One of the key features in boundary-layer transition from laminar to turbulent flow is the intermittent behavior (Emmons 1951). The characteristics of nonturbulent and turbulent regions are obviously different. The intermittency theory, proposed by Emmons and Narasimha (1958), considered the nonturbulent part and the turbulent part of the transitional flow as laminar flow and fully turbulent flow, respectively. However, some recent, conditionally sampled results (e.g., Kuan and Wang, 1989, 1990; Kim et al. 1994) have indicated that the nonturbulent part is highly disturbed and is different from conventional laminar flow and that the turbulent part is still evolving and is different from fully turbulent flow. These results were based on conditionally sampled profiles of the mean velocity, the Reynolds normal stresses, and the Reynolds shear stresses. To improve understanding of the fundamental mechanisms involved in the transitional boundary layer, it is believed necessary to obtain detailed spectral information. The present study was, therefore, undertaken to perform the spectral analysis for both flow and thermal structures in transitional boundary layers.

Boundary-layer spectral measurements rarely have been reported for boundary layers undergoing transition from laminar to turbulent flow. Suder et al. (1988) measured the streamwise velocity component fluctuation spectra in a boundary layer with a

zero-pressure gradient at the point where the rms of the fluctuating velocities was a maximum. The boundary-layer spectra for the lowest free-stream turbulence intensity (0.3%) indicated amplification of the Tollmien-Schlichting (T-S) waves, which followed the behavior predicted by linear stability theory up to the point of turbulent bursting. The boundary-layer spectra for the 0.65% free-stream turbulence intensity case partially followed the behavior predicted by linear stability theory; however, the higher frequency fluctuations were not damped but rather were amplified as the streamwise distance increased until the turbulent bursting point was reached. When the free-stream turbulence intensity was elevated to 0.85%, the boundary-layer spectra showed the same trend as for the 0.65% free-stream turbulence intensity case, but they had a higher energy content at higher frequencies. As turbulent bursting was initiated, the energy of the spectra for all three cases increased at all frequencies. With the increase in the intermittency along the streamwise distance, the energy level increased over the whole frequency range, but the amplitude of the low-frequency disturbances diminished beyond a certain intermittency level. The energy level asymptotically reached a constant value as the boundary layer became fully turbulent. Similar results were reported by Sohn and Reshotko (1991).

Blair (1992) measured the streamwise velocity fluctuation spectra in the transitional boundary layer with a mild favorable pressure gradient ( $K = 0.2 \times 10^{-6}$ ) and a 0.8% free-stream turbulence level. Prior to turbulent bursting, the spectra showed that the signal was dominated by lower frequency disturbances, while the high-frequency portion of the free-stream disturbance spectrum had been largely damped out. In the transition region, the conditionally sampled spectral distributions of the turbulent part, the nonturbulent part, and the total fluctuations were presented.

---

Address reprint requests to Prof. T. Wang, Department of Mechanical Engineering, Clemson University, Box 340921, Clemson, SC 29634-0921.

Received 26 May 1995; accepted 19 September 1995

Comparison of the spectral distributions for the turbulent part showed that the ratio of high-frequency to low-frequency power increased with the streamwise distance. Blair's results indicated that the ratio of production to dissipation was relatively high for early transitional turbulent bursts. To the authors' knowledge, other than the spectra of turbulence energy transport, the turbulent thermal energy spectra for a transitional boundary layer are still lacking in the literature.

The present experiments were conducted in a two-dimensional (2-D) wind tunnel with two free-stream turbulence levels at about 0.5% and 6.4%, respectively, on a heated flat plate. The study focused on three aspects: (1) examining the spectral distribution of fluctuations near the onset of spot formation; (2) examining the evolution of the spectral distribution of fluctuations in the transition process; and (3) examining the spectral analogy between the velocity fluctuation and the temperature fluctuation in the transition process.

## Experimental program

### Wind tunnel

The present research employed a 2-D, open circuit, blowing-type wind tunnel. A detailed description of the design considerations and construction specifications was documented by Kuan (1987). Air is drawn through a filter box and then forced through two grids, a honeycomb, a heat exchanger, a screen pack, and a 9:1 contraction nozzle before entering the test section. The flow rate can be adjusted steplessly by a constant-torque, variable-frequency motor controller. A suction fan and a low-pressure plenum were installed to provide boundary-layer suction at the leading edge.

### Test section

The rectangular test section was 0.15 m wide, 2.4 m long, and 0.92 m high with an aspect ratio of 6. The large aspect ratio ensured two-dimensionality. One of the vertical walls of the test section was instrumented as the test wall. The test wall was composite, consisting of a custom-made, electric heater patch and 185 embedded thermocouples. Measurements were performed by traversing the probe through holes drilled on the wall opposite the test wall. The first measuring hole was located 20 cm downstream of the leading edge, and the rest were arranged so that they were 15 cm apart from each other. Detailed information on the heated test wall is documented in Wang et al. (1992) and Zhou (1993).

### Notation

$E_u(k)$ , $E_v(k)$ , $E_t(k)$	1-D spectra of $u$ , $v$ , and $t$
FSTI	free-stream turbulence intensity, $\sqrt{(u^2 + v^2 + w^2)/3} / \bar{U}_\infty$
$k$	wave number, $\text{m}^{-1}$
$P_{uu}(k)$ , $P_{vv}(k)$ , $P_{vt}(k)$	co-spectra among $u$ , $v$ , and $t$
$t$	instantaneous temperature fluctuation or time
$T^+$	mean temperature in wall units, $(\bar{T}_w - \bar{T}) \rho c_p u^+ / q_w^*$
$u$ , $v$	instantaneous streamwise and cross-stream velocity fluctuations
$u'$ , $v'$ , $t'$	rms values of $u$ , $v$ , and $t$
$u^*$	friction velocity $\equiv \sqrt{\tau_w / \rho}$

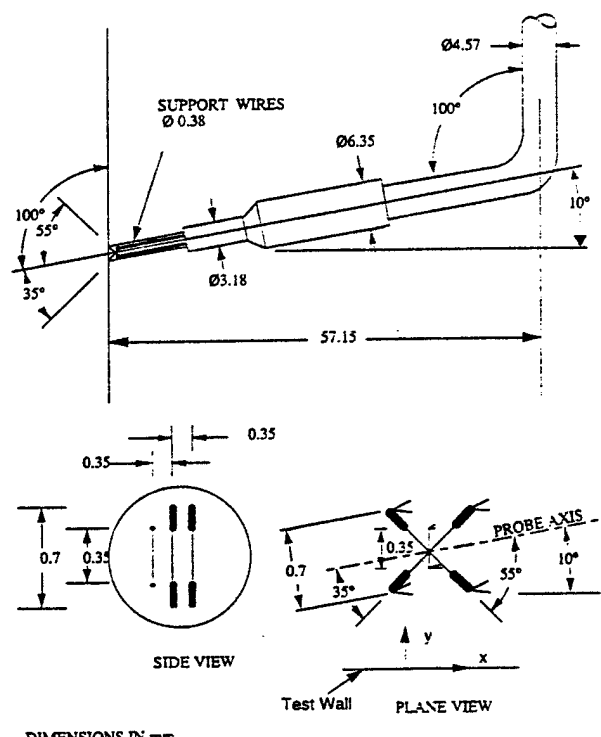


Figure 1 Three-wire boundary-layer sensor for measuring Reynolds stresses and heat fluxes

### Instrumentation and measurements

A three-wire sensor, as shown in Figure 1, was especially designed to measure the instantaneous longitudinal velocity, the cross-stream velocity and the temperature simultaneously. Basically, an "X" array of 1.0-mm long, 2.5- $\mu\text{m}$  diameter, gold-plated tungsten wires was used for velocity measurement. The sensing length was 0.5 mm, etched in the center. The spacing between the wires of the "X" array was 0.35 mm. The temperature sensor was a 1.2- $\mu\text{m}$ , unplated platinum wire located 0.35 mm away from and in a plane parallel to the plane of the "X" array. To allow near-wall measurement and to reduce probe interference, the probe support was bent at an angle of 10° from the wire axis. However, the wires of the "X" array were still

$U^+$  mean streamwise velocity in wall units.  $U/u^*$   
 $x$  streamwise distance from the leading edge  
 $y$  distance away from the wall  
 $Y^+$   $yu^+ / v$

### Greek

$\tau_w$  wall shear stress  
 $\Gamma$  intermittency  
 $\Lambda$  integral length scale,  
 $\bar{U} \int_0^\infty u(t) u(t + \tau) / (u^2 d\tau)$   
 $\rho$  density

### Subscripts

$\infty$  in the free stream  
 $w$  at the wall

perpendicular to each other. A more detailed probe description and the qualification of this probe are contained in Shome (1991).

A TSI IFA 100 Intelligent Flow Analyzer System was used to operate the "X" array hot wires in a constant temperature mode to measure velocities. A DISA M20 temperature bridge was used to operate the cold wire in the constant current mode to measure temperature. A TSI Model 157 signal conditioner was used for low-pass filtering of the cold wire anemometer signals. The streamwise velocity, the cross-stream velocity, and the temperature were measured simultaneously by the three-wire probe.

The sampling rate was 2 kHz. A low-pass filter of 1 kHz was employed to remove aliasing errors. The choice of a 2 kHz sampling rate was a compromise between the existing data acquisition storage memory size, the frequency response of the cold wire (approximately 3000 Hz), the duration of each experiment (approximately 30 hours), and the significance of the information that can be obtained at frequency ranges higher than 1000 Hz. The three-wire probe simultaneously takes signals from two hot wires and one cold wire; because the cold wire had the poorest frequency response of the three, the sampling rate was primarily limited by the frequency response of the cold wire. To investigate the significance of spectra information beyond 1000 Hz, a higher sampling rate of 30 kHz was used for velocity signals in several locations in the transitional region. It was found that the energy beyond 1000 Hz was less than 1% in the near-wall region, less than 5% in the outer boundary layer, and approximately 10% in the free stream at a free-stream velocity of 12 m/s. The evolution of the spectra at the higher frequency end does not provide any further insight into the physics beyond the data taken at 2 kHz. Therefore, it is believed that the present data are adequate to indicate the trend of spectral evolution in transitional boundary layers and that the sampling rate is an optimum choice under the existing conditions. No compensation was made for the cold wire, because the frequency response (approximately 3000 Hz) of the cold wire is higher than the sampling rate (2000 Hz). Detailed information of the method for determining the frequency response of the cold wire can be found in Keller (1993).

#### Free-stream turbulence

Two free-stream turbulence levels were performed for this study. The lower-level case, with  $FSTI = 0.5\%$  and  $\bar{U}_\infty = 12.24$  m/s, was used as the baseline case. For the higher-level case,  $FSTI = 6.4\%$  and  $\bar{U}_\infty = 1.7$  m/s. The elevated turbulence was generated by a biplane grid inserted upstream of the wind tunnel contraction. The free-stream turbulence distribution, the integral length scale in the streamwise direction, and the power spectrum are shown in Figure 2. A detailed discussion of the integral length scale and the free-stream power spectra is contained in Zhou and Wang (1995). The method of Chua and Antonia (1990) was used for correcting temperature contamination of the hot wires.

The power spectrum of a fluctuation signal was taken as the square of the magnitude of the Fourier transform of the signal. The co-spectra of two fluctuations were taken as the real part of the multiplication of the Fourier transform of one signal and the conjugate of the Fourier transform of another signal. The fast Fourier transform (FFT) technique was used in the process. Each signal contained 1024 points, and each power spectrum was an average of 40 signals.

#### Results and discussion

In this experiment, a boundary layer was allowed to undergo transition naturally from laminar to fully turbulent flow. The results of the baseline mean velocity profiles and the mean temperature profiles, plotted in wall units, are shown in Figures 3

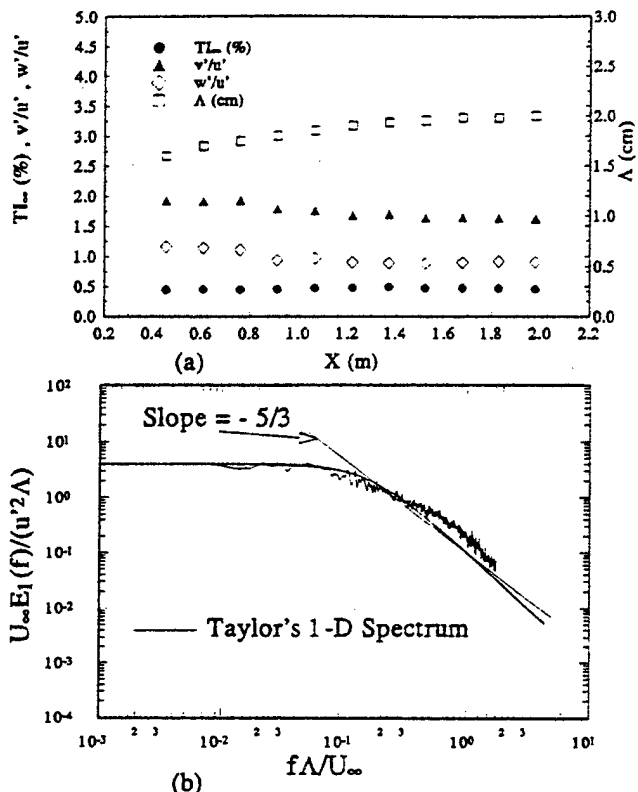


Figure 2 Free-stream turbulence (a) intensities and length scales and (b) spectral distribution

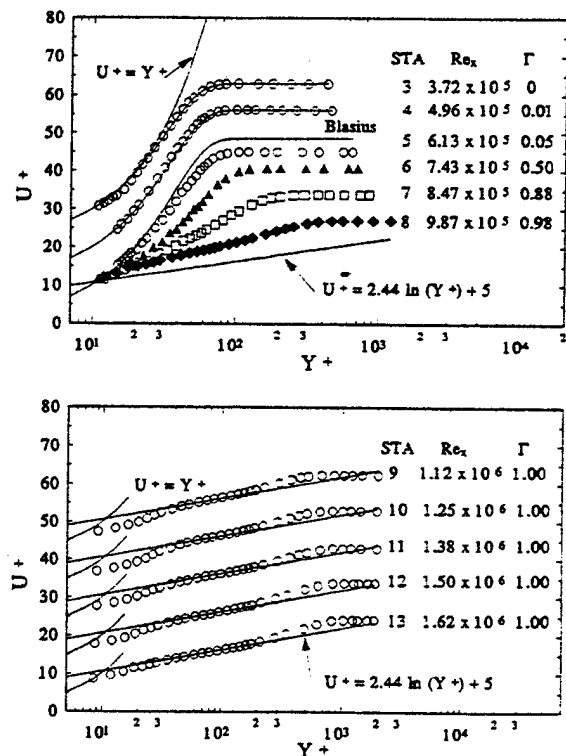


Figure 3 Mean velocity profiles,  $U^+$  versus  $Y^+$  for the baseline case

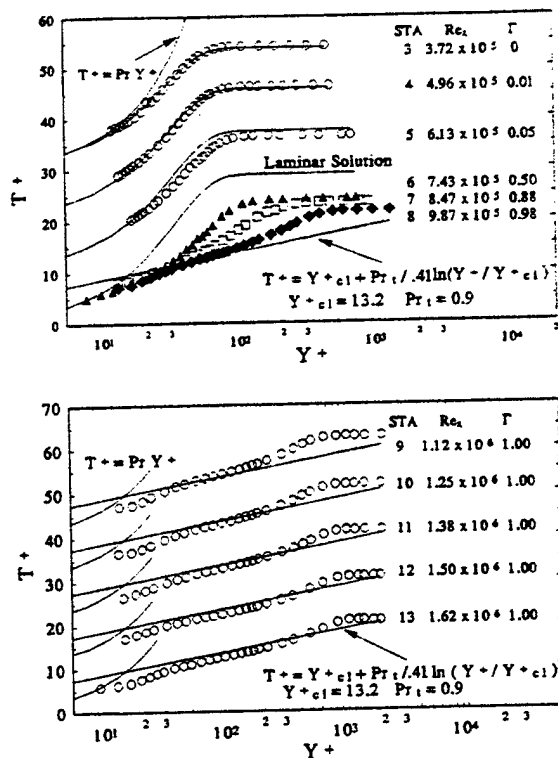


Figure 4 Mean temperature profiles,  $T^+$  versus  $Y^+$  for the baseline case

and 4, respectively. As seen in these two figures, the flow at stations 3 and 4, which follows the Blasius velocity distribution and has negligible intermittency, was clearly laminar flow. The flow at stations 9–13, which exhibited “law of the wall” characteristics over a sufficient range of  $Y^+$  and had 100% intermittency,

was clearly turbulent. The flow at stations 5–8, having intermittency between zero and one, was transitional, neither displaying turbulent, log-linear behavior nor matching the Blasius profile. The distributions of other statistical quantities across the boundary layer are documented in Wang et al. (1992, 1996).

#### Disturbances near the onset of transition

The transition started between stations 5 and 6. The baseline velocity signals at stations 3, 4, 5, and 6, taken at the location where  $u'$  reached its maximum across the boundary layer of each station, are shown in Figure 5. As shown in this figure, the velocity signals at stations 3 and 4 were dominated by low-frequency oscillations. At station 5, relatively higher frequency fluctuations appeared in the velocity signal. Such relatively higher frequency oscillations are manifestations of typical 2-D (T-S) instability waves; they are not turbulent fluctuations. At station 6, the flow was obviously intermittent between the region with sinusoidal-like, low-frequency fluctuations and the region with high-frequency fluctuations. According to the linear instability theory, the most amplified T-S wave frequency range at stations 3 to 6 for the baseline case is approximately between 40 Hz and 200 Hz, or between  $60 \text{ m}^{-1}$  and  $250 \text{ m}^{-1}$  in terms of wave numbers.

To see the amplified disturbances clearly, velocity signals that have been high-pass filtered to retain wave numbers above  $60 \text{ m}^{-1}$  were taken, and the results are shown in Figure 6. As shown, the T-S wave fluctuations were amplified between stations 4 and 5.

To see the velocity fluctuation energy distributions over different frequencies, one-dimensional power spectra of the longitudinal velocity fluctuations were processed from stations 3 to 6 at the maximum  $u'$  locations, as shown in Figure 7. As this figure illustrates, most of the fluctuation energy at stations 3 and 4 was contained in the very low wave number range (95% was under  $60 \text{ m}^{-1}$ ). At station 5, the fluctuation in the T-S wave number range ( $60 \sim 250 \text{ m}^{-1}$ ) was amplified. At station 6, the fluctuation energy contained in the high wave number range was much higher than that at stations 3 to 5.

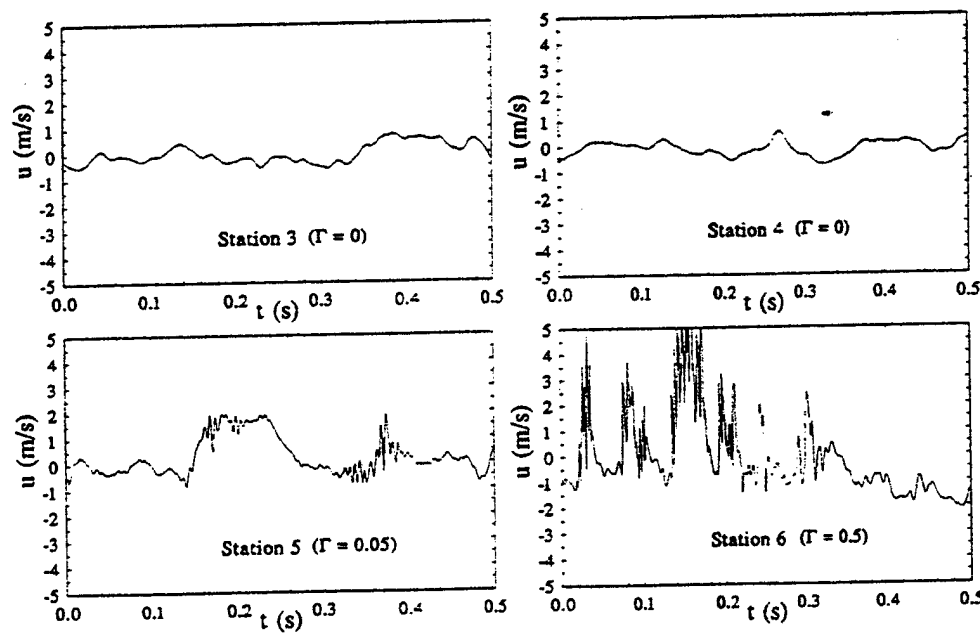


Figure 5 Velocity  $u$  signals, at maximum  $u'$  locations for the baseline case

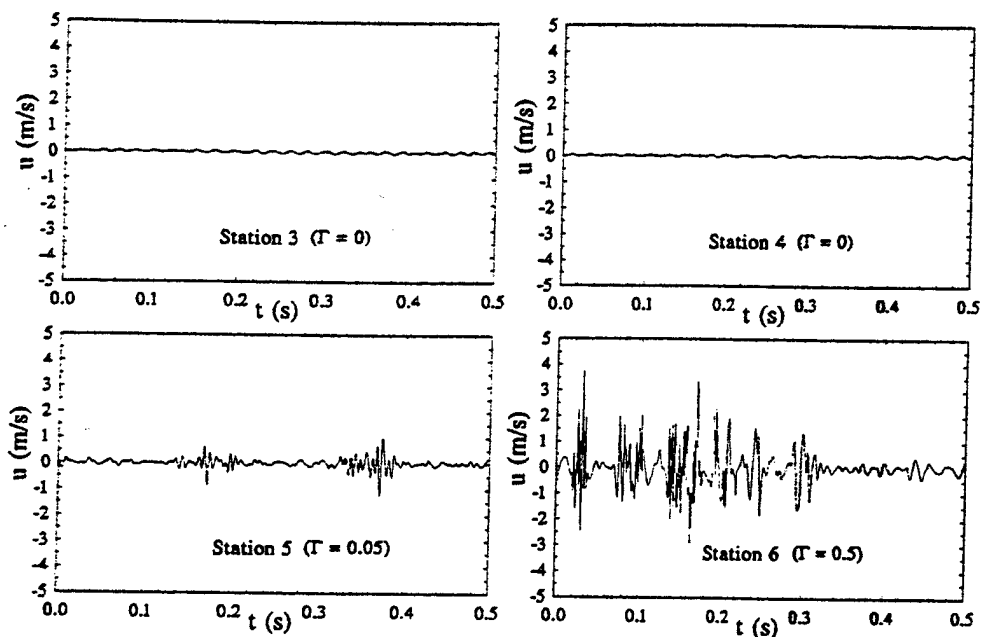


Figure 6 Velocity  $u$  signals high-pass filtered for  $k > 60 \text{ m}^{-1}$  (or 40 Hz) at maximum  $u'$  locations for the baseline case

In Figure 7, some "humps" (sinusoidal-like waves) are apparent in the power spectrum at station 5. Generally, such "humps" in a spectrum can be caused by two possible influences: (1) the finite window effect on some sinusoidal fluctua-

tions contained in the time-domain signal; or (2) nonperiodic wave forms, such as nonperiodic pulses, in the time-domain signal. To investigate the source of these humps, the power spectrum of each data piece was examined. An average power spectrum is an average of the power spectra for 40 datapieces; each datapiece contains 1024 datapoints obtained in a sampling duration of 0.512 seconds. These humps only appeared in some of the power spectra of those signals containing nonperiodic, finite-width impulses. One such impulse is shown in Figure 8. This impulse is clearly related to the change of the mean value as the signal passed a turbulent spot or wave packet. This impulse may be recognized as the first turbulent wave packet observed in the velocity signals. If this turbulent wave packets were removed, the humps in the power spectrum of the velocity signal would disappear, as shown in Figure 9. Therefore, a sinusoidal-like power spectrum signifies the earlier transition region that occurs when distinctive turbulent wave packets pass nonperiodically. These sinusoidal humps disappear when the occurrence of the turbulent wave packet; i.e., the intermittency, increases, as shown at station 6 in Figure 7. A region of high energy contained between 60 and  $250 \text{ m}^{-1}$  can be seen even after removal of the

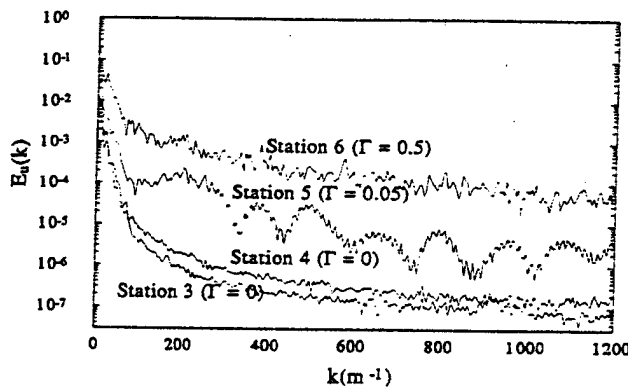


Figure 7 Power spectra of  $u$  velocity fluctuations at maximum  $u'$  locations for the baseline case

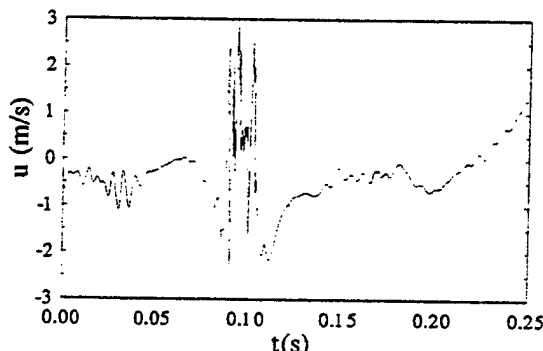


Figure 8 Velocity signal containing a turbulent wave packet at station 5 for the baseline case

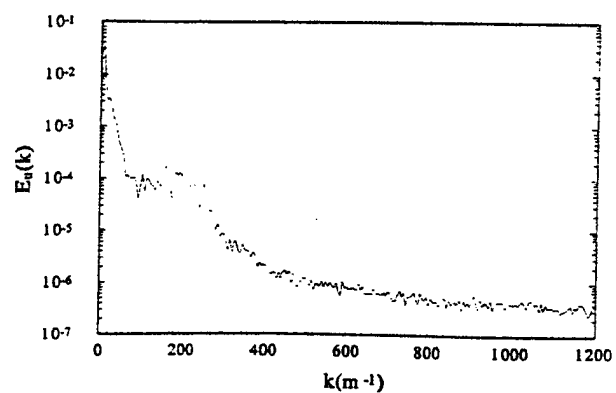


Figure 9 Power spectrum of the signal in Figure 7 after removal of the turbulent wave packet at station 5 for the baseline case

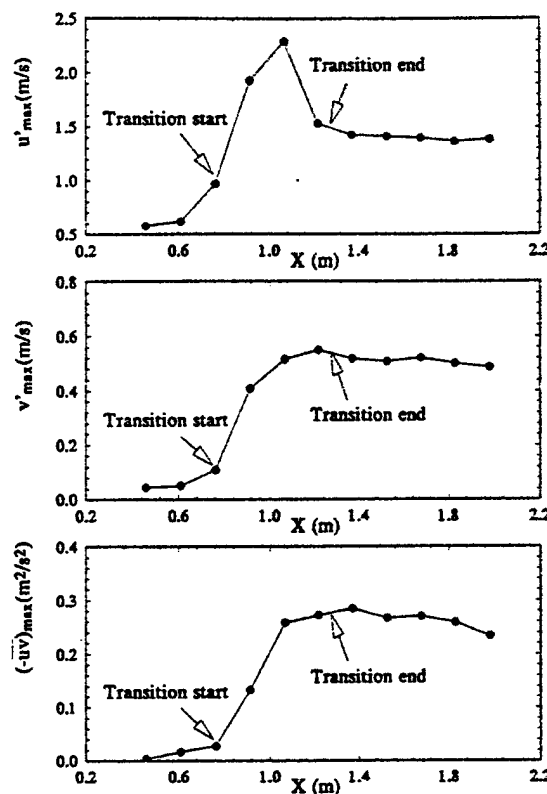


Figure 10 Streamwise evolution of peak velocity fluctuations and Reynolds shear stresses for the baseline case

wave packet in Figure 9. This verifies the statement made earlier that the linear T-S wave frequencies contribute to the oscillations of the nonturbulent part of the velocity signals between wave packets.

#### Spectral distributions of velocity fluctuations in wave packets and their streamwise evolution in the transition process

Before discussing the spectral distributions of the velocity fluctuations, it would be helpful to review the streamwise evolution of the peak  $u'$ ,  $v'$ , and  $\bar{uv}$  values during the transition process, as shown in Figure 10. Each point represents the maximum value across the boundary layer at a fixed  $x$ -location. As shown in this figure, the peak value of  $u'$  at each station reached its maximum value at approximately two-thirds of the transition region (station 7,  $X = 1.07$  m;  $\Gamma = 0.88$ ), and then decayed gradually to a nearly constant value in the turbulent region. However, the peak values of  $v'$  and  $\bar{uv}$  increased to their maximum values in the later part of the transition region, and each maintained an approximately constant value into the turbulent region. Further discussion of possible energy transport related to these phenomena can be found in Kuan and Wang (1990) and is not repeated here.

The peak locations of  $u'$  and  $\bar{uv}$  in the boundary layer at station 7 in the transition region, as replotted in Figure 11, were very different. The maximum  $u'$  occurred at around  $y/\delta = 0.1$ ; whereas, the maximum  $\bar{uv}$  (approximately twice the wall shear) occurred at around  $y/\delta = 0.35$  (or  $Y^+ \approx 70$ ). To our intuition, the region of high  $u'$  should have been an indication of high turbulent energy production. To check on this, the turbulence energy production term  $(-\bar{uv}\delta u/\delta y)$ , which extracts energy from the mean flow, was calculated and normalized, and the results are shown in Figure 11. The results indicate that the peak location of the local turbulence production coincided with the

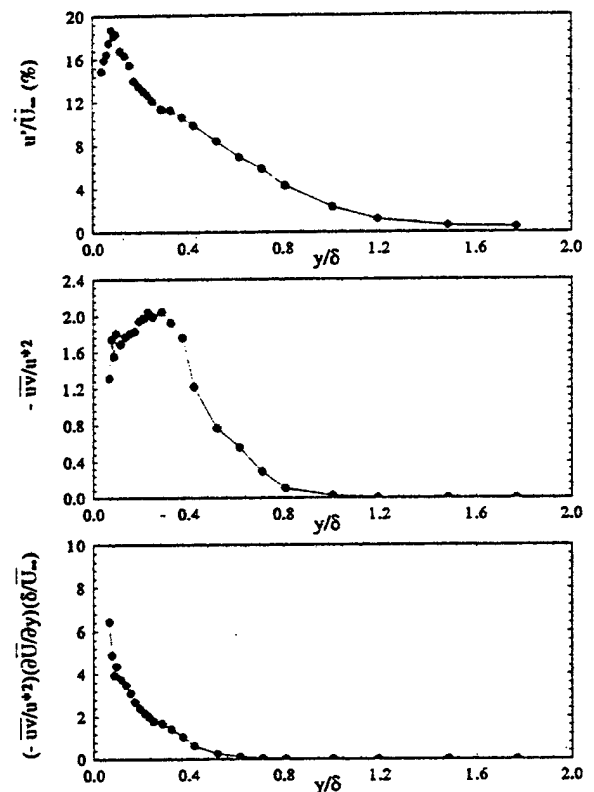


Figure 11 Distribution of Reynolds stresses and turbulent energy production at station 7 for the baseline case

peak location of  $u'$ . This evidence implies that the high  $u'$  values are more likely caused by local turbulence production than by convection from upstream.

It is interesting to find out what causes the high Reynolds shear stress,  $\bar{uv}$ . Because the region of maximum  $\bar{uv}$  values do not coincide with those of turbulent production, the comparison made in Figure 11 does not suggest that high Reynolds shear stress is related to high turbulence production. However, because the maximum  $\bar{uv}$  occurred at around  $Y^+ \approx 70$ , it was conjectured that the region of high Reynolds shear stress may have been a manifestation of conventional vortex break-up activity or fluid ejection attributable to bursting. Physically, this conjecture combined with the results in Figure 11 suggests that the breakups that occurred at the tip of the hairpin vortices might have produced

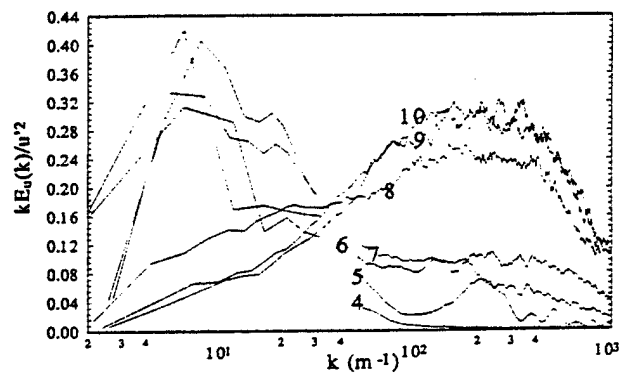


Figure 12 Power spectra of  $u$  velocity fluctuations at the maximum  $u'$  locations for the baseline case

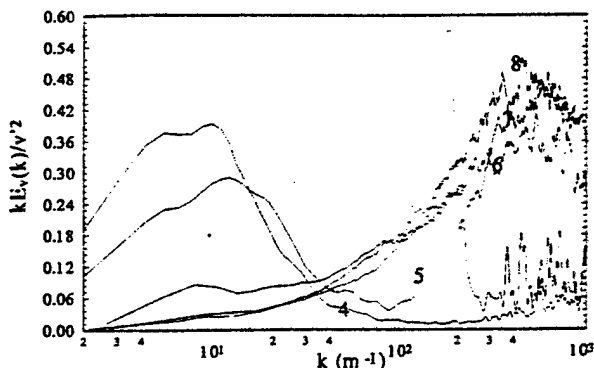


Figure 13 Power spectra of  $v$  velocity fluctuations at the maximum  $u'$  locations for the baseline case

large turbulent shear stress, rather than turbulence energy, in a magnitude of twice the local wall shear.

Spectral analysis of the  $u$  and  $v$  velocity fluctuations can provide further information about the energy transfer process.

As discussed in the preceding section, once the transition was initiated near station 5, the power spectrum in the high wave number range increased rapidly with increasing distance downstream. This increase can be seen in Figure 12. The power spectrum at the wave number range higher than  $60 \text{ m}^{-1}$  is believed to be derived mainly from the fluctuations in the turbulent wave packets. Information on spectra with frequencies higher than  $1000 \text{ Hz}$  (or wave numbers higher than approximately  $1000 \text{ m}^{-1}$  for the baseline case) is not available, because the sampling rate was 2000 points/s, and the Nyquist principle implies that spectra information is only meaningful for frequencies lower than one-half of the sampling frequency.

One-dimensional power spectra of  $u$  and  $v$  and their co-spectra obtained at the maximum  $u'$  locations for the baseline case, normalized by the corresponding variance, are presented in Figures 12, 13, 14, and 15. In these figures, the power spectra or co-spectra are weighted with wave number in the form  $kE(k)$  and are plotted as a function of  $\ln(k)$ . The area under the curve represents the total energy or variance, which equals 1 after normalization since

$$E(k)dk = kE(k)d\ln(k) \quad (1)$$

Similar to the evolution of the spectra of  $u$  (Figure 12), the evolution of the spectra of  $v$  in Figure 13 also shows that the fraction of energy contained in the low wave number range ( $k < 60 \text{ m}^{-1}$ ) decreased while the fraction of energy contained in the high wave number range ( $k > 60 \text{ m}^{-1}$ ) increased during the

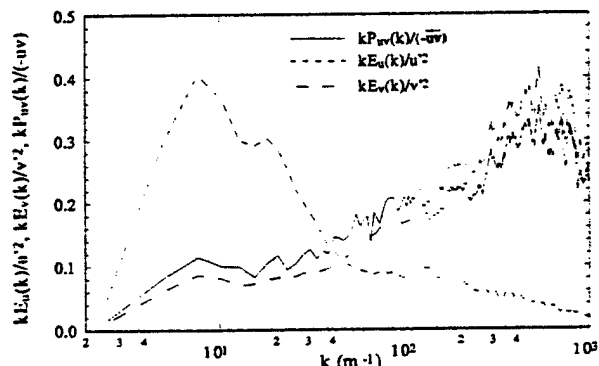


Figure 14 Comparison among  $E_v(k)$ ,  $E_v(k)/v'^2$ , and  $P_{uv}(k)/v'^2$  at the maximum  $u'$  location of station 6 for the baseline case

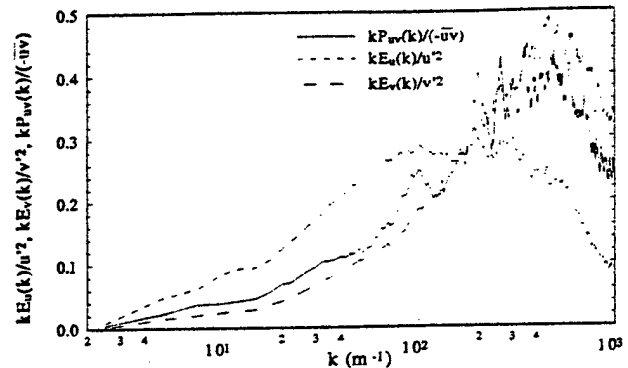


Figure 15 Comparison among  $E_u(k)$ ,  $E_v(k)$ , and  $P_{uv}(k)$  at the maximum  $u'$  location of station 12 for the baseline case

transition process. The evolution of this process was faster for  $v$  than it was for  $u$ . For  $v$ , the power spectra changed dramatically from station 5 to station 6 and reached an equilibrium from station 7 to station 10. It is interesting to see that the instability at around  $180 \text{ m}^{-1}$  at station 5 is especially amplified in Figure 13. A rapid change in the  $u$  power spectra occurred later between station 7 and station 8, and equilibrium was not reached until downstream of station 9. These observations are consistent with the maximum  $u'$  and  $v'$  evolutions shown in Figure 10.

In the late transition and early turbulent regions (downstream of station 8), there was a plateau of high energy content between  $100 \text{ m}^{-1}$  and  $400 \text{ m}^{-1}$  for the power spectra of  $u$  (Figure 12). In contrast, the range of high wave number for the power spectra of  $v$  was within  $300 \text{ m}^{-1}$  to  $1000 \text{ m}^{-1}$ . The peak locations of the power spectra of  $v$  occurred near the end of the plateau region of the power spectra of  $u$ . This may imply that the energy transfer from the longitudinal velocity fluctuations ( $u$ ) to the cross-stream velocity fluctuations ( $v$ ) is most effective in the high wave number range (between  $300 \text{ m}^{-1}$  and  $1000 \text{ m}^{-1}$  for the baseline case). This is consistent with the cascading theory of turbulence energy, with the recipients of energy being in smaller eddies. This transfer of energy from  $u$  to  $v$  may largely take place through the correlation with the pressure fluctuations (return-to-isotropy terms), as is mentioned later in Figure 18. The pressure fluctuations seem to be the only communication channel between the  $u'^2$  and the  $v'^2$  transport equations.

The co-spectra between  $u$  and  $v$  at station 6 in the early transition region and at station 12 in the turbulent region are shown in Figures 14 and 15. In these figures, the co-spectra are seen to have been affected by both velocity fluctuations, but the effect of  $v$  is dominant. This suggests that the turbulent shear

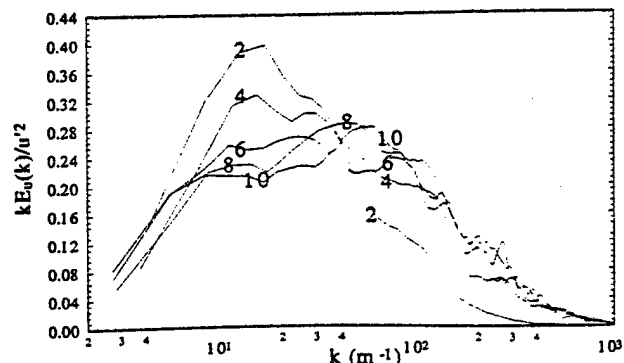


Figure 16 Power spectra of  $u$  velocity fluctuations at the maximum  $u'$  locations for the case with  $\text{FSTI} = 6.4\%$

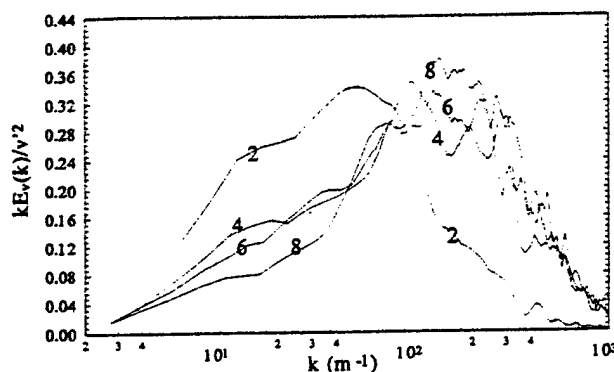


Figure 17 Power spectra of  $v$  velocity fluctuations at the maximum  $u'$  locations for the case with FSTI = 6.4%

stress is predominantly driven by  $v$ , even in the presence of higher magnitudes of  $u$ . This provides an important insight into the dominance of  $v$  activity in the transport of turbulent shear stress. The higher magnitudes of  $u'$  below  $50 \text{ m}^{-1}$  are streamwise unsteadiness, so it does not correlate well with the turbulent shear.

#### Elevated FSTI case

The normalized power spectra of the  $u$  and  $v$  velocity fluctuations for the elevated FSTI case (6.4%) at maximum  $u'$  locations are shown in Figures 16 and 17. In these figures, the turbulence energy is negligible beyond  $1000 \text{ m}^{-1}$ . For the fluctuations, the energy above  $30 \text{ m}^{-1}$  (Figure 16) was amplified; the energy below  $30 \text{ m}^{-1}$  was damped but maintained at a higher level than for the baseline case (Figure 12). The peak for the  $u$  spectrum in the late transitional and early turbulent region occurred at around  $40 \sim 70 \text{ m}^{-1}$  for the 6.4% FSTI case (Figure 16), while the peak occurred at around  $200 \sim 400 \text{ m}^{-1}$  for the baseline case (Figure 12). The peak of the  $v$  spectrum in the late transitional and early turbulent region took place at around  $100 \sim 200 \text{ m}^{-1}$  for the elevated FSTI case (Figure 17), while the peak is at around  $500 \text{ m}^{-1}$  for the baseline case (Figure 13). These differences in the wave number ranges containing the primary turbulence energy may have been caused by the difference between the free-stream

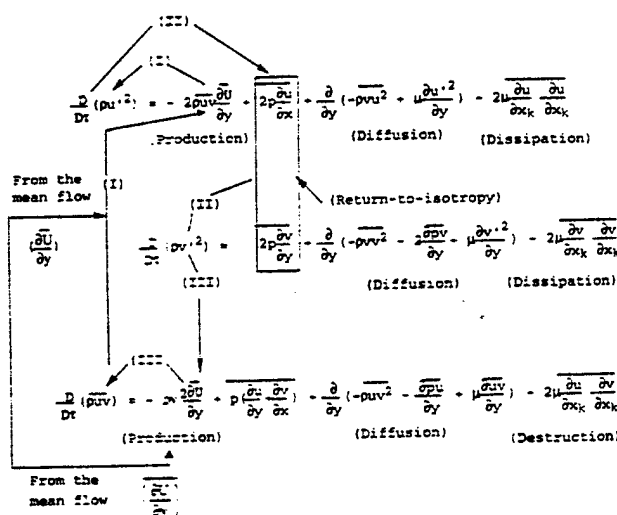


Figure 18 Hypothetical primary energy transfer processes in a transitional boundary layer

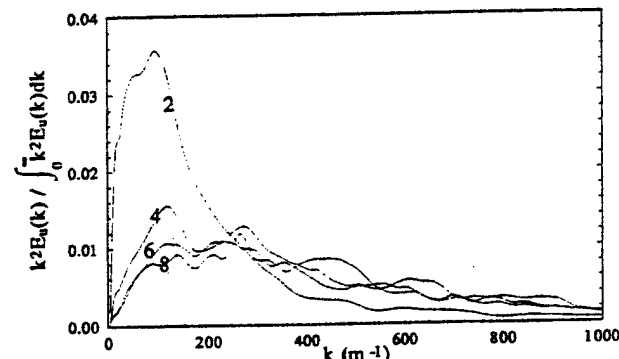


Figure 19 Normalized dissipation energy spectra of  $u^2$  at the maximum  $u'$  locations for the case with FSTI = 6.4%

velocities. Recall that the free-stream velocity was  $12.24 \text{ m/s}$  for the baseline case and  $1.7 \text{ m/s}$  for the high-turbulence case.

The term  $(\partial u / \partial x)^2$  of the dissipation energy terms

$$\left\{ -2\mu \frac{\partial u}{\partial x_k} \frac{\partial u}{\partial x_k} \right\}$$

in the  $u'$  transport equation (see Figure 18) can be estimated from the  $u$  spectrum. Based on Taylor's hypothesis,  $(\partial u / \partial x)^2$  can be shown to be proportional to

$$\frac{4\pi^2}{U^2} \int_0^\infty k^2 E_u(k) dk$$

$(\partial u / \partial x)^2$  is used here to approximately represent the dissipation energy terms in the  $u^2$  transport equation. Similarly,  $(\partial v / \partial x)^2$  is used to approximately represent the dissipation energy terms

$$\left\{ -2\mu \frac{\partial v}{\partial x_k} \frac{\partial v}{\partial x_k} \right\}$$

in the  $v^2$  transport equation. The streamwise evolution of the normalized spectral dissipation energy distributions of  $u'$  and  $v'$  for a low-velocity, high-free-stream turbulence case ( $\bar{U}_x = 1.7 \text{ m/s}$ ; FSTI = 6.4%) are shown in Figures 19 and 20. By comparing these two figures with the  $u$  and  $v$  spectra in Figures 16 and 17, it is apparent that the evolution of the spectral distribution of the dissipation energy was faster than that of the corresponding turbulence power spectrum. The evolution of the dissipation energy distributions for the  $u$  component was similar to that for the  $v$  component, with more energy being dissipated at a higher

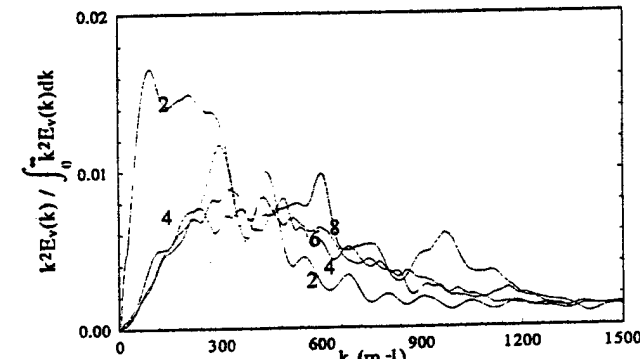


Figure 20 Normalized dissipation energy spectra of  $v^2$  at the maximum  $u'$  locations for the case with FSTI = 6.4%

wave number range as the transition proceeded. This implies that the cascading process at a high wave number (with small eddies) is faster than at a low wave number (with large eddies).

Based on the aforementioned discussion, the major energy transfer process in the transition region can be hypothesized, as in Figure 18. Once the bursts occur at the final stage of the formation of 3-D vortices, a turbulent shear stress distribution ( $\bar{uv}$ ) forms around the bursts at about  $Y^+ \approx 70 \sim 100$  (Figure 11), and energy transfers from the mean flow to the longitudinal velocity fluctuations (process I) through the energy production term  $\{-\bar{uv}\partial\bar{U}/\partial y\}$  in the near-wall region (Figure 11). Then, some energy from the longitudinal velocity fluctuations transfers to the cross-stream velocity fluctuations at a higher wave number range (Figures 12 and 13) through the return-to-isotropy terms, which seem to be the only communication channel between the  $u^2$  and  $v^2$  transport equations (process II). The Reynolds shear stress, which is driven by the cross-stream velocity fluctuations as shown in Figure 14, increases, extracting more energy from the mean flow via the production term

$$\left\{ -\bar{uv}^2 \frac{\partial \bar{U}}{\partial y} \right\}$$

(process III). The increased turbulent shear stress then extracts more energy from the mean flow to  $u'$  through process I again. This energy transfer process forms the main routes for production of  $u'$ ,  $v'$ , and  $\bar{uv}$  (processes I, II, and III) with supplying pipelines of energy from the mean flow that have branches to each component through diffusion and dissipation. At the same time, the cascading process transfers the low wave number fluctuation energy to the high wave number fluctuation energy in the wave number domain, and the energy is dissipated into heat. Dissipations of  $u'$  and  $v'$  reach the "asymptotic spectra" (Figures 19 and 20) of typical turbulent boundary layer profiles first, followed by the  $v'^2$  spectrum (Figures 10, 13, and 17). Once  $v'^2$  attains the asymptotic spectrum, the production of the Reynolds shear stress reaches its limit, and the energy transfer from the mean flow to the longitudinal velocity fluctuations becomes saturated. Eventually,  $u'^2$  starts to decay (Figure 10) because of the limited supply of energy from the mean flow and constant dissipation through the cascading process; it reaches the asymptotic state last. This scenario is based on spectral information obtained from maximum  $u'$  locations in the boundary layer and along the streamwise direction. The effect of diffusion across the boundary layer is not included in the above discussion.

#### Spectral analogy between velocity and temperature fluctuations

Comparisons of the normalized power spectra among the  $u$ ,  $v$ , and  $t$  fluctuations at the maximum  $u'$  locations for station 6 and

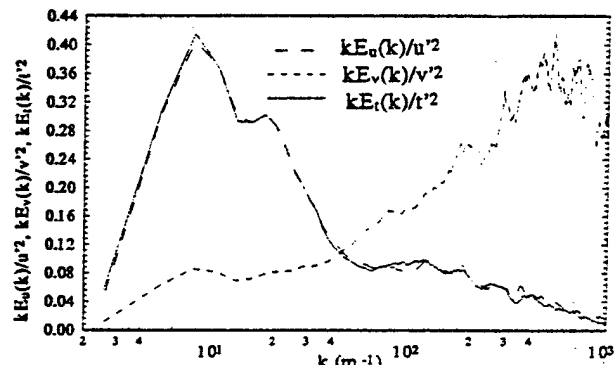


Figure 21 Comparison among  $E_u(k)$ ,  $E_v(k)$ , and  $E_t(k)$  at the maximum  $u'$  location of station 6 for the baseline case

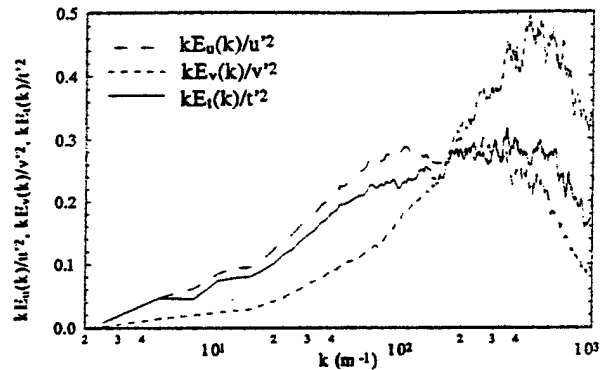


Figure 22 Comparison among  $E_u(k)$ ,  $E_v(k)$ , and  $E_t(k)$  at the maximum  $u'$  location of station 12 for the baseline case

station 12 are shown in Figures 21 and 22. As is evident in these figures, the thermal power spectra of the  $t$  temperature fluctuations are very close to the spectra of the  $u$  velocity fluctuations in the early transitional region with a large portion of energy contained in the wave number range less than  $80 \text{ m}^{-1}$ . Conversely, the  $v$  spectrum contains more energy in the higher wave number range with a maximum value around  $500 \text{ m}^{-1}$  (Figure 21). In the early turbulent region at station 12, a large portion of the energy of  $u$  and  $t$  has moved to wave numbers higher than  $80 \text{ m}^{-1}$  (Figure 22). It is interesting to see all three curves in Figure 22 cross at the same wave number, approximately  $180 \text{ m}^{-1}$ , which happens to be the most amplified wave number at station 5 in Figure 13. The implication of this synchronized "cross-over"

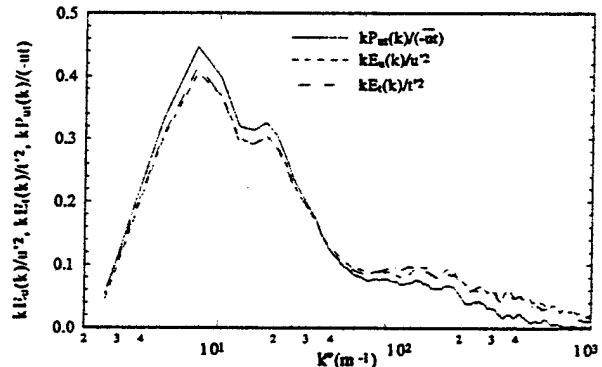


Figure 23 Comparison among  $E_u(k)$ ,  $E_v(k)$ , and  $P_{ut}(k)$  at the maximum  $u'$  location of station 6 for the baseline case

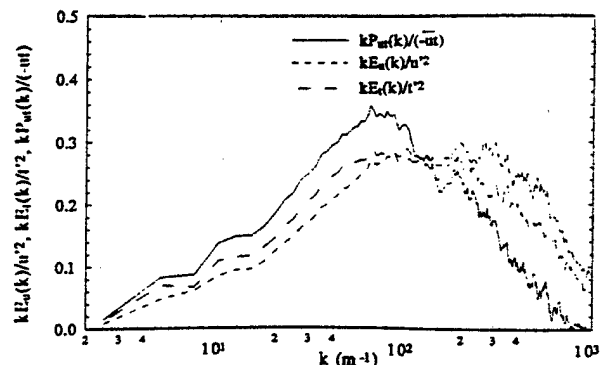


Figure 24 Comparison among  $E_u(k)$ ,  $E_v(k)$ , and  $P_{ut}(k)$  at the maximum  $u'$  location of station 12 for the baseline case

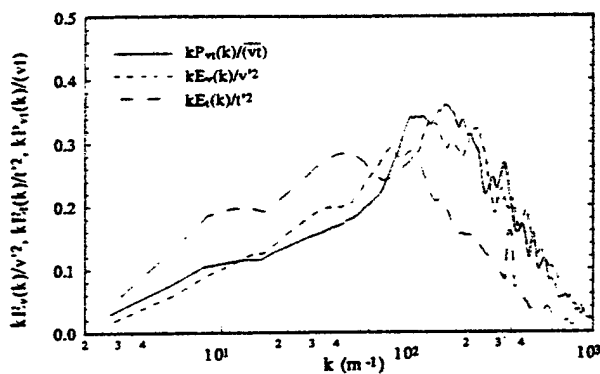


Figure 25 Comparison among  $E_v(k)$ ,  $E_t(k)$ , and  $P_{vt}(k)$  at the maximum  $u'$  location of station 6 for the baseline case

can be interpreted as the impact of the  $v$  fluctuations on the  $t$  fluctuations. If we look back at the spectra in the transitional region in Figure 21,  $u$  and  $t$  almost exactly overlapped; however, in the early turbulent region in Figure 22, the  $t$  curve seems to be pulled down by the  $v$  curve in the wave number range less than  $180 \text{ m}^{-1}$  and pulled up by the  $v$  curve above  $180 \text{ m}^{-1}$ . Although the deviation of  $t$  from  $u$  is not large, the effect of  $v$  on passive temperature fluctuations is very significant, because the magnitude of the  $v$  fluctuations is smaller than that of the  $u$  fluctuations. It should be noted that the magnitudes in Figure 22 are normalized values.

Comparison among the normalized spectra of the  $u$  and  $t$  fluctuations and their co-spectra for the baseline case is shown in Figure 23 at station 6 and in Figure 24 at station 12. Generally, the correlation between the longitudinal velocity and the temperature fluctuations is better at the low wave number range than at the high wave number range in both the transitional and the turbulent regions. It should be remembered that at wave numbers lower than  $120 \text{ m}^{-1}$ , the velocity fluctuations are more associated with unsteadiness than with turbulence.

In an elevated FSTI case (6.4%), comparisons among the spectra of  $v$  and  $t$  fluctuations and their co-spectra in the transition region (station 6) are shown in Figure 25. Similar to the co-spectra between the  $u$  and  $v$  velocity fluctuations, the co-spectra between the  $v$  and  $t$  fluctuations are strongly affected by the  $v$  spectrum. The  $\bar{v}t$  correlation (Figure 25) is better than the  $\bar{u}t$  correlation (Figure 23) in the higher wave number range. This may suggest that the cross-stream Reynolds heat flux ( $\bar{v}t$ ) is transported by smaller eddies than is the streamwise Reynolds heat flux ( $\bar{u}t$ ).

## Conclusion

A spectral analysis of boundary-layer transition on a heated flat plate was conducted at FSTI = 0.5% and 6.4%. The spectra of  $u$ ,  $v$ , and  $t$  and their co-spectra  $\bar{u}t$  and  $\bar{v}t$  were processed at the maximum  $u'$  locations of each streamwise measuring station. The linear T-S instability wave amplification was observed in the case with 0.5% FSTI.

The results indicate that the peak location of the turbulence production ( $y/\delta = 0.1$ ) coincides with the peak location at  $u'$ ; whereas, the region of high turbulent shear ( $y/\delta \approx 0.35$  or  $Y = 70$ ) produces little turbulence energy. The high turbulent shear stress was speculated to be associated with the break-up activity of the hairpin vortices.

Once the transition starts, a large fraction of  $u'$  energy is contained in the lower wave number range (less than  $60 \text{ m}^{-1}$ ); whereas, the  $v'^2$  energy is contained in the higher wave number range (near  $600 \text{ m}^{-1}$  and beyond). A primary energy transfer

process for a transitional boundary layer is hypothesized (Figure 18). The return to isotropy terms play an important role in transferring  $u$  component energy to the  $v$  component, especially in the high wave number range. The  $v$  spectrum reaches the asymptotic distribution of a typical turbulent boundary layer faster than the  $u$  spectrum does during the streamwise evolution in the transitional region (Figures 10, 12, and 13). The turbulent shear stress ( $\bar{uv}$ ) was predominantly driven by  $v$  even in the presence of higher magnitudes of  $u$ . The dissipation power spectra for both  $u$  and  $v$  evolves faster than the turbulence power spectra of  $u$  and  $v$  in the transitional process.

The power spectrum of the temperature fluctuations coincides with that of the longitudinal velocity fluctuations in the early to middle transitional flow, but it is significantly affected by the  $v$  spectrum in the late transitional and early turbulent flow regions. The correlation between the  $u$  velocity fluctuations and the temperature fluctuations is stronger at a low wave number range than at a high wave number range. For the elevated free-stream turbulence intensity case, the turbulence energy is contained in a narrower wave number band than in the low turbulence intensity case. The cross-stream Reynolds heat flux ( $\bar{vt}$ ) is transported by smaller eddies than is the streamwise Reynolds heat flux ( $\bar{ut}$ ).

## References

- Blair, M. F. 1992. Boundary layer transition in accelerating flows with intense free-stream turbulence, Part 1 — Disturbances upstream of transition onset; Part 2 — The zone of intermittent turbulence. *J. Fluids Eng.* 114, 313-332
- Chua, L. P. and Antonia, R. A. 1990. Turbulent Prandtl number in a circular jet. *Int. J. Heat Mass Transfer*, 33, 331-339
- Emmons, H. W. 1951. The laminar-turbulent transition in a boundary layer — Part I. *J. Aeronaut. Sci.* 18, 490-498
- Keller, F. J. 1993. Flow and thermal structures in heated transitional boundary layers with and without streamwise acceleration. Ph.D. dissertation, Department of Mechanical Engineering, Clemson University, Clemson, SC, USA
- Kim, J., Simon, T. W. and Kestoras, M. 1994. Fluid mechanics and heat transfer measurements in transitional boundary layers conditionally sampled on intermittency. *J. Turbomachinery*, 116, 405-416
- Kuan, C. L. 1987. An experimental investigation of intermittent behavior in the transitional boundary layer. M.S. thesis, Department of Mechanical Engineering, Clemson University, Clemson, SC, U.S.A.
- Kuan, C. L. and Wang, T. 1989. Some intermittent behavior of transitional boundary layers. AIAA Paper 89-1890
- Kuan, C. L. and Wang, T. 1990. Investigation of intermittent behavior of transitional boundary layers using a conditional averaging technique. *Exp. Thermal Fluid Sci.* 3, 157-170
- Narasimha, R. 1958. On the distribution of intermittency in the transition region of a boundary layer. *J. Aeronaut. Sci.* 24, 711-712
- Shome, B. 1991. Development of a three-wire probe for the measurement of Reynolds stresses and heat fluxes in transitional boundary layers. M.S. thesis, Department of Mechanical Engineering, Clemson University, Clemson, SC, USA
- Sohn, K. H. and Reshotko, E. 1991. Experimental study of boundary layer transition with elevated free-stream turbulence on a heated flat plate. NASA CR-187068
- Suder, K. L., O'Brien, J. E. and Reshotko, E. 1988. Experimental study of bypass transition in a boundary layer transition. NASA TM-100913
- Wang, T., Keller, F. J. and Zhou, D. 1992. Experimental investigation of Reynolds shear stresses and heat fluxes in a transitional boundary layer. In *Fundamental and Applied Heat Transfer Research for Gas Turbine Engines*, ASME HTD — Vol. 226, 61-70
- Wang, T., Keller, F. J. and Zhou, D. 1996. Flow and thermal structures in a transitional boundary layer. *Exper. Thermal Fluid Sci.*, to appear
- Zhou, D. 1993. Effects of elevated free-stream turbulence and streamwise acceleration on flow and thermal structures in transitional boundary layers. Ph.D. Dissertation, Department of Mechanical Engineering, Clemson University, Clemson, SC, U.S.A.
- Zhou, D. and Wang, T. 1995. Effects of elevated free-stream turbulence on flow and thermal structures in transitional boundary layers. *J. Turbomachinery*, 117, 407-417

# Effects of Criterion Functions on Intermittency in Heated Transitional Boundary Layers With and Without Streamwise Acceleration

F. J. Keller

T. Wang

Department of Mechanical Engineering,  
Clemson University,  
Clemson, SC 29634-0921

Attempting to understand the mechanisms of momentum and thermal transports in transitional boundary layers has resulted in the use of conditional sampling to separate the flow into turbulent and nonturbulent portions. The choice of a proper criterion function to discriminate between the two flow conditions is critical. A detailed experimental investigation was performed to determine the effects of different criterion functions on the determination of intermittency for application in heated transitional boundary layers with and without streamwise acceleration. Nine separate criterion functions were investigated for the baseline case without pressure gradient and three cases with streamwise pressure gradient. Inherent differences were found to exist between each criterion function's turbulence recognition capabilities. The results indicate that using a criterion function based on Reynolds shear stress,  $(\partial u v / \partial \tau)^2$ , for turbulent / nonturbulent discrimination in a heated transitional boundary layer is superior to a single velocity or temperature scheme. Peak values in intermittency for the early to midtransitional region were found to occur away from the wall at approximately  $y / \delta = 0.3$  for all cases. To match the universal intermittency distribution of Dhawan and Narasimha (1958), the minimum values of intermittency at  $y / \delta \approx 0.1$  should be used as the representative "near-wall" values.

## Introduction

Boundary layer transition from laminar to turbulent flow has been recognized as an important feature in the through-flow of a gas turbine (Graham, 1979, 1984; Mayle, 1991). Heat transfer in a turbulent boundary layer with a moderate Prandtl number is typically treated as a passive process controlled by the turbulent momentum transport. For a gas turbine blade, where as much as 50–80 percent of the turbine blade surface is covered with flow undergoing laminar-turbulent transition (Turner, 1971), this relation between momentum and thermal transport has not been verified. In addition, turbine blades are exposed to diverse pressure gradients that may compound these transport differences. Recognizing and understanding the fundamental mechanisms involved in transitional convective heat transfer are keys to improving the heat transfer modeling and enhancing the accuracy of thermal load predictions on gas turbine blades.

Attempting to understand the mechanisms in transitional

momentum and thermal transports has resulted in the use of conditional sampling to separate the flow into turbulent and nonturbulent portions. Conditional sampling techniques used in turbulent boundary layer and shear flows are many; however, their application to heated transitional flow is not well developed. The choice of a proper criterion function to discriminate between the two flow conditions is critical. The use of temperature as a passive contaminant to discriminate between the turbulent and nonturbulent portions as done in turbulent boundary layer flows and shear flows is questionable in transitional boundary layers since discrepancies between the momentum and thermal transport in a transitional boundary layer exist. Blair (1982, 1992), Sharma (1987), and Volino and Simon (1991) determined that the length of transition for accelerating flows is longer for the thermal than for the momentum boundary layer. Sharma recommended the use of a separate intermittency factor for the thermal boundary layer under these conditions. In light of these observations, a need exists to determine the sensitivity of the intermittency factor in the heated transitional boundary layer to the choice of criterion function.

Emmons' (1951) statistical theory of transition introduced the concept of an intermittency factor for calculation in the

Contributed by the International Gas Turbine Institute and presented at the 38th International Gas Turbine and Aeroengine Congress and Exposition, Cincinnati, Ohio, May 24–27, 1993. Manuscript received at ASME Headquarters February 18, 1993. Paper No. 93-GT-67. Associate Technical Editor: H. Lukas.

transitional boundary layer. Emmons proposed that the turbulent patches could be treated as fully turbulent flow and the nonturbulent patches as laminar flow. The bulk flow properties could then be reconstructed as  $X = (1 - \Gamma)X_{nt} + \Gamma X_t$ . For example, the skin friction coefficient in the transitional region could be found from the intermittency factor and the appropriate combinations of the turbulent and laminar values;  $C_f = (1 - \Gamma)C_{f,nt} + \Gamma C_{f,t}$ . By knowing the intermittency factor at any streamwise location, the bulk properties of the transitional boundary layer could be determined. Treating the turbulent portion of transitional flow as a fully turbulent flow and the nonturbulent portion as a laminar flow is a widely used engineering practice (Arnal, 1984; Narasimha, 1985; Mayle, 1991). This practice has been recently questioned by Kuan and Wang (1990). Their concern was not on the concept of intermittency but on the adequacy of treating the turbulent portion as a fully turbulent flow and the nonturbulent portion as a laminar flow. They concluded that both turbulent and nonturbulent portions of the transitional flow are different from their counterparts in the fully turbulent and laminar flow.

The determination of the turbulent and nonturbulent portions of the transition region and their subsequent separation relies on the technique of conditional sampling. This technique was discussed in detail by Hedley and Keffer (1974) and Muck (1980). It is comprised of three main stages: selection of a criterion function, determination of a threshold level, and generation of an intermittency function.

Turbulent flow is a three-dimensional rotational flow characterized by the dissipation of mechanical energy into heat through a cascade of eddies of diminishing sizes. The criterion function should be ideally representative of this turbulence and offer a good contrast between the turbulent and nonturbulent portions. However, detection of an energy cascade requires spectral analysis and renders an instantaneous decision for or against turbulence difficult. Fluctuating vorticity was used by Corrsin and Kistler (1955), but this requires the use of a complex probe capable of spatial differentiation and is considered by most too difficult to implement, especially in a transitional boundary layer.

Chen and Blackwelder (1976), Muck (1980), and Antonia (1981) considered the use of a passive scalar such as temperature to be superior to velocity or vorticity as a criterion function. However, Muck (1980) pointed out that the question remains whether the thermal interface coincides with the turbulent (vorticity) interface. For a fully turbulent heated

boundary layer, turbulent/nonturbulent discrimination occurs primarily in the outer boundary layer where the turbulent fluid is rotational and the nonturbulent fluid is irrotational. The temperature in the irrotational portion remains constant and is lower than the temperature in the turbulent regions. The classic temperature discrimination scheme uses the temperature directly and identifies "hot" fluid as turbulent and "cold" fluid as nonturbulent. The validity of this classic scheme needs to be re-examined in the transitional boundary layer where the vorticity dynamics are different. The dynamics of the vortices on the rotational/irrotational interface of the fully turbulent boundary are different than the vortex tubes on the boundary between the turbulent and nonturbulent portion in a transitional boundary layer. The temperature in the irrotational portion of the turbulent outer boundary layer maintains a constant lower temperature than the rotational portion. However, the temperature of the nonturbulent portion of the transitional boundary layer is not necessarily lower than the temperature in the turbulent portion. In the transitional boundary layer, the temperature profile, similar to the velocity profile, will alternate between a laminarlike profile and a turbulentlike profile. In addition, the "calming region" at the trailing edge of a turbulent patch imposes difficulty for discriminating the turbulent/nonturbulent portions since both fluctuating magnitudes and mean values are changing. No such calming region is observed in the interface between a turbulent boundary layer and free stream.

Difficulties also arise in using velocity fluctuations. Velocity fluctuations are not unique to the turbulent fluid and may be due to amplified oscillations of the free-stream disturbances or Tollmien-Schlichting waves. As a result, some procedure must be used to desensitize it. Also, spurious dropouts (short regions where the criterion function falls below the threshold level indicating nonturbulent flow) occur within a turbulent burst and some form of smoothing is required. Smoothing may take the form of a running average to eliminate the spurious dropouts or the use of a holding time where any excursions shorter than the holding time are still considered turbulent. Hedley and Keffer (1974) recommended  $[(\partial^2 u / \partial \tau^2)^2 + (\partial^2 v / \partial \tau^2)^2]$  or  $[(\partial u / \partial \tau)^2 + (\partial v / \partial \tau)^2]$  for use as the discrimination scheme stating that the Reynolds shear stress has a lack of definition at the interface leading edge. Antonia (1972) used  $(\partial u v / \partial \tau)^2$  and reported a sharp drop in the Reynolds shear stress at the interface conflicting with the results of Hedley and Keffer.

## Nomenclature

$C_f$  = skin friction coefficient =  $\tau_w / (\rho \bar{U}_x^2 / 2)$   
 $C_p$  = pressure coefficient =  $(P - P_{ref}) / [(1/2) \rho \bar{U}_{x,ref}^2]$   
 $K$  = pressure gradient parameter =  $(\nu / \bar{U}_x^2) \partial \bar{U}_x / \partial x$   
 $P$  = static pressure  
 $Re_x$  = Reynolds number =  $\bar{U}_x x / \nu$   
 $t$  = instantaneous fluctuation in temperature  
 $t'$  = rms value of temperature fluctuation  
 $T$  = instantaneous temperature  
 $u, v, w$  = instantaneous velocity fluctuations in streamwise, cross-stream, and spanwise directions

$u', v', w'$  = rms values of velocity fluctuations  
 $u^*$  = friction velocity =  $\sqrt{\tau_w / \rho}$   
 $U, V$  = instantaneous velocities  
 $\bar{U}$  = mean velocity  
 $U^+ = \bar{U} / u^*$   
 $\bar{u}v$  = mean Reynolds shear stress  
 $\bar{u}t$  = mean Reynolds streamwise heat flux  
 $\bar{u}t$  = mean Reynolds cross-stream heat flux  
 $x$  = coordinate in streamwise direction  
 $y$  = coordinate normal to the surface  
 $Y^- = yu^* / \nu$   
 $\Gamma$  = intermittency factor

$\delta$  = boundary layer thickness at 0.995  $U_x$

$\delta^*$  = displacement thickness

$\epsilon$  = turbulent dissipation rate

$\nu$  = kinematic viscosity

$\xi$  = length in transition region =  $x_{\Gamma=0.75} - x_{\Gamma=0.25}$

$\rho$  = density

$\tau$  = time

$\tau_w$  = shear stress on the wall

## Subscripts

$\infty$  = free-stream value

$nt$  = nonturbulent

ref = reference location at  $x = 20$  cm

$s$  = onset of transition

$t$  = turbulent

$w$  = at the wall

Muck (1980) investigated several discrimination schemes and concluded using  $|\partial u^* / \partial \tau|$  or  $|\partial^2 u^* / \partial \tau^2|$  worked best and was closest to the temperature scheme.

The threshold value is the minimum value of the criterion function set just above the background noise and nonturbulent fluctuations. Several different methods for choosing a threshold level have been proposed. Corrsin and Kistler (1955) plotted the cumulative distribution functions of the intermittency as a function of threshold value. The point of maximum curvature was then used to select the threshold value. This method worked well when the intermittency was low but was unreliable for high values of intermittency (Muck, 1980). Hedley and Keffer (1974) raised the threshold level and determined the average time duration of all the nonturbulent zones of the discrimination scheme until a constant value was reached. This process was repeated for all streamwise and cross-section locations. A similar threshold value was observed when the beginning of the constant time average duration was reached. This single value was used for all locations. However, this method is very sensitive to spurious dropouts and the smoothing procedure. Antonia (1972) set the threshold equal to a fraction (0.3) of the overall average of the function. With all these different schemes being tried what remains clear is that there is no rational method of choosing a threshold value. It is typically adjusted by trial and error until the results conform with the individual researchers expectations (Muck, 1980).

The above-mentioned investigations were performed in fully turbulent boundary layers. These same ideas are usually extended into transitional boundary layers but it remains to be verified because the flow and thermal structures in the transitional boundary layer are different from those in the turbulent boundary layer as explained previously. The work presented in this paper is a systematic investigation performed to determine the effects of different criterion functions on intermittency in a heated transitional boundary layer, to establish an adequate conditional sampling technique to separate the flow into the appropriate turbulent/nonturbulent portions, and to investigate specifically the difference between velocity and thermal intermittency if it exists. Experiments were first performed in a transitional boundary layer flow over a flat surface without a streamwise pressure gradient and followed by three cases of accelerated boundary layer at three different  $K$  values.

## Experimental Program

**Test Facility.** The test facility used in this research program consisted of a two-dimensional, open circuit, blowing type wind tunnel. The maximum air speed was 35 m/s, uniform within 0.7 percent and steady within 1 percent over a 20-hour period. An inlet airflow filter box was covered with a layer of Rayon-viscous felt capable of filtering out particles larger than 5  $\mu\text{m}$ . The free-stream air temperature was controlled by the heat exchanger and the air conditioning system in the laboratory and could be maintained within 0.5°C over a period of 20 hours and uniformly within 0.1°C. A suction fan and low-pressure plenum were installed at the leading edge to provide suction. A detailed description of the wind tunnel is provided by Kuan (1987) and Kuan and Wang (1990).

To provide the two-dimensional flow required in this investigation, the test section was designed with a large aspect ratio of 6. The test section was 0.15 m wide, 2.4 m long, and 0.92 m high consisting of a heated test wall, an outer observation wall, a top wall cover, and a bottom wall table. A composite construction was utilized for the rectangular 2.4 m  $\times$  0.92 m heated test wall. The back surface was covered with 25.4 cm of R30 fiberglass insulation to minimize back-plane conduction losses. The heating pad consisted of a

heater foil sandwiched between glass cloth and silicon rubber sheets. A 1.56-mm-thick aluminum sheet was vulcanized to the front surface of the heater pad to ensure uniformity of the heat flux. A 1.56 mm polycarbonate sheet was placed on the front surface to provide a smooth test surface on which the air flows and measurements were taken. One hundred eighty-five 3-mil E-type thermocouples were embedded beneath the test surface and were strategically placed along the test surface to capture the evolution of the wall heat transfer during the transitional flow process.

Fourteen measuring holes of 2.54 cm diameter were drilled along the centerline axis and eight measuring holes of equal diameter were drilled along the off-centerline in the cross-span direction. The first centerline measuring hole (station 1) is located 20 cm from the leading edge with the remaining measuring holes placed every 15 cm (labeled sequentially station 2 through station 14). Plexiglass plugs, flush with the inner surface, were used to plug the holes when measurements were not being taken. Slots cut into the table and the top wall provide for adjustment of the outer wall in order to vary the pressure gradient in the test section. A schematic of the thermocouple layout and the location of the profile measurement locations is shown in Fig. 1. The detailed description of the test section and heated test wall was documented by Wang et al. (1992) and Zhou (1993).

**Geometry of the Test Section.** For the baseline case, with no acceleration, the outer wall of the test section was adjusted to account for the growth of the boundary layer and to maintain a near-zero pressure distribution inside the test section with a variation of pressure coefficient,  $C_p$ , within 1 percent as shown in Fig. 2.

Three different favorable pressure gradients were utilized in this investigation. A constant pressure gradient parameter,  $K$ , was maintained during each case. One of the advantages of using a constant  $K$  over other pressure gradient parameters is that a constant  $K$  can be directly related to the geometry of the test section. By linearly decreasing the wall separation between the inlet and exit, a relatively constant  $K$  value can be obtained. For each acceleration case, the width of the test section inlet was maintained at 15.24 cm and the downstream width was arranged to decrease linearly to the exit plane. An exit width of 14.6 cm was used for the lowest acceleration case of  $K = 0.07 \times 10^{-6}$  while an exit width of 8.9 cm was used for the highest acceleration case of  $K = 0.25 \times 10^{-6}$ . The free-stream velocity distribution and pressure coefficient for each case is shown in Fig. 2. It should be noted that a constant  $K$  flow is inherently different from a Falkner-Skan flow, which has a constant  $\Lambda$  [ $\equiv (\delta^2 / v) (dU_x / dx)$ ] value. For a bounded passage flow, as in the turbine, a use of  $K$ -value to characterize the flow acceleration is more appropriate than the use of  $\Lambda$  even for situa-

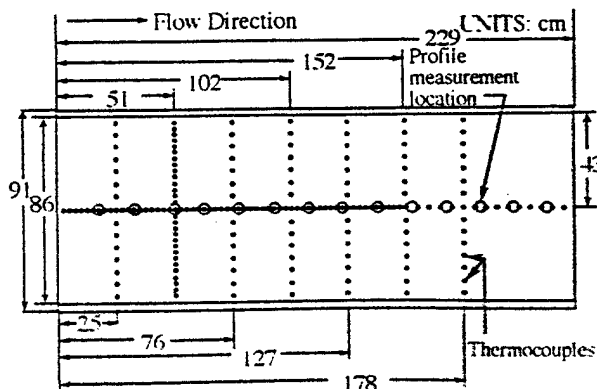


Fig. 1 Thermocouple layout on heated test wall

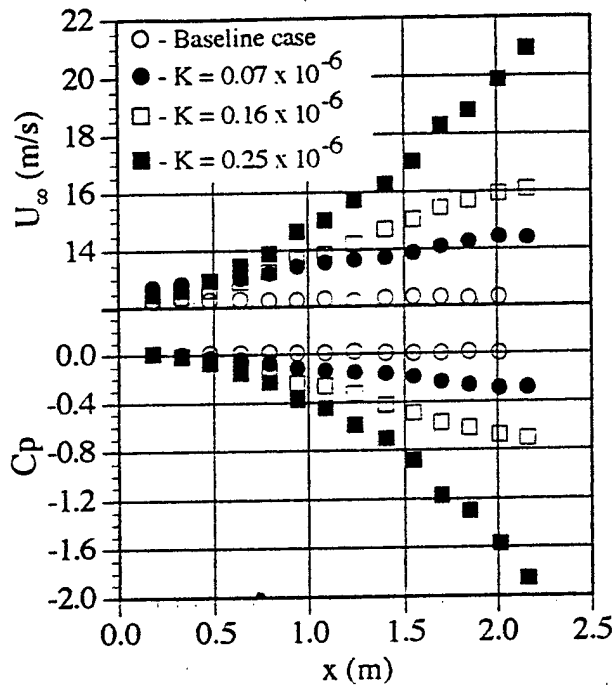


Fig. 2 Free-stream velocity and corresponding  $C_p$  values for each case

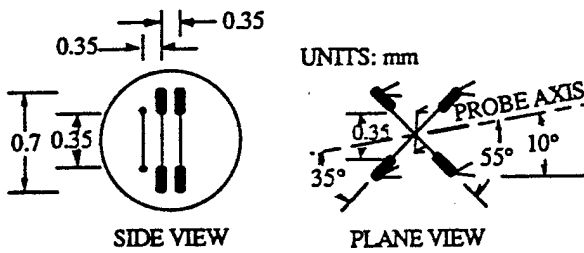


Fig. 3 Three-wire boundary layer sensor

tions with the boundary layer thickness much smaller in comparison with the passage width. Detailed explanations concerning the physical meaning of flow and thermal features of accelerated boundary layers with constant  $K$  values and the differences between a constant  $K$  and a constant  $\Lambda$  flow were made by Zhou and Wang (1992).

**Three-Wire Sensor.** A specially designed miniature three-wire probe was used to measure all the boundary layer velocity and temperature data. This sensor is similar to that used by Sohn et al. (1989). An X array, consisting of 1.0-mm-long and 2.5- $\mu\text{m}$ -dia Wollaston-type platinum-coated tungsten wires, was utilized for the velocity sensors. An active sensing length of 0.5 mm was etched in the center. The X wires were placed orthogonal to each other with a spacing of 0.35 mm. The temperature sensor is a 0.35-mm-long unplated platinum wire 1.2  $\mu\text{m}$  in diameter placed normal to the mean flow direction in a plane parallel to the plane of the cross wire and spaced 0.35 mm from the X array. This orientation for the temperature wire was chosen to eliminate any streamwise temperature gradients. Due to the difficulty in maintaining the accurate sensor arrangement during fabrication when bending the three pairs of prongs, as for a typical boundary layer type probe, the prongs were kept straight: the probe stem was bent at an angle of 10 deg from the probe axis. This angle was chosen to ensure that both of the X wires touched the wall simultaneously without interference between the probe stem and the wall (see Fig. 3). A complete description

of the probe design and qualification, specifically in a heated transitional boundary layer, can be found in Shome (1991).

**Measurements and Instrumentation.** The velocity-sensors were operated in a constant-temperature mode using a TSI model IFA 100 Intelligent Flow Analyzer. The IFA 100 allows simultaneous operation of up to four channels. A DISA M20 temperature bridge was used to operate the temperature sensor in the constant current mode. For future turbulent power and thermal power spectral analysis, TSI Model 157 signal conditioners were used to low pass filter signals from all three sensors. The X-wires of the three-wire sensor were operated at overheat ratios of 1.43 and 1.66. The 1.2  $\mu\text{m}$  temperature sensor was operated with a very low overheat ratio. The probe current was set at 0.1 mA and an amplifier gain of 3500 was used. For convenience, the velocity wires are called hot wires and the temperature wire is called cold wire in this study. The TSI IFA 100 is also equipped with a square wave generator with a frequency range of 0.3–30 kHz and amplitude range of 0–4.5 V. The square wave generator was used to optimize the frequency response of each velocity wire prior to calibration to ensure minimum under or over damping of the wire response. The optimum frequency response found for each velocity wire was approximately 200 kHz. The frequency response of the temperature sensor was experimentally determined ranging from 4800–6400 Hz depending on the velocity using the DISA M20 constant current bridge (see Wang et al., 1992, for details). The data from all three sensors were subsequently sampled at 2 kHz for 20 seconds with the low pass filter set at 1 kHz.

The wind tunnel, the test wall power supply, and the cooling water supply were started at least 12 hours prior to the experimentation. A global measurement for wall temperature distribution was performed by scanning the temperature approximately every two hours. Each time an average of three different scans, which each scan made at a sample rate of 1 channel/second, was obtained. During the measurement of each boundary layer temperature profile, a check of the steadiness of the local wall temperature was performed before, midway, and at the end of each measurement. Both the global and local check served to monitor the steadiness of the wall and the free-stream temperature. For all thermocouple measurements a Metrabyte IEEE-488 general interface I/O expansion board was used. A Fluke 8842A 5½ digit digital multimeter and a Fluke 2205A 100-channel switch controller were interfaced with the IEEE-488 board. Special low voltage scanner modules (Model 2205A-600), each with silver-coated shields, were installed in the switch controller to provide a voltage resolution of 1  $\mu\text{V}$  for thermocouple emf measurements. For each case a uniform heat flux of 335  $\text{W}/\text{m}^2$  was applied to the test wall and the free-stream temperature was maintained at approximately 15°C. The resulting wall temperatures ranged from 24°C to 41°C.

**Conditional Sampling Technique.** Conditional sampling consists of three primary stages: the choice of a criterion function, the determination of a threshold value, and the generation of an intermittency function. The determination of the threshold value and intermittency function are discussed below.

To determine the appropriate threshold value for each criteria function, a "dual-slope method" was used. This method is based on the cumulative distribution of probability density functions (PDF) used by Corrsin and Kistler (1955) and was extended by Kuan and Wang (1991). This method uses a graphic approach to find the threshold value at each location. A program was used to generate the cumulative distribution of intermittency as a function of threshold value. For each data reading, the criterion function was compared to the threshold value. If the value was greater than the

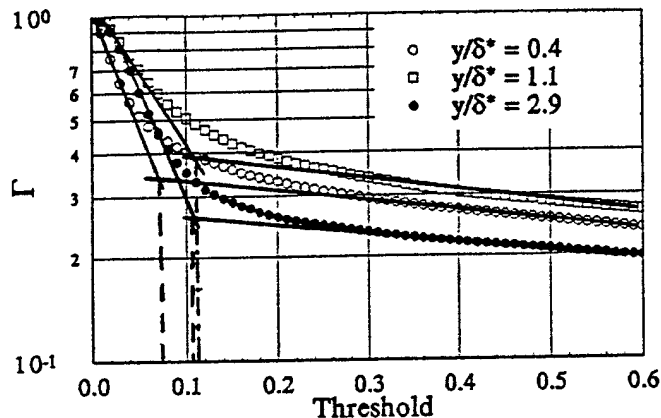


Fig. 4 Cumulative distribution of intermittency for varying threshold value ( $Re_x = 7.43 \times 10^5$  with  $d^2U/dx^2$ )

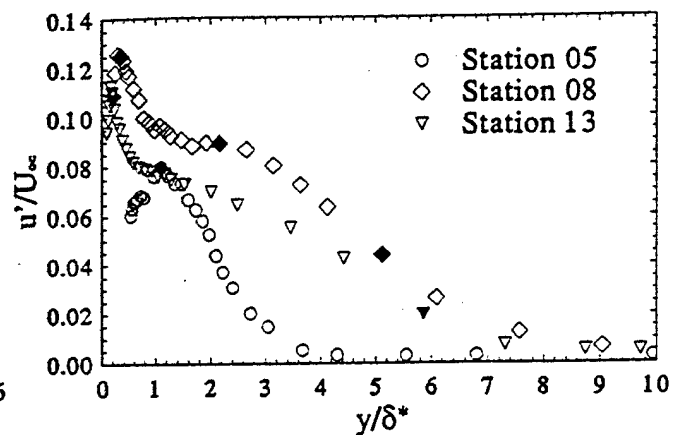


Fig. 6 Distribution of streamwise velocity fluctuations for zero-pressure gradient (shaded symbols represent points investigated)

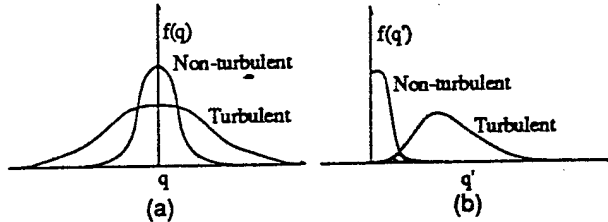


Fig. 5 (a) Possible probability density function for the turbulent and nonturbulent fluid, and (b) final probability density function (Hedley and Keffer, 1974)

threshold, the reading was considered turbulent. If the value was less than the threshold and the next two readings also less than the threshold, the reading was considered nonturbulent. Once all the readings for a given location were categorized, the final intermittency for that threshold was determined. The threshold value was then increased and the process repeated. The resulting intermittency distribution function was then plotted as shown in Fig. 4. When presented in a semi-log coordinate, two straight lines of different slopes were apparent (therefore, named dual-slope method) and the threshold value at the intersection of these two lines was taken as the initial estimate. Further refinement was required to find an optimum value. The reasoning behind this method is as follows. The background noise and fluctuations in the nonturbulent portion are close to a Gaussian probability density,  $f(q)$ . The fluctuations in the turbulent portions also have a Gaussian probability density but with a larger standard deviation (Fig. 5a). By choosing the appropriate criterion function and desensitizing it, the intersecting region of these two curves is minimized (Fig. 5b). The area of intersecting regions depends on the actual flow behaviors. An inevitable overlap region will represent the probability of indeterminable discrimination of turbulence from nonturbulence. For each threshold value 32768 ( $2^{15}$ ) data readings were processed.

After the sampled data were reduced, the intermittency function was obtained. The value of this function is 1 if the flow is turbulent and is 0 otherwise. Due to inherent spurious dropouts amidst turbulent signals, a holding time was introduced to smooth out these spurious dropouts. Hedley and Keffer (1974) suggested an optimum holding time based on the Kolmogorov length scale,  $\eta = (\nu^3/\epsilon)^{1/4}$ . The recommended holding time will be  $\eta$  divided by the convective velocity of the smallest eddies. However, the probe resolution and the digital sample rate must also be considered. The actual holding time is therefore suggested by Hedley and Keffer (1974) to be approximately 15–35 times this Kolmogorov scale. Hedley and Keffer used a value of 4 times the

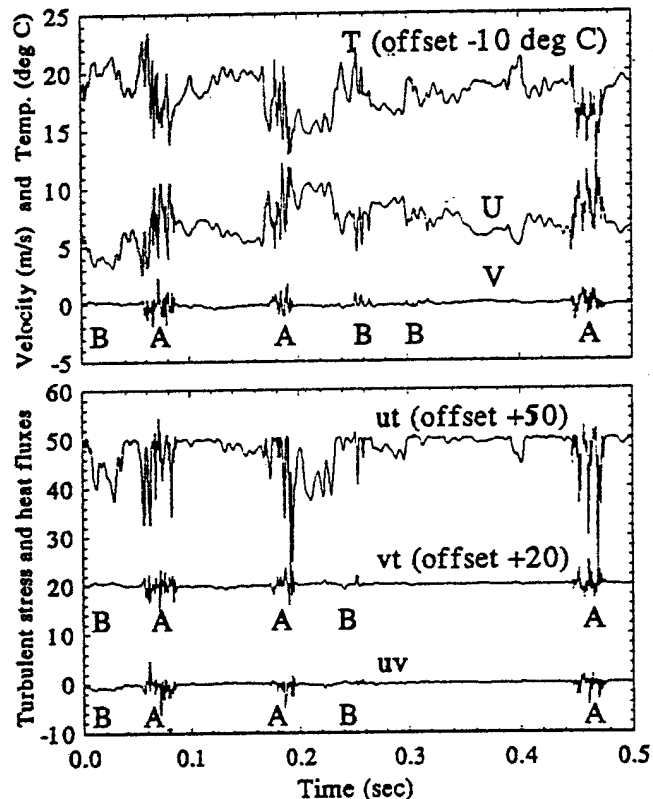


Fig. 7 Signals and correlations for  $\Gamma = 0.5$ ,  $y/\delta^* = 1.1$  (baseline case); A: clearly defined turbulent region; B: questionable region

sampling time interval, which was 0.0004 seconds. Since the eddy size in transitional flow is larger than the eddy size in a fully turbulent flow, the holding time was assigned a larger interval for the transitional flow. For this investigation, with a sample rate of 2 kHz the holding time was set equal to three sampling time intervals, which corresponds to approximately 200 times the Kolmogorov scale for the fully turbulent boundary layer (baseline case).

## Results and Discussion

**Criterion Functions.** All criterion functions were generated from the output signals of the three-wire sensor. The streamwise and cross-stream velocities ( $U$  and  $V$ ), the temperature ( $T$ ), and the corresponding correlations ( $ut$ ,  $vt$ , and

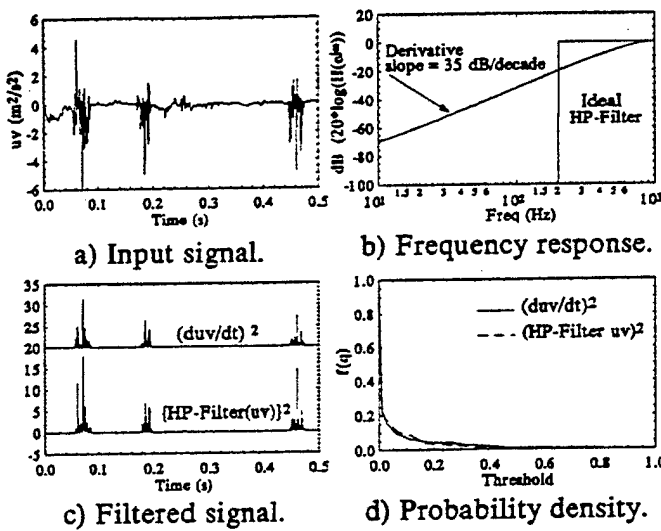


Fig. 8 Comparison of first derivative to ideal digital high-pass filter

$uv$ ) were used. Sixteen locations were investigated for the zero-pressure gradient boundary layer (baseline case). Each cross-stream location was selected based on the distribution of streamwise velocity fluctuations ( $u'$ ). Station 5 ( $Re_x = 6.13 \times 10^5$ ) was the first measuring location to indicate signs of transition in the form of turbulent bursts. A location of  $y/\delta^* = 1.2$  corresponding to the maximum peak in  $u'$  was investigated for this station. For each remaining station in the transition region, stations 6 through 8 ( $Re_x = 7.43 \times 10^5$  through  $Re_x = 9.87 \times 10^5$ ), three cross-stream locations were selected corresponding to the maximum peak in  $u'$ , the plateau region following this maximum peak, and a point near the edge of the boundary layer. For stations 9 through 13 ( $Re_x = 11.2 \times 10^5$  through  $Re_x = 16.2 \times 10^5$ ), a single location near the edge of the boundary layer was investigated. A near-wall point was also investigated for the fully turbulent boundary layer of station 13. Similar points were chosen for each pressure gradient case. Three representative  $u'$  distributions for stations 5, 8, and 13 of the baseline case and the corresponding locations of investigation are shown in Fig. 6. An example of the signals and correlations from the baseline case for station 6 with  $\Gamma = 0.5$  are shown in Fig. 7. It is apparent that turbulent/nonturbulent discrimination from the direct use of  $T$ ,  $U$ , or  $ut$  would be difficult. For  $V$ ,  $vt$ , and  $uv$  the turbulent portions are most clearly defined (labeled *A* in Fig. 7) but several questionable regions still exist (labeled *B*). The raw signals shown in Fig. 7 are inappropriate for use as criterion functions especially with the presence of unsteady oscillations in the nonturbulent portion. A means of desensitizing the signal to the nonturbulent fluctuations must be implemented. The method most commonly used is to high-pass filter the signal or to differentiate the signal with respect to time and square it, thus emphasizing the high-frequency components.

A comparison of the effects of using an ideal digital high-pass filter and taking the derivative of an example signal is shown in Figs. 8(a-d). For all differentiation throughout the analysis, a second-order central-difference technique was utilized. A 0.5 second sample of the Reynolds shear stress sampled at 2 kHz with a 1 kHz analog filter is shown in Fig. 8(a). The frequency response of the first time derivative and the ideal digital high-pass filter with a 200 Hz cutoff frequency are shown in Fig. 8(b). The first time derivative behaves as a high-pass filter with a linear phase and a frequency response with a slope of 35 dB/decade. Applying both the time derivative and the ideal digital high-pass filter

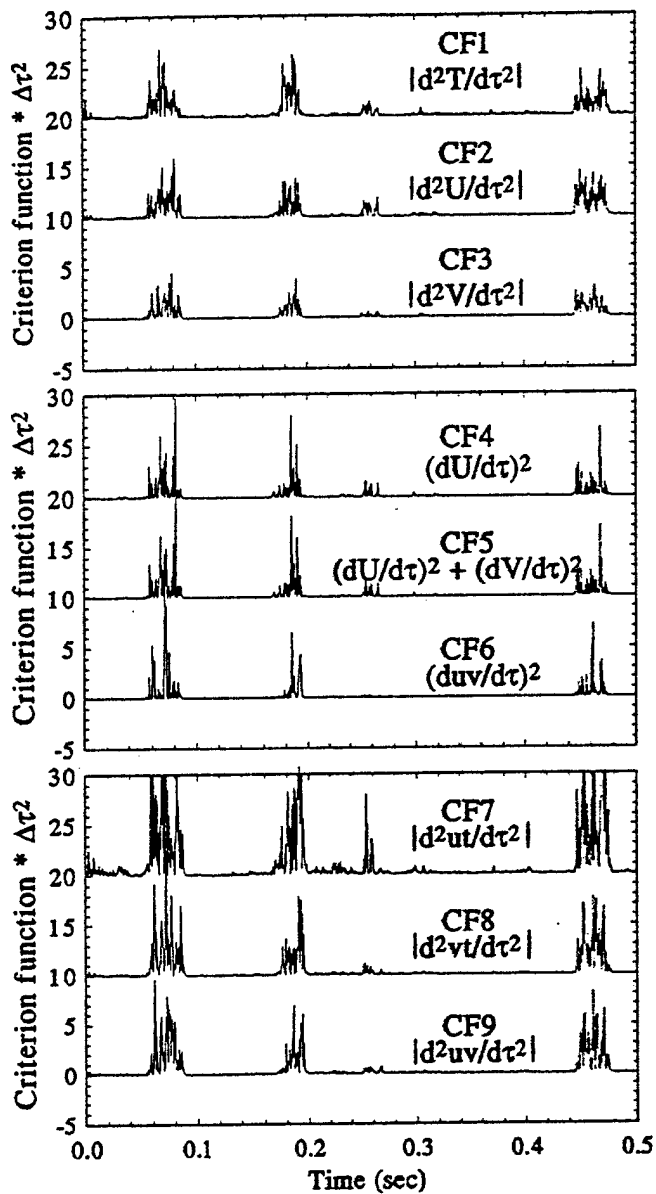


Fig. 9 Corresponding criterion functions for  $\Gamma = 0.5$ ,  $y/\delta^* = 1.1$  (baseline case)

to the signal shown in Fig. 8(a) and squaring, results in the criterion functions shown in Fig. 8(c). The resulting probability distributions for each case are indicated in Fig. 8(d). For the transitional flow signal, no significant differences are observed between using the first time derivative filter and the ideal digital high-pass filter. These results are significant for several reasons. First, using a digital filter in post-acquisition allows more flexibility than using a high-pass analog filter during acquisition. This allows for post-acquisition filter adjustment for different signals and flow conditions. Second, using a low-order derivative is easier to implement and requires less computational time than a higher order digital filter. A higher order filter requires more terms to implement in the time domain than a low-order derivative, thus increasing computational time. Implementation of an ideal digital high-pass filter must be done in the frequency domain, which requires performing an FFT and IFFT, resulting in more than an order of magnitude increase in computational time.

Nine separate criterion functions were investigated for the baseline case and the three pressure gradient cases. An example of the criterion functions investigated corresponding

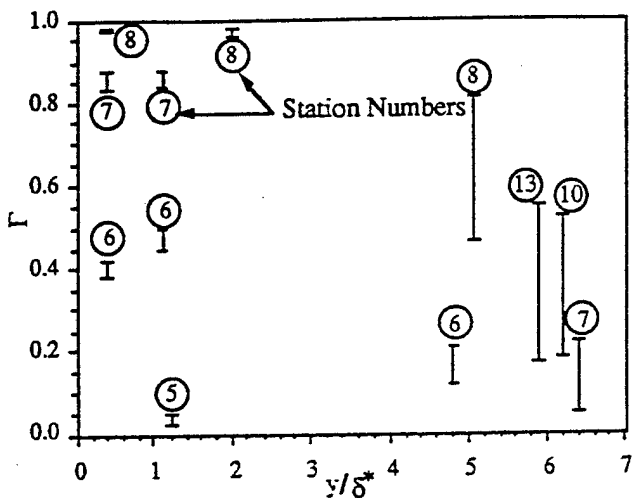


Fig. 10 Intermittency variation for different criterion functions (baseline case)

to the signals in Fig. 7 are shown in Fig. 9. Six criterion functions were based on the second derivative of the signals while three criterion functions were based on the square of the first derivative. In both these figures, 0.5 seconds of data (1000 data points) are shown from the 16.38 seconds (32768 point) record. The intermittency determined from the "dual-slope method" for each criterion function was compared to that obtained by direct observation (the eyeball method). In all cases the discrepancy between the two methods was within 5 percent. From Fig. 9 it is observed that differences in turbulence discrimination exist between the various criterion functions. A larger uncertainty is observed in using the second derivative of the streamwise Reynolds heat flux,  $d^2ut/d\tau^2$  (CF7). The demarcation between the turbulent and nonturbulent portions for this criterion function is not as pronounced as the others. This correlation could not be desensitized to low-frequency unsteadiness, resulting in several false turbulence readings. This low-frequency unsteadiness was more apparent in several of the other signals (not shown in this paper). The intermittency values obtained using criterion functions based on temperature (CF1) or a single velocity signal (CF2 through CF5) were comparable within 5 percent throughout the transition region. No advantage was gained by combining velocity signals (CF5), as recommended by Hedley and Keffer (1974). Using criterion functions based on  $uv$  (CF6 and CF9) or  $vt$  (CF8) resulted in intermittency values 0.14 to 0.38 lower in the outer boundary layer region ( $y/\delta > 4.0$ ) than the values found from the single-signal-based criterion functions. These discrepancies occurred in the late transitional and early turbulent regions (stations 8–13). The range of intermittency values determined for several locations of the baseline case are presented in Fig. 10. The large variation in the outer boundary layer is apparent. This same procedure was repeated for each pressure gradient case with similar results (Figs. 11 and 12). A complete listing of all the intermittency and threshold values for each criterion function was documented by Keller (1993). The intermittency determined for each criterion function from the "dual-slope method" was compared to the eyeball method for verification and was always within 5 percent. It is apparent from these results that near-wall intermittency values were similar regardless of the criterion function. Only in the outer boundary layer were significant differences observed. The results from using the temperature based scheme, CF1, were consistent with the results from the other single signal schemes (CF2 through CF5) for all cases investigated. No differences were found using the temperature-based criterion

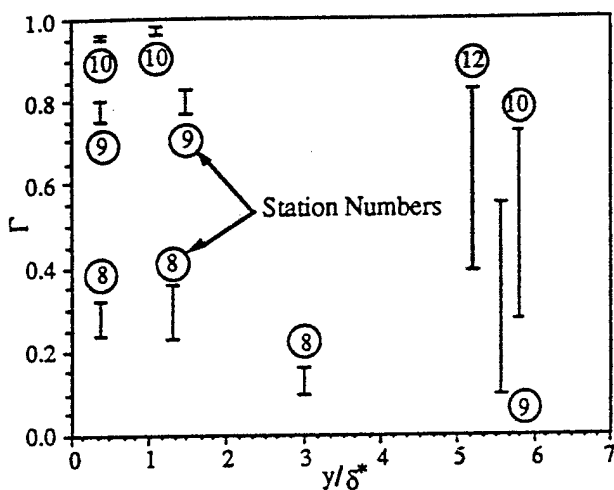


Fig. 11 Intermittency variation for different criterion functions ( $K = 0.07 \times 10^{-6}$ )

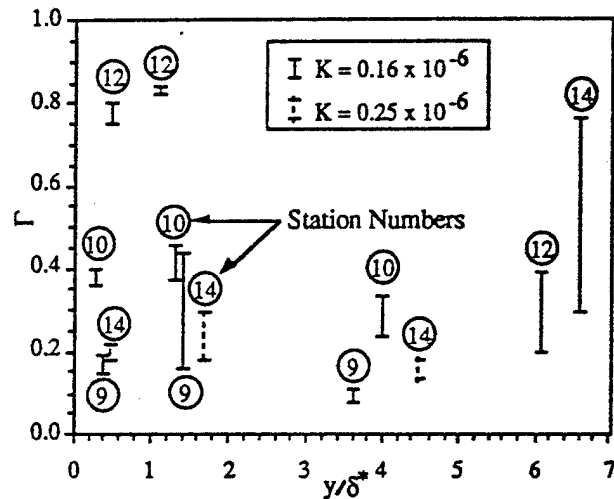


Fig. 12 Intermittency variation for different criterion functions ( $K = 0.16 \times 10^{-6}$  and  $K = 0.25 \times 10^{-6}$ )

function to support the use of separate thermal intermittency factor.

From the results above the criterion functions were divided into two groups, the single signal schemes (CF1 through CF5) and the correlation schemes (CF6 through CF9). One criterion function from each group was selected for further investigation. CF2 was chosen from the first group and CF6 from the second. Each of these criterion functions showed the greatest demarcation between the turbulent and nonturbulent portion of the flow for their respective groups. In addition, these two criterion functions are the ones most commonly used by researchers.

**Best Criterion Function.** Several factors were considered for determining which criterion function is the best choice for use in the transitional boundary layer. These factors include: (1) a sharpness in demarcation between turbulent and nonturbulent portions of the flow, (2) a small variation of threshold value throughout the transition region, (3) a low uncertainty in determining the threshold value, and (4) a low sensitivity of the resulted intermittency to the uncertainty in choosing the threshold value. A single location in the mid-transition region was selected for detailed comparison of the two chosen criterion functions. A location from station 6 for  $y/\delta^* = 1.1$  was selected. For this location, both criterion functions indicated an intermittency value of approximately 0.5.

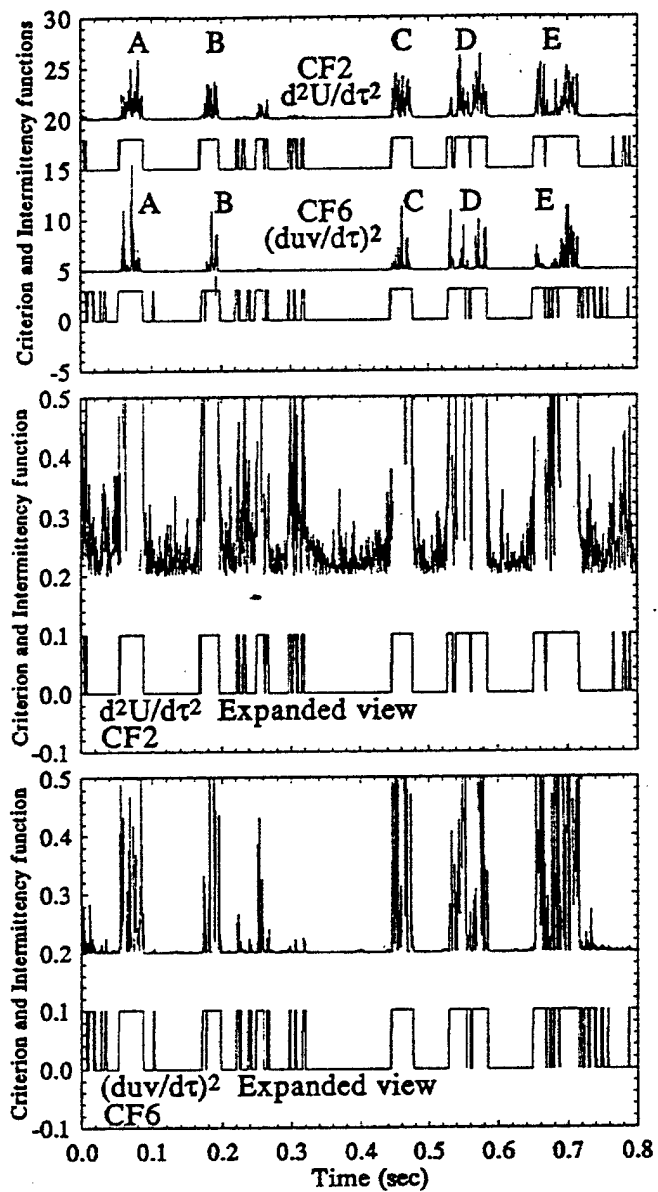


Fig. 13 Comparison of two criterion functions and corresponding intermittency functions,  $\Gamma = 0.5$ ,  $y/\delta^* = 1.1$  (baseline case)

A detailed view of the two criterion functions and the resultant intermittency function is shown in Fig. 13. The raw signals up to 0.5 seconds of Fig. 13 are previously shown in Fig. 7. Both criterion functions are of the same order of magnitude within the regions labeled A-E in Fig. 13. However, each criterion function weights different areas within each region differently. For example, for region E, CF6 indicates intense turbulent activity toward the end of the region with less turbulent activity toward the beginning of the region. CF2 indicates the turbulent activity at the beginning and end of region E is of the same order of intensity. The two different criterion functions do not recognize turbulence equivalently; inherent differences exist. It remains to determine which criterion function more accurately represents turbulence. Also shown in Fig. 13 is an expanded view of each criterion function in order to investigate the detailed structure between and within each region. While regions A-E are of the same order of magnitude, the expanded views show that the areas between these regions are not. CF6 has a much sharper demarcation between the turbulent and non-turbulent portions. This difference results in different varia-

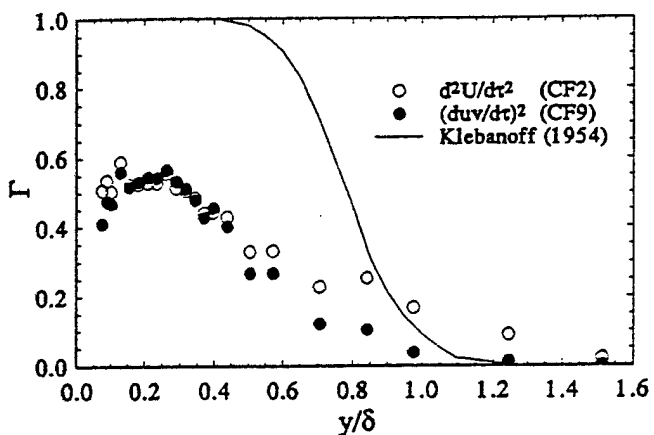


Fig. 14 Intermittency distribution through boundary layer for different criterion functions ( $Re_x = 7.43 \times 10^5$ , baseline case)

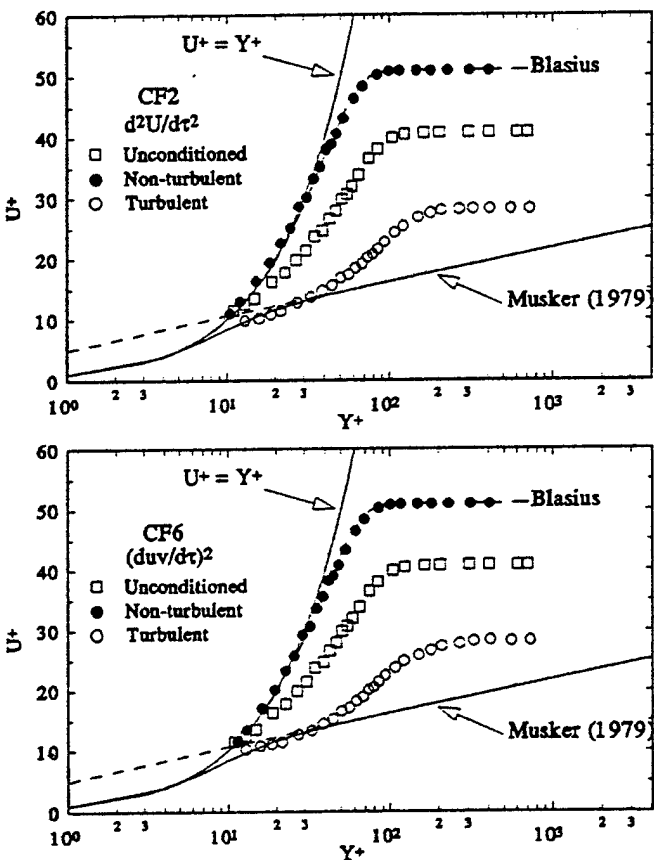


Fig. 15 Comparison of  $U^+$  versus  $Y^+$  for different criterion functions ( $Re_x = 7.43 \times 10^5$ ,  $\Gamma = 0.5$ , baseline case)

tions of threshold value throughout the transition region for each criterion function. For CF2, large variations of the threshold value occur. Typically the threshold value is the smallest very close to the wall and increases nonlinearly, asymptotically approaching a constant value near the edge of the boundary layer. An increase of 500 percent is typical. No quantitative correlation is found to describe this trend. A similar observation was made by Kuan and Wang (1989, 1990) using the same criterion function (CF2). For CF6, negligible variation in the threshold value occur in this study. The results from the "dual-slope method" consistently indicate an almost constant threshold value regardless of location. This nature of a nearly constant threshold value is especially advantageous in the outer boundary layer in the

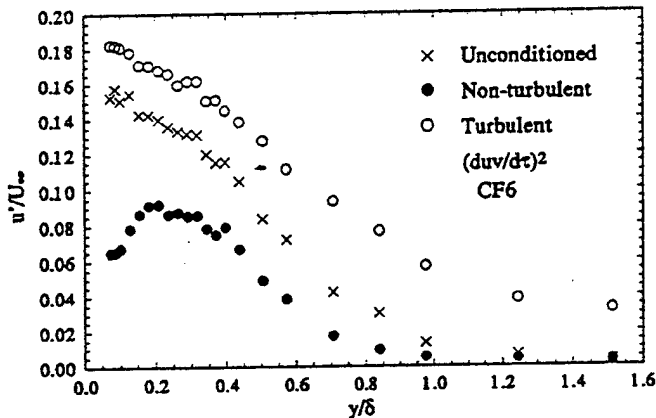
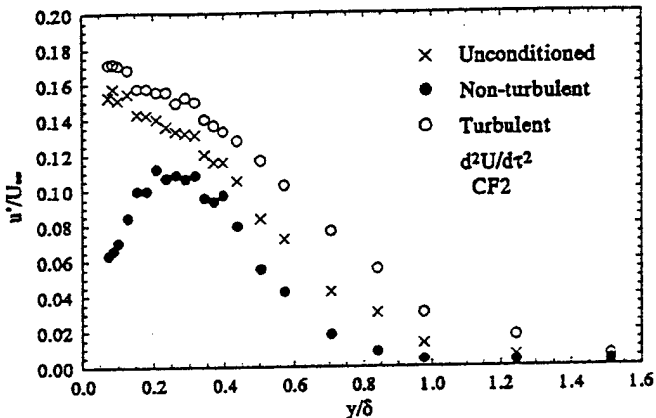


Fig. 16 Comparison of streamwise Reynolds normal stress for different criterion functions ( $Re_2 = 7.43 \times 10^5$ ,  $\Gamma = 0.5$ )

late transitional and turbulent region because the linear slope representing the Gaussian probability density distribution of the nonturbulent portion in the dual-slope diagram (Fig. 4) in these regions becomes very short and vague. The four factors previously mentioned for determining the best threshold value are best satisfied using the Reynolds shear stress. This indicates that the Reynolds shear stress is easier to implement in transitional flow and more accurately indicates the turbulent regions.

While the intermittency factor for the overall record was approximately 0.5 for both criterion functions, the intermittency functions displayed in Fig. 13 indicate that regions identified as turbulent were not the same for each criterion function. For example, region  $E$  is identified as two turbulent bursts using CF2 but was identified as two large bursts with several smaller bursts using CF6. These smaller bursts are not picked up as the turbulent portion when CF2 is used. Sometimes, using the streamwise velocity may indicate the same overall intermittency factor as the Reynolds shear stress but analysis of the turbulent and nonturbulent portions will most likely not yield the same results.

To investigate these differences further, 30 points through the boundary layer at station 6 were conditionally sampled using both criterion functions. Figure 14 shows the distribution of intermittency through the boundary layer. The discrepancy in outer boundary layer intermittency is apparent for  $y/\delta > 0.4$  with  $\Gamma$  from CF6 being consistently lower than  $\Gamma$  from CF2. For  $y/\delta < 0.4$  the intermittency values from each criterion function are nearly identical. The conditionally sampled mean velocity profiles for each criterion function are presented in  $U^+$  versus  $Y^+$  coordinates and are shown in Fig. 15. Both criterion functions result in similar profiles. The nonturbulent portions matched the Blasius profile while the turbulent portions do not exhibit the logarithmic law-of-the-

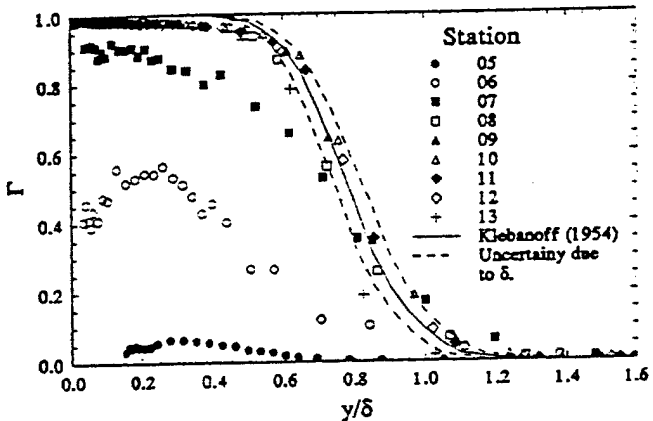


Fig. 17 Intermittency distribution through boundary layer using  $(d(uv)/d\tau)^2$ , baseline case

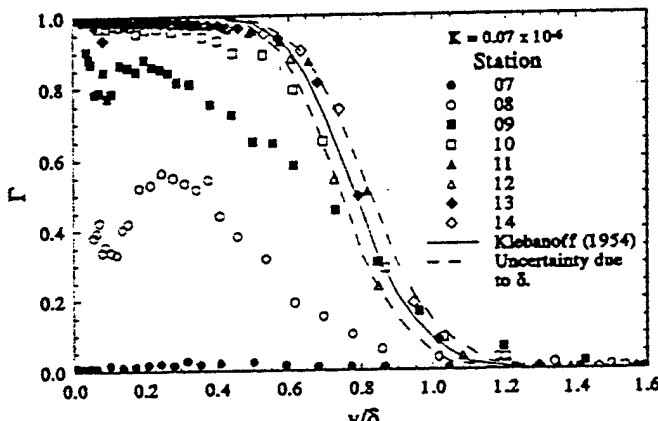


Fig. 18 Intermittency distribution through boundary layer using  $(d(uv)/d\tau)^2$ ,  $K = 0.07 \times 10^{-6}$

wall region. No differences were discernible between the abilities of each criterion function to separate the mean velocity. The conditionally sampled Reynolds normal stresses are shown in Fig. 16 where differences are seen between the results from the two criterion functions. For CF2, the peak intensity in the nonturbulent portion is 11 percent while the corresponding peak intensity for CF6 is 9 percent. Both peak intensities occur at approximately  $y/\delta = 0.3$ . The turbulent part from using CF6 indicates higher values in Reynolds normal stress than the results from using CF2. Similar results are observed for the Reynolds shear stress,  $-\bar{uv}/\bar{u}^2$  (not shown here). The criterion function using streamwise mean velocity under-evaluated the Reynolds stresses in the turbulent portion and overevaluated them in the nonturbulent portion.

**Intermittency Distributions.** Using CF6 as the best criterion function, the intermittency distribution through the transition region for each case was determined. The results are shown in Figs. 17-20. The results for a fully turbulent boundary layer obtained by Klebanoff (1954) are included for comparison. The dashed lines in each figure represent the uncertainty in determining the boundary layer thickness,  $\delta$ . The uncertainty in the mean streamwise velocity for the three-wire sensor is approximately 3 percent, which corresponds to an uncertainty in  $\delta$  of  $\pm 5$  percent. This variation in  $\delta$  results in a large variation in  $\Gamma$  for the fully turbulent profile near the edge of the boundary layer. For the baseline case, the intermittency distributions for stations 8 through 13 are seen to match the fully turbulent profile (within the uncertainty band). Station 6 exhibits a peak in intermittency

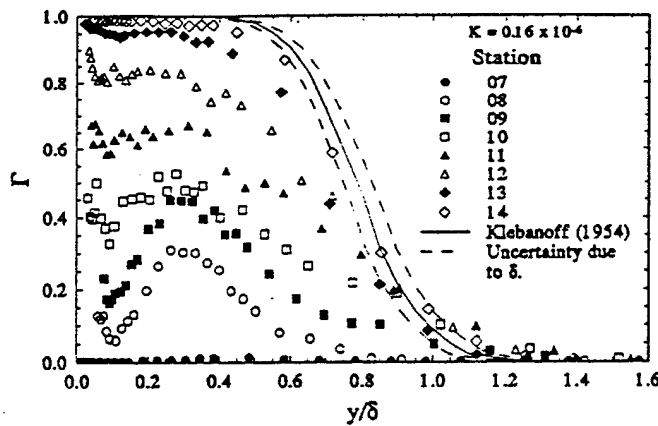


Fig. 19 Intermittency distribution through boundary layer using  $(duv/dz)^2$ ,  $K = 0.16 \times 10^{-6}$

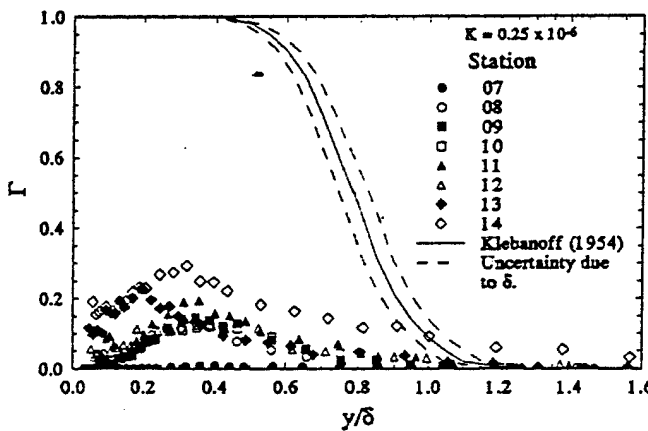


Fig. 20 Intermittency distribution through boundary layer using  $(duv/dz)^2$ ,  $K = 0.25 \times 10^{-6}$

away from the wall similar to that reported by Kuan and Wang (1989, 1990), Sohn et al. (1989), and Gostelow and Walker (1990). For the acceleration cases of  $K = 0.07 \times 10^{-6}$  and  $K = 0.16 \times 10^{-6}$  (Figs. 18 and 19, respectively), similar observations are made. In the late transitional and early turbulent regions intermittency distributions match the fully turbulent results of Klebanoff. Peak values in intermittency for the early to midtransitional regions occur away from the wall at approximately  $y/\delta = 0.3$  for all three accelerating cases. As  $K$  increases, the length of transition increases, thus allowing more stations to be measured in the transition region. For  $K = 0.16 \times 10^{-6}$  in Fig. 19, three profiles are observed to have intermittency peaks away from the wall. These peaks disappear approximately midway through the transition region. Visual inspection of the instantaneous correlation signals verifies that the frequency of breakdown increases to a maximum away from the wall then decreases toward zero in the free stream. A similar observation was made by Kuan and Wang (1990), who attributed these peaks to the overhang of a typical turbulent spot. Blair (1992) did not observe the peak in his experiment in a transitional boundary layer with a free-stream turbulent of 0.8 percent and  $K = 0.2 \times 10^{-6}$ . However, he reported observing a near-wall minimum and a peak at about  $y/\delta = 0.3$  in the intermittency distribution in higher turbulence cases (1.9 and 2.5 percent). Mayle (1991) pointed out the controversy on the peak in intermittency distribution across the boundary layer and attributed it to the differences in the turbulent flow discrimination schemes used to determine intermittency. As early as 1958, Dhawan and Narasimha concluded that al-

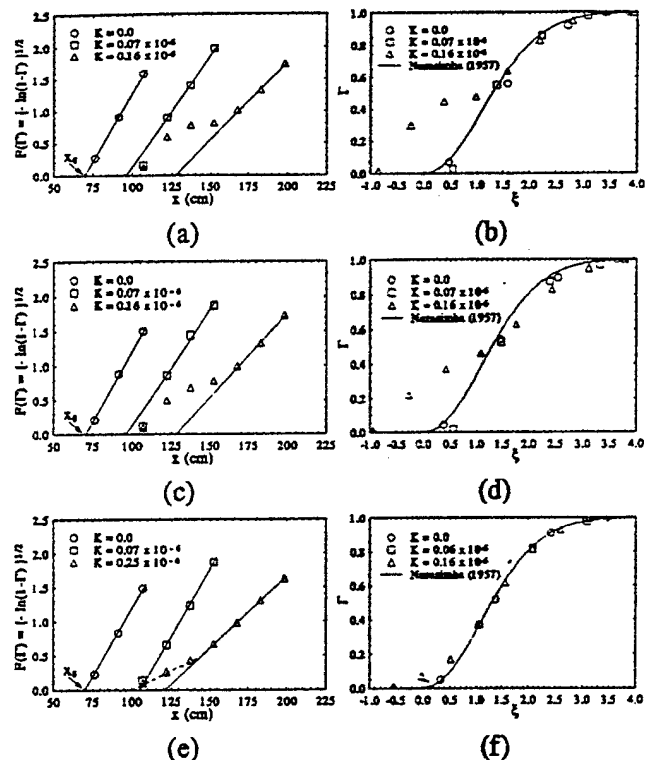


Fig. 21 Determination of  $x_s$  and corresponding representative near wall intermittency in  $\Gamma$  versus  $x$  coordinates using the value of  $\Gamma$  at different  $y/\delta$  locations as the representative intermittency

though the  $\Gamma(y)$  variation is probably important to the detailed structure of the turbulent motion associated with the turbulent spots, the value near the wall is the characteristic property for the transition region. These authors believe the peak intermittency at about  $y/\delta = 0.3$  in the early to middle transitional boundary layer is real and it reflects the stretching of a turbulent spot away from the wall. This vortex stretching is a very important part of the vortex dynamics during the early transitional process.

The general appearance of the intermittency distribution across the boundary layer of an accelerated flow is very similar to that of a nonaccelerated flow; however, a distinctive near-wall minimum exists at about  $y/\delta = 0.1$  for most of the stations even as late as  $\Gamma = 0.9$  (Figs. 18 and 19). The intermittency value increases at a clear trend toward the wall from this minimum, which is not observed in the baseline case in Fig. 17. For the strongest accelerating case,  $K = 0.25 \times 10^{-6}$ , the intermittency distributions for stations 8 to 11 are almost identical (see Fig. 20). This implies a strong suppression of the growth of turbulent spots. The transition process for this case is not completed at the exit of the test section of the current facility.

To find the intermittency factor,  $\Gamma(x)$ , through the transition region, the method first developed by Dhawan and Narasimha (1958) was used. Dhawan and Narasimha proposed a "universal" intermittency distribution of the form

$$\Gamma(x) = 1 - \exp[-0.412(x - x_s)/\xi^2]$$

where

$$\xi = x_{\Gamma=0.75} - x_{\Gamma=0.25}$$

The applicability of using this technique in boundary layer flows subjected to pressure gradients was discussed by Narasimha et al. (1984).

To determine the start of transition,  $x_s$ , the following

procedure is taken following their recommendations. The function  $\sqrt{-\ln(1 - \Gamma(x))}$  is plotted versus  $x$  and a straight line fit to the data between  $0.25 < \Gamma < 0.75$ . The  $x$  intercept is  $x_s$ . An appropriate value of  $\Gamma(x)$  to represent the intermittency at each  $x$  location must still be determined in light of the nonuniform distribution of intermittency across the boundary layer. Mayle (1991) stated that most researchers who use anemometers to determine the intermittency typically chose the near-wall value to be around  $y/\delta = 0.2$ . In order to look into this issue, three locations were chosen for the selection of the representative intermittency value,  $\Gamma(x)$ : the location of the intermittency peak (approximately  $y/\delta = 0.3$ ), the value at  $y/\delta = 0.2$  as suggested by Mayle, and the value at the local minimum near the wall ( $y/\delta \approx 0.1$ ) for using the peak value of intermittency (note: since the flows for  $K = 0.25 \times 10^{-5}$  never completed transition in the

present facility they are excluded from further discussion). For  $K = 0.16 \times 10^{-5}$ , only the results for  $\Gamma(x) > 0.6$  followed a linear relation when plotted in  $F(\Gamma)$  versus  $x$  coordinates. The representative intermittency distribution obtained from these results are shown in Fig. 21(b). Too large a deviation from the universal distribution is observed for  $K = 0.16 \times 10^{-6}$  to justify using the peak value in  $\Gamma$ . This procedure was repeated for the intermittency values obtained at  $y/\delta = 0.2$  and the results are shown in Figs. 21(c) and 21(d). The representative intermittency distribution still shows a large variation from the correlation of Dhawan and Narasimha (1958). The results using the values of intermittency obtained from the minimum near the wall ( $y/\delta \approx 0.1$ ) are shown in Figs. 21(e) and 21(f). For  $K = 0.16 \times 10^{-6}$ , two linear regions of different slopes are present in the  $F(\Gamma)$  versus  $x$  coordinate similar to the results of Narasimha et al. (1984) and Blair (1992). Narasimha (1985) termed this sudden change in flow behavior "subtransition," indicating the flow changes from a subcritical to a supercritical state. The near-wall intermittency distribution is seen to match the "universal" distribution of Dhawan and Narasimha with slightly higher values for  $K = 0.16 \times 10^{-6}$  in the early transition region. Acharya (1985) and Blair (1992) measured the streamwise distribution of boundary layer intermittency for flows with  $K > 0$  and both reported a similar observation. The results of the near-wall intermittency distributions indicate that in order to match the correlation of Dhawan and Narasimha (1958), the near-wall value of intermittency at  $y/\delta \approx 0.1$  should be used instead of at  $y/\delta \approx 0.2$  suggested by Mayle (1991).

## Conclusions

The effects of different criterion functions on the determination of intermittency were investigated for application in heated transitional boundary layers with and without streamwise acceleration. Nine separate criterion functions were investigated for the zero-pressure gradient baseline case and three constant  $K$ , accelerated cases. The criterion functions were classified into two general categories: single signal schemes, those based in  $U$ ,  $V$ , and  $T$ , and correlation schemes, those based on  $uv$ ,  $vt$ , or  $ut$ . For the baseline case, criterion functions based on the correlation schemes resulted in intermittency values 0.14 to 0.38 lower in the outer boundary layer region ( $y/\delta^* > 4.0$ ) than the values found from the single signal schemes. Similar differences were found for the accelerated cases. No differences were found using the temperature-based criterion function to support the use of a separate thermal intermittency factor in accelerated flows.

Inherent differences exist between each criterion function's turbulence recognition capabilities. Each criterion function weights different areas within a turbulent burst differently. No differences were discernible between the abilities of each

criterion function to separate the mean velocity; however, the results of using single-signal schemes tended to underevaluate the Reynolds stresses in the turbulent portion and overestimate them in the nonturbulent portion. A criterion function based on Reynolds stress,  $(\partial u v / \partial \tau)^2$ , resulted in the sharpest demarcation between turbulent and nonturbulent portions of the flow. This criterion function also had a negligible variation of threshold value throughout the transition region with the lowest uncertainty in determining the threshold value and the lowest sensitivity of the resultant intermittency to the variation of the threshold value. These results indicate that using the Reynolds shear stress for turbulent/nonturbulent discrimination in a heated transitional boundary layer is superior to a single velocity or temperature scheme. A criterion function based on the streamwise velocity,  $(\partial U / \partial \tau)^2$ , results in "near-wall" intermittency values within 5 percent of the values obtained from using  $(\partial u v / \partial \tau)^2$  and may be easier to implement since only a single-wire probe is required. However, this criterion function has a higher uncertainty in determining the threshold value and has a higher sensitivity of the resultant intermittency to the variation of the threshold value. In addition, using the streamwise velocity may indicate the same overall intermittency factor as the Reynolds shear stress but analysis of the turbulent and nonturbulent portions would not always yield the same results.

Peak values in intermittency for the early to midtransitional regions were found to occur away from the wall at approximately  $y/\delta = 0.3$  for the baseline case and three accelerated cases. A distinctive near-wall minimum in intermittency and a clear trend of increasing values of intermittency toward the wall from this minimum were observed for the accelerating flow cases. To match the universal intermittency distribution of Dhawan and Narasimha (1958), the values of intermittency at this near-wall minimum  $y/\delta \approx 0.1$  should be used as the representative "near-wall" values.

Using a digital time derivative is considered superior for use as a criterion function to an ideal digital high-pass filter since no significant differences are observed between the two methods in determining the probability densities of a transitional flow and the derivative requires less computational time.

## Acknowledgments

This program was sponsored by the Air Force Office of Scientific Research (Grant No. AFOSR-89-0324) and the Office of Naval Research (Grant No. N00014-89-J-3105). The program monitors are Major Dan Fant and Dr. Gabriel Roy, respectively.

## References

- Acharya, M., 1985, "Pressure-Gradient and Free-Stream Turbulence Effects on Boundary Layer Transition," *Brown Boveri Report KLR 85-127 C*.
- Antonia, R. A., 1972, "Conditionally Sampled Measurements Near the Outer Edge of a Turbulent Boundary Layer," *J. Fluid Mech.*, Vol. 56, pp. 1-18.
- Antonia, R. A., 1981, "Conditional Sampling in Turbulence Measurement," *Ann. Rev. Fluid Mech.*, pp. 131-156.
- Arnal, D., 1984, "Description and Prediction of Transition in Two-Dimensional, Incompressible Flow," *AGARD-R-709*, 2-1.
- Blair, M. F., 1982, "Influence of Free-Stream Turbulence on Boundary Layer Transition in Favorable Pressure Gradients," *ASME Journal of Engineering for Power*, Vol. 104, pp. 743-750.
- Blair, M. F., 1992, "Boundary Layer Transition in Accelerating Flows With Intense Freestream Turbulence; Part 1—Disturbances Upstream of Transition Onset, Part 2—The Zone of Intermittent Turbulence," *ASME Journal of Fluids Engineering*, Vol. 114, pp. 313-322.
- Chen, C. P., and Blackwelder, R. F., 1976, "Large-Scale Motion in a Turbulent Boundary Layer: A Study Using Temperature Contamination," *J. Fluid Mech.*, Vol. 89, part 1, pp. 1-31.

Corrsin, S., and Kistler, A. L., 1955, "Free-Stream Boundaries of Turbulent Flows," NACA Rept. 1244.

Dhawan, S., and Narasimha, R., 1958, "Some Properties of Boundary Layer Flow During the Transition From Laminar to Turbulent Motion," *J. Fluid Mech.*, Vol. 3, pp. 418-436.

Emmons, H. W., 1951, "The Laminar-Turbulent Transition in a Boundary Layer—Part I," *J. Aero. Sci.*, Vol. 18, pp. 490-498.

Gostelow, J. P., and Walker, G. J., 1990, "Similarity Behavior in Transitional Boundary Layers Over a Range of Adverse Pressure Gradients and Turbulence Levels," *ASME JOURNAL OF TURBOMACHINERY*, Vol. 113, pp. 617-625.

Graham, R. W., 1979, "Fundamental Mechanisms That Influence the Estimate of Heat Transfer to Gas Turbine Blades," *ASME Paper No. 79-HT-43*.

Graham, R. W., ed., 1984, *Transition in Turbines*, Symposium Proceedings, NASA TM-79128.

Hedley, T. B., and Keffer, J. F., 1974, "Turbulent/Nonturbulent Decisions in an Intermittent Flow," *J. Fluid Mech.*, Vol. 64, Part 4, pp. 625-644.

Keller, F. J., 1993, "Flow and Thermal Structures in Heated Transitional Boundary Layers With and Without Streamwise Acceleration," Ph.D. Dissertation, Dept. of Mech. Engr., Clemson University, Clemson, SC.

Klebanoff, P. S., 1954, "Characteristics of Turbulence in a Boundary Layer With Zero Pressure Gradient," NACA Technical Note #1247, supersedes NACA TN#3178.

Kuan, C. L., 1987, "An Experimental Investigation of Intermittent Behavior in the Transitional Boundary Layer," M.S. Thesis, Dept. of Mech. Engr., Clemson University, Clemson, SC.

Kuan, C. L., and Wang, T., 1989, "Some Intermittent Behavior of Transitional Boundary Layer," *AIAA Paper No. 89-1890*.

Kuan, C. L., and Wang, T., 1990, "Investigation of Intermittent Behavior of Transitional Boundary Layer Using a Conditional Averaging," *Exp. Thermal Fluid Sci.*, Vol. 3, pp. 157-170.

Mayle, R. E., 1991, "The Role of Laminar-Turbulent Transition in Gas Turbine Engines," *ASME JOURNAL OF TURBOMACHINERY*, Vol. 113, pp. 509-537.

Muck, K. C., 1980, "Comparison of Various Schemes for the Generation of the Turbulent Intermittency Function," IC AERO Report 80-03.

Musker, A. J., 1979, "Explicit Expression for the Smooth Wall Velocity Distribution in a Turbulent Boundary Layer," *ALAA Journal*, Vol. 17, No. 6, June, pp. 655-657.

Narasimha, R., 1957, "On the Distribution of Intermittency in the Transition Region of a Boundary Layer," *J. Aero. Sci.*, Vol. 24, pp. 711-712.

Narasimha, R., Devasia, K. J., Gururani, G., and Badri Narayanan, M. A., 1984, "Transitional Intermittency in Boundary Layers Subjected to Pressure Gradient," *Experiments in Fluids* 2, pp. 171-176.

Narasimha, R., 1985, "The Laminar-Turbulent Transition Zone in the Boundary Layer," *Prog. Aerospace Sci.*, Vol. 22, pp. 29-80.

Sharma, O. P., 1987, "Momentum and Thermal Boundary Layer Development on Turbine Airfoil Suction Surfaces," *AIAA Paper No. 87-1918*.

Shome, B., 1991, "Development of a Three-Wire Probe for the Measurement of Reynolds Stresses and Heat Fluxes in Transitional Boundary Layers," M.S. Thesis, Dept. of Mech. Engr., Clemson University, Clemson, SC.

Sohn, K. H., O'Brien, J. E., and Reshotko, E., 1989, "Some Characteristics of Bypass Transition in a Heated Boundary Layer," NASA TM 102126.

Turner, A. B., 1971, "Local Heat Transfer Measurements on a Gas Turbine Blade," *J. Mech. Engr. Sci.*, Vol. 13, No. 1, pp. 1-12.

Volino, R. J., and Simon, T. W., 1991, "A Review of Bypass Transition in Boundary Layers," *NASA CR-187187*.

Wang, T., Keller, F. J., and Zhou, D., 1992, "Experimental Investigation of Reynolds Shear Stresses and Heat Fluxes in a Transitional Boundary Layer," *Fundamental and Applied Heat Transfer Research for Gas Turbine Engines*, ASME HTD-Vol. 226, pp. 61-70.

Zhou, D., and Wang, T., 1992, "Laminar Boundary Layer Flow and Heat Transfer With Favorable Pressure Gradient at Constant K Values," *ASME Paper No. 92-GT-246*.

Zhou, D., 1993, "Flow and Thermal Structures in Heated Transitional Boundary Layers With Elevated Free-Stream Turbulence and Pressure Gradients," Ph.D. Dissertation, Dept. of Mech. Engr., Clemson University, Clemson, SC.

If you are planning  
To Move, Please  
Notify The  
ASME-Order Dep't  
22 Law Drive  
Box 2300  
Fairfield, N.J. 07007-2300

Don't Wait!  
Don't Miss An Issue!  
Allow Ample Time To  
Effect Change.

**Change of Address Form for the Journal of Turbomachinery**  
**Present Address—Affix Label or Copy Information from Label**

Print New Address Below

Name			
Attention			
Address			
City	State or Country	Zip	



The Society shall not be responsible for statements or opinions advanced in papers or discussion at meetings of the Society or of its Divisions or Sections, or printed in its publications. Discussion is printed only if the paper is published in an ASME Journal. Authorization to photocopy material for internal or personal use under circumstance not falling within the fair use provisions of the Copyright Act is granted by ASME to libraries and other users registered with the Copyright Clearance Center (CCC) Transactional Reporting Service provided that the base fee of \$0.30 per page is paid directly to the CCC, 27 Congress Street, Salem MA 01970. Requests for special permission or bulk reproduction should be addressed to the ASME Technical Publishing Department.

Copyright © 1997 by ASME

All Rights Reserved

Printed in U.S.A.

## INTERMITTENT FLOW AND THERMAL STRUCTURES OF ACCELERATING TRANSITIONAL BOUNDARY LAYERS, PART 1: MEAN QUANTITIES

Ting Wang and F. Jeffrey Keller\*

Department of Mechanical Engineering  
Clemson University  
Clemson, South Carolina, U.S.A.

### ABSTRACT

A conditional sampling technique was employed to separate the turbulent and non-turbulent parts of accelerated boundary layers undergoing laminar-turbulent transition on a uniformly heated flat plate. Tests were conducted with zero pressure gradient and two levels of streamwise acceleration parameter:  $K=0.07 \times 10^{-6}$  and  $0.16 \times 10^{-6}$

The conditionally sampled distribution of the skin friction coefficients revealed that the values for  $C_f$  in the non-turbulent and turbulent portions significantly deviated from the respective laminar and turbulent correlations. These deviations increased as acceleration increased. Reconstructing the local average  $C_f$  values using the laminar and fully turbulent correlations consistently overestimated the unconditioned  $C_f$  values. Using the conditionally sampled data for reconstructing  $C_f$  values provided better results, but does not necessarily result in the same unconditioned  $C_f$  values.

The mean velocity profiles from the turbulent portions had the appearance of a low-Reynolds-number turbulent boundary layer with a large wake region. In the late transition region, as acceleration increased, the wake region in the turbulent portion was suppressed relative to the unconditioned result. The integral parameters,  $\delta^*$ ,  $\theta$ , and shape factor,  $H$  were conditionally sampled and analyzed.

### NOMENCLATURE

$C_f$	- skin friction coefficient, $\tau_w / (\rho \bar{U}_\infty^2 / 2)$
$C_p$	- $\frac{P - P_{ref}}{\frac{1}{2} \rho U_\infty^2}$
$H$	- shape factor, $\delta^* / \theta$
$K$	- pressure gradient parameter, $\frac{v}{U_\infty^2} \frac{d\bar{U}_\infty}{dx}$
$P_{ref}$	- Reference pressure at Station 1

\*F.J. Keller is currently working at Accuracy Microsensors, Inc.  
Pittsford, New York.

$\bar{T}$	- mean temperature
$u_\tau$	- friction velocity, $\sqrt{\tau_w / \rho}$
$\bar{U}$	- mean velocity
$U^+$	- $\bar{U} / u_\tau$
$x$	- coordinate in streamwise direction
$x_s$	- at onset of transition
$y$	- coordinate normal to the surface
$y^+$	- $y u_\tau / v$
Greek	
$\delta$	- boundary layer thickness at 0.995 $U_\infty$
$\delta^*$	- displacement thickness
$\varepsilon_M$	- turbulent (or eddy) viscosity
$\Gamma$	- intermittency factor
$v$	- kinematic viscosity
$\theta$	- momentum boundary layer thickness
$\rho$	- density
$\tau_w$	- shear stress on the wall
$\infty$	- free-stream value

### INTRODUCTION

A better understanding of momentum and thermal transport during the laminar-turbulent transition process is one of the key factors toward improving the prediction of the thermal load on gas turbine blades (Graham, 1979 and 1984, Mayle, 1991). Transition from laminar to turbulent boundary layer flow significantly increases the local wall shear stresses and the convective heat transfer rates. These increases must be appropriately factored into the design of gas turbine blades, since as much as 50 to 80% of the surface of a typical turbine blade is commonly covered by flow undergoing transition (Turner, 1971). A recent 4-part paper by Halstead, et al. (1995) specifically pointed out, through rotating multistage tests, the importance of laminar-turbulent transition in axial compressors and turbines. In the newest heavy-frame industrial H-type Advanced Gas Turbine Systems (Farmer and

Presented at the International Gas Turbine & Aeroengine Congress & Exhibition  
Orlando, Florida — June 2–June 5, 1997

This paper has been accepted for publication in the Transactions of the ASME  
Discussion of it will be accepted at ASME Headquarters until September 30, 1997

Fulton, 1995), adoption of closed-loop steam cooling eliminates the need for conventional air film cooling in the first two stages; therefore, correct prediction of the laminar-turbulent transition becomes more essential. An unsatisfactory prediction of the location and streamwise coverage of transition on gas turbine blades can result in either reduced longevity and reliability of the blade or reduced engine performance below design objectives. For example, Graham (1979) shows that a  $56^{\circ}\text{C}$  error in temperature prediction can result in an order-of-magnitude decrement in vane life.

One of the undeniable features in the laminar-turbulent transition is the intermittent behavior between non-turbulent and turbulent flows. Among many different transitional flow models, the intermittency model (Dhawan and Narasimha, 1958) is always physically more realistic than any other model, since the actual transitional flow is intermittent. For the purpose of engineering practice, statistical measurements of flow and thermal structures in this intermittent heat flow play an important role in improving understanding of fundamental aspects of flow mechanisms, as well as contributing to the database and methodologies of prediction models. In non-accelerated flows, Kuan and Wang (1990) and Kim et al. (1994) have pointed out that the turbulent part of the transitional flow is different from the fully-developed turbulent flow, and the non-turbulent part is not an extension of the upstream laminar flow. Blair (1992) investigated the intermittent flow in accelerating transitional boundary layers. He concluded that the turbulence kinetic energy within the turbulent parts exceeded fully turbulent boundary layer levels. He also conducted spectral analysis for the turbulent parts of flow and observed that the ratio of dissipation to production increased through transition. Sohn et al. (1989) analyzed conditionally-sampled transitional flow for various FSTI cases and concluded that the transport processes occurring in the turbulent spots will not be well modeled by standard turbulence models used in equilibrium turbulent boundary layers. Solomon, Walker, and Gostelow (1995) incorporated the linear-combination method with a calculation method that continuously adjusts the spot growth parameters in response to the changes in the local pressure gradient through transition. The results showed reduced sensitivity to errors in predicting the onset of transition. Therefore, providing the information regarding the individual flow and thermal characteristics of the non-turbulent and turbulent parts, respectively, of the transitional flows is indispensable for the intermittency model, for example, the model proposed by Steelant and Dick (1996), and the linear-combination integral boundary layer method presented by Dey and Narasimha (1988).

In gas turbine through-flows, the accelerated boundary layers typically occur in the transition pieces downstream of the combustor, near the leading edge of the suction side of the blades, and near the aftbody of the pressure side of the blades. The effects of streamwise favorable pressure gradients on the flow and thermal structures of unconditionally sampled transitional flow have been reported by Keller and Wang (1996). This paper will present conditionally sampled results of the same flows.

The objectives of this paper are (a) to investigate the intermittent flow and thermal structures of the transitional boundary layers (b) to study the effects of streamwise acceleration on the intermittent behavior of these structures (c) to provide a database for transitional flow modeling, and (d) to provide information for future studies in elevated free-stream conditions (Wang and Zhou, 1997).

## EXPERIMENTAL PROGRAM

The detailed experimental facility, instrumentation, data acquisition and experimental procedures have been documented by Wang et al. (1992). Therefore, only a brief description of the experimental program will be provided.

**Wind Tunnel.** The present study employed a 2-D, open circuit, blowing-type wind tunnel, as shown in Fig. 1. The flow rate could be adjusted from 0.5 to 35 m/s. The steadiness of the free-stream velocity and temperature could be maintained, respectively, within 1% and  $0.5^{\circ}\text{C}$  for a 24-hour period; the uniformity was within 0.7% and  $0.1^{\circ}\text{C}$ .

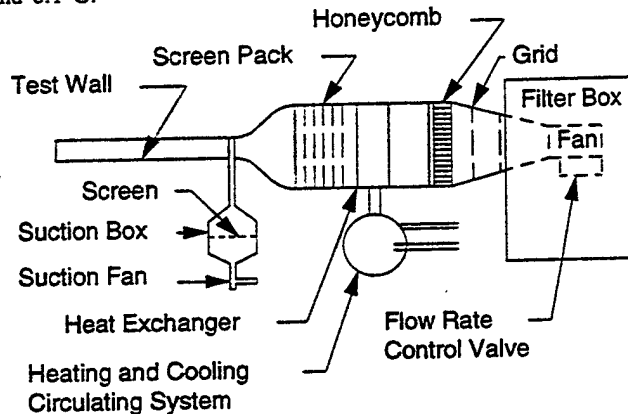


Fig. 1. Wind Tunnel Test Facility

**Test Section.** The rectangular test section was 0.15 m wide, 2.4 m long and 0.92 m high with an aspect ratio of 6. This large aspect ratio reduced edge effects and ensured two-dimensionality of the boundary layer flow in the center span of the test section. One of the test section walls served as the test wall. The heat patch inside the test wall was constructed of a serpentine heater foil sandwiched between glass cloth and silicon rubber sheets. The surface temperature was measured by 184 76-mm (3-mil) E-type thermocouples embedded between the heater and the plexiglass surface. Fourteen measuring holes were drilled along the center line of the outer observation wall. Measurements were obtained by traversing probes through the holes into the test section. The spacing between the centerline thermocouples was 2.54 cm (1 inch), and the spacing between the measuring holes was 15.24 cm (6 inches). Boundary layer suction was applied at the leading edge of the test section.

The outer observation wall was manipulated to achieve constant-K flows. Three different cases were conducted in the present study: Baseline ( $K=0$ ),  $K1 = 0.07 \times 10^{-6}$  and  $K2 = 0.16 \times 10^{-6}$ . The pressure coefficient distributions are shown in Fig. 2. The detailed geometry of the test section was described in Keller and Wang (1996).

**Instrumentation and Data Reduction.** A single hot wire and a three-wire sensor were used in this study. The single hot wire was used to measure each station before using the 3-wire sensor. Since the single wire can measure very close to the wall (approximately  $Y^+=2$ ), the results of the single wire were used to guide the 3-wire sensor to locate the wall position ( $y=0$ ) and to determine the skin friction.

The three-wire sensor was specifically designed to simultaneously measure the two velocity components and the

temperature. Basically, the three-wire sensor consisted of an X-array of gold-plated tungsten wires for measuring velocities and a 1.2- $\mu\text{m}$  platinum wire for measuring temperature. The two X-wires were operated in constant temperature mode. The 1.2- $\mu\text{m}$  platinum wire was operated at a very low current of 0.1 mA (cold wire) in the constant current mode.

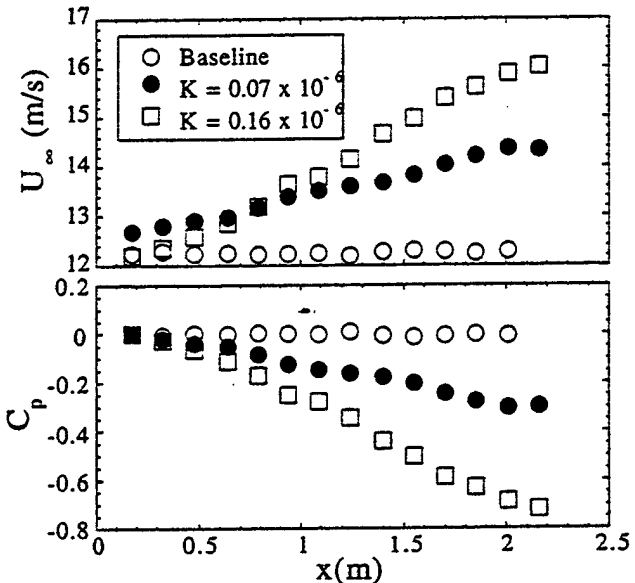


Fig 2. Free-stream velocity and corresponding  $C_p$  values for each case.

A TSI Model IFA 100 Intelligent Flow Analyzer System was used as a constant temperature anemometer. A DISA M20 temperature bridge was used for operating the cold wire in the constant current mode. A 12-bit A/D data acquisition board and a high-speed data acquisition software, STREAMER, were used to acquire data. The sampling rate was 2 KHz, and the sampling duration was 20 seconds. For more detailed description of the 3-wire sensor, see Shome (1991) or Wang and Keller (1996).

#### DETERMINATION OF SKIN FRICTION COEFFICIENT AND WALL POSITION

The skin friction coefficient,  $C_f$ , is an important parameter for characterizing the boundary layers since it changes significantly from laminar to turbulent through the transition region. Direct measurement of  $C_f$  is difficult, expensive and time consuming, not suitable for the heated wall, and may not be fast enough to sense the instantaneous wall shear stress change of the turbulent spots. However, with the information from the mean velocity profiles, the following can be indirectly determined, based on the nature of the boundary layer:

- In the non-turbulent part, the mean velocity varies linearly with distance from the wall in the near-wall region. The values of  $\Delta U/\Delta y$  from several mean velocity data points close to the wall were measured by the single wire and used to approximate the velocity gradient at the wall to calculate  $C_f$ .
- In the turbulent part, the mean velocity gradient near the wall is so large that the linear approximation of mean velocity

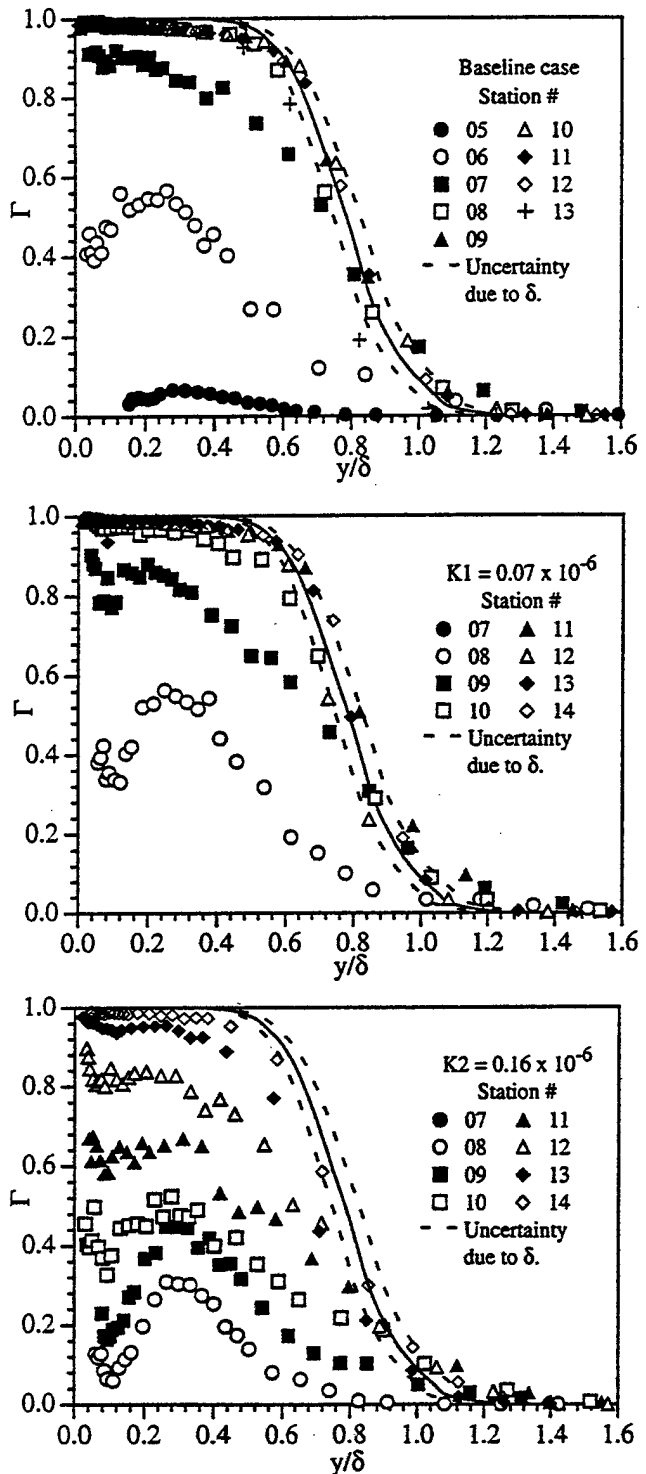


Fig 3. Intermittency distributions through boundary layers.

gradient near the wall may lead to a large error. The Clauser technique (Clauser, 1956) was used instead to estimate the value of  $C_f$  and the wall position by the best fitting of  $U^+$

falling within the log-linear region. Some subjectivity was exercised to determine the "best fit," since the slope of the log-linear region varies as  $K$  changes.

## CONDITIONAL SAMPLING TECHNIQUE

Conditional sampling consists of three primary stages: the choice of a criterion function, the determination of a threshold value, and the generation of an intermittency function. In turbulent/non-turbulent discrimination, one commonly used method for identifying a criterion function is to differentiate the velocity signal with respect to time and square it, thus emphasizing the high frequency components. As pointed out by Keller and Wang (1995), performing the differentiation procedure was actually equivalent to conducting a digital high pass filtering. They also indicated that using the Reynolds shear stress,  $uv$ , as the criterion function for turbulent/non-turbulent discrimination in a heated transitional boundary layer is superior to the scheme of using single velocity or temperature as the criterion function. They indicated that using  $uv$  signals as the criterion function possesses the following merits: (a) sharpness in demarcation between the turbulent and non-turbulent portions of the flow, (b) small variation of threshold values across the boundary layer and throughout the transition region, (c) low uncertainty in determining the threshold values, and (d) low sensitivity of the resultant intermittency to the uncertainty in choosing the threshold value. Therefore, squares of the first derivatives of the  $uv$  signal were used in this study as the criterion function.

From each data reading, the criterion function was compared to the threshold value. If the value was larger than the threshold, the reading was considered turbulent. If the value was less than the threshold and the next three readings (i.e., hold time) were also less than the threshold, the reading was considered non-turbulent. The value of the intermittency function was equal to 1 if the flow was turbulent; the value was 0 if the flow was non-turbulent. The intermittency distributions for each case are shown in Fig. 3. A single intermittency value at about  $y/\delta = 0.1$  was selected as the representative for each station. Keller and Wang (1995) has shown that using near-wall intermittency values at about  $y/\delta = 0.1$  best matches the universal intermittency distribution (Dhawan and Narasimha, 1958) in streamwise direction. Representative velocity signals are presented in the Appendix.

The threshold value was determined based on the cumulative intermittency distribution curve originally introduced by Hedley and Keffer (1974). An improved "dual-slope" method based on the cumulative intermittency distribution curve was developed by Kuan and Wang (1990). This curve represents the variation of the integral of the probability density function (PDF) as the threshold value increases from zero. This method uses a graphical approach to find the threshold value at each location. Based on this method, two straight lines of different slopes are apparent most of the time when the cumulative intermittency distribution is plotted on a semi-log coordinate with the threshold value. The different slopes are caused by the different characteristics of probability density distributions for the turbulent and non-turbulent part, respectively. A steeper slope represents the non-turbulent part, which indicates smaller standard deviation. The approximate threshold value is then taken to be the value corresponding to the intersection of the straight lines. Fine tuning can be made to make the overall distribution of intermittency factors smooth. The reasoning behind this method and the detailed analysis of using nine different criterion functions for conditionally sampling the heated, accelerating flows, were discussed by Keller and Wang (1995). It

should be noted that in the "real" gas turbine environment, the flow is highly disturbed by periodic wakes, a clear discrimination between turbulent patches and non-turbulent parts becomes difficult.

## RESULTS AND DISCUSSION

The test conditions and the onset and end of transition are shown in Table 1. The unconditionally sampled results were previously analyzed by Keller and Wang (1996). The measurement locations located in the transitional region for each case were conditionally sampled. Flow and thermal structures of four stations for the baseline case, four stations for the K1 case, and seven stations for the K2 case were separated into turbulent and non-turbulent parts.

	Baseline	$K1=0.07 \times 10^{-5}$	$K2=0.16 \times 10^{-5}$	
FSTI at $x_s$	0.5	0.4	0.4	
$U_{\infty}$ (m/s) at Sta.1 ( $x = 18$ cm)	12.24	12.68	12.20	
Onset of transition	$x(\text{cm})$ $Re_x$ $Re_{\delta^*}$ $Re_{\theta}$	68 $5.50 \times 10^5$ 1294 492	107 $9.46 \times 10^5$ 1322 541	115 $10.3 \times 10^5$ 1233 544
End of transition	$x(\text{cm})$ $Re_x$ $Re_{\delta^*}$ $Re_{\theta}$	137 $11.2 \times 10^5$ 1826 1302	168 $15.7 \times 10^5$ 1874 1282	213 $21.7 \times 10^5$ 1880 1235
Length of transition	$x(\text{cm})$ $Re_x$ $Re_{\delta^*}$ $Re_{\theta}$	69 $5.70 \times 10^5$ 532 810	61 $6.24 \times 10^5$ 552 741	98 $11.4 \times 10^5$ 647 691

Table 1. Test Conditions for the Baseline ( $K=0$ ) and Two Accelerating Case

**Skin-Friction Coefficient.** The conditionally sampled distributions of the  $C_f$  values for the baseline case and the accelerating cases are shown in Fig. 4. The  $C_f$  values from the original unconditioned results are included for comparison.

For the baseline case, the non-turbulent  $C_f$  values follow the laminar correlation up through station 06 ( $\Gamma = 0.50$ ). Beyond this mid-transition point, the non-turbulent  $C_f$  values show progressive deviation from the laminar correlation. For station 08 ( $\Gamma = 0.98$ ), the last transitional station, the non-turbulent  $C_f$  value exceeds the laminar correlation by 65%. For the turbulent portion, a reverse trend occurs. Significant deviation from the fully turbulent correlation is observed in the early transition regions and the  $C_f$  value approaches the fully turbulent correlation as transition ends. A similar observation was made by Kuan and Wang (1990) and Kim et al. (1994) for the zero-pressure gradient flat plate case. Kuan and Wang reported that the  $C_f$  values in the non-turbulent portion were significantly greater than the laminar correlation throughout the transition region, and  $C_f$  values in the turbulent part were approximately 6% higher than the turbulent correlation. For the accelerating cases K1 and K2, a similar trend is observed. The  $C_f$  values follow the laminar values obtained from the STAN5 program up through  $\Gamma = 0.37$  for both cases and then begin to deviate. As the  $K$  value increases, the deviation from the laminar values in the late transition stage is not as large as is observed in the baseline case. The  $C_f$  values for the turbulent portions deviate significantly from the turbulent correlation in the early transition region and

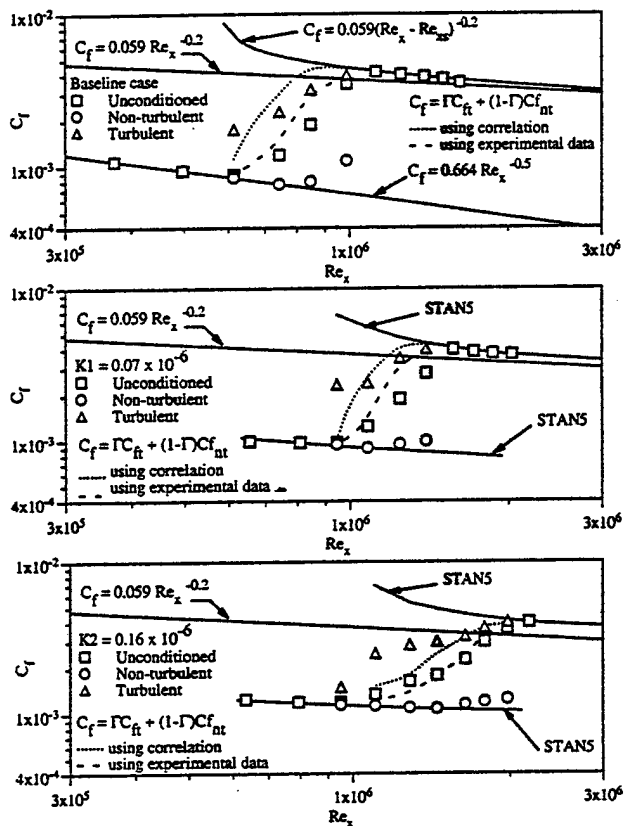


Fig. 4. Comparison of the reconstructed skin-friction coefficient values by using the intermittency model with the conditionally sampled experimental data versus the values from laminar and fully-turbulent correlations. Data presentation starts at station 3.

approach the turbulent correlation as the transition process proceeds. Also shown in Fig. 4 are the results for reconstructing the unconditioned  $C_f$  values using the local near-wall intermittency with (a) the respective laminar and turbulent correlations and (b) the conditionally sampled experimental data.

Using the laminar and turbulent correlations to obtain a local overall  $C_f$  value, as is done in intermittency weighted transitional flow analysis, consistently overestimates the experimentally determined unconditioned  $C_f$  values. This result indicates that the skin friction in the non-turbulent and turbulent portions do not behave as a simple extension of laminar and fully turbulent flow, respectively. Reconstructing total  $C_f$  using the conditionally sampled experimental data provides better results than using the fully turbulent and laminar correlations but does not necessarily result in the original unconditioned  $C_f$  values. This is not surprising since a single representative near-wall intermittency was used in the reconstruction formula for each  $x$ -location while the local  $\Gamma(y)$  value, which varied with  $y$ , was used in separating the velocity data. This result may indicate that a single near-wall intermittency value may not adequately represent the characteristic property for the transition region, and that the  $\Gamma(y)$  variation may play an important role. Regarding the issue of  $\Gamma(y)$  variation, Dhawan and Narasimha (1958) stated that although the  $\Gamma(y)$

variation was probably important to the detailed structure of the turbulent motion associated with the spots, the near-wall value was the characteristic property for the transition region. Nevertheless, with the complexity involved in the transition flow, using a single  $\Gamma$  at each  $x$ -location to represent the evolution of the transition process is an important first step in transition modeling. If a single  $\Gamma$  is to be selected, Keller and Wang (1995) suggested the intermittency value at  $y/\delta=0.1$  would be appropriate. Other opinions about the selection of a single representative intermittency value were discussed by Professor M.W. Johnson in Gostelow and Blunden's paper (1988).

**Integral Parameters.** A large uncertainty exists in determining boundary layer thickness and integral parameters for the conditionally sampled portions. For the early transition region, low intermittencies provide very few turbulent values for analysis. This results in a large scatter of the data. Similarly, in the late transition region, high intermittencies provide very few non-turbulent values for analysis. The largest uncertainty occurs in the turbulent portions. As the edge of the boundary layer is approached, the intermittency drops off rapidly, resulting in fewer turbulent readings. This results in a larger scatter in the velocity profile in the outer boundary layer at the turbulent portion. Therefore, determination of the boundary layer thickness, displacement thickness, and momentum thickness is more uncertain for the turbulent portion than for the non-turbulent portion. The results for each of the three cases are shown in Fig. 5 through 7. For each case, the displacement thickness for the non-turbulent portion exhibits little deviation from the unconditioned values. For the turbulent portion,  $\delta^*$  is consistently greater than the unconditioned values. Evaluation of the momentum thickness confirms that a higher momentum loss is associated with the turbulent portion of the flow. As  $K$  increases, significant deviation of these parameters, including the shape factor, from the unconditioned data occurs. This raises further questions about the applicability of treating each portion in the boundary layer as an extension of their respective laminar and fully turbulent counterparts.

**Mean Velocity and Temperature Profiles.** The conditionally sampled velocity profiles for the baseline case are shown in Figure 8. The velocity profiles for the non-turbulent part follow the Blasius profile up through station 06. In the late transition region, stations 07 through 08, the non-turbulent profiles follow the viscous sublayer relation ( $U^+ = Y^+$ ) very well in the inner boundary layer, up to approximately  $Y^+ = 30$ , but deviate from the Blasius profile in the outer layer. This deviation from the Blasius profile apparently affects the wall shear and explains why the  $C_f$  values increasingly deviate from the laminar correlation as transition proceeds. Kim et al. (1994) hypothesized that this higher stress at the wall was due to disturbances in the nonturbulent region as a result of the passage of turbulent spots. Transition at the leading edge of a turbulent spot is abrupt; however, at the trailing edge the flow slowly relaxes back to the non-turbulent value through the calmed region. For a high intermittency, turbulent spots pass frequently and the non-turbulent portion is continually disturbed which results in higher velocity gradients near the wall thus increasing the skin friction above the laminar value. Another phenomenon, which is present in the non-turbulent portion and may result in a higher skin friction, is the amplification of sinusoidal oscillations. Both of these behaviors are observed in instantaneous velocity traces, which exhibit the

slow relaxation period (calmed region) after the passage of a turbulent spot and the presence of amplified oscillations between spots. The turbulent profiles for stations 06 through 08 have the appearance of a low-Reynolds-number turbulent boundary layer

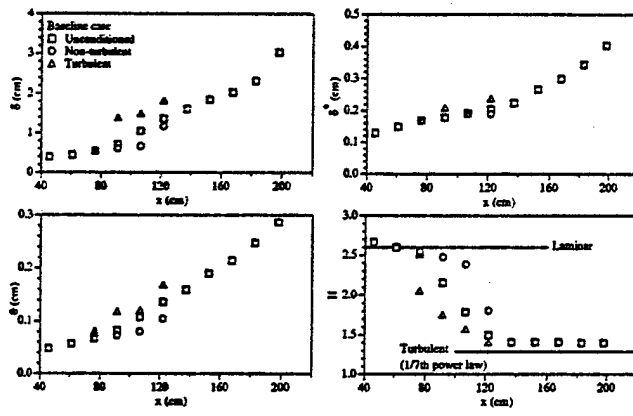


Fig. 5 Conditionally sampled boundary layer integral parameters for the baseline case.

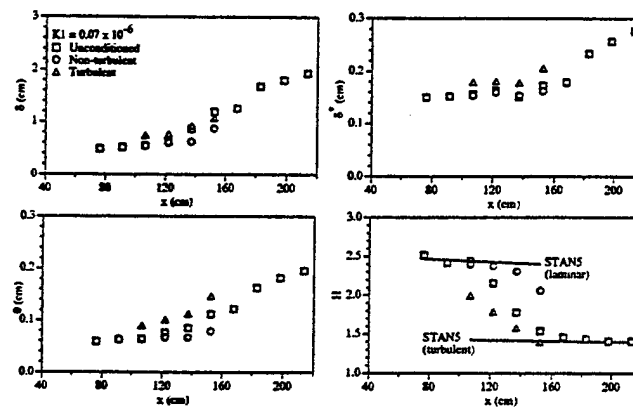


Fig. 6 Conditionally sampled boundary layer integral parameters for the K1 case.

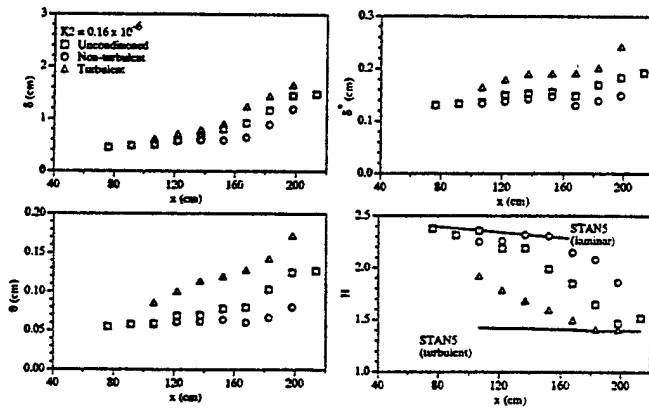


Fig. 7 Conditionally sampled boundary layer integral parameters for the K2 case.

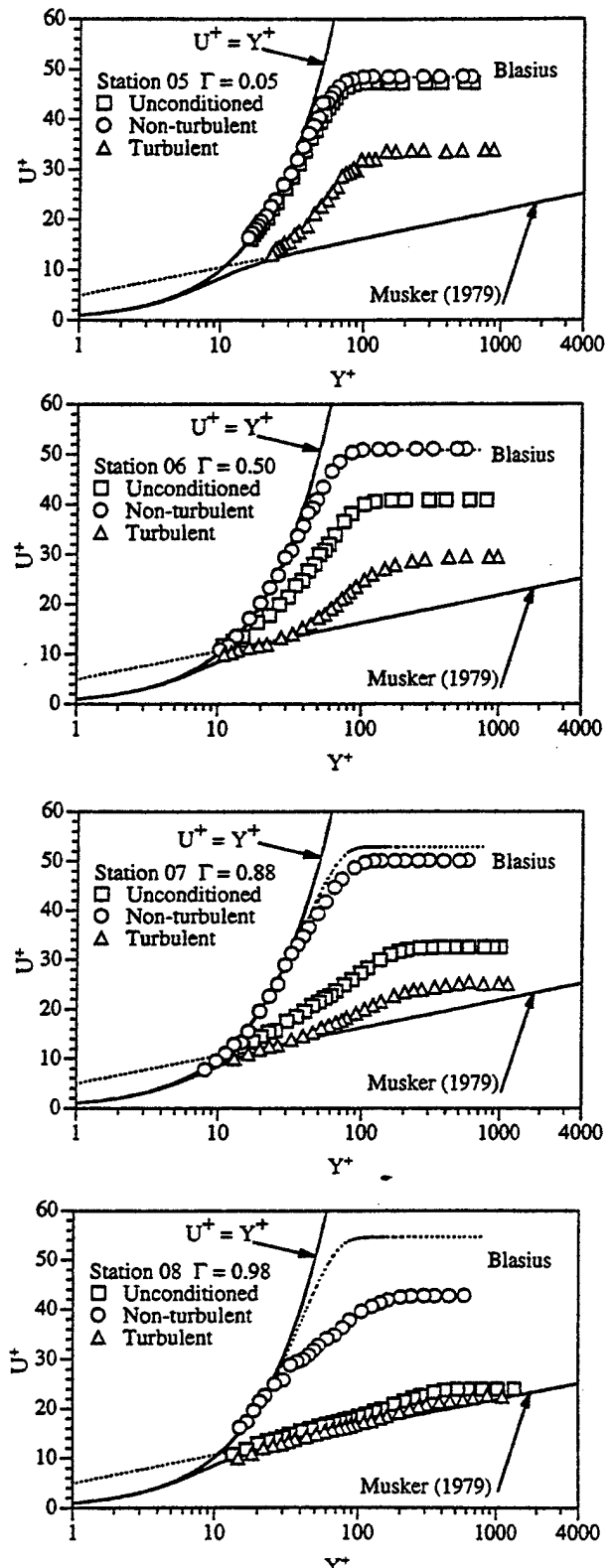


Fig. 8 Conditionally sampled mean velocity profiles for the baseline case (in wall units).

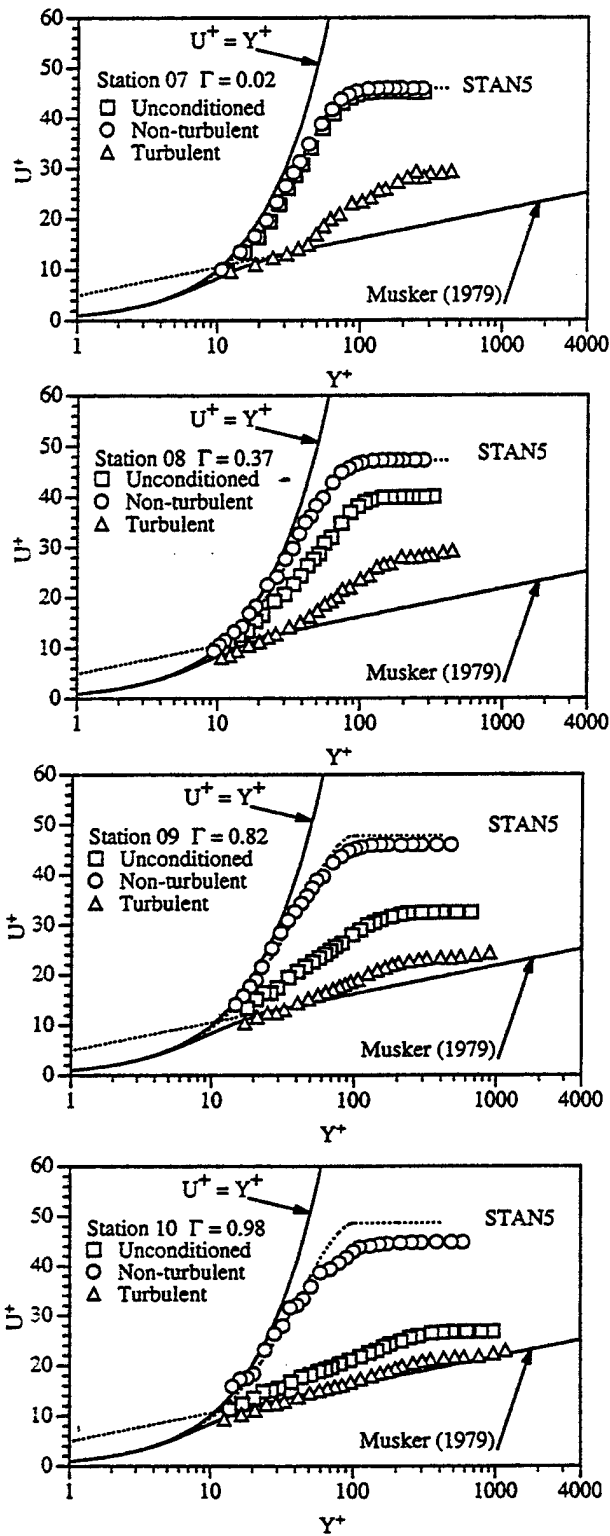


Fig 9. Conditionally sampled mean velocity profiles for the K1 case (in wall units).

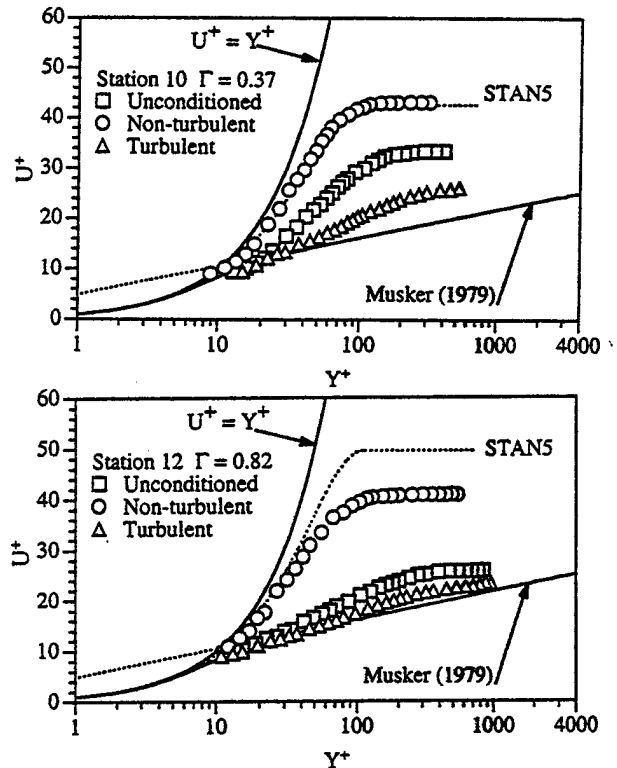


Fig. 10 Conditionally sampled mean velocity profiles for the K2 case.

with a short linear-log region and a large wake region. However, the turbulent profile of station 08 exhibits a depressed wake region. A similar observation for the mean velocity profiles was made by Kuan and Wang (1990), Kim et al. (1994), and Sohn and Reshotko (1991).

The mean velocity profiles for the accelerating case K1 are shown in Fig. 9 through 10. The results are similar to those observed for the baseline case. The non-turbulent velocity profiles follow the profiles obtained from the STAN5 program for the early transition region, up through  $\Gamma = 0.37$ . In the late transition region, the non-turbulent profiles follow the STAN5 laminar profile very well in the inner boundary layer, but deviate from the laminar profile in the outer layer. Standard  $k-\epsilon$  turbulence model with a correction of damping coefficient due to acceleration (Lauder and Spalding, 1974) is used in the STAN5 calculation. The turbulent profiles also have the appearance of a low-Reynolds-number turbulent boundary layer with a large wake region. In the late transition region, as  $\Gamma$  increases, the non-turbulent portion deviates more from the corresponding laminar profile, and the turbulent portion moves more close to the fully-turbulent profile, as can be seen by comparing station 9 in Fig. 9 and station 12 in Fig. 10 both have the same intermittency factor, 0.82.

Conditional sampling of the mean temperature profiles were difficult to present in  $T^+$  versus  $Y^+$  coordinates. As a turbulent spot passes over the test surface, the surface temperature begins to immediately change, but the thermocouples, embedded beneath the test surfaces, were not able to respond to the fast passing turbulent spots, which had a duration from 10 ms to 50 ms. Therefore, the conditionally sampled mean temperature profiles are not presented in this paper. However, the thermal structure in the boundary layer will be presented in Part 2 of this paper.

## CONCLUSION

A conditional sampling technique was employed to separate the turbulent and non-turbulent parts of accelerated boundary layers undergoing laminar-turbulent transition on a uniformly heated flat plate. Tests were conducted with zero pressure gradient and two levels of streamwise acceleration:  $K = 0.07 \times 10^{-6}$  and  $0.16 \times 10^{-6}$ . The results are summarized below.

- The values for  $C_f$  in the non-turbulent and turbulent portions significantly deviated from the respective laminar and turbulent correlations. These deviations reduced as acceleration increased.
- Reconstructing the local average  $C_f$  values using the laminar and fully turbulent correlations consistently overestimated the experimentally determined unconditioned  $C_f$  values. Using the conditionally sampled data for reconstructing  $C_f$  values provided better results, but does not necessarily result in the same unconditioned  $C_f$  values.
- The mean velocity profiles from the turbulent portions had the appearance of a low-Reynolds-number turbulent boundary layer with a large wake region. In the late transition region, as acceleration increased, the wake region in the turbulent portion was suppressed relative to the unconditioned result.
- For each case, the displacement thickness for the non-turbulent portion exhibited little deviation from the unconditioned values. For the turbulent portion, the displacement was consistently greater than the unconditioned values.
- Evaluation of the conditionally sampled momentum thickness confirmed that the higher loss of momentum in the transition region than the corresponding laminar flow was a direct result of the turbulent portion of the boundary layer.

## ACKNOWLEDGEMENT

This research was sponsored by the Air Force Office of Scientific Research (Grant No. F49620-94-1-0126). The program manager was Dr. James McMichael.

## REFERENCES

Blair, M.F., 1992, "Boundary-Layer Transition in Accelerating Flows with Intense Free-Stream Turbulence : Part 1-Disturbances Upstream of Transition Onset; Part 2-The Zone of Intermittent Turbulence," ASME Journal of Fluids Engineering, Vol. 114, pp. 313-332.

Clauser, F.H., 1956, "The Turbulent Boundary Layer," Advances in Applied Mechanics, Vol. 4, pp. 1-51.

Dey, J. and Narasimha, R., 1988, "An Integral Method for the Calculation of 2-D Transitional Boundary Layers," Fluid Mechanics Report 88 FM 7, Indian Institute of Science, Bangalore.

Dhawan, S. and Narasimha, R. 1958, "Some Properties of Boundary Layer Flow During the Transition From Laminar to Turbulent Flow," Journal of Fluid Mechanics, Vol. 3, pp. 418-436.

Farmer, R. and Fulton, K. 1995, "Design 60% Net Efficiency in Frame 7/9 H Steam-Cooled CCGT," Gas Turbine World, May-June, pp. 12-22.

Gostelow, J.P. and Blunden, A.R., 1988, "Investigations of Boundary Layer Transition in an Adverse Pressure Gradient," ASME J. of Turbomachinery, Vol. 111, pp. 366-375.

Graham, R.W., 1979, "Fundamental Mechanisms That Influence the Estimate of Heat Transfer to Gas Turbine Blades, ASME paper" 79-HT-43, ASME NASA TM-79128.

Graham, R.W.(editor), 1984, Transition in Turbines, Symposium Proceedings, NASA CP-2386.

Halstead, D.E., Wisler, D.C., Okiishi, T.H., Walker, G.J., Hodson, H.P. and Shin, H., 1995, "Boundary Layer Development in Axial Compressor and Turbines," Part 1: Composite Picture; Part 2: Compressors; Part 3: LP Turbines; Part 4: Computations and Analyses. ASME papers 95-GT-460, 461, 462, 463.

Hedley, T.B. and Keffer, J.F., 1974, "Turbulent/Non-turbulent Decisions in an Intermittent Flow," Journal of Fluid Mechanics, Vol. 64, pp. 625-644.

Keller, F.J., 1993, "Flow and Thermal Structures in Heated Transitional Boundary Layers with and without Streamwise Acceleration," Ph.D. Dissertation, Department of Mechanical Engineering, Clemson University, Clemson, S.C.

Keller, F.J. and Wang, T., 1995, "Effects of Criterion Functions on Intermittency in Heated Transitional Boundary Layers with and Without Streamwise Acceleration," ASME Journal of Turbomachinery, Vol. 117, pp. 154-165.

Keller, F.J. and Wang, T., 1996, "Flow and Thermal Behavior in Transitional Boundary Layers with Streamwise Acceleration," ASME Journal of Turbomachinery, Vol. 118, pp. 314-326.

Kim, J., Simon, T.W., and Kestoras, M. 1994, "Fluid Mechanics and Heat Transfer Measurements in Transitional Boundary Layers Conditionally Sampled on Intermittency," ASME Journal of Turbomachinery, Vol. 116, pp. 405-416.

Kuan, C.L. and Wang, T., 1990, "Investigation of the Intermittent Behavior of a Transitional Boundary Layer Using a Conditional Averaging Technique," Experimental Thermal and Fluid Science, Vol. 3, pp. 157-170.

Lauder, B.G., and Spalding, D.B., 1974, "The Numerical Computation of Turbulent Flows," Computer Methods in Applied Mechanics and Engineering, Vol. 3, p. 269.

Mayle, R.E., 1991, "The Role of Laminar-Turbulent Transition in Gas Turbine Engines," ASME Journal of Turbomachinery, Vol. 113, pp. 509-537.

Musker, A.J., 1979, "Explicit Expression for the Smooth Wall Velocity Distribution in Turbulent Boundary Layers," AIAA Journal, Vol. 17, No. 6, June, pp. 655-657.

Narasimha, R. 1985, "The Laminar-Turbulent Transition Zone in a Boundary Layer," Prog. Aero. Sci., Vol. 22, pp. 29-80.

Shome, B., 1991, "Development of a Three-Wire Probe for the Measurement of Reynolds Stresses and Heat Fluxes in Transitional Boundary Layers," M.S. Thesis, Department of Mechanical Engineering, Clemson University, Clemson, S.C.

Sohn, K.H., OBrien, J.E., and Reshotko, E., 1989, "Some Characteristics of Bypass Transition in a Heated Boundary Layer," Proceeding of the 7th Turbulent Shear Flow Symposium, p. 61-70.

Sohn, K.H. and Reshotko, E., 1991, "Experimental Study of Boundary Layer Transition with Elevated Free-Stream Turbulence on a Heated Plate," NASA CR-187068.

Solomon, W. J., Walker, G. J., and Gostelow, J.-P., 1995, "Transition Length Prediction for Flows with Rapidly Changing Pressure Gradients," ASME paper 95-GT-241.

Steelant, J. and Dick, E., 1996, "Modelling of Bypass Transition with Conditional Navier-Stokes Equations Coupled to an Intermittency Transport Equation," International Journal for Numerical Methods in Fluids, Vol. 23, pp. 193-220.

Turner, A.B., 1971, "Local Heat Transfer Measurements on a Gas Turbine Blade," Journal of Mechanical Engineering Sciences, Vol. 13, 1, pp. 1-12.

Wang, T., Keller, F.J. and Zhou, D., 1992, "Experimental Investigation of Reynolds Shear Stresses and Heat Fluxes in a

Transitional Boundary Layer," ASME HTD Vol. 226, Fundamental and Applied Heat Transfer Research for Gas Turbine Engines, pp. 61-70.

Wang, T., Keller, F.J., and Zhou, D., 1996, "Flow and Thermal Structures in a Transitional Boundary Layer," Experimental Thermal and Fluid Science, Vol. 12, pp.352-363.

Wang, T. and Zhou, D., 1997, "Conditionally Sampled Flow and Thermal Structures of a Transitional Boundary Layer at Elevated Free-Stream Turbulence," to be presented at the ASME Fluid Engineering Summer Meeting, Vancouver, Canada.

## APPENDIX

Representative raw velocity traces at about  $y/\delta = 0.1$  in a duration of 0.5 seconds for each transition stations are shown below.

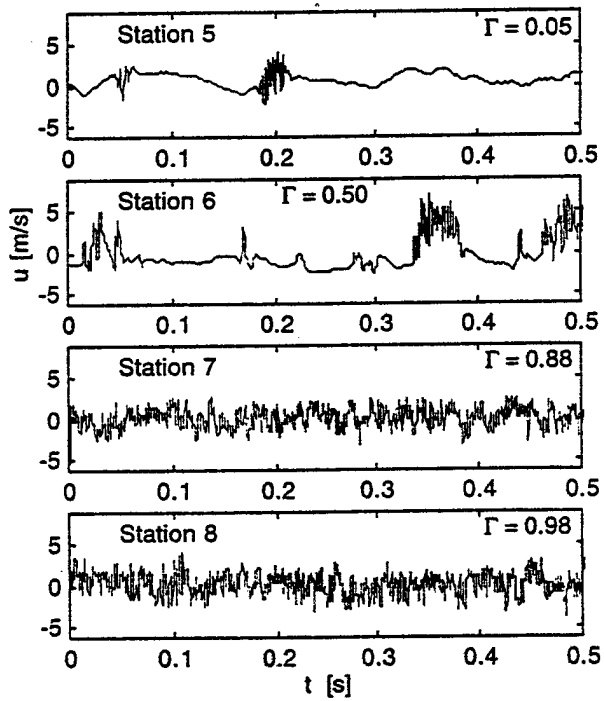


Fig. A1. Instantaneous  $u$  signals for the baseline case at  $y/\delta = 0.1$ .

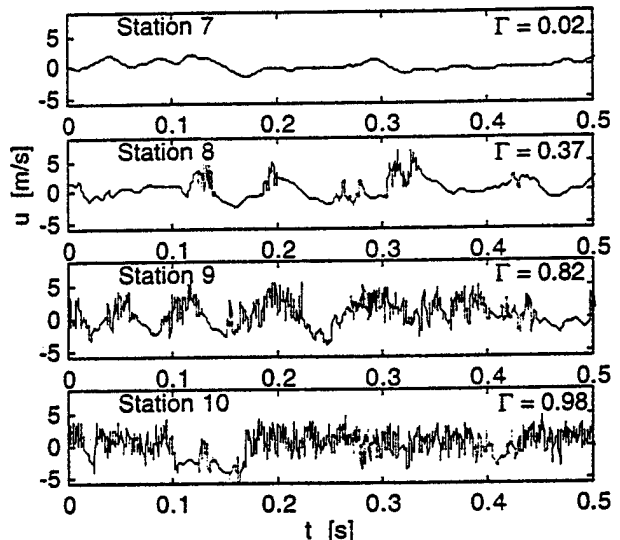


Fig. A2. Instantaneous  $u$  signals for the K1 case at  $y/\delta = 0.1$ .

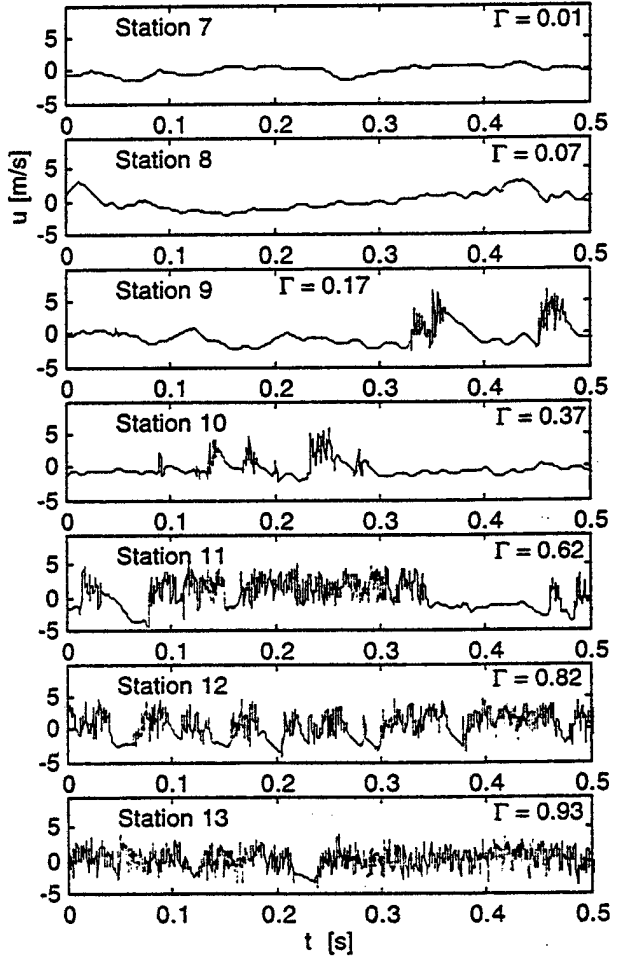


Fig. A3. Instantaneous  $u$  signals for the K2 case at  $y/\delta = 0.1$ .



The Society shall not be responsible for statements or opinions advanced in papers or discussion at meetings of the Society or of its Divisions or Sections, or printed in its publications. Discussion is printed only if the paper is published in an ASME Journal. Authorization to photocopy material for internal or personal use under circumstance not falling within the fair use provisions of the Copyright Act is granted by ASME to libraries and other users registered with the Copyright Clearance Center (CCC) Transactional Reporting Service provided that the base fee of \$0.30 per page is paid directly to the CCC, 27 Congress Street, Salem MA 01970. Requests for special permission or bulk reproduction should be addressed to the ASME Technical Publishing Department.

Copyright © 1997 by ASME

All Rights Reserved

Printed in U.S.A.

## INTERMITTENT FLOW AND THERMAL STRUCTURES OF ACCELERATING TRANSITIONAL BOUNDARY LAYERS, PART 2: FLUCTUATION QUANTITIES

Ting Wang and F. Jeffrey Keller\*

Department of Mechanical Engineering  
Clemson University  
Clemson, South Carolina, U.S.A.

### ABSTRACT

The conditionally sampled fluctuation quantities of non-accelerating and accelerating heated transitional boundary layers were analyzed. The results indicated that the values of  $u'$ ,  $v'$ ,  $uv$ , and  $ut$  in the turbulent part of the transitional flow were higher than those values in the fully-developed turbulent flow. These higher values were believed to be manifestations of the vigorous activities involved in the transition process. The contributions to the unconditioned  $u'$  by "mean-step" change due to the alternating behavior between turbulent and non-turbulent flows are about 20% in the near-wall region, but are negligible for  $Y^+ > 30$ . The turbulent part  $uv$  values are higher than the fully turbulent and unconditioned values in the inner boundary layer but lower in the outer boundary layer. The mean-step change has negligible effect on unconditioned  $uv$  values. As acceleration increases, both  $u'$  and  $t'$  in the turbulent part are suppressed; however, turbulent part  $u'$  is still higher than the unconditioned  $u'$ . Acceleration promotes streamwise Reynolds heat flux ( $ut$ ) transport in both turbulent and non-turbulent parts. A second peak of the turbulent part  $ut$  occurs at around  $Y^+ = 120$  as acceleration increases. The turbulent part eddy viscosity values are much lower than those in the fully turbulent flow.

### NOMENCLATURE

$C_p$	-	specific heat
$K$	-	pressure gradient parameter, $\frac{v}{U_\infty^2} \frac{dU_\infty}{dx}$
$q''_w$	-	wall heat flux
$Re$	-	Reynolds number
$T$	-	instantaneous temperature
$t'$	-	rms value of temperature fluctuations
$u', v'$	-	rms values of velocity fluctuations

\*F.J. Keller is currently working at Accuracy Microsensors, Inc.  
Pittsford, New York.

$u_\tau$	-	friction velocity, $\sqrt{\tau_w / \rho}$
$U^+$	-	$\bar{U}/u_\tau$
$\bar{uv}$	-	Reynolds shear stress
$\bar{ut}$	-	streamwise Reynolds heat flux
$Y^+$	-	$yu_\tau / v$

### Greek

$\delta$	-	boundary layer thickness at 0.995 $U_\infty$
$\epsilon_M$	-	turbulent (or eddy) viscosity
$\Gamma$	-	intermittency factor
$\nu$	-	kinematic viscosity
$\rho$	-	density
$\tau_w$	-	shear stress on the wall

### Subscripts:

$\infty$	-	free-stream value
$t$	-	turbulent
$nt$	-	non-turbulent

### INTRODUCTION

The results of Part 1 provided conditionally sampled mean values in the turbulent and non-turbulent parts in the intermittent, transitional boundary layers. Part 2 will focus on the fluctuation quantities. These fluctuation quantities provided information regarding the production of turbulent kinetic energy, turbulent shear stress transports, and turbulent heat flux transport, which are necessary for modeling turbulence and verifying CFD results. The instantaneous traces of velocity or turbulence shear stress can also serve as an important database for verifying the results from direct numerical analysis (DNS).

Blair (1992) employed an ensemble-averaging technique to analyze the turbulent burst profiles of randomly passing turbulent patches in accelerating boundaries with intense free-stream

turbulence. He discovered that as much as one-half of the streamwise-component unsteadiness, and much of the apparent anisotropy observed near the wall, was not produced by turbulence, but by the steps in velocity between the turbulent and non-turbulent zones of flow. His results regarding the turbulence kinetic energy indicated that the non-turbulent part preserved the characteristics of a highly disturbed laminar boundary layer all the way through transition.

The objectives of this paper are to provide a detailed analysis of the conditionally sampled fluctuation quantities in heated transitional boundary layers and investigate the effects of streamwise acceleration on the development of these fluctuation quantities in the transition process.

## RESULTS AND DISCUSSION

The effects of acceleration on the unconditioned flow and thermal structures have been discussed by Keller and Wang (1996). This paper will focus on the conditionally sampled results.

### Streamwise and Cross-Stream Velocity Fluctuations ( $u'$ and $v'$ ).

For the Reynolds normal stresses, the unconditioned values obtained in the transitional boundary layer are a combination of the non-turbulent and turbulent portions plus the intermittent alternation between the non-turbulent and turbulent mean values, as shown below.

$$u'^2 = \Gamma u'_t^2 + (1-\Gamma) u'_{nt}^2 + \Gamma(1-\Gamma) (\bar{U}_t - \bar{U}_{nt})^2. \quad (1)$$

The first term and second term on the right side of equation 1 can be directly obtained by conditional sampling and are termed non-turbulent contribution and turbulent contribution, respectively. The last term can be calculated from the conditionally sampled data. It is commonly referred to as the "mean-step contribution" and has been speculated as the cause of the peak values of unconditioned  $u'$  found in the transitional boundary layer, which exceed the peak values found in a fully turbulent boundary layer (Schubauer and Klebanoff, 1956). The qualitative value of this "mean-step contribution" may be inferred by comparing the  $u'$  values obtained in the non-turbulent and turbulent portions to the unconditioned result. Note, as previously discussed, that the intermittency drops off rapidly at the edge of the boundary layer resulting in fewer turbulent readings. Too few points in this region for the turbulent portion result in a large scatter in the data. Therefore, if the intermittency in the outer boundary layer region of turbulent portion dropped below 0.005 the data were omitted from presentation. The conditionally sampled results of  $u'$  for the baseline case are shown in Fig. 1. The non-turbulent portion exhibits a peak intensity of 7.5% at  $Y^+ \approx 35$  ( $y/\delta^* \approx 1.3$ ) for station 05 ( $\Gamma = 0.05$ ), which is slightly below the 8% peak value for the unconditioned result which occurs at the same  $Y^+$  location. The maximum value of  $u'$  in the turbulent part is 16% and is greater than the 8% reached for the unconditioned result, as well as the 10% value of the fully turbulent flow at station 13 for the same  $Y^+$  location. For station 06 ( $\Gamma = 0.50$ ) the peak intensity for the non-turbulent portion increases to 9.5%. The peak magnitude for the unconditioned result is 16% at this station and occurs closer to the wall at  $Y^+ \approx 15$  ( $y/\delta^* \approx 0.3$ ). The peak magnitude in  $u'$  for the turbulent portion for station 06 increases to 18.5% and still exceeds the unconditioned value. At station 6 in Fig. 1, the individual contributions from turbulent, non-turbulent, and mean-

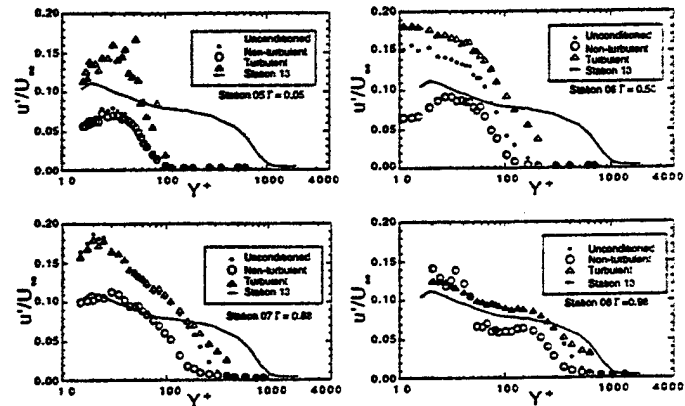


Fig. 1 Conditionally sampled  $u'$  for the baseline case.

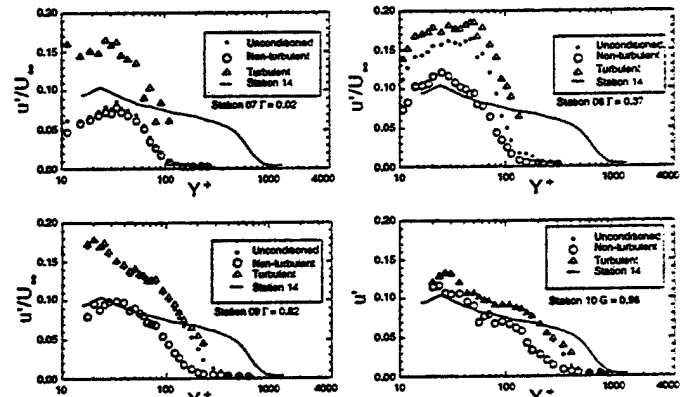


Fig. 2 Conditionally sampled  $u'$  for the K1 case.

step change to the unconditioned  $u'$  in eq. 1 are 64%, 13%, and 23% at the 3rd data point ( $Y^+ = 14.9$ ); 73%, 23%, and 4% at the 6th point ( $Y^+ = 26.8$ ); 79%, 19%, and 2.2% at the 14th point ( $Y^+ = 58.6$ ). It is clear that the turbulent part is the major term. The non-turbulent and mean-step change terms are minor terms that actually pull down the turbulent part  $u'$  values. Therefore, the unconditioned  $u'$  values become lower than the turbulent part values. The contribution from the mean-step change to  $(u')^2$  is about 23% and about 14% to  $u'$  value in the near wall region. This mean-step contribution drastically reduces as  $Y^+ > 30$ .

In the late transition region, stations 07 through 08, the peak intensity in the non-turbulent part continues to increase in magnitude. At station 07 ( $\Gamma = 0.88$ )  $u'$  in the turbulent portion is slightly below the unconditioned result, indicating a contribution from the mean-step alternation. For station 08 ( $\Gamma = 0.98$ ), the peak intensity in  $u'$  for the non-turbulent portion exceeds both the turbulent and unconditioned values near the wall. Kuan and Wang (1990) observed a similar occurrence in the late transition region and determined it was a direct result of large magnitude low frequency unsteadiness (not turbulence) in the non-turbulent intervals between the turbulent spots. Sohn et al. (1989) had a similar observation. The near-wall peak of turbulent portion decreases in magnitude from station 07 to station 08. This decrease of  $u'$  in the late transition region is most probably caused by the

effects of viscous dissipation. The conditionally sampled results of  $u'$  indicate that large magnitudes observed in the transition region are a direct result of the turbulent fluctuations in the turbulent portion, and the mean-step contribution is not a major factor. Similar observations were made by Kuan et al.(1989), Kim et al. (1989), Sohn and Reshatko (1991), and Blair (1992). These results suggest that the level of turbulent activity indicated by the unconditioned values in the transitional boundary layer is not an accurate measure of the true turbulent activity and that turbulence models using fully turbulent boundary layers to model the transport processes occurring in the turbulent spots require correction.

The conditionally sampled  $u'$  profiles for the accelerating cases are shown in Figs. 2 and 3. An interesting difference occurs between the non-turbulent portions of the accelerating cases and the baseline case. For the baseline case, the peak magnitude of  $u'$  in the non-turbulent portion increases from station 05 ( $\Gamma = 0.05$ ) up through station 07 ( $\Gamma = 0.88$ ). For the K1 case, the peak magnitude of  $u'$  in the non-turbulent portion increases from 8% at station 07 ( $\Gamma = 0.02$ ) to 12.5% at station 08 ( $\Gamma = 0.37$ ) and then decreases to 10.5% by station 09 ( $\Gamma = 0.82$ ). For the K2 case, the non-turbulent  $u'$  peak magnitude increases from 7.5% at station 07 ( $\Gamma = 0.01$ , not shown) to 13% at station 08 ( $\Gamma = 0.07$ ). The peak magnitude then decreases to 12% at station 09, finally to about 9% at station 10 ( $\Gamma = 0.37$ ) and is maintained about 9% to 10% through station 13 ( $\Gamma = 0.93$ ). This evolution of the peak value of  $u'$  indicates that as  $K$  increases,  $u'$  of the non-turbulent portion is suppressed at an earlier stage. This is consistent with the results of Schubauer and Skramstad (1947) which showed a favorable pressure gradient damps boundary layer non-turbulent oscillations in a pre-transitional boundary layer and may also suggest that this damping effect continues through the transition process.

The results for  $u'$  in the turbulent portions are similar to the baseline case. The  $u'$  values are greater than the unconditioned values in the early transition region through  $\Gamma = 0.37$  for both K1 and K2 cases. In the late transition region ( $\Gamma > 0.6$ ) the unconditioned values of  $u'$  slightly exceed the values in the turbulent portion in the near wall region indicating a mean-step contribution. This is especially noticed for station 12 of the K2 case shown in Fig. 3. As with the baseline case, the level of turbulent energy indicated by the turbulent portion in the accelerating transitional boundary layer is very different from the turbulence energy in the fully turbulent flow.

The conditionally sampled cross-stream fluctuations,  $v'$ , for the baseline case is shown in Fig. 4. There are two interesting observations. For the non-turbulent portion, the peak of  $v'$  increases from approximately 0.6% at station 05 ( $\Gamma = 0.05$ ) to 1% at station 06 ( $\Gamma = 0.50$ ) and finally to 2% at station 08 ( $\Gamma = 0.98$ ). This increase in  $v'$  as the transition process develops is most likely caused by the presence of amplified oscillations still present in the boundary layer and by the relaxation period (calm region) after the passage of a turbulent spot, since part of the low-frequency oscillations in the calm region is grouped into the non-turbulent portions. For the turbulent portion, the  $v'$  magnitude reaches the fully turbulent value by station 06 ( $\Gamma = 0.50$ ). As transition proceeds, the location of the peak magnitude migrates closer to the wall but the absolute magnitude of the peak value changes very little.

The conditionally sampled  $v'$  profiles for the accelerating cases are shown in Figs. 5 and 6. The effect of increasing  $K$  on  $v'$  in

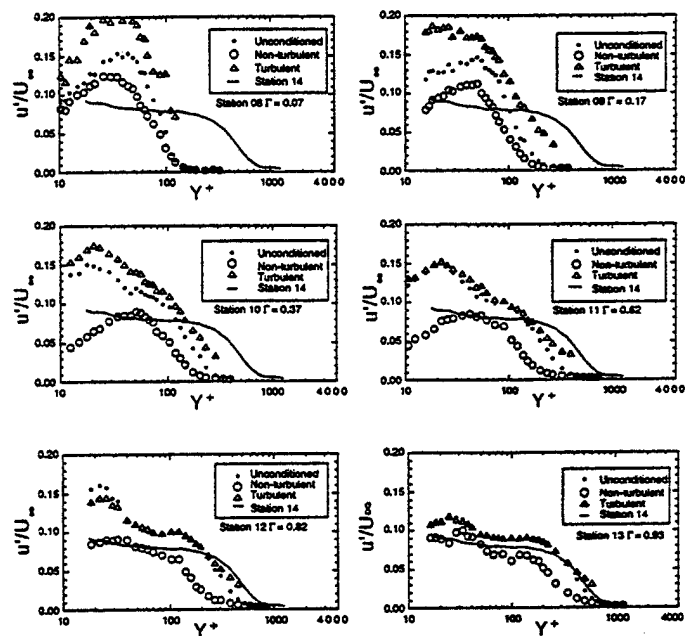


Fig. 3 Conditionally sampled  $u'$  for the K2 case.

the non-turbulent portion is similar to the effect on  $u'$  (i.e., an applied favorable pressure gradient suppresses the velocity fluctuations in the non-turbulent portion and that this suppression is greater and occurs earlier in the transition process as the pressure gradient increases). The turbulent portion of  $v'$  for all three cases is never exceeded by the unconditioned values. This is due to the mean value of the cross-stream velocity,  $\bar{V}$ , being near zero for both the turbulent and non-turbulent portions. There is no significant mean-step contribution.

**Reynolds Shear Stress ( $\bar{uv}$ ).** The reconstruction formula for the Reynolds shear stress is given as:

$$\bar{uv} = \Gamma \bar{uv}_t + (1 - \Gamma) \bar{uv}_{nt} + \Gamma(1 - \Gamma)(\bar{U}_t - \bar{U}_{nt})(\bar{V}_t - \bar{V}_{nt}) \quad (2)$$

Since the results from  $v'$  indicate the mean-step between  $\bar{V}_t$  and  $\bar{V}_{nt}$  is almost null, the last term of equation 2 is not expected to have a significant contribution on the overall Reynolds shear stress. The evolution of the conditionally sampled Reynolds shear stress,  $\bar{uv}$ , for the baseline case is shown in Fig. 7.

The non-turbulent contribution to the shear stress throughout the transition region is relatively small. This shows the weak correlation between the streamwise and cross-stream velocity fluctuations in the non-turbulent portions. The turbulent portion immediately increases above the wall shear and above the unconditioned result, obtaining a magnitude nearly three times the wall shear at station 05 ( $\Gamma = 0.05$ ). The peak magnitude remains at about three times the wall shear at station 06 ( $\Gamma = 0.50$ ) and then begins to decay, reaching a value of 1 by station 08 ( $\Gamma = 0.98$ ). This evolution of the turbulent shear indicates that the unconditioned values are not representative of the true turbulent

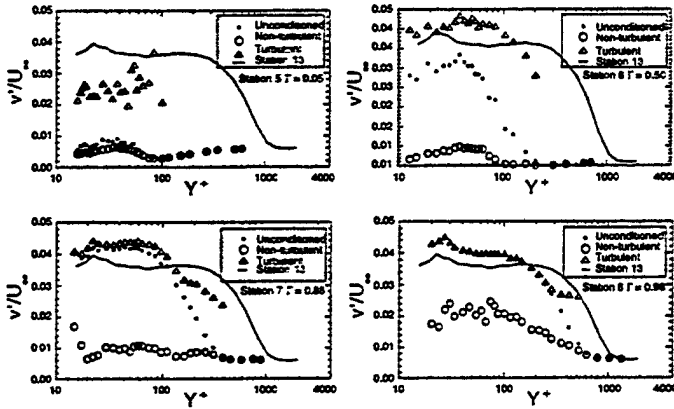


Fig. 4 Conditionally-sampled  $v'$  for the baseline case.

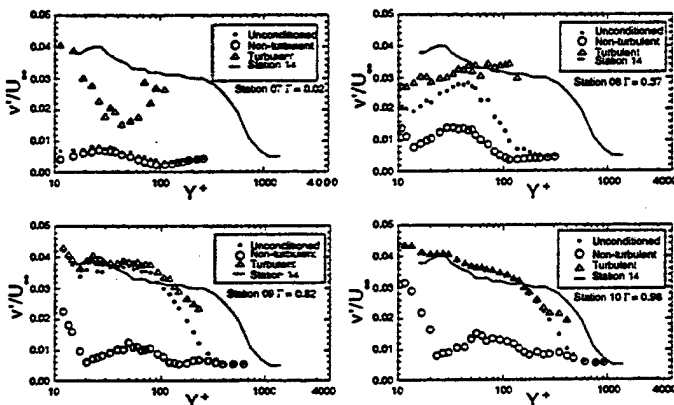


Fig. 5 Conditionally sampled  $v'$  for the K1 case.

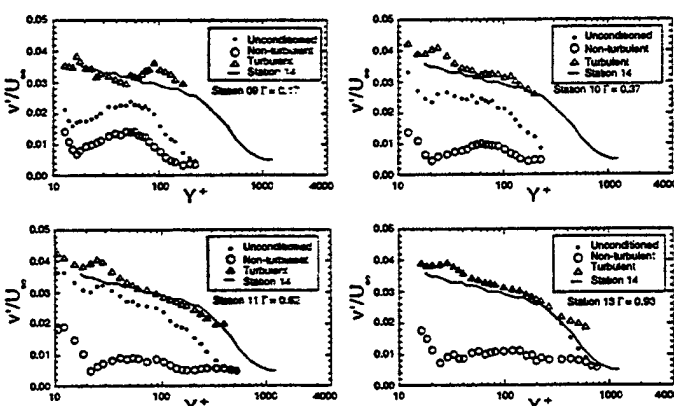


Fig. 6 Conditionally sampled  $v'$  for the K2 case.

shear through the transition process. To provide additional insight into the turbulent shear, the results for the baseline case are replotted in Fig. 8 but are normalized by the individual  $C_f$  values obtained for each portion (i.e., the turbulent and non-turbulent values shown in Fig. 4 of Part 1). By presenting the Reynolds shear stress in this manner, the peak magnitudes in the turbulent portion are significantly reduced. The peak magnitudes of  $\bar{uv}$  in the turbulent portion for stations 05 through 07 still exceed the wall shear but not by the magnitude previously seen in Fig. 7. For station 06 ( $\Gamma = 0.50$ ),  $\bar{uv}$  in the turbulent portion reaches a maximum of approximately 1.4 and occurs at  $Y^+ \approx 100$ , not at  $Y^+ \approx 40$  shown by the unconditioned portion. The trend of the Reynolds shear distribution in the turbulent portion for station 07 is similar to that observed in station 06 even though the unconditioned values are not similar. Note that the  $uv/(U_T)^2$  values in the turbulent portion at station 7 in Fig. 8 become lower than the unconditioned values because the  $C_f$  values used in the turbulent portion in Fig. 8 are much higher than the unconditioned  $C_f$  values used in Fig. 7. For station 07 ( $\Gamma = 0.88$ ) the peak of  $\bar{uv}$  in the turbulent portion is 1.3 times greater than the wall shear. This supports the statement that the turbulent shear is generated within the turbulent portion of the flow and away from the wall at approximately  $Y^+ = 70-100$  and that the higher turbulent shear away from the wall is not due to the mean-step contribution.

Fig. 7 provides information of the absolute magnitude difference of  $\bar{uv}$  between non-turbulent and turbulent parts since a constant value of  $U_T$  is used for all three parts. Fig. 8 provides information of normalized  $\bar{uv}$  values relative to the shear wall shear stress of each part respectively. Both presentation methods are informative and provide physical insights to the evolution of turbulence transports in the transition process. However, limited by the paper length, only the second normalization method is used for the accelerating cases in this paper. The complete data presentation can be found in Keller's dissertation (1993).

Selected conditionally sampled results of the Reynolds shear stress for the accelerating cases normalized by the respective  $C_f$  values of each portion are shown in Figs. 9 and 10. For the K2 case (Fig. 10), comparison of  $\bar{uv}$  between the unconditioned and turbulent portions between station 10 ( $\Gamma=0.37$ ) and 11 ( $\Gamma=0.62$ ) reveals that the distribution of turbulent shear is more uniform

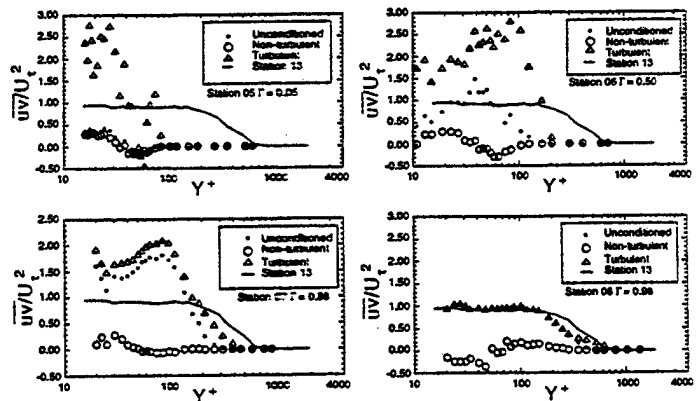


Fig. 7 Conditionally sampled Reynolds shear stress for the baseline case (normalized by unconditioned  $C_f$ ).

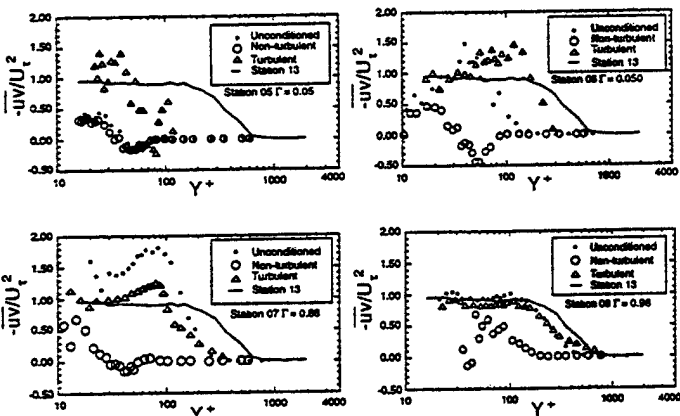


Fig. 8 Conditionally sampled Reynolds shear stress for the baseline case (normalized by individual  $C_f$  of each portion).

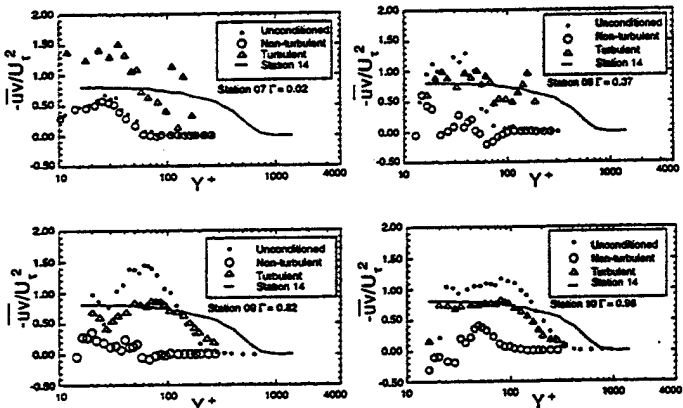


Fig. 9 Conditionally sampled Reynolds shear stress for the K1 case (normalized by individual  $C_f$  of each portion).

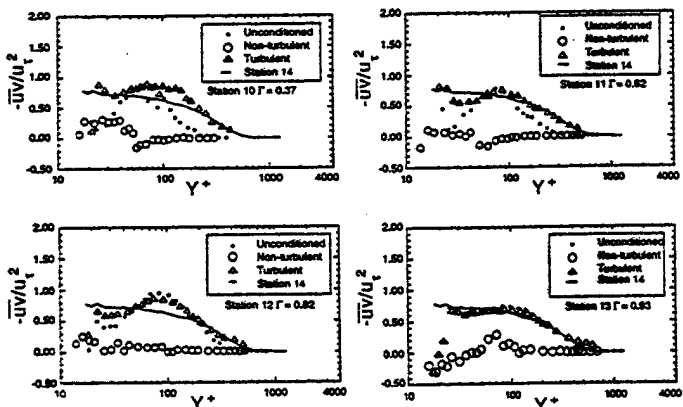


Fig. 10 Conditionally sampled Reynolds shear stress for the K2 case (normalized by individual  $C_f$  of each portion).

through the inner boundary layer for the turbulent portion than the unconditioned result. For example, in the inner boundary layer at station 10 ( $\Gamma = 0.37$ )  $\bar{u}v$  for the unconditioned data reaches a maximum value at  $Y^+ = 60$  and quickly decreases in magnitude as the wall is approached, while  $\bar{u}v$  in the turbulent portion remains at a relatively constant value. In the outer boundary layer, for  $Y^+ > 50$ ,  $\bar{u}v$  for the unconditioned data rapidly decreases to a zero magnitude by  $Y^+ = 200$ , whereas for the turbulent portion,  $\bar{u}v$  slowly decays in magnitude in the outer boundary layer. This difference is partly caused by the engulfing of the intermittent irrotational flow from the free stream. As transition progresses, these differences become less pronounced and  $\bar{u}v$  for the unconditioned data and the turbulent portion are nearly indistinguishable by station 13.

**RMS Temperature Fluctuations ( $t'$ ).** The conditionally sampled RMS temperature profiles, normalized by  $T_w - T_\infty$  for the baseline case are shown in Fig. 11. The profiles are similar to those observed in the  $u'$  profiles shown in Fig. 1. The non-turbulent portion exhibits a peak intensity of 0.045 at  $Y^+ \approx 35$  ( $y/\delta^* \approx 1.3$ ) at station 05 ( $\Gamma = 0.05$ ) which is slightly below the 0.05 peak value for the unconditioned result which occurs at the same  $Y^+$  location. For station 06 ( $\Gamma = 0.50$ ) the peak intensity for the non-turbulent portion increases to 0.075 and remains at  $Y^+ \approx 35$ . The peak magnitude for the unconditioned result is 0.12 at this station and occurs closer to the wall  $Y^+ \approx 15$  ( $y/\delta^* \approx 0.3$ ). In the late transition region, stations 07 through 08, the peak intensity in the non-turbulent part continues to increase in magnitude but does not migrate closer to the wall until station 08. For station 08 ( $\Gamma = 0.98$ ), the peak intensity in  $t'$ , similar to the result of  $u'$  for the non-turbulent portion, exceeds both the turbulent and unconditioned values near the wall. This can be contributed by the unsteadiness (not turbulence) of the highly-disturbed non-turbulent portion. For station 05 ( $\Gamma = 0.05$ ), the maximum value of  $t'$  in the turbulent part reaches 0.10 which is greater than the 0.05 reached in the unconditioned part for the same  $Y^+$  location. For station 06 ( $\Gamma = 0.50$ ), the peak magnitude in  $t'$  for the turbulent portion increases to 0.15 at  $Y^+ \approx 15$  ( $y/\delta^* \approx 0.3$ ) and still exceeds the unconditioned value. At station 07 ( $\Gamma = 0.88$ )  $t'$  in the turbulent portion for  $Y^+ < 40$  is slightly below the unconditioned result; this indicates a contribution from the step alternation in mean temperature. The near-wall peak of turbulent portion decreases in magnitude from station 07 to station 08. The secondary peak that was seen to occur at  $Y^+ \approx 200$  for the unconditioned result also occurs in both the non-turbulent and turbulent portions. This indicates that this second peak is not majorly caused by the mean-step contribution but rather is a direct result of the temperature fluctuation.

The conditionally sampled  $t'$  profiles for the accelerating cases are shown in Figs. 12 and 13. The effect of a favorable pressure gradient is seen to be most significant in the non-turbulent portion. For the K2 case, the broad peak in the  $t'$  profiles for the non-turbulent portion occurring at  $Y^+ \approx 40$  for station 09, continually increases in magnitude. At station ( $\Gamma = 0.62$ ), the peak intensity in  $t'$  occurs at  $Y^+ \approx 100$  and is approximately the same magnitude as both the turbulent and the unconditioned value. By station 13 ( $\Gamma = 0.93$ ) the peak intensity in  $t'$  for this region is

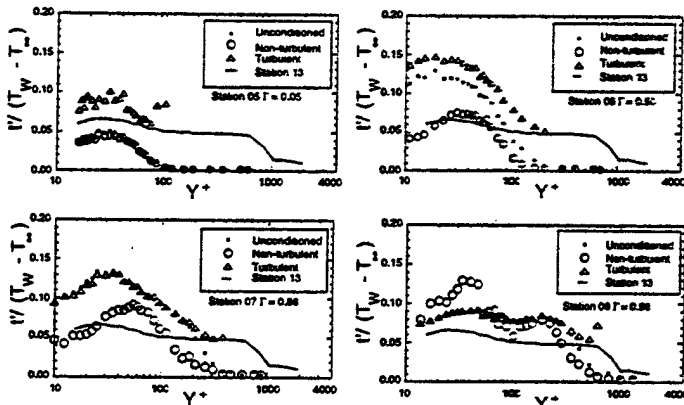


Fig. 11 Conditionally sampled RMS temperature for the baseline case.

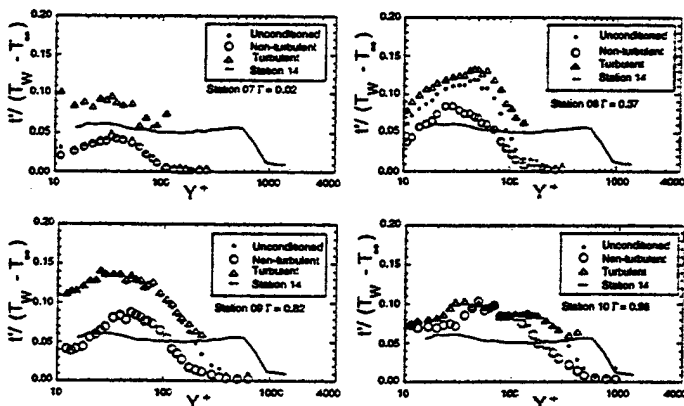


Fig. 12 Conditionally sampled RMS temperature for the K1 case.

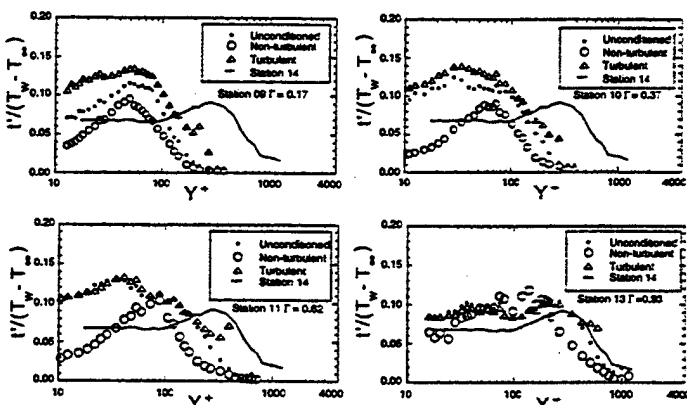


Fig. 13 Conditionally sampled RMS temperature for the K2 case.

greater than both the turbulent part and the unconditioned values. This behavior did not occur in the corresponding  $u'$  profiles where the fluctuations in the non-turbulent portion never exceeded the unconditioned or the turbulent part values in the K2 case. The exact reason for this phenomenon is not clear. Probably, this difference is caused by the fact that pressure gradients directly interact with the momentum transport but not with the thermal transport.

**Reynolds Heat Fluxes ( $\bar{u}t$ ).** The conditionally sampled streamwise Reynolds heat flux,  $\bar{u}t$ , for the baseline case is shown in Fig. 14. The peak intensity in the non-turbulent portion occurs at the same cross-stream location as was observed in the  $t'$  profiles. At station 05 ( $\Gamma = 0.05$ ) the magnitude of the peak intensity is approximately 3.5. By station 06 ( $\Gamma = 0.50$ ) this peak intensity in  $\bar{u}t$  increases to 7.0 and maintains this level until station 08 ( $\Gamma = 0.98$ ). For the turbulent portion,  $\bar{u}t$  exceeds the wall heat flux by more than a factor of 15 at station 05. By station 06 ( $\Gamma = 0.50$ ) this value has increased to over 20. The large values of convective heat transfer in the streamwise direction,  $\bar{u}t$ , are a result of the turbulent transport within the turbulent portions.

The conditionally sampled results of  $\bar{u}t$  for the accelerating cases are shown in Figs 15 and 16. The results indicate that the effect of a favorable pressure gradient is to increase the convective heat transfer in the streamwise direction,  $\bar{u}t$ , in both the turbulent and non-turbulent portions relative to the baseline case. The presence of a relatively large  $\bar{u}t$  value in the non-turbulent portion does not necessarily indicate that a significant turbulent transport of heat is occurring but only that  $u$  and  $t$  are correlated due to the unsteadiness of the flow. A second peak around  $Y^* = 12.0$  appears downstream of station 11. The reason for this second peak in accelerating flow is not clear. The results of the cross-stream Reynolds heat flux,  $\bar{v}t$ , are not presented here due to a large uncertainty in  $\bar{v}t$  measurements, as discussed by Wang et al. (1992).

**Eddy Viscosity,  $\varepsilon_M$ .** The results of the conditionally sampled eddy viscosity,  $\varepsilon_M$ , normalized by the molecular viscosity are shown in Figs. 17 and 18. For the baseline case, the values obtained in the turbulent portion are larger than the unconditioned values but are significantly below the fully turbulent values obtained at station 13 (see Fig. 17). As  $K$  increases, both the turbulent part and the unconditioned  $\varepsilon_M$  values decrease.

## CONCLUSION

A conditional sampling technique was employed to analyze the fluctuation quantities in the turbulent and non-turbulent parts of accelerated boundary layers undergoing laminar-turbulent transition on a uniformly heated flat plate. The results indicated that the increased magnitudes of the unconditionally sampled  $u'$  and  $t'$  were discovered to be a direct result of the fluctuations in the turbulent portions. The "mean-step" contribution to  $u'$  due to the alternating behavior between turbulent and non-turbulent flows were about 20% in the near-wall region but were negligible for  $Y^* > 30$ . The peak intensity of  $u'$  and  $t'$  in the non-turbulent portion was suppressed at an earlier stage, as acceleration increased. The peak magnitude of  $uv$  in the turbulent parts of the accelerating cases exceeded the wall shear but not by the magnitude seen in the baseline case. The

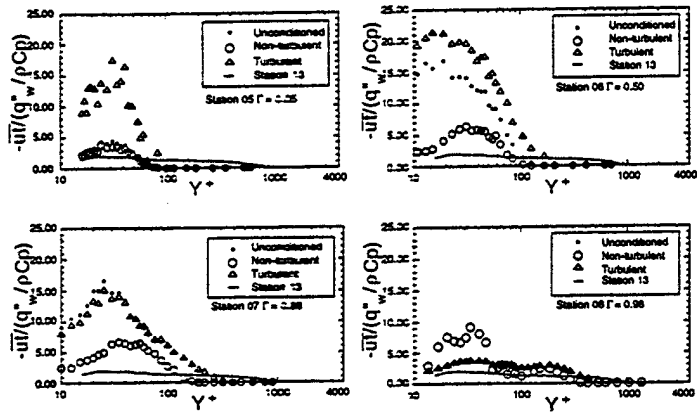


Fig. 14 Conditionally sampled Reynolds streamwise heat flux for the baseline case.

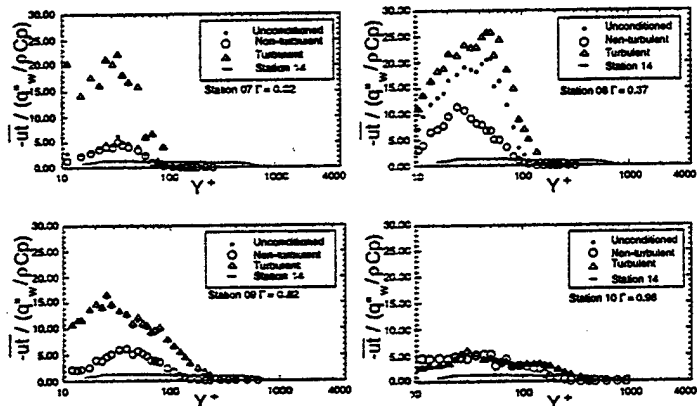


Fig. 15 Conditionally sampled Reynolds streamwise heat flux for the K1 case (in wall units).

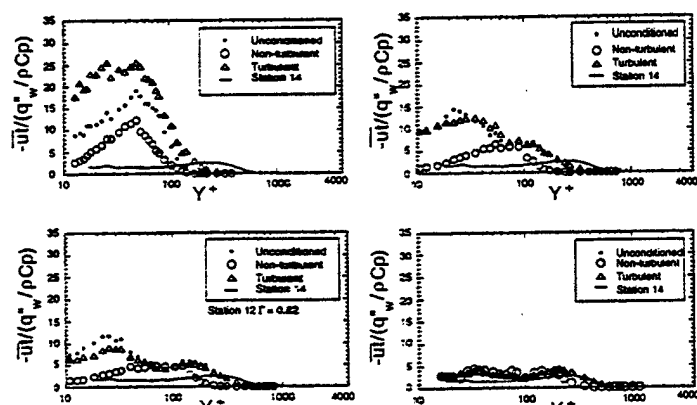


Fig. 16 Conditionally sampled Reynolds streamwise heat flux for the K2 case.

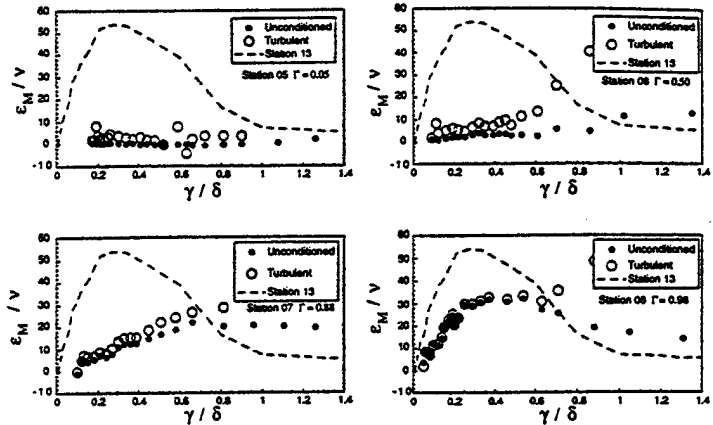


Fig. 17 Conditionally sampled eddy viscosity for the baseline case.

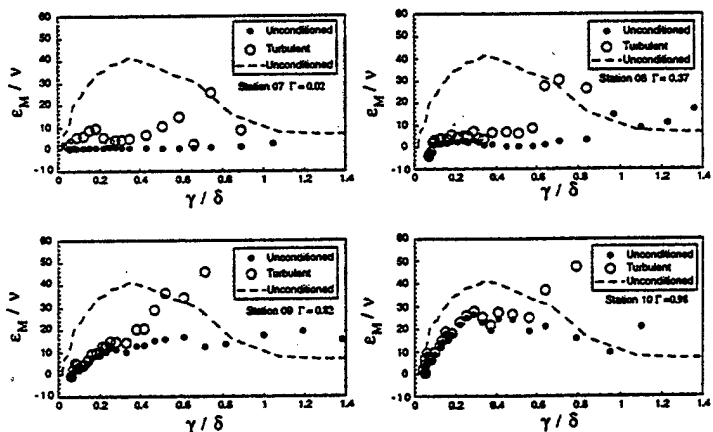


Fig. 18 Conditionally sampled eddy viscosity for the K1 case.

turbulent part  $uv$  values were higher than the fully turbulent and unconditioned values in the inner boundary layer but lower in the outer boundary layer. The "mean-step" contribution to unconditioned  $uv$  values was negligible. As acceleration increased,  $uv$  in the turbulent portion was more uniformly distributed through the inner boundary layer than the unconditioned results.

In accelerating cases, the peak of  $v'$  of the turbulent portion reached the fully turbulent value in the middle of the transition at  $\Gamma = 0.5$  and changed little downstream. The effect of acceleration on non-turbulent portion  $v'$  is similar to non-turbulent portion  $u'$ . The unconditionally sampled RMS temperature fluctuations,  $t'$ , exceeded both the turbulent and non-turbulent values throughout most of the boundary layer. This indicated that a mean-step contribution to the large unconditioned  $t'$  values was not negligible. The effect of acceleration on  $t'$  was seen to be most significant in the non-turbulent portion. The streamwise Reynolds heat flux transport,  $ut$ , increased as acceleration increased in both turbulent and non-

turbulent portions of the boundary layers. A second peak of  $u_t$  of the turbulent part at around  $y^+=120$  appeared as  $K$  increased.

For the baseline case, the values of eddy viscosity, obtained in the turbulent portion were larger than the unconditionally sampled values and were significantly below the fully turbulent values.

## ACKNOWLEDGEMENT

This research was sponsored by the Air Force Office of Scientific Research (Grant No. F49620-94-1-0126). The program manager was Dr. James McMichael.

## REFERENCES

Blair, M.F., 1992. "Boundary-Layer Transition in Accelerating Flows with Intense Free-Stream Turbulence : Part 1-Disturbances Upstream of Transition Onset; Part 2-The Zone of Intermittent Turbulence," ASME Journal of Fluids Engineering, Vol. 114, pp. 313-332.

Keller, F.J., 1993, "Flow and Thermal Structures in Heated Transitional Boundary Layers with and without Streamwise Acceleration," Ph.D. Dissertation, Department of Mechanical Engineering, Clemson University, Clemson, S.C.

Keller, F.J. and Wang, T., 1996, "Flow and Thermal Behavior in Transitional Boundary Layers with Streamwise Acceleration," ASME Journal of Turbomachinery, Vol. 118, pp. 314-326.

Kim, J., Simon, T.W., and Kestoras, M. 1994, "Fluid Mechanics and Heat Transfer Measurements in Transitional Boundary Layers Conditionally Sampled on Intermittency," ASME Journal of Turbomachinery, Vol. 116, pp.405-416.

Kuan, C.L. and Wang, T., 1990, "Investigation of the Intermittent Behavior of a Transitional Boundary Layer Using a Conditional Averaging Technique," Experimental Thermal and Fluid Science, Vol. 3, pp. 157-170.

Schubauer, G.B. and Skramstad, H.K., 1947, "Laminar-Boundary Layer Oscillations and Transition on a Flat Plate," NACA Report No. 909.

Schubauer, G.B., and Klebanoff, P.S., 1956, "Contributions on the Mechanics of Boundary-Layer Transition," NACA Technical Note #1289, Supercedes NACA TN 3489.

Sohn, K.H., O'Brien, J.E., and Reshotko, E., 1989, "Some Characteristics of Bypass Transition in a Heated Boundary Layer," Presented at the 7th Turbulent Shear Flow Symposium, pp. 2.4.1-2.4.6.

Sohn, K.H. and Reshotko, E., 1991, "Experimental Study of Boundary Layer Transition with Elevated Free-Stream Turbulence on a Heated Plate," NASA CR-187068.

Wang, T., Keller, F.J. and Zhou, D., 1992, "Experimental Investigation of Reynolds Shear Stresses and Heat Fluxes in a Transitional Boundary Layer," ASME HTD Vol. 226, Fundamental and Applied Heat Transfer Research for Gas Turbine Engines, pp. 61-70.

Wang, T., Keller, F.J., and Zhou, D., 1996, "Flow and Thermal Structures in a Transitional Boundary Layer," Experimental Thermal and Fluid Science, Vol. 12, pp.352-363.

FEDSM 97-3109

## CONDITIONALLY SAMPLED FLOW AND THERMAL STRUCTURES OF A TRANSITIONAL BOUNDARY LAYER AT ELEVATED FREE-STREAM TURBULENCE

Ting Wang  
Dadong Zhou

Department of Mechanical Engineering  
Clemson University  
Clemson, South Carolina 29634-0921  
Tel: (864) 656-56730  
Fax: (864) 656-44325

### ABSTRACT

In the elevated free-stream turbulence intensity (FSTI) condition, the laminar flow is highly disturbed. The stage of linear-instability amplification triggered by infinitesimal disturbances is bypassed. The nonlinear instability, triggered by finite-amplitude disturbance, dominates in the bypass transition. Due to the highly disturbed condition in the laminar part, the turbulent and non-turbulent parts of the transitional flow become difficult to discern. Because of this, the conventional conditional sampling technique encounters difficulty and large uncertainty. A modified method using a single slope on the turbulent part of the accumulative probability diagram to determine the threshold was made. This modified method was convenient to apply and was theoretically verified. Use of the turbulence transport behavior,  $\bar{u}\bar{v}$ , as the criterion function was found superior to the use of the turbulence energy,  $u'$ , for separating the turbulent and non-turbulent signals in elevated FSTI conditions. The conditionally sampled results for FSTI ranging from 0.5% to 6.4% indicate that  $u'$ ,  $v'$ ,  $\bar{t}'$  and  $\bar{u}\bar{t}$  are high in the non-turbulent part. This is contrary to the low FSTI cases; whereas,  $\bar{u}\bar{v}$  and  $v\bar{t}$  are low in the non-turbulent part, which is similar to the low FSTI cases.

### NOMENCLATURE

$C_f$  = skin-friction coefficient,  $\tau_w/(\rho \bar{U}_\infty^2/2)$   
 $c_p$  = specific heat, J/kg-K  
FSTI = free-stream turbulence intensity  
 $q''$  = heat flux, w/m<sup>2</sup>

Re = Reynolds number =  $u_\infty x/\nu$

$t$  = instantaneous temperature fluctuation or time

$\bar{t}'$  = rms value of  $t$

$\bar{T}$  = mean temperature

$T^+$  = mean temperature in wall units,  $(\bar{T}_w - \bar{T}) \rho c_p u^*/q'' w$

$u$ ,  $v$  = instantaneous streamwise and cross-stream velocity fluctuations, m/s

$u'$ ,  $v'$  = rms values of  $u$  and  $v$ , m/s

$u^* = \sqrt{\tau_w/\rho}$ , friction velocity, m/s

$\bar{U}$  = mean streamwise velocity, m/s

$U^+ = \bar{U}/u^*$

$x$  = streamwise distance from leading edge, m

$y$  = distance away from the wall, mm

$Y^+ = yu^*/\nu$

$\delta$  = boundary layer thickness at  $\bar{U} = 0.995 \bar{U}_\infty$

$\Gamma$  = intermittency

$\Lambda$  = integral length scale,  $\bar{U} \int_0^\infty u(t)u(t+\tau)/u^2 d\tau$  (m)

$\nu$  = kinematic viscosity, m<sup>2</sup>/s

$\rho$  = density, kg/m<sup>3</sup>

$\tau$  = shear stress, N/m<sup>2</sup>

### Subscripts

w = at the wall

$\infty$  = in the free stream

### INTRODUCTION

A better understanding of momentum and thermal

transport during the laminar-turbulent transition process is one of the key factors toward improving the prediction of the thermal load on gas turbine blades (Graham, 1979 and 1984, Mayle, 1991). Transition from laminar to turbulent boundary layer flow significantly increases the local wall shear stresses and the convective heat transfer rates. These increases must be appropriately factored into the design of gas turbine blades, since as much as 50% to 80% of the surface of a typical turbine blade is commonly covered by flow undergoing transition. A recent 4-part paper by Halstead, et al. (1995) specifically pointed out the importance of laminar-turbulent transition in axial compressors and turbines from rotating multistage tests. In the newest heavy-frame industrial H-type Advanced Gas Turbine Systems (Farmer and Fulton, 1995), the adoption of closed-loop steam cooling eliminates the need for conventional air film cooling in the first two stages; therefore, correct prediction of the laminar-turbulent transition becomes more essential. An unsatisfactory prediction of the location and streamwise coverage of transition on gas turbine blades can result in either reduced longevity and reliability of the blade or reduced engine performance below design objectives. For example, Graham (1979) shows that a  $56^{\circ}\text{C}$  error in temperature prediction can result in an order-of-magnitude decrement in vane life.

In gas turbine environments, one of the most important factors affecting the transition process is the elevated free-stream turbulence intensity (FSTI). In the compressors, the FSTI varies from 2% to 4%. In the inlet of turbines, disturbances from the upstream combustors may cause background FSTI ranging from 2% to 10%. In addition, very high FSTI ranging from 10% to 20% is imposed periodically on the blades by the wakes following the trailing edges of the vanes. This elevated FSTI expedites the onset of transition and shortens the length of transition. Unlike numerous fundamental studies in the low FSTI flow, detailed flow structures involved in the transition from the laminar to turbulent flow in elevated FSTI environments have yet to be investigated. The conventionally-recognized Emmon's turbulent spot hairpin vortices, and K breakdown may not exist in the elevated FSTI conditions; rather, some kind of turbulent wave packets have been observed intermittently passing in the disturbed laminar boundary layer.

For the purpose of engineering practice, statistical measurements of flow and thermal structures play an important role in improving the understanding of certain fundamental aspects of flow mechanisms, as well as contributing to the prediction models. One of the undeniable features in the laminar-turbulent transition in a low free-stream turbulence flow is the intermittent behavior between laminar and turbulent flows. This intermittent behavior also

appears in the boundary layer at elevated free-stream turbulence, although the delineation between the disturbed laminar (or non-turbulent) and the turbulent part become vague. Among many different transitional flow models for predicting the skin-friction coefficients, surface heat transfer rate, and end of transition, the intermittency model is always physically more realistic than any other models, since the actual transitional flow is intermittent.

In the low FSTI flows, Kuan and Wang (1990) and Kim et al. (1994) have pointed out that the non-turbulent part of the transitional flow is different from the fully-developed turbulent flow, and the non-turbulent part is not an extension of the upstream laminar flow. Sohn et al. (1989) analyzed conditionally sampled results for 1% FSTI cases and concluded that the transport processes occurring in the turbulent spots will not be well modeled by standard turbulence models used in equilibrium turbulent boundary layers (Blair 1992). Therefore, linear combination of the laminar and fully-developed turbulent flow characteristics using the intermittency function may not be appropriate. It is postulated that a similar situation occurs in the elevated FSTI conditions. This motivates the present study to apply a conditional sampling technique to obtain the statistical features of the non-turbulent and turbulent part flow respectively in the transitional flow under elevated FSTI conditions from 3% to 6.4%. Since the laminar part is highly disturbed, demarcation between the non-turbulent and turbulent parts becomes difficult. This paper will especially address this issue. The results of this paper are expected to contribute to the improved understanding of intermittent behavior during bypass transition and to provide a database for the bypass transition models, for example, by Steelant and Dick (1996).

## EXPERIMENTAL PROGRAM

The detailed experimental facility, instrumentation, data acquisition and reduction, and experimental procedures have been documented in Wang et al. (1992). Therefore, only a brief description of the experimental program will be provided.

**Wind Tunnel.** The present study employed a 2-D, open circuit, blowing-type wind tunnel. The flow rate could be adjusted from 0.5 to 35 m/s. The steadiness of the free-stream velocity and temperature could be maintained, respectively, within 1% and  $0.5^{\circ}\text{C}$  for a 24-hour period; the uniformity was within 0.7% and  $0.1^{\circ}\text{C}$ .

**Test Section.** The rectangular test section was 0.15 m wide, 2.4 m long, and 0.92 m high with an aspect ratio of 6. This large aspect ratio reduced edge effects and ensured two-dimensionality of the boundary layer flow in the center

span of the test section. One of the test section walls served as the test wall. The heat patch inside the test wall was constructed of a serpentine heater foil sandwiched between glass cloth and silicon rubber sheets. The surface temperature was measured by 184 76- $\mu\text{m}$  (3-mil) E-type thermocouples. Fourteen measuring holes were drilled along the outer observation wall centerline in the test section, and measurements were obtained by traversing probes through the holes into the test section. The spacing between the centerline thermocouples was 2.54 cm (1 inch), and the spacing between the measuring holes was 15.24 cm (6 inches). Boundary layer suction was applied at the leading edge of the test section.

**Turbulence Generating Grids and FSTI.** The background FSTI of the wind tunnel was about 0.5%. The higher turbulence levels from 3.8% to 6.4% in this study were generated by inserting various turbulence-generating grids into the wind tunnel. The test conditions are listed in table 1.

**Table 1. Test Conditions at the Onset of Transition.**

Cases	FSTI (%)	$U_{\infty}$ (m/s)	$\Delta$ (c/m)
Baseline	0.5	13.0	1.8
G1	3.8	2.10	2.2
G2	5.6	1.75	3
G3	6.4	1.70	3.4

Detailed information about the free-stream flow characteristics, including isotropy and power spectra, has been documented by Zhou (1993) and Zhou and Wang (1995), but is not repeated here.

**Instrumentation and Data Reduction.** A three-wire sensor were specifically designed to simultaneously measure the two velocities, the cross-stream velocity components, and the temperature. The development and qualification of this three-wire sensor was described by Shome (1991). The difficulties obtaining measurements encountered in elevated FSTI flows and the solutions to these difficulties were previously discussed by Zhou and Wang (1995) and are briefly described below.

Basically, the three-wire sensor consisted of an X-array of gold-plated tungsten wires for measuring velocities and a 1.2- $\mu\text{m}$  platinum wire for measuring temperature. The two X-wires were operated in constant temperature mode. The method of Chua and Antonia (1990) was used for correcting temperature contamination of the hot wires.

The 1.2- $\mu\text{m}$  platinum wire was operated at a very low current of 0.1 mA (cold wire) in the constant current mode.

In order to sufficiently extend the length of transition for detailed measurements on the test wall, extremely low-speed flows down to 1.7 m/s, were provided for the elevated FSTI cases. At this low speed, relatively low overheat ratios for the X-wires were required to minimize the "cross-talk" between the X-wires and the temperature sensor. This "cross-talk" was primarily caused by the fluctuating radiation emanating from the hot wires to the cold wires. The X-wires generally had better velocity sensitivity at higher overheat ratios. As a compromise, an overheat ratio of about 1.2 was chosen for the X-wires, which made the reading error of the temperature wire caused by the adjacent hot wires negligible. The overheat ratio of 1.2 was obtained by gradually reducing the overheat ratio from 1.6 to a value at which the cold wire reading did not vary even when the hot wires were switched on and off.

At low free-stream velocities, it was found that if the flow direction deviates by a small angle from  $\pm 45^{\circ}$  to the X-wires, a significant change in the results for the Reynolds shear stress ( $uv$ ) and the cross-stream Reynolds heat flux ( $vt$ ) would occur. A typical flow angle of  $1^{\circ}$  can result in a 15% error in the  $uv$  and  $vt$  measurements at a free-stream velocity of 2 m/s. This small flow angle, which can be found by assuming that the mean cross-stream velocity ( $V$ ) is zero in the free stream, was added to the data reduction process. The frequency response of the platinum wire was tested to be from 4000 to 6000 Hz for a velocity range of 2 to 15 m/s. Therefore, frequency compensation was deemed unnecessary. The detailed frequency response test procedure and qualification were discussed in Keller (1993).

A single hot wire was used to measure each station before using the 3-wire sensor. Since the single wire can measure very close to the wall, ( $Y^+=2$ ). The results of the single wire were used to guide the 3-wire sensor to locate wall position ( $Y^+=0$ ).

A TSI Model IFA 100 Intelligent Flow Analyzer System was used as a constant temperature anemometer. A DISA M20 temperature bridge was used for operating the cold wire in the constant current mode. A 12-bit A/D data acquisition board and a high-speed data acquisition software, STREAMER, were used to acquire data. The sampling rate was 2 KHz, and the sampling duration was 20 seconds.

#### DETERMINATION OF SKIN FRICTION COEFFICIENT AND WALL POSITION

The skin friction coefficient  $C_f$  is an important parameter for characterizing the boundary layers since it changes significantly from laminar to turbulent through the transition region. Direct measurement of  $C_f$  is difficult, expensive, time consuming, and not suitable for the heated wall. However, with the information of the mean velocity

profiles, it can be indirectly determined based on the nature of the boundary layer:

- In the laminar boundary layer region, the mean velocity varies linearly with distance from the wall in the near-wall region. The value of  $\Delta U/\Delta y$  from several mean velocity data points close to the wall, measured by a single wire, was used to approximate the velocity gradient at the wall to calculate  $C_f$ . The wall position ( $y=0$ ) was determined by the best fitting of  $U^+$  falling within the linear region ( $U^+ = Y^+$ ).
- In the transitional boundary layer region, the near-wall linear velocity profile was assumed valid. The same method applied in the laminar region was used to find the  $C_f$  values and wall positions.
- In the turbulent boundary layer region, the mean velocity gradient near the wall is so large that the linear approximation of mean velocity gradient near the wall may lead to a large error. The Clauser technique (Clauser, 1956) was used instead to estimate the value of  $C_f$  and the wall position by the best fitting of  $U^+$  falling within the log-linear region.

### CONDITIONAL SAMPLING TECHNIQUE

Conditional sampling consists of three primary stages: the choice of a criterion function, the determination of a threshold value, and the generation of an intermittency function. In turbulent/non-turbulent discrimination, one commonly used method of identifying a criterion function is to differentiate the velocity signal with respect to time and square it, which emphasized the high frequency components. As pointed out by Keller and Wang (1995), performing the differentiation procedure was actually conducting a digital high path filtering. They also indicated that using the instantaneous Reynolds shear stress,  $uv$ , as the criterion function for turbulent/non-turbulent discrimination in a heated transitional boundary layer is superior to the scheme of using single velocity or temperature as the criterion function. They indicated that using  $uv$  signals as the criterion function possesses the following merits: (a) sharpness in demarcation between the turbulent and non-turbulent portions of the flow, (b) small variation of threshold values across the boundary layer and throughout the transition region, (c) low uncertainty in determining the threshold values, and (d) low sensitivity of the resulted intermittency to the uncertainty in choosing the threshold value. Therefore, squares of the first derivatives of the  $uv$  signal were used in this study as the criterion function. From each data reading, the criterion function was compared to the threshold value. If the value was larger than the threshold, the reading was considered turbulent. If the

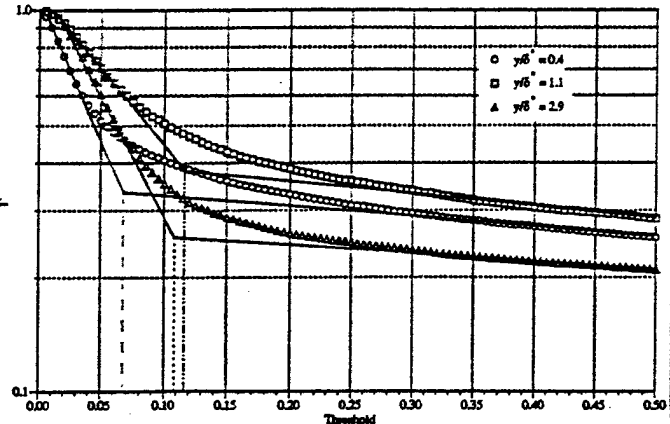


Fig. 1a. Threshold Value Determined by the Dual-Slope Method for Cases with Two Distinctive Slopes on the Cumulative Intermittency Distribution Diagram

value was less than the threshold and the next three readings (i.e., hold time) were also less than the threshold, the reading was considered non-turbulent. The value of the intermittency function was equal to 1 if the flow was turbulent; the value was 0 if the flow was non-turbulent. The threshold value was determined based on the cumulative intermittency distribution curve originally introduced by Hedley and Keffer (1974). An improved "dual-slope" method based on the cumulative intermittency distribution curve was developed by Kuan and Wang (1990). This curve represents the variation of the integral of the probability density function (PDF) as the threshold value increases from zero. This method uses a graphical approach to find the threshold value at each location. Based on this method, two straight lines of different slopes are apparent most of the time when the cumulative intermittency distribution is plotted on a semi-log coordinate with the threshold value. The different slopes are caused by the different characteristics of probability density distributions for the turbulent and non-turbulent part, respectively. A steeper slope represents the non-turbulent part, which indicated smaller standard deviation. The approximate threshold value is then taken to be the value corresponding to the intersection of the straight lines (Fig. 1a). The reasoning behind this method was discussed by Keller and Wang (1995). One disadvantage of this method is that sometimes the straight line of the cumulative intermittency distribution curve corresponding to the non-turbulent portion is not apparent. This happens particularly in the late transition region in a low FSTI flow because of the large intermittent factor and in the high FSTI flows studied in this paper and the elevated disturbances in the non-turbulent part of the flow. In this study, a modified method was used to determine the threshold value by only

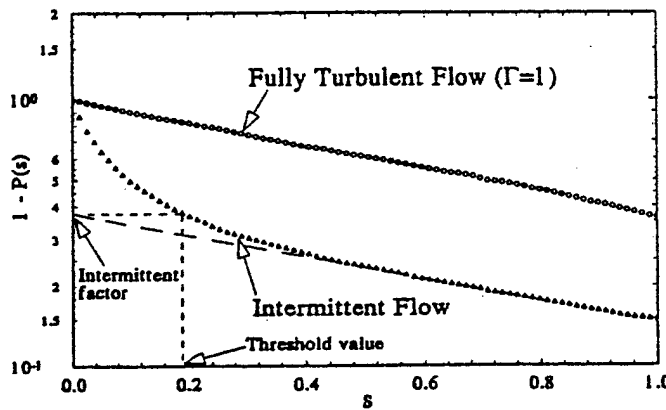


Fig. 1b. Threshold Value Determined by the Modified Method for Elevated FSTI Cases with Only One Distinctive Slope

using the slope of the turbulent portion of the cumulative intermittency distribution and is explained below.

When the non-turbulent part of the transition flow is highly disturbed, the cumulative intermittency curve in Fig. 1a becomes nonlinear as shown in Fig. 1b and a straight line cannot be easily drawn. From this observation, one might expect that the intermittent factor in the transition region could be obtained only by investigating the straight line corresponding to the turbulent portion. Based on the experimental data of the present study, the PDF of the criterion function for the turbulent flow is close to  $(1/A)e^{-s/A}$ , where "s" is the criterion function and "A" is proportional to the standard deviation. For an intermittent flow, PDF can be expressed as:

$$p(s) = (1 - \Gamma)p_{nt}(s) + \Gamma \left( \frac{1}{A} e^{-s/A} \right) \quad (1)$$

where  $p_{nt}(s)$  is the PDF for non-turbulent region and  $\Gamma$  is the intermittent factor. The cumulative probability PDF then can be obtained as:

$$P(s) = (1 - \Gamma) \int_0^s p_{nt}(s) ds + \Gamma \left( \frac{1}{A} \int_0^s e^{-s/A} ds \right) \quad (2)$$

The fluctuations of the criteria function in the non-turbulent region are much smaller than those in the turbulent region since the high frequency components have been emphasized after the original signal was differentiated. Therefore, for a

large value of  $s$ ,  $\int_0^s p_{nt}(s) ds$  is very close to 1, but

$\int_0^s e^{-s/A} ds$  is still a strong function of  $s$ . Equation (2) can be approximated for large values of  $s$  as:

$$P(s) = (1 - \Gamma) + \Gamma \left( \frac{1}{A} \int_0^s e^{-s/A} ds \right)$$

$$P(s) = 1 - \Gamma e^{-s/A}$$

$$1 - P(s) = \Gamma e^{-s/A}$$

$$\ln(1 - P(s)) = \ln \Gamma - s/A \quad (3)$$

$1 - P(s)$  is the cumulative intermittency function. Based on equation (3), the cumulative intermittency function plotted as  $\ln(1 - P(s))$  vs.  $s$  is a straight line for a large value of  $s$ . The intercept of this with the vertical axis is the intermittent factor. Once the intermittency is determined, the threshold value is obtained as shown in Fig. 1b. Therefore, using a single slope in the large value region of the criterion function to find an appropriate threshold value is justified and is convenient for the situation when no two distinctive slopes can be found, as in the present study of the elevated FSTI flows.

Note that one assumption made during the derivation is that the fluctuations of the criterion function in the non-turbulent portion are smaller than those in the turbulent portion. In elevated FSTI flows, the non-turbulent portion of the streamwise velocity fluctuations are disturbed so the high-frequency unsteadiness in the non-turbulent part cannot be easily separated from the turbulent in the turbulent portion. However, the Reynolds shear stress ( $\bar{uv}$ ), which indicated the physical turbulence transport, is much better than  $u$ , which is related to the turbulence energy, in demarcating the difference between turbulent and non-turbulent parts of the flow, as can be seen in Fig. 2.

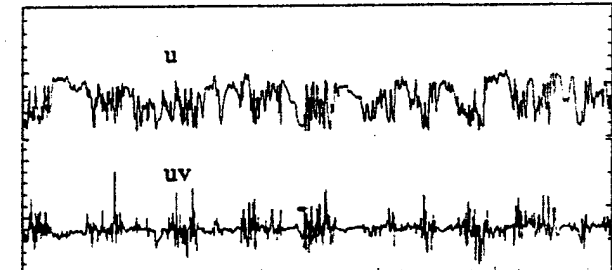


Fig 2a. Representative Instantaneous Signals of  $u$  and  $(uv)$  in a Transitional Boundary Layer with FSTI=6.4%.

## RESULTS AND DISCUSSION

Analysis has been performed for cases with FSTI of 3.8%, 5.5% and 6.4%, respectively at the onset of transition. Limited to the paper length, only the G3 case (6.4%) is presented in this paper. The baseline case used for comparison is documented in Wang et al. (1996). The unconditionally sampled results of the present study were reported in detail in Zhou and Wang (1995). These above

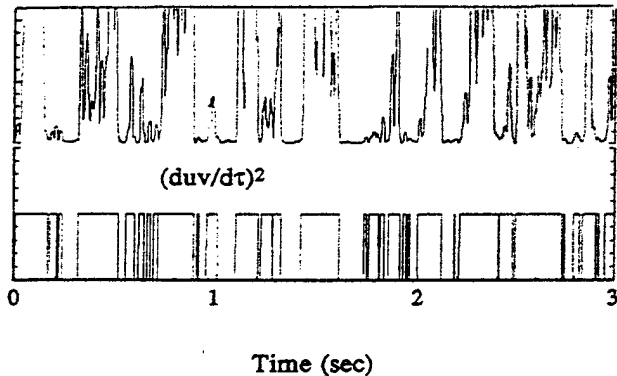


Fig.2b. An Example of the Criterion Function  $[d(uv)/d\tau]^2$  and Intermittency Functions

two papers will be helpful for analyzing the results of the present paper. The conditionally sampled results for FSTI cases of 3.8% and 5.5% were reported by Zhou (1993).

The profiles of the intermittency factor  $\Gamma(y)$  across the boundary layer at different streamwise locations for the G3 case are shown in Fig. 3. The intermittency factor data directly obtained are relatively scattered for the high FSTI case. Therefore a smoothing scheme using a moving average of five data points was employed. Only the smoothed results are presented in Fig. 3.

As shown in Fig. 3, the intermittency factor drops near the wall  $y/\delta < 0.1$  even in the turbulent station. This trend is different from the baseline case where a region of constant intermittency factor in the near-wall region was observed (Keller and Wang, 1995). This near-wall reduction of intermittency is different from the intermittency factor decrease in the outer boundary layer region. The reduction of  $\Gamma$  in the outer boundary layer is caused by the entrainment of the irrotational flow from the free stream. The intermittency factor reduction near the wall may be caused by the low Reynolds number effect in high FSTI cases. Recall that the elevated FSTI cases were conducted with low free-stream velocities in order to obtain sufficient transitional region in the test section. For the low Reynolds number case, the viscous sublayer based on  $y/\delta$  for the same  $Y^+$  value becomes thicker.

The streamwise evolution of the peak value of  $\Gamma$  of three elevated FSTI cases can be presented by the "universal" intermittency distribution, proposed by Dhawan and Narasima (1958), within a 10% band (not shown here see Zhou 1993).

#### CONDITIONALLY SAMPLED MEAN VELOCITY PROFILES

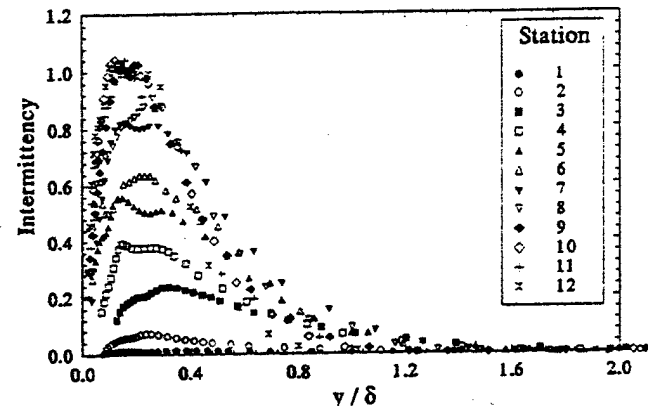


Fig. 3 Intermittency Distributions for G3 Case

Plots of conditionally sampled mean velocity profiles normalized by wall unit are shown in Fig. 4 for the G3 case. Three profiles: non-turbulent, unconditioned and turbulent parts of intermittent flow, are shown in each of these figures along with the viscous sublayer correlation,  $U^+ = Y^+$ , and the log law-of-the-wall curve for reference. The non-turbulent profiles represent the average of velocity data obtained during time segments when the intermittency function is zero. The turbulent profiles represent the  $U$  average of velocity data obtained during time segments when the intermittency function is one. Individual  $C_f$  of each part (non-turbulent or turbulent) was used to plot these three profiles. These  $C_f$  values were determined by using the methods described earlier according to non-turbulent, unconditioned, and turbulent profiles respectively.

For elevated FSTI, as shown in Fig. 4, the non-turbulent part profiles at low  $\Gamma$  (Station 3) agree well with the corresponding low FSTI laminar profiles, but start to deviate at higher  $\Gamma$  (Stations 5 and 8). The turbulent part profiles do not conform to the linear-log region until  $\Gamma=0.98$  (Station 8), and no wake region can be observed at this high FSTI level. The determined  $C_f$  values for the non-turbulent and turbulent parts are shown in Fig. 5, respectively. Also shown in Fig. 5 are the results for reconstructing the unconditioned  $C_f$  values using the local near-wall peak intermittency and a linear combination of the values obtained (a) from the experimental velocity profiles and (b) the corresponding laminar and fully turbulent correlations. Reconstructed total  $C_f$  values differ from the experimentally determined unconditioned  $C_f$  values. This result indicates that the skin friction in the non-turbulent turbulent portions does not behave as the laminar and turbulent flow at corresponding  $Re_x$ , respectively.

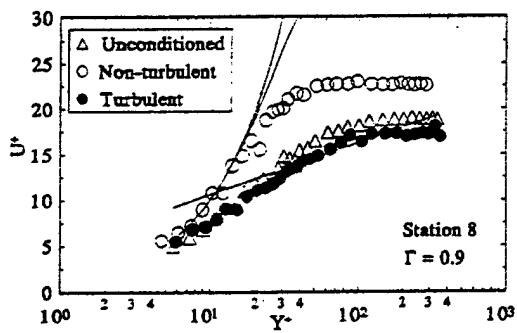
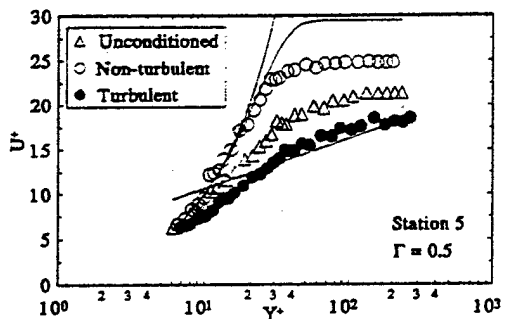
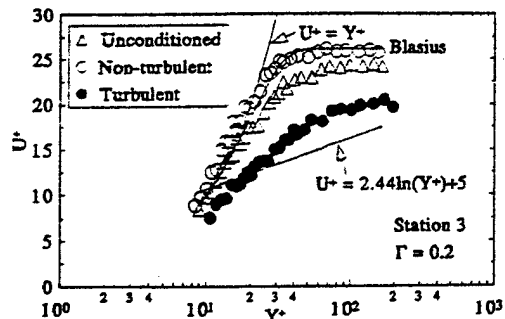


Fig. 4. Conditional Sampling Results.  $U^+$  vs.  $Y^+$ , G3 Case.

#### CONDITIONALLY SAMPLED FLUCTUATION PROFILES

Conditionally sampled streamwise velocity fluctuation ( $u'/U_\infty$ ) profiles at selected streamwise locations for the G3 case are presented in Fig. 6. The peak magnitudes of the non-turbulent part are about the same as the magnitudes of the turbulent part. This observation was different from that of the low FSTI cases of Kuan and Wang (1990), where the peak magnitudes of the turbulent part are much higher than the non-turbulent part.

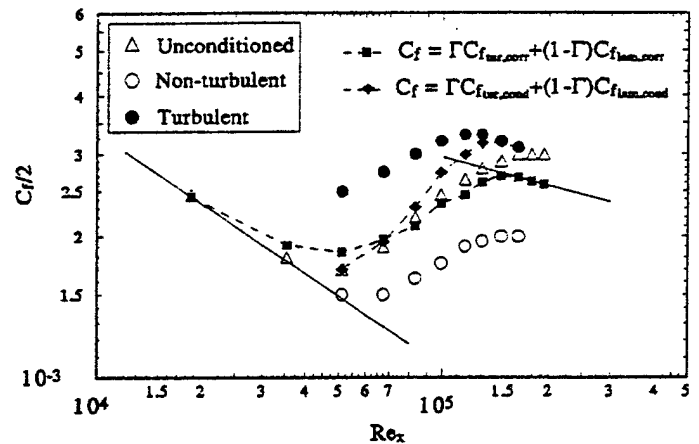


Fig. 5. Conditional Sampling Results,  $C_f/2$  vs.  $Re_x$ , G3 Case.

Comparison between the mean velocity profiles (Fig. 4) and  $u'$  in Fig. 6 shows that the non-turbulent part is highly disturbed at the elevated FSTI case; even the non-turbulent mean velocity profiles follow the low FSTI Blasius profile. The "step change" between the mean turbulent part and mean non-turbulent part does not have a major contribution to the overall unconditioned  $u'$  in the elevated FSTI case. If the step change were significant, the magnitude of the unconditioned  $u'$  would have been larger than the turbulent part  $u'$ .

Conditionally sampled cross-stream velocity fluctuations ( $v'/U_\infty$ ) profiles at selected streamwise locations for the G3 case are presented in Fig. 7. At low  $\Gamma$  stations (e.g., station 3), the magnitudes of  $v'/U_\infty$  for the unconditioned signals are lower than those in the turbulent part but higher than those in the non-turbulent part. At higher  $\Gamma$  stations (e.g., station 8), the magnitudes of  $v'/U_\infty$  for the unconditioned signal are about the same as those in the turbulent part. The magnitudes of  $v'/U_\infty$  in the non-turbulent part near the wall region are always lower than those in the turbulent part. These observations are similar to those at the low FSTI case, but are different from those of the  $u'/U_\infty$  profiles as shown in Fig. 6. This results in a less isotropic feature of the non-turbulent part for elevated FSTI cases. The above observation also implies that the cross-stream turbulence energy in the turbulent portion is actually higher than unconditioned values. The lower  $v'$  values in the non-turbulent portion are responsible for bringing down the unconditioned  $v'$  value. This also calls attention to cross-stream transport, which is undervalued by the unconditioned results in the elevated FSTI cases.

Conditionally sampled RMS temperature ( $t'/(T_w - T_\infty)$ ) profiles for the G3 case are presented in Fig. 8. The

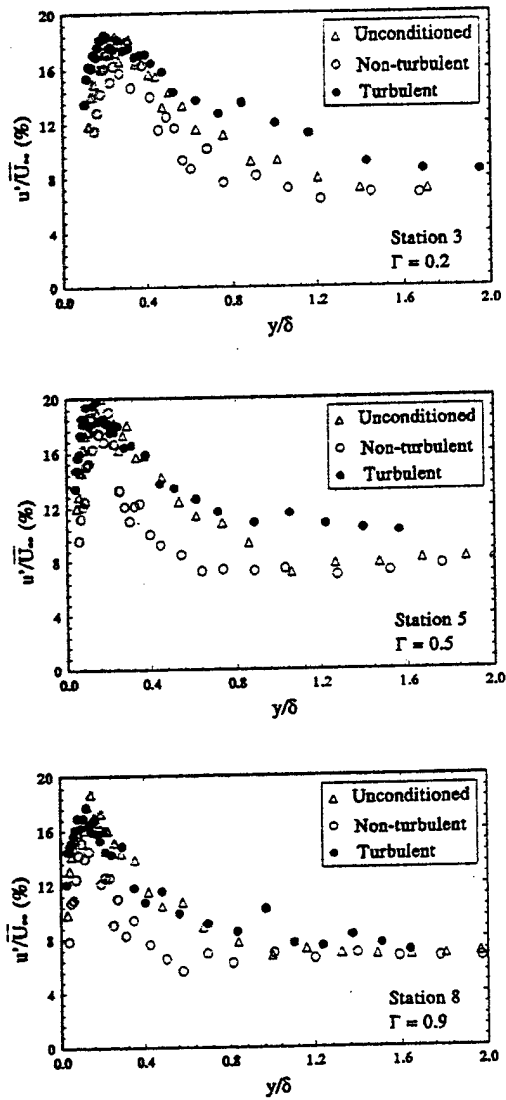


Fig. 6. Conditionally Sampled Results,  $u'/U_{\infty}$  vs.  $y/\delta$ , G3 Case.

comparisons of rms temperature magnitudes in the turbulent part and in the non-turbulent part are similar to those of  $u'/U_{\infty}$  shown in Fig. 6.

Conditionally sampled Reynolds shear stresses ( $\bar{uv}$ ) profiles are shown in Fig. 9. Individual  $C_f$  of each part (unconditioned, non-turbulent, and turbulent) was used to calculate corresponding  $u^*$  and for plotting each profile. As shown in this figure, the normalized Reynolds shear stresses in the turbulent part are about 1.8 times the wall shear stress and have about the same magnitudes of those in the unconditioned signal, but have much higher magnitudes of those in the nonturbulent part. This is similar to the low

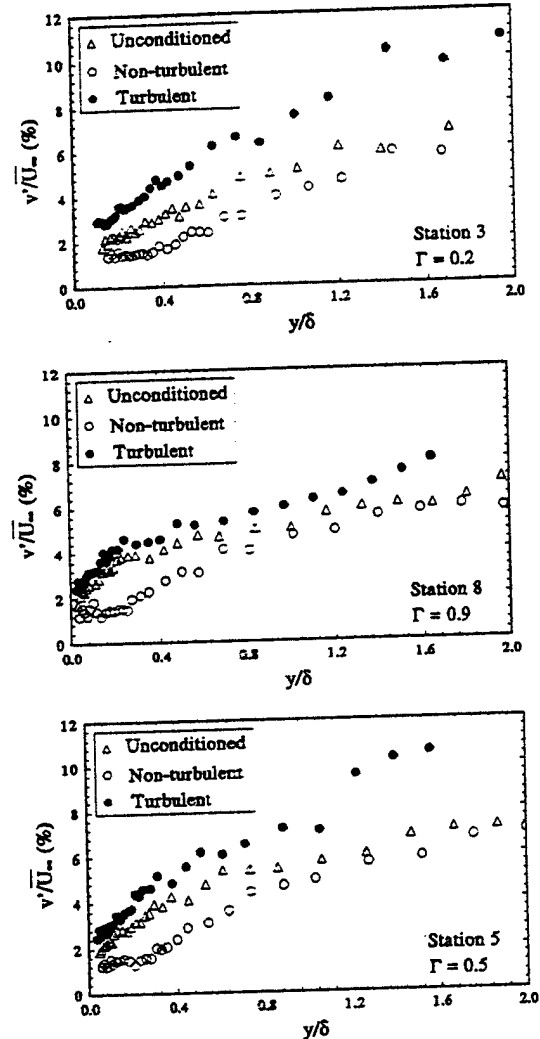


Fig. 7. Conditional Sampling Results,  $v'/U_{\infty}$  vs.  $y/\delta$ , G3 Case.

FSTI cases in Wang and Keller (1997), which showed that the turbulent part of  $\bar{uv}$  was as high as twice of the wall shear and was also higher than the unconditioned  $\bar{uv}$  in the most part of the transition flow. Nevertheless, the high Reynolds shear stress of the turbulent part implies that even  $u'$  and  $v'$  values are high in the non-turbulent part in a highly disturbed environment; the turbulent transport is dominantly accomplished in the turbulent part during the transitional process in a highly disturbed boundary layer.

Conditionally sampled streamwise Reynolds heat fluxes ( $\bar{ut}$ ) profiles are presented in Fig. 10. The averaged unconditioned wall heat fluxes in this figure were used for normalizing the non-turbulent part and the turbulent part. Three differences from the low FSTI case are observed: (i)

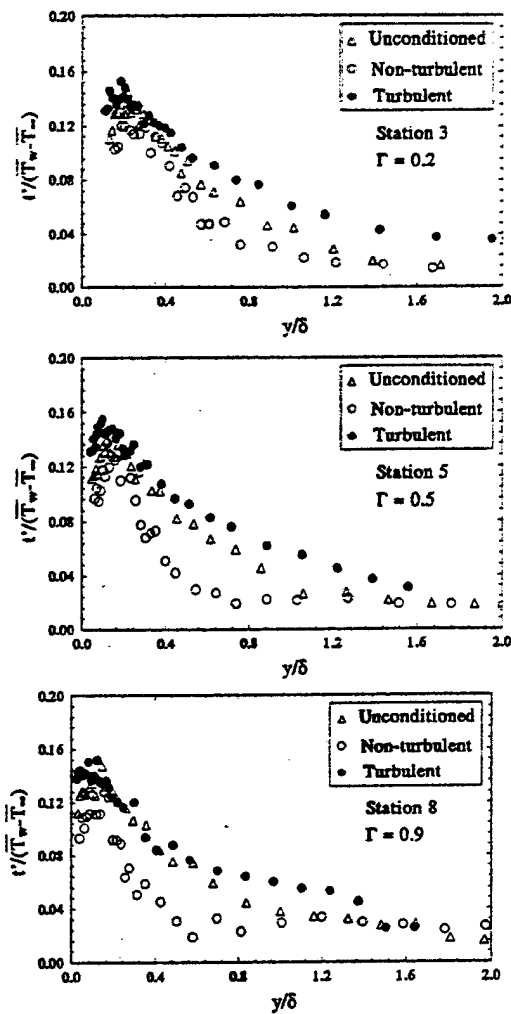


Fig. 8. Conditionally Sampled Results,  $t'/(T_w - T_\infty)$  vs  $y/\delta$ , G3 Case

The turbulent part of  $\bar{u}'$  in the earlier transition region ( $\Gamma < 0.6$ ) is higher than the nonconditioned part, whereas the high FSTI cases, both turbulent and unconditioned parts are of similar magnitudes. (ii) The peak values of the turbulent part for the low FSTI case are about 15 to 22 times of the wall heat flux, whereas they are merely above six times in the high FSTI case. (iii) The non-turbulent part of  $\bar{u}'$  in the low FSTI case is insignificant; whereas, in the high FSTI case, the non-turbulent  $\bar{u}'$  are as high as the turbulent part, in the near-wall region. It is not clear why the elevated FSTI does not enhance the overall turbulent heat flux transport in the streamwise direction, but augments the near-wall non-turbulent part of heat flux transport.

Conditionally sampled cross-stream Reynolds heat fluxes ( $\bar{v}'$ ) profiles are presented in Fig. 11. The magnitudes of the normalized cross-stream Reynolds heat fluxes in the

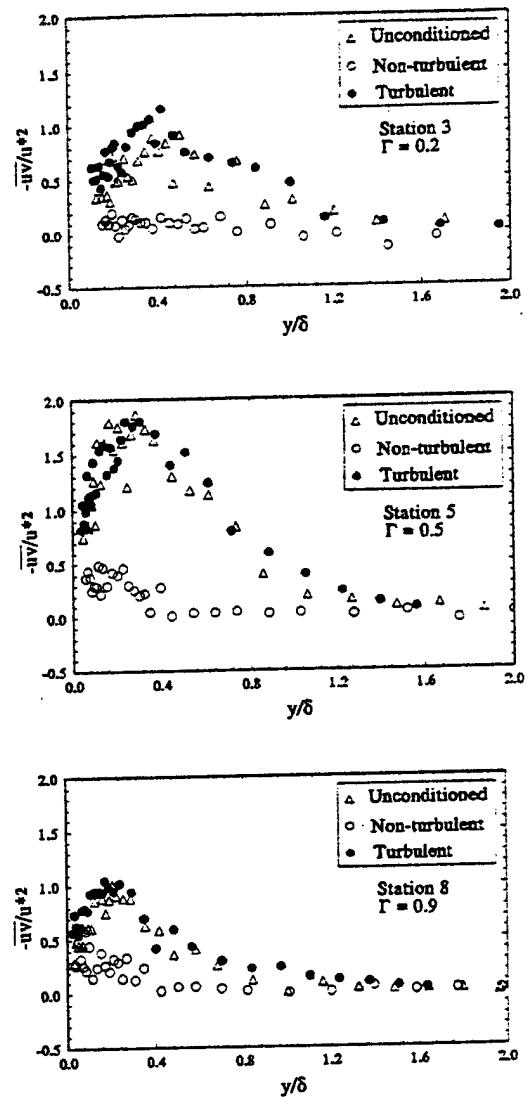


Fig. 9. Conditionally Sampled Results,  $-\bar{u}\bar{v}/\bar{u}'^2$ , G3 Case

turbulent part are higher than the unconditioned part and are much higher than those in the non-turbulent part. This implies that the cross-stream Reynolds heat fluxes, similar to the Reynolds shear stresses, are dominant in transporting momentum and heat flux in elevated FSTI cases. Large non-turbulent fluctuations, a specific feature in high FSTI situations, do not significantly contribute to  $\bar{u}\bar{v}$  and  $\bar{v}'$ , but significantly contribute to  $\bar{u}'$  and  $\bar{u}''$ .

## CONCLUSION

A modified conditional sampling technique was applied to separate the turbulent and non-turbulent parts of the transitional boundary layers subjected to elevated FSTI from 3.8% to 6.4%. This modified method applied one slope on

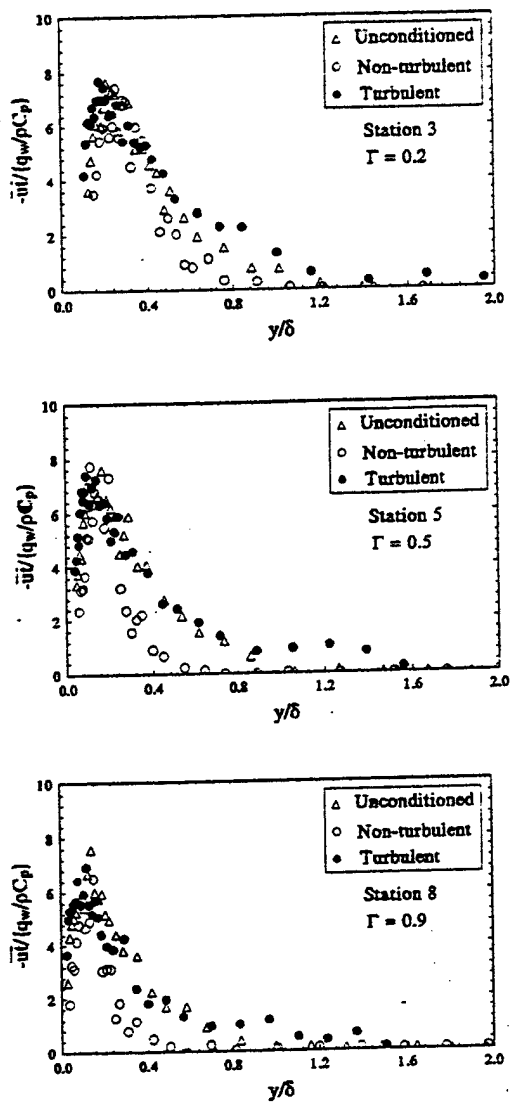


Fig. 10. Conditionally Sampled Results,  $\bar{u}'v'/(q_w/pC_p)$ , G3 Case.

the accumulative probability diagram to determine threshold values. It was convenient to apply and was also theoretically verified. The results showed that using the instantaneous Reynolds stress signal ( $uv'$ ) instead of  $u'$  signal can enhance the certainty for demarcating the turbulent and non-turbulent signals. This implies that using the turbulence transport behavior was superior to employing the turbulence energy for separating the turbulent and non-turbulent signals.

The conditionally-sampled results showed that the non-turbulent part was highly disturbed at elevated FSTI cases as could be seen from the large values of  $u'$ ,  $v'$  and  $\bar{u}'v'$ , which were comparable to the magnitude of the turbulent part. This was contrary to the low FSTI cases. On the other hand, similar to the low FSTI cases, the major turbulence

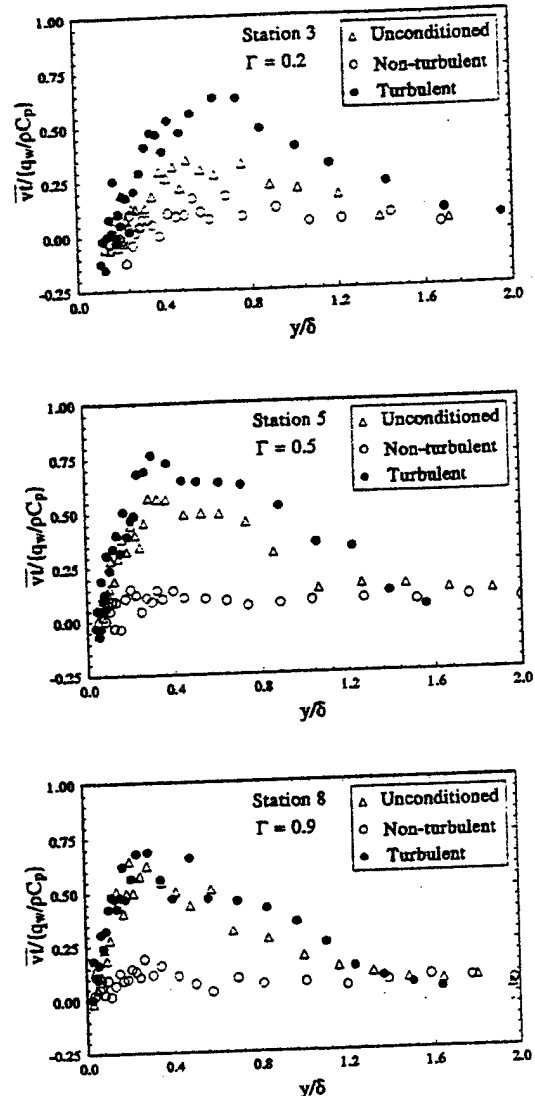


Fig. 11. Conditionaly Sampling Results,  $\bar{u}'v'/(q_w/pC_p)$ , G3 Case.

transports of momentum and heat fluxes, i.e.,  $\bar{u}'v'$  and  $\bar{v}'v'$  were insignificant in the non-turbulent part. This implied that although the velocity trace of the non-turbulent part was hardly distinguishable from the turbulent part in a highly disturbed environment; the underlined flow and thermal transport mechanisms of the non-turbulent part were distinctively different from the turbulent part.

#### ACKNOWLEDGMENT

This program was sponsored by the Office of Naval Research (Grant No: N00014-89-J-3105) and the Air Force Office of Scientific Research (Grant No: F49620-94-1-0126). The program monitors were Dr. Gabriel D. Roy and Dr. James McMichael, respectively.

## REFERENCES

Blair, M.F., "Boundary-Layer Transition in Accelerating Flows with Intense Freestream Turbulence: Part 1- Disturbances Upstream of Transition Onset, Part 2- The Zone of Intermittent Turbulence," ASME Journal of Fluids Engineering, Vol. 114, pp. 331-332.

Chua, L.P. and Antonia, R.A., 1990, "Turbulent Prandtl Number in a Circular Jet," International Journal of Heat and Mass Transfer, Vol. 33, No. 2, pp.331-339.

Clauser, F.H., 1956, "The Turbulent Boundary Layer," Advances in Applied Mechanics, Vol. 4, pp. 1-51.

Farmer, R. and Fulton, K., 1995 "Design 60% Net Efficiency in Frame 7/9 H Steam-Cooled CCGT," Gas Turbine World, May-June, pp. 12-22.

Graham, R.W., 1979, "Fundamental Mechanisms That Influence the Estimate of Heat Transfer to Gas Turbine Blades, ASME paper" 79-HT-43, ASME, NASA TM-79128.

Graham, R.W.(ed.), 1984, "Transition in Turbines," Symposium Proceedings, NASA CP-2386.

Dhawan, S. and Narasimha, R. 1958, "Some Properties of Boundary Layer Flow During the Transition From Laminar to Turbulent Flow," Journal of Fluid Mechanics, Vol. 3, pp. 418-436.

Halstead, D.E., Wister, D.C., Okiishi, T.H., Walker, G.J., Hodson, H.P. and Shin, H., 1995, "Boundary Layer Development in Axial Compressor and Turbines," Part 1: Composite Picture; Part 2: Compressors; Part 3: LP Turbines; Part 4: Computations and Analyses. ASME papers 95-GT-460, 461, 462, 463.

Hedley, T.B. and Keffer, J.F., 1974, "Turbulent/Non-turbulent Decisions in an Intermittent Flow," Journal of Fluid Mechanics, Vol. 64, pp. 625-644.

Keller, F.J. and Wang, T., 1995, "Effects of Criterion Functions on Intermittency in Heated Transitional Boundary Layers With and Without Streamwise Acceleration," ASME Journal of Turbomachinery, Vol. 117, pp. 154-165.

Keller, F.J., 1993, "Flow and Thermal Structures in Heated Transitional Boundary Layers With and Without Streamwise Acceleration," Ph.D. Dissertation, Department of Mechanical Engr., Clemson University, Clemson, S.C.

Kim, J., Simon, T.W., and Kestoras, M. 1994, "Fluid Mechanics and Heat Transfer Measurements in Transitional Boundary Layers Conditionally Sampled on Intermittency," ASME Journal of Turbomachinery, Vol. 116, pp.405-416.

Kuan, C.L. and Wang, T., 1990, "Investigation of the Intermittent Behavior of a Transitional Boundary Layer Using a Conditional Averaging Technique," Experimental Thermal and Fluid Science, Vol. 3, pp. 157-170.

Mayle, R.E., 1991, "The Role of Laminar-Turbulent Transition in Gas Turbine Engines," ASME Journal of Turbomachinery, Vol. 113, pp. 509-537.

Shome, B., 1991,"Development of a Three-Wire Probe for the Measurement of Reynolds Stresses and Heat Fluxes in Transitional Boundary Layers," M.S. Thesis, Department of Mechanical Engr., Clemson University, Clemson, S.C.

Sohn, K.H. and Reshotko, E., 1991, "Experimental Study of Boundary Layer Transition with Elevated Free-Stream Turbulence on a Heated Plate," NASA CR-187068.

Sohn, K.H., OBrien, J.E., and Reshotko, E., 1989, "Some Characteristics of Bypass Transition in a Heated Boundary Layer," Presented at the 7th Turbulent Shear Flow Symposium.

Steelant, J. and Dick, E., 1996, "Modelling of Bypass Transition with Conditional Navier-Stokes Equations Coupled to an Intermittency Transport Equation," International Journal for Numerical Methods in Fluids, Vol. 23, pp. 193-220.

Turner, A.B., 1971, "Local Heat Transfer Measurements on a Gas Turbine Blade,"Journal of Mechanical Engineering Sciences, Vol. 13, 1, pp. 1-12.

Wang, T. and Keller, F.J., 1997, "Intermittent Flow and Thermal Structures of Accelerated Transitional Boundary Layers, Part 1: Mean Quantities and Part 2: Fluctuation Quantities," presented at the ASME Turbo Expo '97, Orlando, FL.

Wang, T., Keller, F.J. and Zhou, D., 1992, "Experimental Investigation of Reynolds Shear Stresses and Heat Fluxes in a Transitional Boundary Layer," ASME HTD Vol. 226, Fundamental and Applied Heat Transfer Research for Gas Turbine Engines, pp. 61-70.

Wang, T., Keller, F.J., and Zhou, D., 1996, "Flow and Thermal Structures in a Transitional Boundary Layer," Experimental Thermal and Fluid Science, Vol. 12, pp.352-363.

Zhou, D., 1993, "Effects of Elevated Free-Stream Turbulence and Streamwise Acceleration on Flow and Thermal Structures in Transitional Boundary Layers," Ph.D. Dissertation, Department of Mechanical Engineering, Clemson University, Clemson, S.C.

Zhou, D. and Wang, T., 1995, "Effects of Elevated Free-Stream Turbulence on Flow and Thermal Structures in Transitional Boundary Layers," ASME Journal of Turbomachinery, Vol. 117, pp. 407-417.

# The Effects of Adverse Pressure Gradients on Momentum and Thermal Structures in Transitional Boundary Layers: Part 1—Mean Quantities

S. P. Mislevy

T. Wang

Department of Mechanical Engineering,  
Clemson University,  
Clemson, SC 29634-0921

*The effects of adverse pressure gradients on the thermal and momentum characteristics of a heated transitional boundary layer were investigated with free-stream turbulence ranging from 0.3 to 0.6 percent. The acceleration parameter,  $K$ , was kept constant along the test section. Both surface heat transfer and boundary layer measurements were conducted. The boundary layer measurements were conducted with a three-wire probe (two velocity wires and one temperature wire) for two representative cases,  $K1 = -0.51 \times 10^{-6}$  and  $K2 = -1.05 \times 10^{-6}$ . The surface heat transfer measurements were conducted for  $K$  values ranging from  $-0.045 \times 10^{-6}$  to  $-1.44 \times 10^{-6}$  over five divergent wall angles. The Stanton numbers of the cases with adverse pressure gradients were greater than that of the zero-pressure-gradient turbulent correlation in the low-Reynolds-number turbulent flow, and the difference increased as the adverse pressure gradient was increased. The adverse pressure gradient caused earlier transition onset and shorter transition length based on  $Re_{\tau}$ ,  $Re_{\delta}^*$ , and  $Re_{\delta}$  in comparison to zero-pressure-gradient conditions. As expected, there was a reduction in skin friction as the adverse pressure gradient increased. In the  $U^+ - Y^+$  coordinates, the adverse pressure gradients had a significant effect on the mean velocity profiles in the near-wall region for the late-laminar and early transition stations. The mean temperature profile was observed to precede the velocity profile in starting and ending the transition process, opposite to what occurred in favorable pressure gradient cases in previous studies. A curve fit of the turbulent temperature profile in the log-linear region for the  $K2$  case gave a conduction layer thickness of  $Y^+ = 9.8$  and an average  $Pr = 0.71$ . In addition, the wake region of the turbulent mean temperature profile was significantly suppressed.*

## Introduction

Transition from laminar to turbulent flow causes an increase in both skin friction and convective heat transfer. Accurate predictions of these increases are important in design considerations; inaccurate predictions can have a serious effect on the aerodynamics of compressor and turbine blades, the reliability of turbine vanes and blades, and the thermal efficiency of gas turbine systems. In order to calculate momentum losses and blade heat transfer, one must be able to predict boundary layer development accurately throughout transition.

Transition can be affected by a number of parameters, such as pressure gradients, surface curvature, free-stream turbulence, surface roughness, and acoustic disturbances, to name a few. Each of these parameters can influence the start and length of transition, the flow characteristics, and the structure of the transitional boundary layer. The focus of this research was to study the isolated effect of adverse (positive) pressure gradients on the flow structure and heat transfer in a transitional boundary layer in order to contribute to the understanding of fundamental physics and to increase the data base so that future transition modeling and computational predictions can be improved.

Schubauer and Skramstad (1948) showed oscillograms of streamwise velocity fluctuations on a flat plate with a nonuniform external velocity distribution. Negative (or favorable) pressure gradients appeared to damp out the oscillations, whereas positive (or adverse) pressure gradients caused a strong amplification and produced earlier transition.

Knapp and Roache (1968) used a smoke-visualization technique and found that an adverse pressure gradient affects the stages of transition differently than does a zero-pressure gradient. Besides a change in the development and shape of the vortex trusses, the formation and breakdown of smoke wave sets occurred at a higher rate than those for the zero-pressure-gradient case, with only a short hesitation between wave sets.

Abu-Ghannam and Shaw (1980) studied natural transition on a flat plate for turbulence intensities of 0.3 to 5 percent and  $\lambda_s$  ranging from 0.06 to -0.08. With their experimental data, in addition to previous available data, a new family of curves was proposed for pressure-gradient cases where the momentum thickness Reynolds number at the start of transition,  $Re_{\tau_0}$ , is a function of  $\lambda_s$  and FSTI. From these curves it was deduced that at a given turbulence level, the effect of the adverse pressure gradient for promoting transition is greater than the effect of the favorable pressure gradient for retarding it. In addition, from the plot of  $Re_{\tau_0}$  versus  $\lambda_s$ , it can be seen that the effect of the pressure gradients becomes less significant than the effect of FSTI as the turbulence level increases, and that small pressure gradients have incrementally more influence than larger ones have for low-FSTI cases. When they plotted the intermittency

Contributed by the International Gas Turbine Institute and presented at the 40th International Gas Turbine and Aeroengine Congress and Exhibition, Houston, Texas, June 5-8, 1995. Manuscript received by the International Gas Turbine Institute February 4, 1995. Paper No. 95-GT-4. Associate Technical Editor: C. J. Russo.

factor against a normalized transition length scale,  $\eta$  ( $= (x - x_s)/(x_e - x_s)$ ), no effect due to pressure gradient could be detected.

The effects of pressure gradient and free-stream turbulence intensity on the length of transition were further studied by Fraser et al. (1988). Their data showed that while the turbulence level remains constant, an increase in the adverse pressure gradient causes a decrease in the transition length Reynolds number. In addition, they found that when the turbulence level is increased beyond 1.4 percent, the free-stream turbulence becomes the dominant controlling parameter. Fraser et al. also concluded that neither the pressure gradient nor the turbulence level has any significant influence on the distribution of intermittency in the transitional boundary layer flows tested, where  $\lambda_\theta < -0.06$  and  $FSTI \leq 1.45$  percent. Acharya (1985) found phenomena similar to that described by Fraser et al., but up to a higher  $FSTI$  value of about 3 percent.

Walker (1989) developed a minimum transition length model based on a continuous breakdown hypothesis which is similar to forced transition and gives reasonable estimates for transition length in adverse pressure gradients. This transition length correlation,  $Re_t = 2.30 Re_{\theta,0}^{1.5}$ , represents the minimum transition length that corresponds to the maximum adverse pressure gradient parameter,  $\lambda_\theta = -0.082$ , for an attached laminar boundary layer at transition inception. The actual transition length should lie between the values predicted by this model and those of zero-pressure-gradient correlations.

Walker and Gostelow (1989) investigated the effects of adverse pressure gradients on the length of boundary layer transition and introduced a correlation for transition length. The experimental investigations were undertaken at an inlet free-stream turbulence intensity of 0.3 percent. The results indicated that  $Re_{\theta,0}$  at the onset of transition declines mildly with a slight increase in the adverse pressure gradient and levels off to a fairly constant value under moderately strong adverse pressure gradients. However, the end of transition occurred much sooner when increasingly adverse pressure gradients were applied. The change in  $Re_{\theta,0}$  at the end of transition was most noticeable when a zero-pressure gradient was replaced by even a weak adverse pressure gradient. This observation is consistent with the conclusions of Abu-Ghannam and Shaw (1980).

Walker and Gostelow (1989) found physical differences in instability waves between zero- and adverse pressure gradients.

In a zero-pressure gradient, transition occurs randomly due to the breakdown of laminar instability waves in sets. However, for an adverse pressure gradient, Tollmien-Schlichting waves appear more regularly, and the flow steadily evolves from random to periodic behavior as the pressure gradient becomes more adverse. The results of Walker and Gostelow (1989) indicate that the shape factor,  $H$ , is close to the local equilibrium turbulent flow value at the 99 percent intermittency point for the zero-pressure-gradient case, but it increasingly exceeds this value as the pressure gradient becomes more adverse, which suggests the possibility that the shape factor may not be settled at the 99 percent intermittency point.

Gostelow and Walker (1991) evaluated their transitional skin-friction values by using the relationship  $C_f = (1 - \Gamma)C_{f,lm} + \Gamma C_{f,turb}$ . The skin-friction value at the onset of transition was determined in the near-wall region by linear extrapolation of  $U^* = Y^*$ , and the skin-friction value at transition completion was obtained by using  $\tau_w/\rho = 0.0464(\nu/U_\infty\delta)^{0.25}U_\infty^2/2$ . Again, the shape-factor value at the end of transition appears to stabilize only for zero and low adverse pressure gradients, with  $dH/dx$  becoming increasingly negative as the pressure gradient becomes more adverse. This means that the shape factor continues to decrease even after intermittency measurements indicate transition completion. Thus, a linear combination of the laminar and turbulent properties in proportion to the intermittency, such as above, may be inappropriate for adverse pressure gradients. Actually, Kuan and Wang (1990) pointed out that even for flow without a pressure gradient, linearly combining the laminar and turbulent properties is questionable, since the nonturbulent part of a transitional flow is highly disturbed laminar flow, and the turbulent part is not fully developed.

Regarding heat transfer within the transition region, Sharma (1987) compared transition lengths between the thermal and momentum boundary layers and found that for flows developing under adverse pressure gradients, the length of transition for the thermal boundary layer is shorter than that of the momentum boundary layer. Sharma modeled the effects of both favorable and adverse pressure gradients on the thermal boundary layer by defining a new thermal intermittency factor that is a function of pressure gradient and momentum thickness Reynolds number for both the thermal and the momentum boundary layers. Although this model gave improved estimates of the heat transfer coefficient on the surface for adverse pressure gradients, not

## Nomenclature

$C_p$ = specific heat	$U, V$ = streamwise and cross-stream instantaneous velocity; $U = U + u$ , $V = V + v$
$C_f$ = skin friction	$U, V$ = mean velocity components
$FSTI$ = free-stream turbulence intensity	$u, v, w$ = instantaneous velocity fluctuations
$= \sqrt{(u'^2 + v'^2 + w'^2)}/3/U_\infty$	$u', v', w'$ = rms value of velocity fluctuations
$H$ = shape factor = $\delta^*/\theta$	$U_{\infty,0}$ = free-stream velocity at station 1
$K$ = acceleration parameter = $(\nu/U_\infty^2)/(dU_\infty/dx)$	$U^* = U/U_\infty$
$L$ = length of transition	$U_f$ = friction velocity = $\sqrt{\tau_w/\rho}$
$Pr$ = turbulent Prandtl number	$UHSL$ = unheated starting length
$q''_w$ = wall heat flux	$x$ = streamwise distance from leading edge
$Re_x$ = local Reynolds number	$x_0$ = unheated starting length
$Re_{\theta,0}$ = displacement thickness Reynolds number = $U_\infty\delta^*/\nu$	$y$ = normal distance from wall
$Re_\theta$ = momentum thickness Reynolds number = $U_\infty\theta/\nu$	$Y^*$ = dimensionless distance from wall = $yU_\infty/\nu$
$St$ = Stanton number, Eq. (1)	$\Gamma$ = intermittency
$T$ = instantaneous temperature = $T + t$	
$T$ = mean temperature	
$T^* = (T_w - T)/\sqrt{\tau_w/\rho(\rho_w C_p)/q''_w} = \sqrt{C_p/2/St}$	

$U, V$ = streamwise and cross-stream instantaneous velocity; $U = U + u$ , $V = V + v$	$\delta$ = boundary layer thickness at 0.995 $U_\infty$
$U, V$ = mean velocity components	$\delta^*$ = displacement thickness = $\int_0^x (1 - U/U_\infty) dy$
$u, v, w$ = instantaneous velocity fluctuations	$\eta$ = normalized transition distance = $(x - x_s)/(x_e - x_s)$
$u', v', w'$ = rms value of velocity fluctuations	$\theta$ = momentum thickness = $\int_0^x (U/U_\infty)(1 - U/U_\infty) dy$
$U_{\infty,0}$ = free-stream velocity at station 1	$\lambda_\theta$ = pressure gradient parameter = $(\theta^2/\nu)(dU_\infty/dx)$
$U^* = U/U_\infty$	$\nu$ = kinematic viscosity
$U_f$ = friction velocity = $\sqrt{\tau_w/\rho}$	$\rho$ = density
$UHSL$ = unheated starting length	$\tau_w$ = shear stress
$x$ = streamwise distance from leading edge	
$x_0$ = unheated starting length	
$y$ = normal distance from wall	
$Y^*$ = dimensionless distance from wall = $yU_\infty/\nu$	
$\Gamma$ = intermittency	

$\delta$ = boundary layer thickness at 0.995 $U_\infty$
$\delta^*$ = displacement thickness = $\int_0^x (1 - U/U_\infty) dy$
$\eta$ = normalized transition distance = $(x - x_s)/(x_e - x_s)$
$\theta$ = momentum thickness = $\int_0^x (U/U_\infty)(1 - U/U_\infty) dy$

$\lambda_\theta$ = pressure gradient parameter = $(\theta^2/\nu)(dU_\infty/dx)$
$\nu$ = kinematic viscosity
$\rho$ = density
$\tau_w$ = shear stress

## Subscripts

$cl$ = conduction layer
$\infty$ = free-stream value
$e$ = end of transition
$s$ = start of transition
$w$ = at the wall
$lm$ = laminar
$turb$ , $t$ = turbulent

much information is available regarding heat transfer inside transitional boundary layers with an adverse pressure gradient. Therefore, in addition to fluid mechanics, detailed experimental investigations of thermal transport are also needed since the Reynolds analogy breaks down when pressure gradients are involved. This paper aims to provide such information. The results of this study, conducted in low free-stream turbulence environments, will serve as the baseline cases for future studies in elevated free-stream environments, which are closer to real gas turbine conditions.

## Experimental Program

The test facility used an existing two-dimensional, open-circuit, blowing-type wind tunnel. A detailed description of the wind tunnel and its qualification is given by Kuan (1987) and Wang et al. (1992). A heat exchanger utilizing a continuous fresh supply of city water was used to keep the free-stream temperature uniform and steady. Boundary layer suction was applied at the leading edge in order to initiate a new boundary layer at the leading edge of the test section.

The test section was 0.15 m wide, 0.92 m high, and 2.4 m long. One 0.92 m  $\times$  2.4 m vertical face of the test section served as the outer wall. This flexible lexan wall allowed for adjustment of the pressure streamwise gradient along the plate.

The opposing 0.92 m  $\times$  2.4 m face functioned as the heated test plate. One hundred and eighty-nine E-type thermocouples, 3 mil in diameter, were embedded in the 0.25-mm 3M-413 tape between the heater and the lexan test wall. Seventy-four of the thermocouples were located along the streamwise centerline of the wall, and the remaining thermocouples were placed in cross-span locations. A foil heater was used, custom-designed such that about 90 percent of the heater area was actively heated. A detailed description of the heated test wall was documented in Wang et al. (1992) and Keller (1993).

**Selection of Pressure Gradient.** A parameter to characterize the effects of the pressure gradients was sought to perform the experiment. The most common parameters used in the literature are:

$$\beta = \frac{\delta^*}{\tau_w} \frac{dP_w}{dx} \quad (\text{Clauser, 1954}),$$

$$\lambda_\theta = \frac{\theta^2}{\nu} \frac{dU_w}{dx} \quad (\text{Thwaites, 1960}),$$

$$\Lambda = \frac{\delta^2}{\nu} \frac{dU_w}{dx} \quad (\text{Pohlhausen, 1921}),$$

$$K = \frac{\nu}{U_w^2} \frac{dC_w}{dx} \quad (\text{Brown and Martin, 1976}),$$

$$\Delta\tau_w = \frac{\nu}{U_w^2} \frac{d\tau_w}{dx} \quad (\text{Patei et al., 1968}), \text{ and}$$

$$p^+ = \frac{\nu}{\rho U_w^2} \frac{dP_w}{dx} \quad (\text{Narayanan et al., 1969}).$$

The first three parameters incorporate the past history of the boundary layer through the use of  $\delta$ , or through an integral parameter, such as  $\delta^*$  or  $\theta$ . For experimental purposes, obtaining constant  $\beta$ ,  $\lambda_\theta$ , and  $\Lambda$  values requires boundary layer measurements that are undesirably time consuming during setup of the test section. The last two parameters require measurement of the wall shear stress, which is also inconvenient. However, the acceleration parameter,  $K$ , sometimes termed the velocity gradient factor, represents the overall free-stream flow-field effect while being independent of the flow history in the boundary layer. The desired constant  $K$  value can be simply obtained by adjusting the inlet velocity and the outer wall angle by first

keeping the outer wall in a wedge configuration and then fine-tuning it locally to accommodate the effect of the boundary layer growth. Therefore, for this study, the degrees of strength of the various pressure gradients were represented by the use of this acceleration parameter,  $K$ . Many researchers attempt to relate the  $\lambda_\theta$  value at transition onset to  $K$  at transition onset through  $\lambda_\theta = \text{Re}_{\theta}^2 K$ , but as pointed out by Zhou and Wang (1992), constant  $K$  and constant  $\lambda_\theta$  (Falkner-Skan) flows are physically different, and comparing a corresponding location between these two flows based on the strength of the pressure gradient at the single location in the flow field requires caution.

At each wall configuration, the absolute value of  $K$  can be increased by decreasing the reference free-stream velocity. The  $K$  values and free-stream velocities were chosen so that the complete laminar-turbulent transition was located on the test wall. For the present study,  $K$  ranges from  $-0.045 \times 10^{-6}$  to  $-1.44 \times 10^{-6}$ , and the acceleration parameter was set equal to a constant streamwise value for each test case.

**Instrumentation.** Two independent, computer-controlled acquisition systems acquired data for both surface heat transfer and boundary layer quantities. One system measured the test plate thermocouple data, and the second system recorded momentum and thermal boundary layer values taken with a thermal anemometry system.

The 189 thermocouples used in the surface heat transfer tests were scanned by a Fluke 2205A Switch Controller at a rate of one reading per second. The average reading of two consecutive scans was obtained for each thermocouple.

A single hot-wire and a three-wire probe were used to make all boundary layer measurements. A single hot-wire TSI model 12185-T1.5 was operated in a constant-temperature mode with an overheat ratio of around 1.8. This single-wire probe was used for velocity measurements as close to the test surface as  $Y^+ \approx 3$  for the present study. These near-wall measurements are essential to obtaining skin-friction coefficients.

The three-wire probe contained two velocity wires (2.5- $\mu\text{m}$ , platinum-coated tungsten wire) and one cold wire (1.5- $\mu\text{m}$  platinum wire). The 2.5- $\mu\text{m}$  wires were arranged to measure the streamwise and cross-stream velocity components in a constant-temperature mode while the cold wire, which operated in a constant current mode with a constant current of 0.1 mA, was used to measure temperature variations. The three-wire probe was used simultaneously to measure velocity and temperature signals. Since adverse pressure gradients reduce transition length, low velocities were used in order to "stretch" the transition region so that more measurement stations (15 cm apart) could be located in the transition region. The "cross-talk" between the hot and cold wires becomes amplified at low velocities, so the velocity wires were compromised to operate with low overheat ratios of around 1.3. At this low overheat ratio, the frequency response of the velocity sensors of the three-wire probe was nevertheless satisfactory with a response between 5 and 15 kHz for velocities from 3 to 10 m/s. The frequency response for the temperature wire was experimentally determined by Keller (1993) to be from 4800 to 6400 Hz. The "cross-talk" (or heat contamination) between the cold and hot wires was found to be negligible by comparing the velocity results obtained with and without the cold wire in operation and the temperature results obtained with and without the hot wires in operation. A sampling frequency of 2 kHz for 20 seconds was used for both the three-wire and single-wire probes. For future spectral analysis (not included in this paper), frequencies above 1 kHz were filtered so as to prevent aliasing errors. A detailed description of this three-wire probe is documented in Wang et al. (1996) and Shorne (1991). Two additional  $x$ -wires were used for measuring  $v'$ ,  $w'$ ,  $\bar{uv}$ , and  $\bar{uw}$ , respectively, in the free stream.

The same data-acquisition system was used to obtain signals from both the single hot-wire and the three-wire probes. The

sensors were attached to a probe holder which was held by a single-axis, micrometer-traversing mechanism capable of moving in 0.005-mm increments. Two TSI IFA-100 constant temperature bridges were used for the hot wires, and a DISA constant current bridge was used for the cold wire. A four-channel MetraByte Simultaneous Sample and Hold box (SSH4) and a DAS-20 A/D converter were used to simultaneously take signals from the three wires.

Both the single hot-wire and the three-wire probe were calibrated in situ in the wind tunnel test section. The temperature sensor of the three-wire probe was calibrated by using a heated free jet in a temperature range of 10°C to 50°C against a calibrated *E*-type thermocouple. The calibration for the thermocouples in the test plate was done at four isothermal conditions (no wall heating) of different free-stream temperatures with a constant free-stream velocity of 13 m/s. The uncertainty of the calibrated thermocouples was within  $\pm 5 \mu V$  ( $\pm 0.08^\circ C$ ).

**Experimental Procedure.** For the surface heat transfer tests, two consecutive scans of all 189 thermocouples were made for each test. The results were then averaged to reduce the effects of any uncontrollable random errors. Steady state was assumed when the centerline Stanton number values varied less than  $\pm 2.0$  percent for all measurement locations.

The boundary layer measurements were made at 30 locations across the boundary layer for each station. Baseline tests (zero-pressure gradient) of both surface heat transfer and boundary layer measurements can be found in Wang et al. (1992, 1996) or Keller (1993); these test results will be used for comparison in this paper.

**Data Reduction.** The surface heat transfer was nondimensionalized in terms of the Stanton number,

$$St = \frac{q''_w}{\rho_w C_p, u_\infty (T_w - T_\infty)} \quad (1)$$

The free-stream air properties and temperature were corrected for both compressibility effects and humid air conditions.

The above wall heat-flux term,  $q''_w$ , was calculated based on an energy balance within the test wall. The heat losses such as upstream and downstream conduction,  $Q_{cond}$ , radiation from the test surface,  $Q_{rad}$ , and back losses,  $Q_{back}$ , were subtracted from the power input,  $Q_{in}$ . Thus, the net heat flux was determined by  $q''_w \Delta A = Q_{in} - Q_{cond} - Q_{rad} - Q_{back}$ , where  $\Delta A$  is the area defined by a 6.45-cm<sup>2</sup> (1-in<sup>2</sup>) element centered around each thermocouple in the test plate. The velocity used in determining the local Stanton number at each thermocouple location was calculated by integrating the acceleration parameter,  $K$ , which was obtained from 14 measured free-stream velocities along the test section. The upstream conduction loss near the leading edge was not corrected, so the uncertainty is higher at the leading edge.

Since no direct measurement of the wall shear stress was made, the skin friction was determined from the shape of the velocity profiles when plotted in terms of the wall coordinates

$U^+$  and  $Y^+$ . For the laminar and turbulent regions, the experimental velocity profiles were converted into wall units and were compared to the numerical results from the STAN5 code (NASA/Lewis version), which is a two-dimensional parabolic solver for boundary layer flows. Using an iterative procedure, the  $C_f$  values and the wall configuration (the distance between the first sample location and the actual test wall surface) were fine-tuned for each profile until each individual profile best matched the STAN5 results in the near-wall region. A mixing length model with a correction for van Driest damping coefficient for adverse pressure gradients was used.

For the transitional boundary layer, the determination of  $C_f$  is more complicated. One method of determining  $C_f$  in transition involves the practice of superimposing weighted laminar and turbulent skin-friction values, but as discussed by Kuan and Wang (1990), this method is at best questionable. A second method involves forcing the two-dimensional momentum integral to close; however, Wang et al. (1985) and Keller (1993) have shown that this method results in unreasonable large values of  $C_f$  due to the three dimensionality of the transition region. A third method is to assume that the velocity profile in the viscous sublayer of a transitional flow still behaves like Couette flow. Based on this assumption, the experimental velocity profiles were matched to the inner-wall ( $Y^+ \leq 5$ ) correlation,  $U^+ = Y^+$ , by using an iterative procedure similar to that used for the laminar flows to determine the skin friction in the transitional flow regime. Velocity data acquired by the single hot wire (not shown in this paper) were used to determine  $C_f$  since it could get closer to the wall than could the three-wire probe. However, the practice of forcing the near-wall mean velocity profiles to match the  $U^+ = Y^+$  curve in the transition region is not appropriate in early transition for adverse pressure-gradient flows due to the counteracting behavior between adverse pressure gradients and transition on the velocity profiles for  $Y^+ < 10$ , as will be discussed later.

The boundary layer temperature data were reduced to the form of mean temperature profiles and plotted as  $T^+$  versus  $Y^+$ . As with the velocity profiles, this data was compared with the numerical results from the STAN5 code in the laminar and turbulent regions. In addition, the profiles for the turbulent region were compared to the conduction-layer correlation,  $T^+ = Pr Y^+$ , in the region very near the wall ( $Y^+ < 5$ ) and to the law-of-the-wall in the log-linear region. For the transition region, the profiles in the near-wall region were matched to the conduction-layer correlation. However, it will be shown later that the data failed to match the log-linear region.

The Reynolds stresses and heat fluxes will be presented in Part 2 of this paper. A detailed uncertainty was performed by Mislevy (1993). Representative uncertainty of the mean quantities is listed in Table 1.

**Uncertainty Analysis.** Following the methodology of Kline and McClintock (1953), an uncertainty analysis was conducted. In order to determine the propagation of the individual uncertainties into the resultant quantities, the sensitivity coefficient was determined by perturbing each independent variable by its uncertainty value within the data reduction program and noting the change in the resultant quantity (Moffat, 1982).

Using this technique, the resultant uncertainties in Stanton number from both fixed and variable inputs resulted in an overall uncertainty in Stanton number of 5 percent. The uncertainty for the three-wire probe is shown in Table 1 for  $y/\delta = 0.2$ . The primary contributor to uncertainty in  $V$ ,  $\bar{w}$ , and  $\bar{u}$  is the angle between the mean flow and the normal to the sensor. The hot-wire calibration equations are the largest contributor to the uncertainty in  $C$  and  $u'$ . The uncertainties in the integral parameters are also summarized in Table 1. The uncertainty in the wall location ( $y = 0$ ) is the major contributor to the uncertainty in displacement thickness,  $\delta^*$ , and momentum thickness,  $\theta$ .

Table 1 Uncertainties of mean quantities and integral parameters

Parameter	Uncertainty (%)
$U$	5.83
$T / T_w - T_\infty$	1.23
$\delta^*$	4.2
$\theta$	6.2
$H$	7.5
$Y^+$	4.7
$U^+$	4.7
$T^+$	3.2

## Results and Discussion

Surface heat transfer measurements were made for constant  $K$  values between  $-0.045 \times 10^{-6}$  and  $-1.44 \times 10^{-6}$  over five divergent wall angles. In order to compare the experimental results in the laminar and turbulent regions, the STAN5 code was run using the free-stream experimental velocity distributions and corrected wall heat fluxes as boundary conditions. The Stanton number distributions for two representative cases are shown in Fig. 1(a). As the adverse pressure gradient in the laminar region increased, the STAN5 predictions increasingly deviated from the zero-pressure-gradient case ( $K = 0$ ). The largest Reynolds number for each laminar prediction curve is the point where the STAN5 breaks down, which indicates a possible boundary layer separation in the computed flow, although this is not necessarily true for the real flow. The Stanton number at this point, which is also the location of the largest deviation, shows about a 26 percent difference from the  $K = 0$  case. In the turbulent region, the STAN5 predictions for adverse pressure gradients also show a deviation from the  $K = 0$  curve; however, it should be noted that varying free-stream velocities at a constant  $K$  value produce significantly different curves in the low-Reynolds-number region. The same pressure distribution ( $K$  value) with different  $U_{\infty}$  results in different Stanton number distributions. The deviation from the zero-pressure-gradient correlation is greater at higher velocities. This is shown in Fig. 1(a) for  $K = -1.05 \times 10^{-6}$  and is not significant in the laminar region.

For comparison, Fig. 1(b) shows the STAN5 skin-friction results. The effect of the adverse pressure gradient on  $C_f$  is stronger than it is on the Stanton number, with larger deviations from  $K = 0$  in both the laminar and turbulent regions. In other words, the Reynolds analogy ( $2St/C_f$ ) between heat and momentum transfer is not valid for adverse pressure-gradient flows due to the greater effect of negative  $K$  on momentum boundary layer structures, as was modeled by the STAN5. In the laminar

region, both the  $C_f$  and the  $St$  are below the  $K = 0$  curve. In the turbulent region, however, the  $C_f$  falls below the  $K = 0$  curve while the  $St$ , although less affected, is higher than the  $K = 0$  curve. The  $C_f$  is little changed by varying the  $U_{\infty}$  for the same  $K$  value although higher velocities result in the prediction of possible separation further upstream. Clauser (1954) found that adverse pressure gradients have a large effect on skin friction for equilibrium turbulent boundary layers and that even relatively small gradients can reduce skin-friction coefficients by up to 50 percent of zero-pressure-gradient values at the same Reynolds number. For favorable pressure-gradient results, however, the opposite was found to be true. In favorable pressure-gradient cases, Zhou (1993) found both the  $C_f$  and the  $St$  in the laminar region to be higher than the  $K = 0$  curve, and in the turbulent region Zhou found the  $C_f$  to be higher than the  $K = 0$  curve while the  $St$  was lower. In addition, Zhou (1993) showed that favorable pressure gradients also have a larger effect on  $C_f$  than on Stanton number.

**Experimental Stanton Number Results.** Figure 2 shows the experimental Stanton number distribution for wall configuration 1, which has the smallest divergent angle (1.2 deg) and thus the lowest constant  $K$  values. At a fixed divergent wall angle, a lower  $U_{\infty}$  results in a higher  $K$  value, and the corresponding laminar correlation curves differ as well, as shown in Fig. 2 with  $U_{\infty}$  values of 2 m/s and 16 m/s. For the sake of clarity, instead of plotting every correlation curve for each velocity in the laminar flow region, only one representative curve for the  $K = 0$  cases is plotted in the remaining  $St$  versus  $Re_x$  figures. The laminar and turbulent correlations for zero-pressure gradient can be found in Kays and Crawford (1980) for a constant heat-flux surface:

$$St_{lam} = 0.453 Pr^{-0.67} Re_x^{-0.5} [1 - (x_0/x)^{0.75}]^{-0.333} \quad (2)$$

$$St_{turb} = 0.03 Pr^{-0.4} Re_x^{-0.2} [1 - (x_0/x)^{0.9}]^{-0.111} \quad (3)$$

The  $St$  values in Fig. 2 initially follow the  $K = 0$  correlation and begin to deviate from this line as the Reynolds number is increased. Near the leading edge, the  $St$  data are lower than the  $K = 0$  correlation, possibly due to the uncorrected upstream conduction loss, as discussed earlier in the uncertainty analysis. Transition starts when the  $St$  reaches a minimum value, which is at about the same  $Re_x$  for all of the cases in this figure due to the low  $K$  values associated with this wall angle. In the early transition region, the Stanton numbers for all of the cases follow a well-ordered distribution until midway through transition. At this point, significant scatter develops, which will be discussed later. Although this scatter is present, there is a trend that shows the end of transition occurring at increasingly lower Reynolds numbers as the adverse pressure gradient increases ( $|K|$  increases).

Figure 3 shows the Stanton number distribution for wall configuration 2 (divergent angle of 2.6 deg) in which stronger decelerated flows were obtained. As can be seen, the higher  $K$  cases result in earlier onset of transition. The Reynolds number at the end of transition could not be determined simply from the wall heat transfer behavior due to the unfamiliar behavior of the Stanton number patterns. There are in fact two noticeable features in the Stanton number distribution in Fig. 3: (1) the local "twist" in the transition region for the smaller  $K$  cases (higher velocities) and (2) the overshoot past the turbulent correlation for the larger  $K$  cases. As the end of transition is approached, there is an increasing overshoot (about 40 percent) beyond the zero-pressure-gradient turbulent correlation as the pressure gradient is increased. These overshoots are consistent within 5 percent of the STAN5 predictions. For clarity, the STAN5 predictions are not shown in Fig. 3; examples of STAN5 predictions are shown in Fig. 1. However, experimental Stanton number data from Orlando et al. (1974) and Blackwell et al. (1972) for all turbulent, equilibrium adverse pressure-

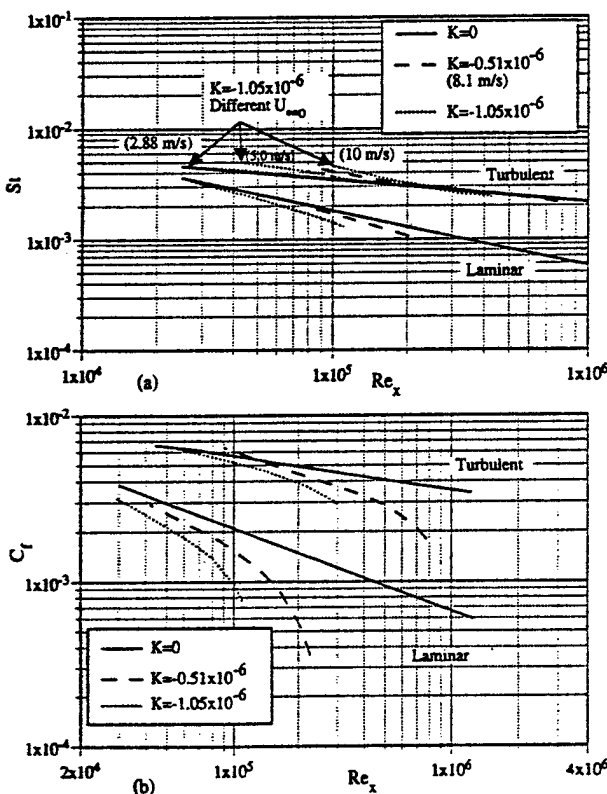


Fig. 1 STAN5 results for (a) Stanton number and (b) skin friction for two constant  $K$  cases

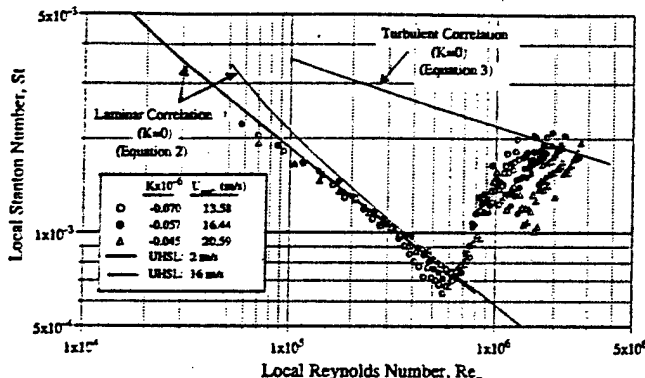


Fig. 2 Local surface heat transfer for wall configuration 1 with a divergent angle of 1.2 deg for various  $K$  values

gradient flows show very close agreement with the zero-pressure-gradient turbulent correlation when plotted against enthalpy thickness Reynolds number. However, no data were available in their studies for the Stanton number when explicitly plotted against Reynolds number based on physical  $x$ . The limited boundary layer measurements (for two cases) in this present study do not provide sufficient enthalpy thickness information for comparison with their data.

The Stanton number distributions for wall configurations 3, 4, and 5 (divergent angles of 3.5, 4.4, and 5.6 deg, respectively) show the same trends in the presence of increasing adverse pressure gradients as did positions 1 and 2, such as overshooting the zero-pressure-gradient turbulent correlation and an earlier onset of transition. Although the earlier transition onset is apparent at each wall angle for increasing  $K$ , Fig. 4 shows the overall effect of constant  $K$  flows produced at different angles and  $U_{\infty}$ . As can be seen, stronger negative constant  $K$  flows produce earlier transition onset regardless of the wall angle. The sharp "twist" in the transition region for the lower  $K$  cases of wall configurations 1 and 2 (Figs. 2 and 3) turns into a broad scatter at the end of transition for cases having larger divergent angles and increasingly higher  $U_{\infty}$ . The overshoot past the zero-pressure-gradient turbulent correlation associated with higher  $K$  values disappears as the  $K$  value is reduced. The slope of the Stanton number distribution in the early transition region appears to become steeper as the  $K$  value increases, reflecting the shorter transition region (based on  $Re_x$ ) that results from increasing the adverse pressure gradient. The Stanton number appears to be a good parameter for determining the onset of transition, but the peculiar distribution and scatter of the Stanton number within the late-transition and turbulent regions makes it difficult to determine the end of transition.

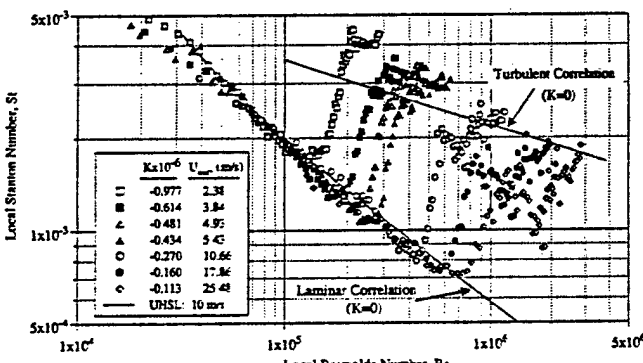


Fig. 3 Local surface heat transfer for wall configuration 2 with a divergent angle of 2.6 deg for various  $K$  values; slower  $U_{\infty}$  results in higher  $K$  value

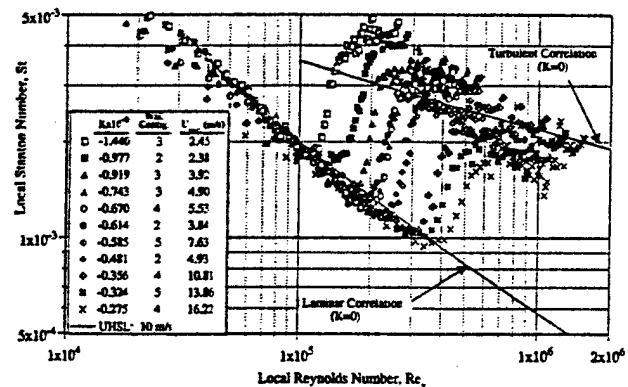


Fig. 4 Comparison of Stanton number for different pressure gradients at wall divergent angles of 1.2, 2.6, 3.5, 4.4, and 5.6 deg

To determine the cause of this scatter, several possible sources were investigated, such as nonconstant heat flux produced by the heater and separation of the boundary layer from the test surface. However, as explained below, neither nonconstant heat flux nor separation was found to be present.

A single hot wire was used to obtain flow information in the boundary layer and skin-friction measurements on the wall for a flow with a reference free-stream velocity of 20.1 m/s and  $K = -0.027 \times 10^{-6}$ . Figure 5 shows an overlay of the skin friction and the Stanton number for this case. Both the  $C_f$  and the Stanton number show the same location for the onset of transition; however, their locations at the end of transition differ markedly. The  $C_f$  overshoots the STAN5 turbulent results by about 5 percent in the early turbulent region and then approaches the turbulent correlation as the Reynolds number increases. However, the Stanton number, as seen before at high  $U_{\infty}$ , develops significant scatter midway through transition with a region that indicates a decrease in the heat transfer coefficient. From information indicated by the flow structures in the boundary layer (such as mean velocity profiles, fluctuating velocities, and shape factors), the turbulent region starts at about  $1.3 \times 10^6$  (or the location of  $C_f, \text{max}$ ). Therefore, if these instabilities are causing the Stanton number scatter, then strangely they are not affecting the mean or fluctuating streamwise velocities (not shown here; see Mislevy, 1993) within the boundary layer. In addition, the  $C_f$  distribution does not suggest the existence of a separation bubble since no near-zero value for the  $C_f$  was found. The actual cause of this peculiar Stanton number distribution is still not known although it seems to be intensified by the application of increased adverse pressure gradients and increased free-stream velocities. At  $K = 0$ , the scatter disappears.

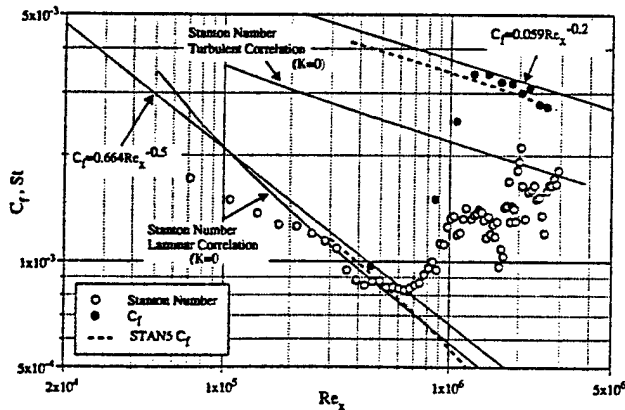


Fig. 5 Centerline Stanton number and skin friction distribution for  $K = -0.027 \times 10^{-6}$  ( $U_{\infty} = 20.1 \text{ m/s}$ )

A direct comparison between two of the adverse pressure gradient and the corresponding baseline results for free-stream velocities of a similar magnitude at  $x = 18$  cm are shown in Fig. 6. Both the onset and the end of transition clearly occur earlier for the decelerating cases than for the corresponding baseline cases.  $K$  versus  $Re_x$  is plotted in Fig. 7, which shows that  $Re_x$  decreases sharply in the presence of weak adverse pressure gradients and then seemingly levels off for stronger adverse pressure gradients. It should be noted that the transition onset data in this figure from Gostelow et al. (1992) are based on the intermittency of the momentum boundary layer, rather than surface heat transfer. The strengths of the adverse pressure gradients of Gostelow et al. (1994) were measured based on  $\lambda_s$  at transition inception. Neither  $K$  nor  $\lambda_s$  values were maintained as a constant in their study. The  $\lambda_s$  values at the onset of transition for the flows of Gostelow et al. were converted to  $K$  values based on the relationship  $K = \lambda_s/Re_x^2$ .

**Boundary Layer Investigation.** In order to gain an understanding of the effects of adverse pressure gradients on the momentum and thermal transport mechanisms in the transitional boundary layer, two representative decelerating cases were chosen for a boundary layer investigation. A medium and a strong adverse pressure gradient were chosen, each at a different wall angle. The obtained  $K$  values were  $K = -0.51 \times 10^{-6}$  at wall configuration 3 (3.5 deg) and  $K = -1.05 \times 10^{-6}$  at wall configuration 2 (2.6 deg), which will be termed K1 and K2, respectively, for the remainder of the discussion. The  $K$  values were determined as described earlier.

The FSTI and the isotropy factors (the ratio of  $v'/u'$  and  $w'/u'$ ) for each case are shown in Fig. 8. The FSTI is fairly constant for each of the three cases ranging from 0.3 to 0.6 percent although the decelerating cases show a slight increase

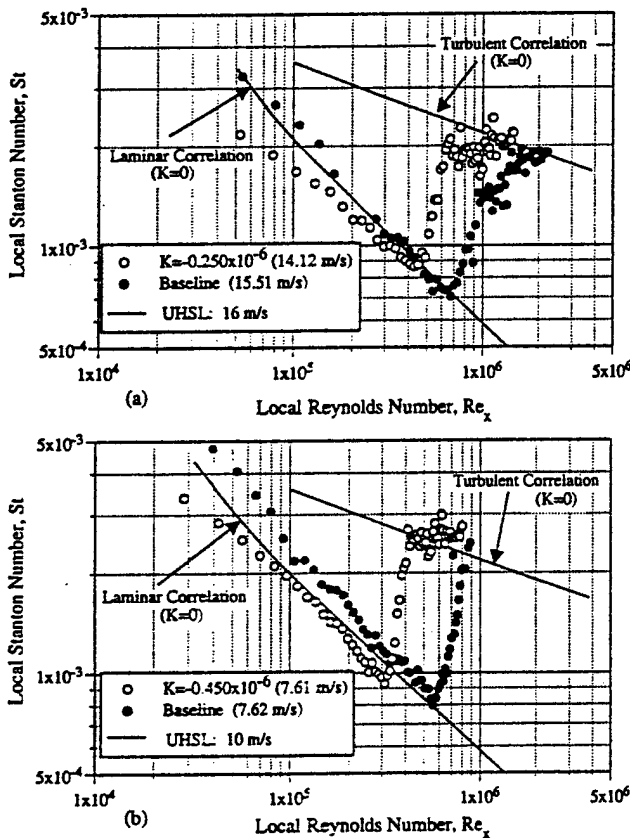


Fig. 6 Comparison of local surface heat transfer behavior between baseline and adverse pressure gradient cases at a similar magnitude of free-stream velocity at  $x = 18$  cm

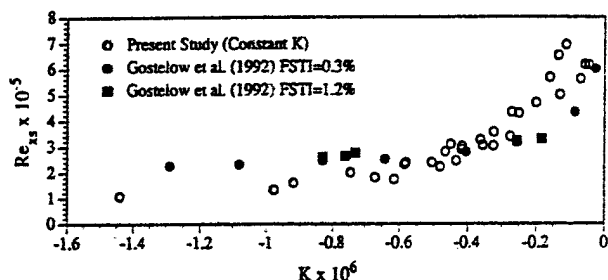


Fig. 7 Comparison of  $Re_x$  with different adverse pressure gradients. The data from Gostelow et al. were plotted by converting its  $\lambda_s$  values at the onset of transition to  $K$  values.

in FSTI downstream. The ratio of  $v'/u'$ , as measured by a  $uv$  x-wire, decreases in the presence of increased adverse pressure gradients. The values are not isotropic, and  $v'$  appears to be suppressed as the adverse pressure gradient is increased. The ratio of  $w'/u'$ , as measured by the  $uw$  x-wire, is mostly isotropic for the baseline and the K1 case. However, for the K2 case,  $w'$  is also suppressed. This can be explained as vortex compression in a divergent channel with thin boundary layers, similar to the explanation of vortex stretching in a contraction by Uberoi (1956) and Tennekes and Lumley (1972): The velocity fluctuations associated with an "eddy" aligned with the mean flow decrease, and those associated with an eddy perpendicular to the mean flow increase in a contraction. This phenomenon is reversed in a divergent channel. Therefore, both  $v'$  and  $w'$  decrease in a divergent channel since they are associated with eddies aligned with the mean flow.

The free-stream integral length scales ( $\lambda$ ) shown in Fig. 8 vary from 1.9 to 3.0 cm and are consistently larger than the baseline case. The scattered distribution of  $\lambda$  for the K2 cases is due to uncertainty in the low-speed flow. The integral length

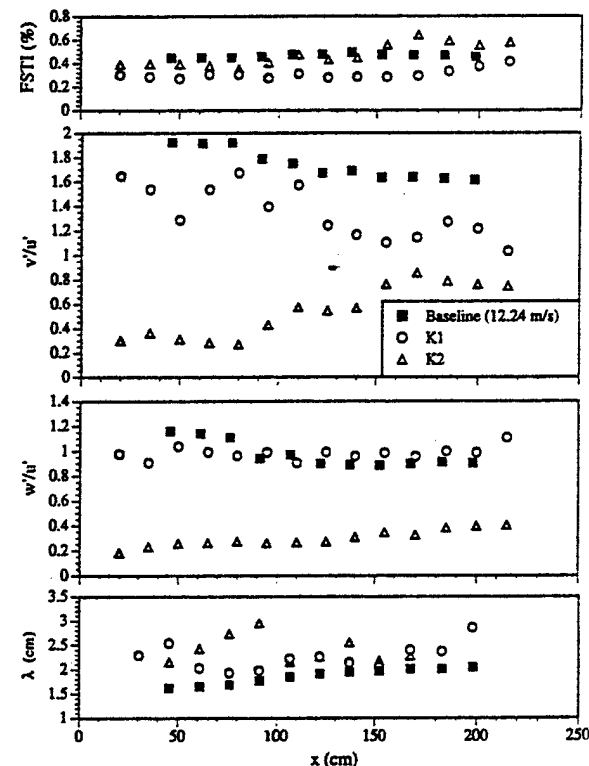


Fig. 8 Streamwise distribution of FSTI,  $v'/u'$ ,  $w'/u'$ , and integral length scale for K1 and K2 cases

scales were calculated by integrating the autocorrelation of  $u'$  to the first zero crossing, which gives the integral time scale, and then, by assuming that the Taylor hypothesis is valid, multiplying the integral time scale by the mean velocity.

**Skin Friction and Integral Parameters.** The variation of the skin-friction coefficient obtained from the measurements of both the single hot-wire and the three-wire probes is shown in Fig. 9. The skin-friction values for laminar and turbulent flow from the STAN5 solutions are also shown in Fig. 9 for comparison. In both the laminar and the turbulent regions, the experimental skin frictions are higher than the STAN5 predictions but are significantly lower than the baseline  $C_f$  values for increasingly adverse pressure gradients. The onset and the end of transition were first chosen at the locations where the skin friction reaches its minimum and maximum, respectively. However, the actual position may occur slightly on either side of the chosen locations due to the space between measurement stations. Therefore, the onset and the end of transition were later cross-checked with the Stanton number distribution, the shape factors, and other mean and fluctuating parameters in the boundary layer. It is also observed that higher negative  $K$  values cause earlier transition onset and shorter transition length in terms of  $Re_x^*$ ,  $Re_\delta^*$ , and  $Re_\theta$  (Table 2).

The integral parameters are shown in Fig. 10. The growth rates of  $\delta$ ,  $\delta^*$ , and  $\theta$  for both of the adverse pressure-gradient cases appear to be about the same, but they are larger than those of the baseline cases. The shape factor,  $H$ , shows larger values in the laminar region than for the baseline case. The shape factors for the decelerated cases rise to about 3.4 before transition onset and then decrease to between 1.5 and 1.6 in the turbulent region. This tendency for  $H$  values to rise at the end of the laminar flow is distinctively different from the tendency for  $H$  values to be lower for the baseline case. Increasingly adverse pressure gradients appear to produce higher values of shape factor in both the laminar and the turbulent regions. The tendency for  $H$  values to rise at the end of the laminar flow also indicates that the rate of increase for  $\delta^*$  is faster than it is for  $\theta$ , as can be seen from the local maximum  $\delta^*$  values at  $x = 60$  cm for the  $K1$  case and at  $x = 80$  cm for the  $K2$  case. For all of the cases in this study, the shape factor has reached its turbulent value by the end of transition. However, Gostelow et al. (1992) reported that  $H$  continues to fall after transition completion for strong adverse pressure gradients ( $\lambda_e \approx -0.05$  to  $-0.07$ ), but that this change is not significant for weak pressure gradients. Gostelow et al. attribute this result to the strong lag effects on the velocity profiles and the shorter transition lengths associated with stronger adverse pressure gradients. Although Gostelow et al. (1994) determined the end of transition based on intermittency ( $\Gamma = 0.99$ ), their mean velocity profiles at this intermittency value follow the log-linear turbulent law-of-

Table 2 Reynolds numbers at onset and end of transition for cases with boundary layer measurements

	Baseline ( $K=0$ )	$K1 = -0.51 \times 10^{-6}$	$K2 = -1.05 \times 10^{-6}$	
$U_\infty$ (m/s)	12.24	8.13	2.88	
PSTI (%) at $x_s$	0.50	0.30	0.35	
Onset of	$Re_x$	$5.50 \times 10^5$	$3.01 \times 10^5$	$1.35 \times 10^5$
Transition	$Re_\delta^*$	1294	1227	986
End of	$Re_\theta$	492	373	294
Transition	$Re_x$	$11.2 \times 10^5$	$4.28 \times 10^5$	$2.33 \times 10^5$
Length of	$Re_\delta^*$	1826	1423	1045
Transition	$Re_\theta$	1302	946	679
	$Re_{x,L}$	$5.70 \times 10^5$	$1.27 \times 10^5$	$0.98 \times 10^5$
Length of	$Re_{\delta^*,L}$	532	196	59
Transition	$Re_{\theta,L}$	810	573	385

the-wall in  $U^+ - Y^+$  coordinates. It will be shown that although no delay in the shape factor was found in this study, the mean velocity profiles at the determined end of transition also follow the log-linear turbulent law-of-the-wall. In addition, the pressure gradients of Gostelow (1994) were defined by the value of  $\lambda_e$  at transition onset, and the physical difference between that flow and a constant  $K$  flow may be a reason for the discrepancy with the current results.

**Mean Velocity and Mean Temperature Profiles.** The  $U^+$  versus  $Y^+$  mean velocity profiles for the three-wire probe were determined as described earlier, using the single hot-wire measurements as a guide. The STAN5 predictions for the velocity profiles in the laminar and turbulent regions were obtained and used as a guide in these regions. These profiles are shown in Fig. 11(a) for the  $K1$  case. In the laminar region, the adverse pressure gradient causes the velocity profile in the near-wall region to pull away from (move above) the Couette flow  $U^+ = Y^+$  curve for locations further downstream. As a result, for station 3 of the  $K1$  case the laminar profile matches the  $U^+ = Y^+$  curve only for  $Y^+ < 2$ . Only stations 2 and 3 are obtained in the laminar region since the STAN5 code breaks down after station 3. In the turbulent region, the STAN5 predicts a shortened and steeper log-linear region and stronger wake regions as  $Re_x$  increases.

Figure 11(b) shows the STAN5 predictions for the  $K1$  case temperature profiles. In the laminar region, the adverse pressure gradient causes the temperature profiles to become increasingly lower than the conduction-layer correlation,  $T^+ = \text{Pr}Y^+$ , as  $Re_x$

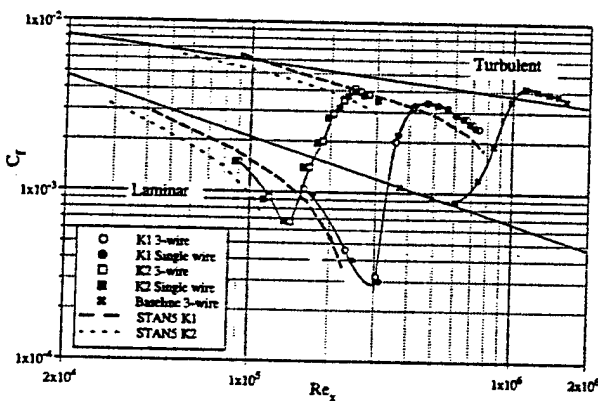


Fig. 9 Comparison of skin friction between the baseline and two decelerating cases with  $K1 = -0.51 \times 10^{-6}$  and  $K2 = -1.05 \times 10^{-6}$

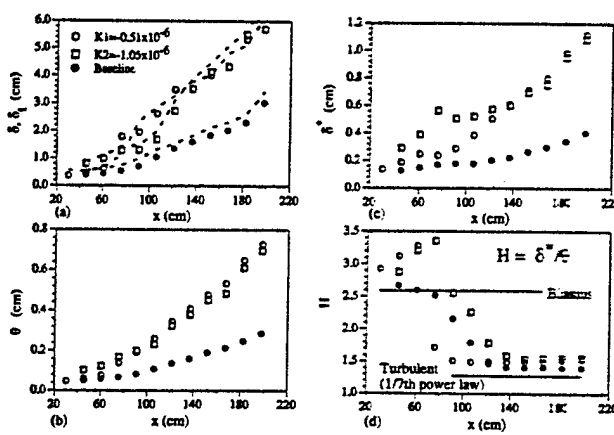


Fig. 10 Boundary layer integral parameters for the baseline,  $K1$ , and  $K2$  cases (--- thermal boundary layer thickness,  $\delta_t$ )

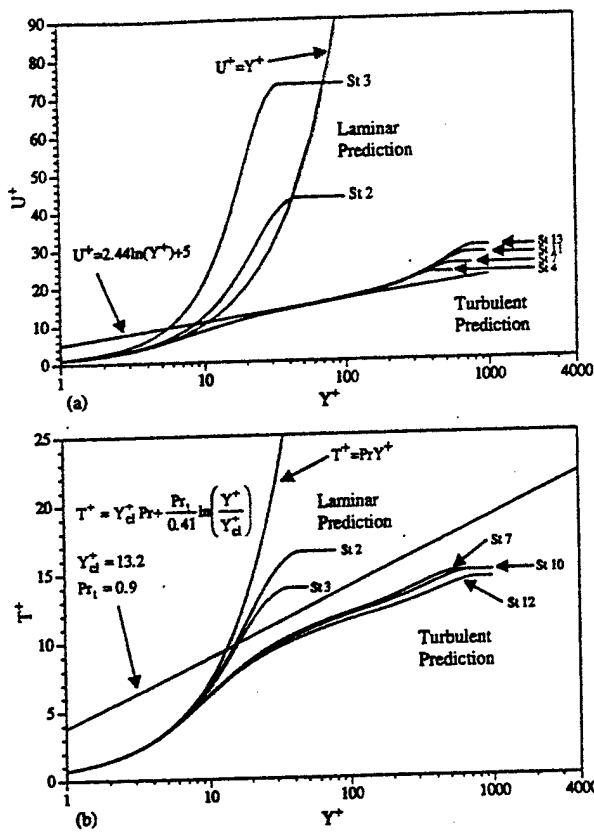


Fig. 11 Results of the STAN5 prediction of (a) velocity profiles and (b) temperature profiles for corresponding stations of  $K_1 = -0.51 \times 10^{-6}$

increases. This phenomenon is opposite to the effect of the adverse pressure gradient on the velocity profiles. In the turbulent region, the STAN5 predictions show an increasing undershoot of the thermal law-of-the-wall with an indistinct log-linear region.

Although the STAN5 predicts a possible separation of the laminar boundary layer, no separation was observed in the test section of the present study. Both adverse pressure-gradient cases used in the boundary layer investigation were checked for separation. A 3/4-in.-long tuft on the end of a 2-ft rod was used to probe the near-wall boundary layer over the entire plate, and no separation was detected. In addition, for the region of interest the experimental Stanton number distribution has a smooth distribution well into the transition region, showing no sign of separation. Third, the skin-friction data obtained from the measured velocity profiles do not show a near-zero value (a necessary condition for separation) anywhere along the test plate.

Due to paper length restrictions, the mean velocity and temperature profiles for the  $K_2$  case only are shown in this paper in Figs. 12 and 13. For the  $K_2$  case, the mean velocity profiles followed the laminar computational solution up through station 4. Consistent with the Stanton number results, which show that transition does not start until after station 5, the mean velocity profiles indicate that the transition starts between stations 5 and 6. The flow is transitional for stations 6 through 9 and reaches the fully turbulent profile for stations 10 to 13. One problem related to transitional velocity profiles in an adverse pressure gradient is the determination of the near-wall mean velocity profile in the early transition region. Due to the reduction in skin friction relative to the zero-pressure-gradient case, the near-wall laminar profiles of the decelerated flows move higher away from the  $U^+ = Y^+$  curve as  $Re$  increases downstream and then move back toward  $U^+ = Y^+$  once transition starts. As a result,

there is the question of where the early transitional profiles should lie for  $Y^+ < 10$ . In the absence of any theoretical velocity profiles or proven numerical predictions as guidelines, the choice of the location of the near-wall velocity profiles relative to the  $U^+ = Y^+$  curve can have a significant effect on the determination of the skin-friction coefficient in the early transition region. For the purpose of this study, the location of the first few near-wall data points were chosen to be close to the  $U^+ = Y^+$  curve so as to provide a smooth transition in  $C_f$  from its laminar to turbulent values. In the turbulent flow region (stations 11–13), the velocity profiles apparently have a shortened log-linear region with a steeper slope.

The mean temperature profiles for the  $K_2$  case are shown in Fig. 13. The mean temperature profiles are in good agreement with the STAN5 results in the laminar region. The transition of the temperature profiles appears to start between stations 4 and 5, which is earlier than the evolution of the mean velocity profiles. For station 6, the mean temperature profile does not show a trend that would match the conduction-layer correlation,  $T^+ = Pr Y^+$ . This can be attributed to increased uncertainty in determining skin friction from the transitional mean velocity profiles and in finding the wall location ( $y = 0$ ) for this station due to the effect of the adverse pressure gradient. The uncertainty in determining  $C_f$  affects the uncertainty of the  $Y^+$  and  $T^+$  values. In the turbulent region, the effect of the adverse pressure gradient is to push the mean temperature profiles increasingly below the log-linear curve of a zero-pressure-gradient flow. A curve fit of the turbulent temperature profile in the log-linear region,  $T^+ = Y_d^+ Pr + (Pr/0.41) \ln [Y^+ / Y_d^+]$ , gives a conduction layer thickness of  $Y_d^+ = 9.8$  and an average  $Pr = 0.71$ , while the wake region is apparently suppressed due to the increase in the adverse pressure gradient. Although use of

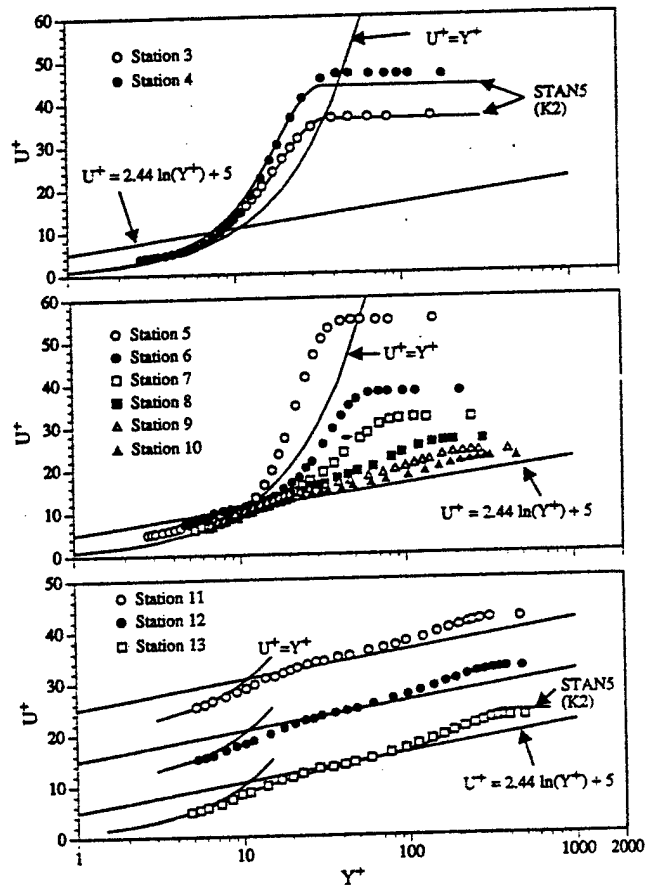


Fig. 12 Mean velocity profiles from the three-wire probe in wall units for  $K_2 = -1.05 \times 10^{-6}$

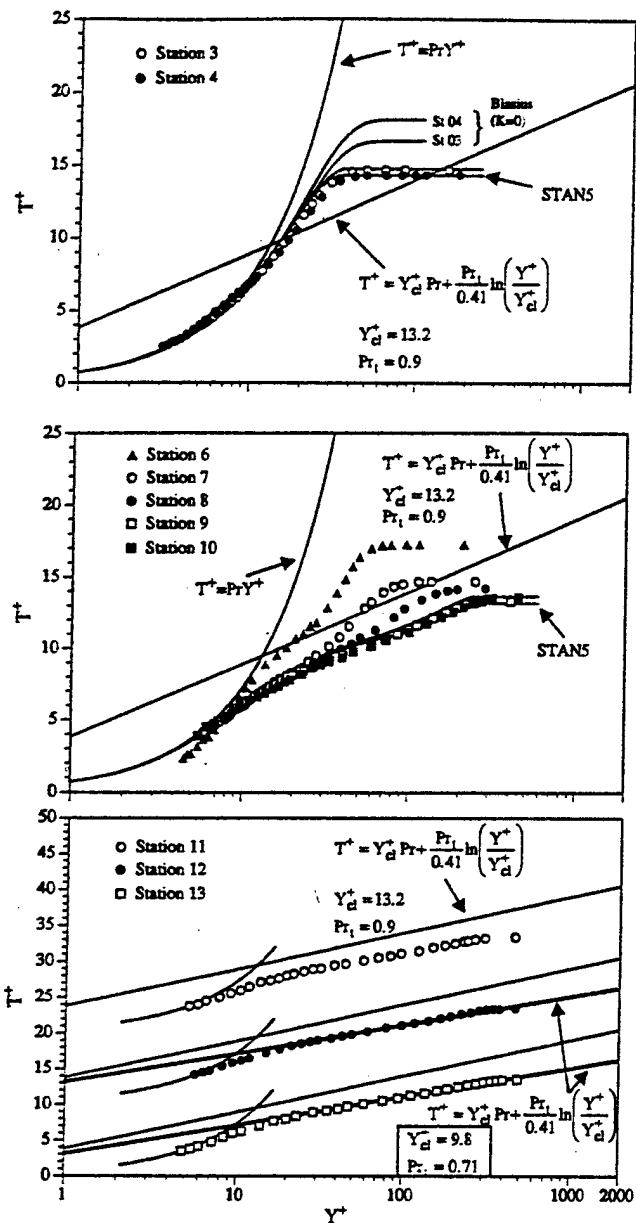


Fig. 13 Mean temperature profiles from the three-wire probe in wall units for  $K2 = -1.05 \times 10^{-3}$

the slope of  $T^+ - Y^+$  profiles as the average  $Pr$ , has yet to be verified for adverse pressure gradient flows, the value of  $Pr_l = 0.71$  is consistent with data from Blackwell et al. (1972). They found that turbulent Prandtl numbers decrease to approximately between 0.6 and 0.8 in the log-linear region with the application of an adverse pressure gradient. It is interesting to note that the velocity profiles in the laminar region under an adverse pressure gradient in  $U^+ - Y^+$  coordinates have an upward trend relative to the Couette flow correlation  $U^+ = Y^+$  (due to a significant reduction of  $C_f$ ) as  $Re_x$  increases, while the temperature profiles in  $T^+ - Y^+$  coordinates move downward from the conduction-layer correlation  $T^+ = Pr Y^+$ , which is opposite to the evolution of temperature profiles for zero-pressure-gradient flow.

In addition, for the  $K2$  case it is clear that the evolution of temperature reaches fully turbulent flow through the transition region more quickly (at station 9) than does the evolution of velocity, which reaches fully turbulent flow at station 11. The results above indicate that the development of thermal transport in decelerating transitional boundary layers leads the develop-

ment of momentum transport. Sharma (1987) also found similar results for adverse pressure gradients due to this difference in the thermal and momentum transport and showed that current transitional modeling schemes fail to predict the thermal boundary layer. More experimental results are needed to develop improved transitional flow models.

### Conclusion

As seen from the surface heat transfer results, streamwise deceleration caused an earlier onset of transition (smaller  $Re_x$ ) relative to a zero-pressure gradient. There was a sharp decrease in the transition onset Reynolds number ( $Re_x$ ) for weak adverse pressure gradients, while for strong adverse pressure gradients,  $Re_x$  seemingly approached an asymptotic value. The variation of the Stanton number distribution along the streamwise direction in the early transition region increased faster as the  $K$  value increased, reflecting a shorter transition region (based on  $Re_x$ ).

The Stanton numbers for some cases followed a well-ordered distribution until midway through transition, at which point significant scatter and waviness developed. This region of scatter and waviness increased with decreasing  $K$  values (or increasing  $U_{\infty}$ ). The  $C_f$  distribution obtained from the velocity measurements showed a smooth curve from the laminar to turbulent flow without the scatter and waviness seen in the Stanton number distribution.

In the  $St$  versus  $Re_x$  figures, the Stanton number distributions are apparently above the zero-pressure-gradient turbulent correlation. This difference increased as the adverse pressure gradient increased. The Stanton number in the turbulent portion decreased with a milder slope downstream than the slope of the zero-pressure-gradient turbulent correlation.

From the boundary layer results, higher negative  $K$  values caused earlier transition onset and shorter transition lengths in terms of  $Re_x$ ,  $Re_{\delta}$ , and  $Re_{\theta}$ . Increasing the adverse pressure gradient produced higher values of shape factor in both the laminar and the turbulent regions. Different from the zero-pressure-gradient case, the shape factors for both of the adverse pressure-gradient cases rose to a maximum at the end of the laminar flow. For all cases, the shape factor had almost reached its turbulent value by the end of transition.

For the laminar mean velocity profiles, the adverse pressure gradient induced smaller  $C_f$  values and caused the near-wall velocity profiles to pull away from (move above) the  $U^+ = Y^+$  curve at locations further downstream. However, for the laminar mean temperature profiles, the adverse pressure gradient caused the near-wall temperature profiles to become lower than the  $T^+ = Pr Y^+$  curve, opposite to its effect on the velocity profiles. The turbulent mean velocity profiles of the decelerated flow show a shortened log-linear region with steeper slopes than the baseline case. The turbulent mean temperature profiles for the decelerated flow have thinner conduction layers ( $Y_{cl}^+$ ) and lower  $Pr$ , than the baseline case. For the  $K2$  case, a curve fit in the thermal law-of-the-wall region results in  $Y_{cl}^+ = 9.8$  and  $Pr_l = 0.71$ . Through the transition region, the streamwise evolution of the temperature profiles achieved fully turbulent flow faster than did the evolution of the velocity profiles. However, this lag of the momentum transport behind the thermal transport in the transition process did not appear to become more pronounced with increasing negative  $K$ .

### References

- Abu-Ghannam, B. J., and Shaw, R., 1980, "Natural Transition of Boundary Layers—The Effects of Turbulence, Pressure Gradient, and Flow History," *Journal of Mech. Engr. Science*, Vol. 22, No. 5, pp. 213–228.
- Acharya, M., 1985, "Pressure-Gradient and Free-Stream Turbulence Effects on Boundary-Layer Transition," Brown Boveri Research Center, Baden, Switzerland, Rept. KLR 85-127C.
- Blackwell, B. F., Kays, W. M., and Moffat, R. J., 1972, "The Turbulent Boundary Layer on a Porous Plate: An Experimental Study of the Heat Transfer Behavior with Adverse Pressure Gradients," Report No. HMT-16, Ther-

mosciences Division, Department of Mechanical Engineering, Stanford University.

Brown, A., and Martin, B. W., 1976, "The Use of Velocity Gradient Factor as a Pressure Gradient Parameter," *Proc. IMechE*, Vol. 190, pp. 277-285.

Clauer, F. H., 1954, "Turbulent Boundary Layers in Adverse Pressure Gradients," *Journal of the Aeronautical Sciences*, Vol. 21, pp. 91-108.

Fraser, C. J., Milne, J. S., and Gardiner, I. D., 1988, "The Effect of Pressure Gradient and Free-Stream Turbulence Intensity on the Length of Transitional Boundary Layers," *Proc. IMechE*, Vol. 202, No. C3, pp. 195-203.

Gostelow, J. P., and Walker, G. J., 1991, "Similarity Behavior in Transitional Boundary Layers Over a Range of Adverse Pressure Gradients and Turbulence Levels," *ASME JOURNAL OF TURBOMACHINERY*, Vol. 113, pp. 617-625.

Gostelow, J. P., Blunden, A. R., and Walker, G. J., 1994, "Effects of Free-Stream Turbulence and Adverse Pressure Gradients on Boundary Layer Transition," *ASME JOURNAL OF TURBOMACHINERY*, Vol. 116, pp. 392-402.

Kays, W. M., and Crawford, M. E., 1980, *Convective Heat and Mass Transfer*, 2nd ed., McGraw-Hill, New York.

Keller, F. J., 1993, "Flow and Thermal Structures in Heated Transitional Boundary Layers With and Without Streamwise Acceleration," Ph.D. Dissertation, Dept. of Mech. Engr., Clemson University, Clemson, SC.

Kline, S. J., and McClintock, J., 1953, "Describing Uncertainties in Single-Sample Experiments," *Mechanical Engineering*, Vol. 75, Jan., pp. 3-8.

Knapp, C. F., and Roache, P. J., 1968, "A Combined Visual and Hot-Wire Anemometer Investigation of Boundary-Layer Transition," *AIAA Journal*, Vol. 6, No. 1, pp. 29-36.

Kuan, C. L., 1987, "An Experimental Investigation of Intermittent Behavior in the Transitional Boundary Layer," M.S. Thesis, Dept. of Mech. Engr., Clemson University, Clemson, SC.

Kuan, C. L., and Wang, T., 1990, "Investigation of Intermittent Behavior of Transitional Boundary Layers Using a Conditional Averaging Technique," *Experimental Thermal and Fluid Science*, Vol. 3, pp. 157-170.

Mislevy, S. P., 1993, "The Effects of Adverse Pressure Gradients on the Momentum and Thermal Structures in Transitional Boundary Layers," M.S. Thesis, Dept. of Mech. Engr., Clemson University, Clemson, SC.

Moffat, R. J., 1982, "Contributions to the Theory of Single-Sample Uncertainty Analysis," *ASME Journal of Fluids Engineering*, Vol. 104, pp. 250-260.

Narayanan, M. A., Badri, X. X., and Ramjee, V., 1969, "On the Criteria for Reverse Transition in a Two-Dimensional Boundary Layer Flow," *Journal of Fluid Mechanics*, Vol. 35, Part 2, pp. 225-241.

Orlando, A. F., Moffat, R. J., and Kays, W. M., 1974, "Heat Transfer in Turbulent Flows Under Mild and Strong Adverse Pressure Gradient Conditions for an Arbitrary Variation of the Wall Temperature," *Proc. 1974 Heat Transfer and Fluid Mechanics Institute*, pp. 91-104.

Patel, V. C., and Head, M. R., 1968, "Reversion of Turbulent to Laminar Flow," *Journal of Fluid Mechanics*, Vol. 34, Part 2, pp. 371-392.

Pohlhausen, K., 1921, "Zur Näherungsweise Integration der Differentialgleichung der Laminare Reibungsschicht," *ZAMM*, Vol. 1, pp. 252-268.

Schubauer, G. B., and Skramstad, H. K., 1948, "Laminar Boundary Layer Oscillations and Transition on a Flat Plate," NACA Report No. 909.

Sharma, O. P., 1987, "Momentum and Thermal Boundary Layer Development on Turbine Airfoil Suction Surfaces," Paper No. AIAA-87-1918.

Shome, B., 1991, "Development of a Three-Wire Probe for the Measurement of Reynolds Stresses and Heat Fluxes in Transitional Boundary Layers," M.S. Thesis, Dept. of Mech. Engr., Clemson University, Clemson, SC.

Tennekes, H., and Lumley, J. L., 1972, *A First Course in Turbulence*, MIT Press, pp. 83 and 103.

Thwaites, B., ed., 1960, *Incompressible Aerodynamics*, Oxford University Press, pp. 61-64.

Uberoi, Mahinder S., 1956, "Effect of Wind-Tunnel Contraction on Free-Stream Turbulence," *J. of the Aeronautical Sciences*, pp. 754-764.

Walker, G. J., and Gostelow, J. P., 1989, "Effects of Adverse Pressure Gradients on the Nature and Length of Boundary Layer Transition," *ASME JOURNAL OF TURBOMACHINERY*, Vol. 112, pp. 196-205.

Walker, G. J., 1989, "Transitional Flow on Axial Turbomachine Blading," *AIAA Journal*, Vol. 27, No. 5, pp. 595-602.

Wang, T., Keller, F. J., and Zhou, D., 1992, "Experimental Investigation of Reynolds Shear Stresses and Heat Fluxes in a Transitional Boundary Layer," *Fundamental and Applied Heat Transfer Research for Gas Turbine Engines*, ASME HTD-Vol. 226, pp. 61-70.

Wang, T., Keller, F. J., and Zhou, D., 1996, "Flow and Thermal Structures in a Transitional Boundary Layer," *Journal of Experimental Fluid and Thermal Science*, Vol. 12, pp. 352-363.

Wang, T., Simon, T. W., and Buddavarapu, J., 1985, "Heat Transfer and Fluid Mechanics Measurements in Transitional Boundary Layer Flows," *ASME Journal of Engineering for Gas Turbines and Power*, Vol. 107, pp. 1007-1015.

Zhou, D., 1993, "An Experimental Investigation of Transitional Flow With Elevated Levels of Free-Stream Turbulence," Ph.D. Dissertation, Dept. of Mech. Engr., Clemson University, Clemson, SC.

Zhou, D., and Wang, T., 1992, "Laminar Boundary Layer Flow and Heat Transfer With Favorable Pressure Gradient at Constant  $K$  Values," ASME Paper No. 92-GT-246.

# The Effects of Adverse Pressure Gradients on Momentum and Thermal Structures in Transitional Boundary Layers: Part 2—Fluctuation Quantities

S. P. Mislevy

T. Wang

Department of Mechanical Engineering,  
Clemson University,  
Clemson, SC 29634-0921

*The effects of adverse pressure gradients on the thermal and momentum characteristics of a heated transitional boundary layer were investigated with free-stream turbulence ranging from 0.3 to 0.6 percent. Boundary layer measurements were conducted for two constant- $K$  cases,  $K1 = -0.51 \times 10^{-6}$  and  $K2 = -1.05 \times 10^{-6}$ . The fluctuation quantities,  $u'$ ,  $v'$ ,  $t'$ , the Reynolds shear stress ( $\bar{uv}$ ), and the Reynolds heat fluxes ( $\bar{vt}$  and  $\bar{ut}$ ) were measured. In general,  $u'/U_\infty$ ,  $v'/U_\infty$ , and  $\bar{vt}$  have higher values across the boundary layer for the adverse pressure-gradient cases than they do for the baseline case ( $K = 0$ ). The development of  $v'$  for the adverse pressure gradients was more actively involved than that of the baseline. In the early transition region, the Reynolds shear stress distribution for the  $K2$  case showed a near-wall region of high-turbulent shear generated at  $Y^+ = 7$ . At stations farther downstream, this near-wall shear reduced in magnitude, while a second region of high-turbulent shear developed at  $Y^+ = 70$ . For the baseline case, however, the maximum turbulent shear in the transition region was generated at  $Y^+ = 70$ , and no near-wall high-shear region was seen. Stronger adverse pressure gradients appear to produce more uniform and higher  $t'$  in the near-wall region ( $Y^+ < 20$ ) in both transitional and turbulent boundary layers. The instantaneous velocity signals did not show any clear turbulent/nonturbulent demarcations in the transition region. Increasingly stronger adverse pressure gradients seemed to produce large nonturbulent unsteadiness (or instability waves) at a similar magnitude as the turbulent fluctuations such that the production of turbulent spots was obscured. The turbulent spots could not be identified visually or through conventional conditional-sampling schemes. In addition, the streamwise evolution of eddy viscosity, turbulent thermal diffusivity, and  $Pr$ , are also presented.*

## Introduction

The previous paper (Part 1) reported the results of an investigation into wall heat transfer, wall friction, and the mean flow structure within the transitional boundary layer under an adverse pressure gradient. In order to understand better the flow structure and the fundamental physics in the transitional boundary layer, information regarding the fluctuating quantities is needed. The fluctuating quantities investigated in this study include typical parameters such as the Reynolds normal and shear stresses ( $u'^2$ ,  $v'^2$ , and  $\bar{uv}$ ), the streamwise Reynolds heat fluxes ( $\bar{vt}$  and  $\bar{ut}$ ), the eddy viscosity ( $\epsilon_u$ ), and the turbulent thermal diffusivity ( $\epsilon_H$ ), which are needed for future transitional flow modeling and heat transfer.

Researchers such as Acharya (1985), Gostelow et al. (1994), Gostelow and Walker (1991), and Gostelow and Blunden (1989) have investigated transitional boundary layers subjected to adverse pressure gradients and have determined mean velocity distributions, integral parameters (discussed in Part 1), and intermittency values. These researchers used an on-line intermittency meter with a preset threshold value to determine the intermittency values. Gostelow (1991) presented the velocity

traces for what he considered to be zero, moderate, and strong adverse pressure gradients, with corresponding  $\lambda_e$  values at transition onset of 0, -0.034 and -0.069, respectively. Gostelow (1991) showed that for the strong pressure gradient ( $\lambda_e = -0.069$ ), the velocity traces are marked by the continuous appearance of instability waves, which show a greater uniformity of amplitude than is present at lower pressure gradients. The amplitude and frequency of the Tollmien-Schlichting waves are higher than they are at lower pressure gradients and are generally on the same order of magnitude as the fluctuations in the turbulent spots. In addition, Gostelow also stated that the continuous way in which turbulence appears during transition in an adverse pressure gradient makes the turbulent spots much more difficult to characterize, and thus intermittency measurements are open to greater error. In fact, Arnal (1984) stated that intermittency is less apparent even when transition occurs under only a slight adverse pressure gradient since the instability waves exhibit higher amplitudes, making the turbulent spots difficult to distinguish. These previous results seem to indicate that the high turbulent-spot production rate and the shorter transition lengths associated with adverse pressure gradients may be linked to some physical changes occurring in the flow structure in the transition region.

However, very little information regarding the fluctuating quantities under adverse pressure-gradient conditions has been documented in the literature. Recent work by Keller and Wang (1996) and Keller (1993) has provided detailed measurements

Contributed by the International Gas Turbine Institute and presented at the 40th International Gas Turbine and Aeroengine Congress and Exhibition, Houston, Texas, June 5-8, 1995. Manuscript received by the International Gas Turbine Institute February 4, 1995. Paper No. 95-GT-5. Associate Technical Editor: C. J. Russo.

of flow and thermal structures for transitional boundary layers subjected to constant  $K$  favorable pressure gradients. Since favorable pressure gradients appear to damp out oscillations and delay transition onset whereas adverse pressure gradients cause strong amplification of instabilities and produce early transition, it would seem reasonable to assume that results obtained under a favorable pressure gradient would be somewhat opposite to those obtained under adverse conditions, and that they would give insight into what might be expected under such conditions.

As might be expected, in the presence of a favorable pressure gradient, the laminar boundary layer can tolerate higher streamwise fluctuations ( $u'$ ) without undergoing transition than it can in the zero-pressure-gradient (baseline) case. With increasing positive  $K$  values, the magnitudes of  $u'/U_\infty$  and  $\bar{uv}/U_\infty^2$  are reduced relative to the zero-pressure-gradient flow at each streamwise location having similar intermittency ( $\Gamma$ ) values. In addition, with increasing  $K$  values favorable pressure gradients appear to suppress local turbulent shear generation at  $Y^+ = 100$ . The peak magnitude of the Reynolds streamwise heat flux ( $\bar{u}t$ ) in the transition region is approximately 20 times that of the wall heat flux for favorable pressure gradients, while for the zero-pressure gradient it has a magnitude that is 17 times that of the wall heat flux.

The results presented in this paper are intended to provide insight into both the momentum and the heat transfer behavior induced by an adverse pressure gradient. These results include instantaneous velocity signals as well as fluctuating quantities in the form of Reynolds stresses and heat fluxes.

**Experimental Program.** The same test facility and experimental equipment was used as described in Part 1. Briefly, a two-dimensional, open-circuit wind tunnel was used that had a test section consisting of a heated flat plate and a divergent outer wall for setting constant  $K$  pressure gradients. A three-wire probe and a hot-wire anemometry system were used to make instantaneous measurements of velocity and temperature in the boundary layers. The determination of the wall location ( $y = 0$ ) was guided by a single hot-wire measurement.

Detailed boundary layer measurements are made for two cases,  $K1 = -0.51 \times 10^{-6}$  and  $K2 = -1.05 \times 10^{-6}$ . The free-stream turbulence intensities at the onset of transition are 0.3 and 0.35 percent, respectively. The uncertainties of the fluctuating quantities near  $y/\delta = 0.2$  are listed in Table 1.

## Results and Discussion

**Velocity Signals.** Instantaneous velocity signals are often helpful in showing flow characteristics and in detecting ambiguous regions between transitional and turbulent flows. The instant-

Table 1 Uncertainties of fluctuating quantities

Parameter	Uncertainty (%)
$u'$	4
$v'$	24
$\bar{uv}$	11
$\bar{vt}$	12
$\bar{ut}$	4
$\epsilon_M$	11
$\epsilon_H$	12
$Pr_t$	13

taneous streamwise velocity signals were first investigated to see how an adverse pressure gradient affects these signals in comparison to the effect of a zero-pressure-gradient flow (baseline). The baseline case was conducted by Wang et al. (1992, 1996) and is documented in detail in Keller's dissertation (1993). The signals were taken at the  $y/\delta$  location where the rms streamwise velocity fluctuations reach a maximum in the boundary layer. Figure 1 shows representative velocity signals for the baseline case along with the corresponding intermittency ( $\Gamma$ ) values for each station. These intermittency values were determined by Keller and Wang (1995) by using  $\bar{uv}$  as the criterion function,  $(d\bar{uv}/d\tau)^2$  as the high-pass filter, and the "dual-slope" method on cumulative intermittency distribution to determine the appropriate threshold values. The intermittency value is zero for a laminar flow and 1.0 for a fully turbulent flow. As can be seen, the baseline signals show low-frequency oscillations in the laminar region (stations 4 and 5). These sinusoidal-like oscillations increase in magnitude as transition is approached. In the transition region (station 6), there are distinct turbulent/nonturbulent regions, which show the intermittent passing of turbulent spots or turbulent wave packets. After the spots coalesce into the fully turbulent region, the velocity signal (station 13) shows high-frequency fluctuations characteristic of a zero-pressure-gradient turbulent boundary layer.

In comparison, the velocity signals for the adverse pressure-gradient cases,  $K1 = -0.51 \times 10^{-6}$  and  $K2 = -1.05 \times 10^{-6}$ , are shown in Figs. 2 and 3, respectively. Since these two cases have lower free-stream velocities than does the baseline case, longer time frames are used in Figs. 2 and 3 in order to ensure that the flow travels approximately the same distance as the baseline during the time frame presented. For the  $K1$  case, the transition region, determined from the Stanton number distribu-

## Nomenclature

$K$ = acceleration parameter = $(\nu/U_\infty^2)(dU_\infty/dx)$	$u', v', w'$ = rms value of velocity fluctuations
$Pr_t$ = turbulent Prandtl number	$U_{\infty 0}$ = free-stream velocity at station 1
$Re_x$ = local Reynolds number	$U_\tau$ = friction velocity = $\sqrt{\tau_w/\rho}$
$T$ = instantaneous temperature = $T + t$	$U_\infty$ = free-stream velocity
$T$ = mean temperature	$\bar{uv}$ = Reynolds shear stress
$t$ = temperature fluctuation	$\bar{ut}$ = streamwise Reynolds heat flux
$t'$ = rms value of temperature fluctuations	$\bar{vt}$ = cross-stream Reynolds heat flux
$U, V$ = streamwise and cross-stream instantaneous velocity	$x$ = streamwise distance from leading edge
$U, V$ = mean streamwise and cross-stream mean velocity components	$y$ = normal distance from wall
$u, v, w$ = instantaneous velocity fluctuations	$Y^+$ = dimensionless distance from wall = $yU_\tau/\nu$

$u', v', w'$ = rms value of velocity fluctuations	$\delta$ = boundary layer thickness at $0.995U_\infty$
$U_{\infty 0}$ = free-stream velocity at station 1	$\Gamma$ = intermittency
$U_\tau$ = friction velocity = $\sqrt{\tau_w/\rho}$	$\epsilon_H$ = turbulent thermal diffusivity = $-\bar{v}t/(\partial T/\partial y)$
$U_\infty$ = free-stream velocity	$\epsilon_M$ = eddy viscosity = $-\bar{u}v/(\partial u/\partial y)$
$\bar{uv}$ = Reynolds shear stress	$\eta$ = dimensionless distance = $(x - x_s)/(x_e - x_s)$
$\bar{ut}$ = streamwise Reynolds heat flux	
$\bar{vt}$ = cross-stream Reynolds heat flux	
$x$ = streamwise distance from leading edge	
$y$ = normal distance from wall	
$Y^+$ = dimensionless distance from wall = $yU_\tau/\nu$	

## Subscripts

$\infty$ = free-stream value
$e$ = end of transition
$s$ = start of transition
$w$ = at the wall

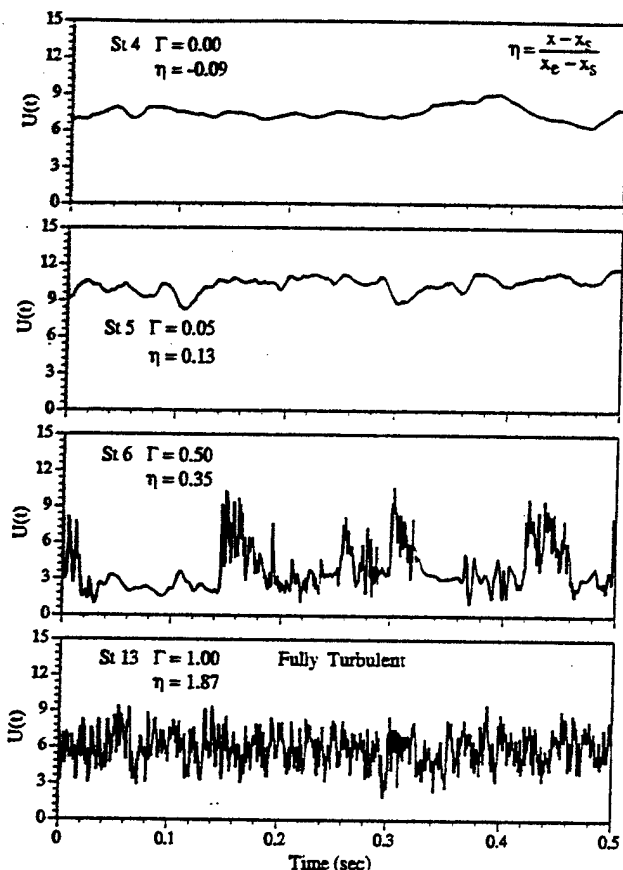


Fig. 1 Representative velocity signals from the three-wire probe for the baseline case taken at  $u'_{\max}$  ( $U_{\infty} = 12.24$  m/s)

tion and the mean velocity profiles in Part 1, starts just after station 4 and ends between stations 6 and 7. The nature of the velocity signals for the *K1* case are different from those for the baseline case in the following respects: (a) in the pretransition laminar region, no obvious oscillations are observed, (b) in the transition region (stations 5 and 6), there are no distinct turbulent/nonturbulent regions (or intermittency) as were found for the baseline case, and (c) in the turbulent region, the frequencies of the velocity fluctuations are lower than in the transition region for the *K1* case, whereas for the baseline, the frequencies of the turbulent fluctuations are maintained at about the same level as in the turbulent wave packets of the baseline transition region. Arnal (1984) showed that for decelerated flows, the instability waves in the pretransition region are smaller and look similar to those for a zero-pressure gradient. However, just prior to transition onset (1.5 cm for Arnal, 1984), the unstable waves can reach amplitudes larger than those for a zero-pressure gradient. In the current study, the fast change from pretransition laminar to transitional flow is a likely reason that these high-amplitude waves in the pretransition region were not captured.

The velocity signals for the *K2* case are shown in Fig. 3. From the Stanton number distribution and the mean velocity profiles in Part 1, transition was determined to start after station 5 and end around station 10. In the pretransition laminar region (station 5), only very weak but relatively uniform sinusoidal oscillations are seen. In the early (station 6) to midtransition region (stations 7 and 8), the velocity signals are obviously dominated by low-frequency fluctuations. However, calculation indicates that these seemingly low oscillation frequencies are much higher than Tollmien-Schlichting wave frequencies due to the low free-stream velocities ( $U_{\infty} = 2.88$  m/s). Even in the turbulent region, the velocity signals do not contain the high-frequency fluctuations that were present in both the *K1*

case and the baseline, but, similar to the *K1* case, the frequencies of the velocity fluctuations in the turbulent region are lower than those in the transition region. For the current study, velocity signals across the boundary layer for the transition region were also investigated in addition to those at  $u'_{\max}$ . However, there was not any appreciable difference in characteristics between the signals for each station.

An attempt was made to determine the intermittency in the transition region; however, due to the lack of distinguishable turbulent/nonturbulent regions, the method of cumulative power density function used by Hedley and Keffler (1974), Kuan and Wang (1990), and Keller and Wang (1995) for determining intermittency gave unreliable results. Even at stations located far downstream in the turbulent region, this method could not consistently predict an intermittency of 1.00 in the inner boundary layer because some patches of reduced fluctuation frequencies were mistakenly selected as nonturbulent regions by the current method. These lower frequency oscillations were conjectured to be partially due to the lower free-stream velocities ( $U_{\infty} = 8.13$  m/s for *K1* and  $U_{\infty} = 2.88$  m/s for *K2*). However, Zhou (1993) used free-stream velocities on the order of 2 m/s with FSTI between 3 and 5 percent in a zero-pressure-gradient flow and found clear turbulent/nonturbulent regions, which yielded consistent intermittency results. Therefore, lower free-stream velocities may be less a cause of the lack of distinctive intermittency than are the adverse pressure gradients.

This raises the question of the nature of natural turbulent spots (in contrast to those artificially generated) in a transitional boundary layer subjected to an adverse pressure gradient. Igashiki et al. (1988) stated that they had observed the formation of turbulent spots in a zero-pressure gradient, but that no spots were observed in the largest adverse pressure gradient case for all of the free-stream velocities tested ( $\sim 8$  to 35 m/s). The

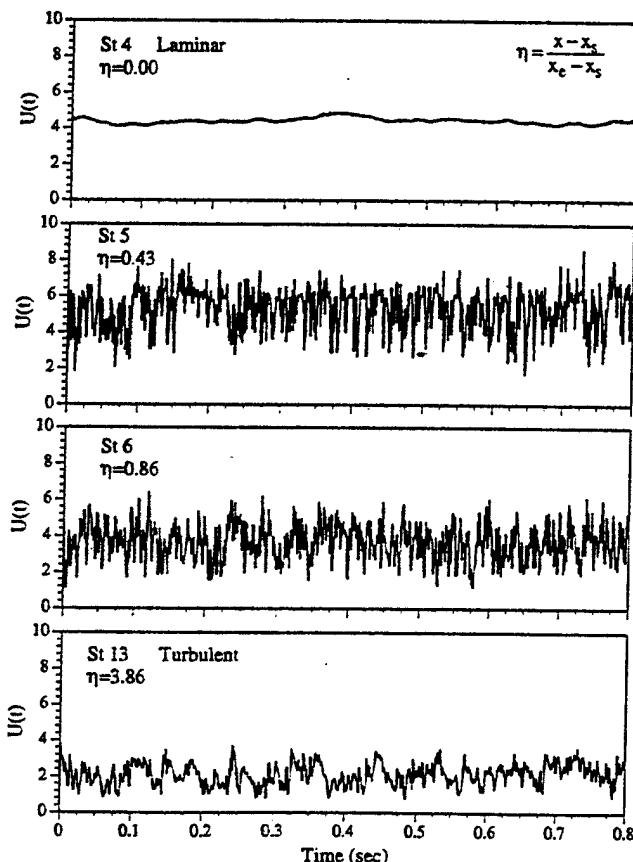


Fig. 2 Representative velocity signals from the three-wire probe for *K1* taken at  $u'_{\max}$  ( $U_{\infty} = 8.13$  m/s)

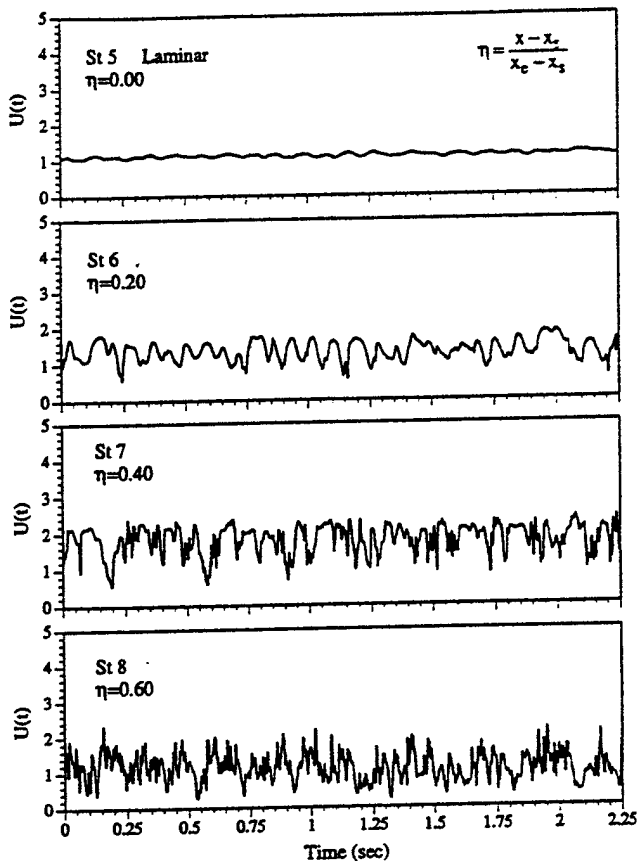


Fig. 3(a) Velocity signals from the three-wire probe for K2 taken at  $u'_{\max}$  ( $U_{\infty} = 2.88$  m/s)

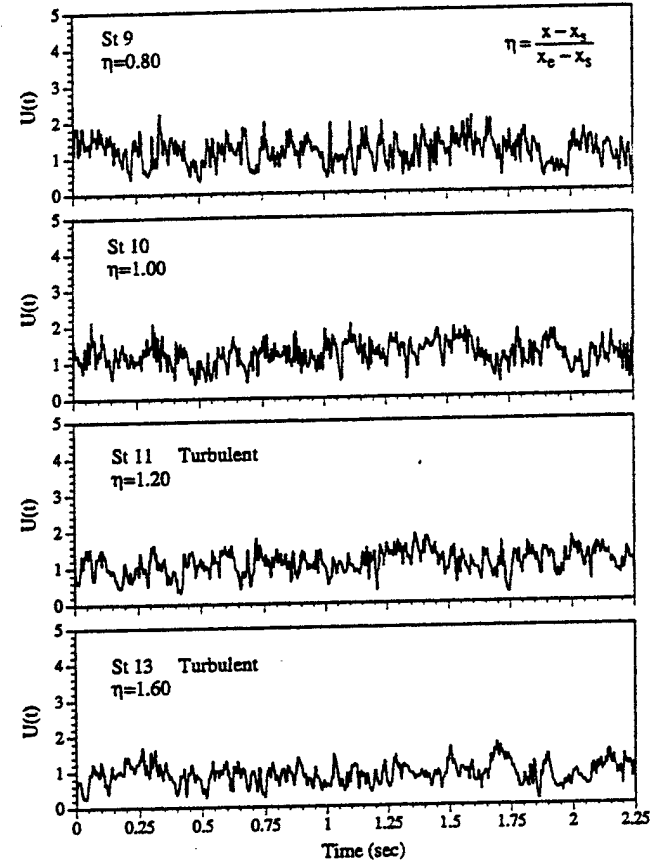


Fig. 3(b) Velocity signals from the three-wire probe for K2 taken at  $u'_{\max}$  ( $U_{\infty} = 2.88$  m/s)

pressure gradient was defined based on the half-angle of a divergent channel (3.6 deg for the largest pressure gradient), and the free-stream velocity distribution was approximately linear. Arnal (1984) also showed that velocity signals recorded in the middle of the transition region for strong adverse pressure gradients did not present any trace of turbulent spots. For this current study, in which the tests were conducted under a constant  $K$  pressure gradient, there also are no clearly defined turbulent/nonturbulent regions in the velocity signals.

Knapp and Roache (1968) stated that there are physical differences between the development of vortex trusses in zero and adverse pressure gradients. Since the initiation of turbulent spots occurs through the appearance of high-frequency fluctuations near the heads of the vortex trusses (or hairpin vortex legs), a change in the development of these trusses could possibly affect the development of turbulent spots through the transition region. In addition, the fact that an adverse pressure gradient causes transition to become a continuous process with only a short hesitation between the breakdown of wave sets may "disguise" any developing turbulent spots, especially for stronger gradients. For the current results, this makes the calculation of intermittency and turbulent spot production rate unreliable. Therefore, a nondimensional length scale,  $\eta = (x - x_s)/(x_e - x_s)$ , will be used in order to reflect the relative location of each station within the transition region for the decelerating cases (note:  $\eta < 0$  indicates the pretransition laminar region and  $\eta > 1$  indicates the posttransition turbulent region).

**Streamwise Velocity Fluctuations ( $u'$ ).** The streamwise evolution of  $u'$  for the K1 case is shown in Fig. 4. The zero-pressure gradient (baseline) results are also shown for the sake of comparison. For the K1 case, the change of  $u'$  along the streamwise direction in the pretransition (or late-laminar) re-

gion appears small when compared with the baseline case. However, once transition starts, the production of  $u'$  increases faster than in the baseline case (not shown here; see Wang et al., 1996). The  $u'$  reaches a maximum value of about 16 percent at station 5. The major difference in the  $u'$  distribution between the baseline and the K1 case is the broad region ( $10 \leq Y^+ \leq 70$ ) in which the  $u'$  value reaches a virtual plateau (15 ~ 16 percent) in contrast to the sharp peak of the production region for the baseline case near  $Y^+ = 20$ . As the end of transition approaches, the  $u'$  distribution across the boundary layer becomes similar to that of the baseline but with magnitudes about 5 percent higher than the baseline case between  $Y^+ = 20$  and  $Y^+ = 200$  and up to 30 percent higher in the near-wall region ( $Y^+ < 20$ ).

The streamwise evolution of  $u'/U_{\infty}$  for the K2 case is shown in Fig. 5 in wall units. As for the K1 case in Fig. 4, in the pretransition region the change of  $u'/U_{\infty}$  in the streamwise direction is smaller and is of lower magnitude than the baseline. However, once transition starts, there are two distinct peaks of equal magnitude for station 6 at  $Y^+ = 7$  and  $Y^+ = 30$ , respectively. These peaks develop into a broad region of relatively constant  $u'$  from  $Y^+ = 15$  to  $Y^+ = 50$  at station 7 ( $\eta = 0.40$ ), which is similar to K1 at  $\eta = 0.43$ . In the turbulent region (downstream of station 10), the near-wall peak of  $u'/U_{\infty}$  at  $Y^+ = 15$  appears to still be changing, while from  $Y^+ = 50$  to  $Y^+ = 200$ ,  $u'/U_{\infty}$  does not vary from station to station. Due to the lower free-stream velocity ( $U_{\infty} = 2.88$  m/s) of the K2 case, more stations are involved in the transition region, and measurements with the three-wire probe can reach  $Y^+ = 5$  due to the thicker boundary layer. In general,  $u'/U_{\infty}$  has a broader spread of elevated values across the boundary layer for the adverse pressure-gradient cases than for the baseline case.

**Cross-Stream Velocity Fluctuations ( $v'$ ).** The cross-stream evolution of  $v'$  for the  $K1$  and  $K2$  cases is shown in Figs. 6 and 7, respectively. The development of  $v'$  for the  $K1$  and  $K2$  cases is more active than it is for the baseline. Throughout transition, the  $v'/U_\infty$  values of the decelerated cases continually exceed the corresponding values for the baseline and remain higher into the turbulent region. In the turbulent region for the baseline case (Fig. 6), the values of  $v'$  for  $40 < Y^* < 200$  are fairly constant, with a value of 3.7 percent. However, for the  $K1$  case, such a region of constant  $v'$  values is only seen immediately after the end of transition at station 7 and is not present in the  $K2$  cases (Fig. 7). Farther downstream into the fully turbulent region, a similar region of constant  $v'$  values evolves into a distribution with decreasing magnitudes of  $v'$  toward the wall. For the zero-pressure-gradient case, the evolution of  $v'$  reaches its maximum value in the middle of the transition region and maintains at that maximum value throughout the remaining transition region and into the turbulent region, as will be shown later in Fig. 8. The explanation for this phenomenon provided by Kuan and Wang (1990) is that the increased turbulent energy and dissipation reach equilibrium earlier in the cross-stream direction than they do in the streamwise direction. However, in the decelerated cases, the  $v'$  evolution seems to be correlated more closely with the  $u'$  distribution. It can be seen in both Figs. 6 and 7 that the  $v'/U_\infty$  distribution reaches its maximum value at station 5 ( $\eta = 0.43$ ) for the  $K1$  case and station 8 ( $\eta = 0.60$ ) for the  $K2$  case. Then, similar to  $u'/U_\infty$ ,  $v'/U_\infty$  gradually decreases to its fully turbulent value. This trend of development for  $v'$  indicates the significance of increased magnitudes of cross-stream turbulence energy and the involvement of  $v'$  in the whole transition process.

The streamwise evolution of the maximum  $u'/U_\infty$  and  $v'/U_\infty$  at each station for the  $K1$  and  $K2$  cases is shown in Fig. 8.

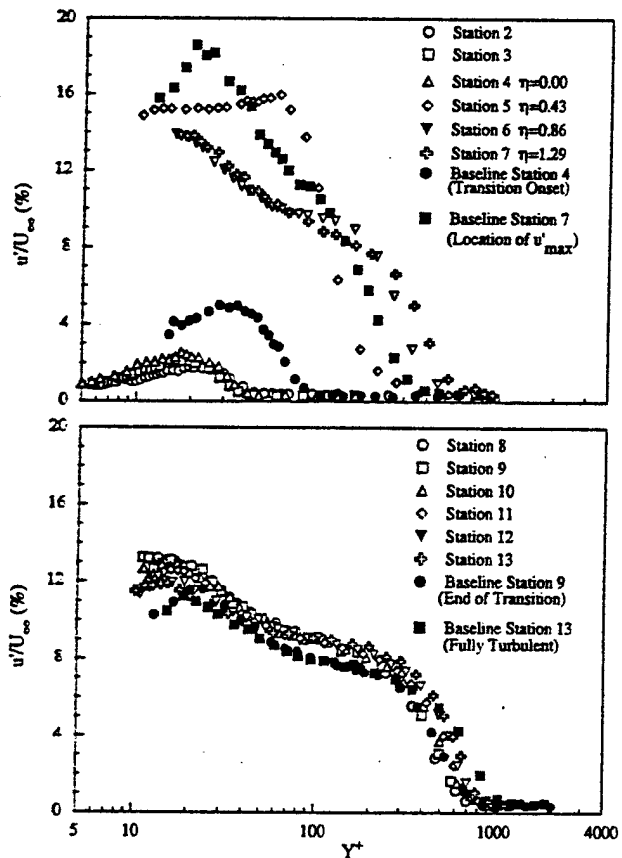


Fig. 4 Streamwise velocity fluctuation distribution for  $K1 = -0.51 \times 10^{-6}$  in wall units

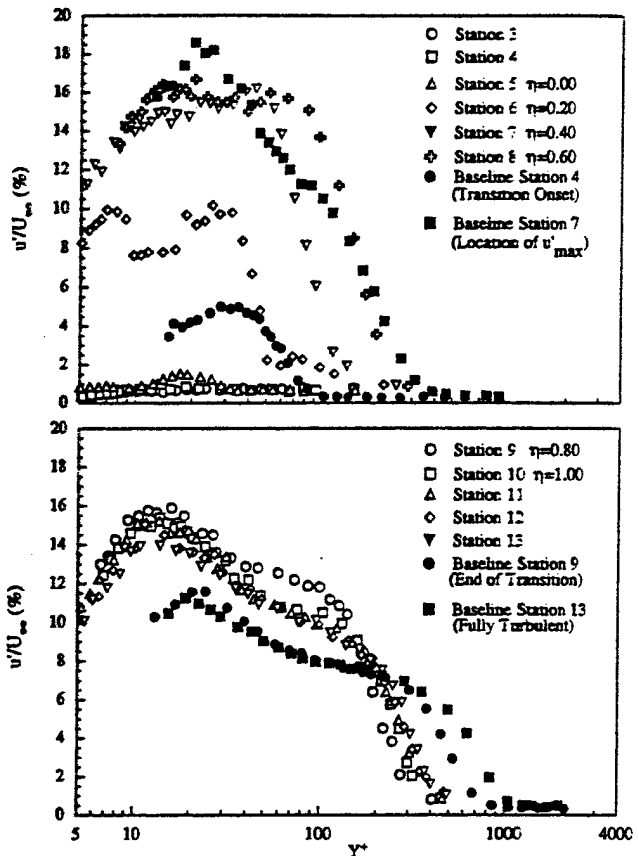


Fig. 5 Streamwise velocity fluctuation distribution for  $K2 = -1.05 \times 10^{-6}$  in wall units

The decelerated cases seem to be more effective in transferring turbulence energy from the streamwise direction to the cross-stream direction in the transition and turbulent regions. That this turbulence transfer is more effective is evident from the higher  $v'_{max}$  values throughout the transition for both the  $K1$  and  $K2$  cases as compared to the baseline. In the turbulent region,  $u'_{max}$  increases with increased adverse pressure gradients, and for the stronger adverse pressure gradient (the  $K2$  case), there is less reduction in  $u'_{max}$  from the transition to the turbulent values. Looking at  $v'_{max}$ , there is a strong increase in  $v'$  in the transition region, and it continues to be higher than the baseline case into the turbulent region. It is also plausible that the increased  $v'$  values may not indicate a passively effective energy transfer from  $u'$  to  $v'$ , but rather they indicate an active production of turbulence energy in the cross-stream direction.

**Reynolds Shear Stress ( $\bar{u}v$ ).** The distributions of the Reynolds shear stresses for the  $K1$  and  $K2$  cases are shown in Figs. 9 and 10. Baseline Reynolds shear stress distributions at three selected stations (at the onset and the end of transition and at the location with the highest  $u'$ ) are also included for comparison. For the higher adverse pressure-gradient case,  $K2$  in Figure 10, the pretransition turbulent shear stress is essentially negligible. However, a sharp increase in the turbulent shear, about 410 percent of the wall shear, occurs at station 6 ( $\eta = 0.20$ ) in the near-wall region at  $Y^+ = 7$  with a second peak forming at  $Y^+ = 25$  at about 60 percent of the wall shear. At locations farther downstream within the transition region, the near-wall maximum turbulent shear somehow reduces in magnitude while the turbulent shear, between  $Y^+ = 10$  and  $Y^+ = 100$ , rises significantly, as can be seen at station 7 ( $\eta = 0.40$ ). At station 8 for the  $K2$  case in Fig. 10, the near-wall region of the turbulent shear decreases to 130 percent of the

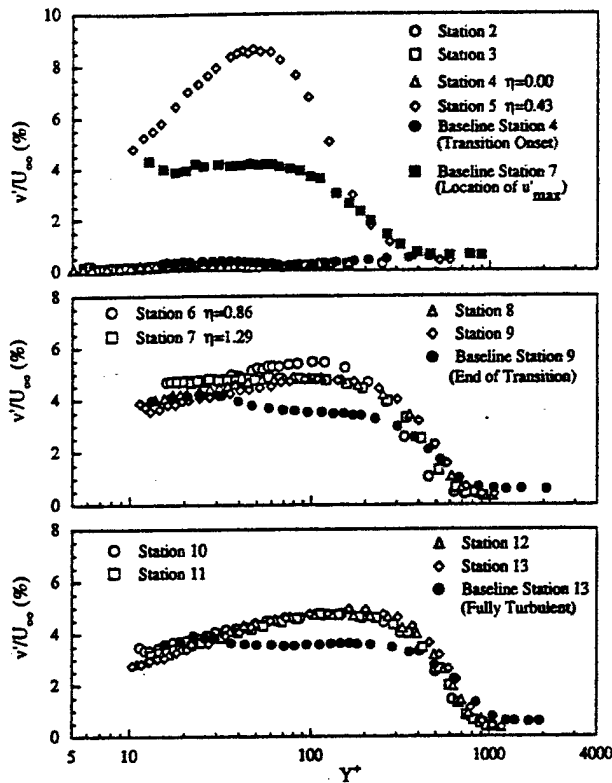


Fig. 6 Cross-stream velocity fluctuation distribution for  $K_1 = -0.51 \times 10^{-6}$  in wall units

wall shear, but a concentrated high-turbulent shear, about 310 percent of the wall shear, appears around  $Y^+ = 70$ , which corresponds to the region of maximum turbulent shear at station 7 for the baseline case. It seems that this turbulent shear peak at  $Y^+ = 70$  corresponds to the breakdown of the rising vortex tubes away from the wall, and that this is the same mechanism that induces the high-turbulent shear at  $Y^+ = 70$  for the zero-pressure-gradient case. Therefore, it is clear that the early near-wall high-turbulent shear generated at  $Y^+ = 7$  at station 6 and the subsequent spreading of turbulent shear from station 6 to station 7 are unique characteristics triggered by higher adverse pressure gradients.

It seems that not until the later stages of transition does the increased turbulent shear away from the wall at  $Y^+ = 70$  impose on the wall shear and affect the turbulent shear across the boundary layer. As can be seen in Figs. 9 and 10, in contrast to the baseline case, neither the  $K_1$  nor the  $K_2$  cases have a region of constant turbulent shear in the fully turbulent boundary layers, although the distribution of  $\bar{uv}$  at station 13 for  $K_2$  is flatter for  $Y^+ < 100$  than it is at station 13 for the  $K_1$  case (Fig. 9). For the  $K_1$  case in Fig. 9, no near-wall high-turbulent shear (similar to that at  $Y^+ = 7$  of station 6 for the  $K_2$  case) is observed in the transition region, whereas the typical high shear, around  $Y^+ = 70$ , reaches 500 percent of the wall shear. This may be caused by either (a) a short physical  $x$  length over transition due to the associated higher velocities ( $U_{infty} = 8.13$  m/s) so that the event of near-wall high-turbulent shear was not captured or (b) the fact that  $K_1$  is a milder adverse pressure gradient than  $K_2$  so that the near-wall high-turbulent shear production is not pronounced. In summary, the effect of the adverse pressure gradient significantly increases turbulent shear production throughout the transition region, which is opposite to the effect of favorable pressure gradients (Keller and Wang, 1996), which reduce the ratio of turbulent shear over wall shear in comparison to the zero-pressure-gradient case.

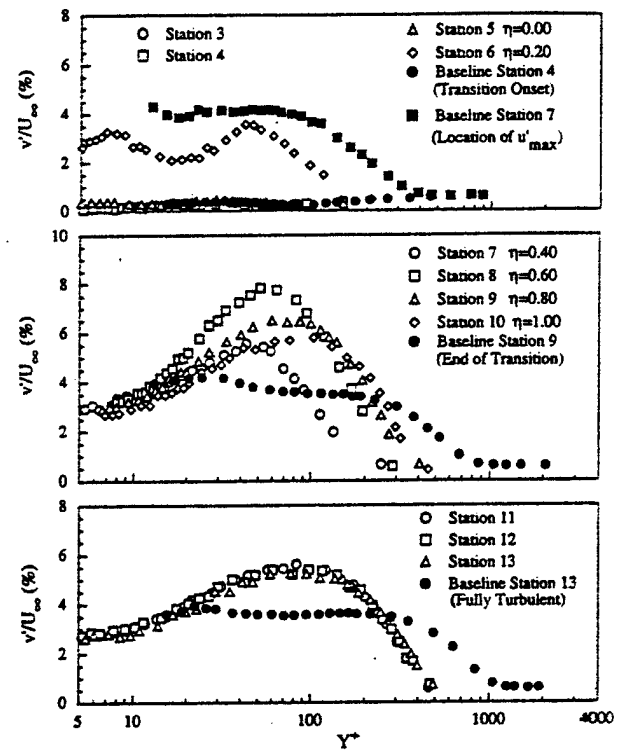


Fig. 7 Cross-stream velocity fluctuation distribution for  $K_2 = -1.05 \times 10^{-6}$  in wall units

**rms Temperature Fluctuations ( $t'$ ).** The distribution of rms temperature fluctuations,  $t'$ , is shown in Fig. 11 for the  $K_2$  case only. These rms values are normalized by  $T_w - T_\infty$  and are presented in wall units. The evolution of  $t'$  for the  $K_2$  case during transition is similar to that of  $u'$  in Fig. 5. Two peaks appear in  $t'$  at station 6 in Fig. 11, although the near-wall peak at  $Y^+ = 13$  does not exactly correspond to the peak position of  $u'$  ( $Y^+ = 7$ ) in Fig. 5. In the later stages of transition, the  $t'$  distribution at station 8 maintains a nearly constant value of 12 percent in the region of  $10 < Y^+ < 50$  before receding to the asymptotic values in the turbulent boundary layer at station 13. The  $t'$  values in the turbulent flow are larger than they are

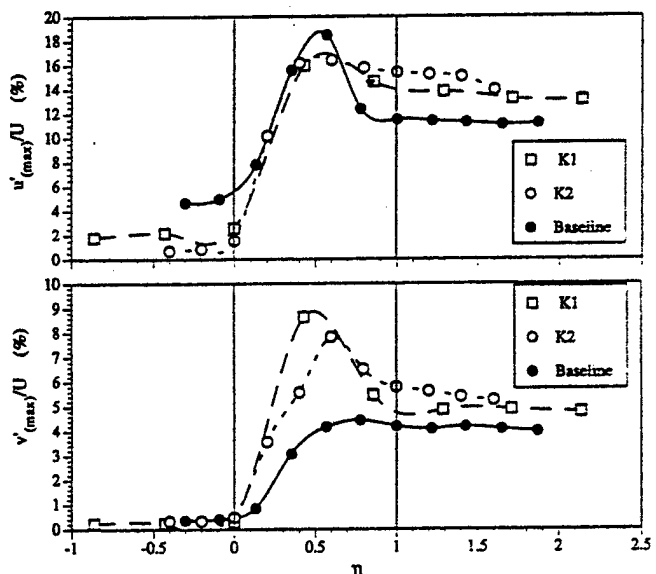


Fig. 8 Distribution of maximum velocity fluctuations

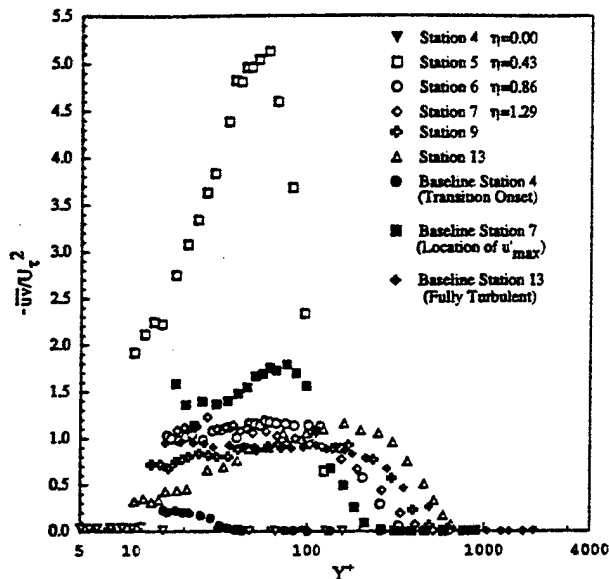


Fig. 9 Reynolds shear stress distribution for  $K_1 = -0.51 \times 10^{-6}$  in wall units

for both the  $K_1$  case (not shown, see Mislevy, 1993) and the baseline case in the near-wall region. For the  $K_2$  case, the  $t'$  distribution reaches the value of a turbulent flow at about station 10 or 11. The development of  $t'$  lags behind that of mean temperature, which was shown in Part I to reach fully turbulent flow at station 9. In other words, the evolution of rms temperature fluctuations under adverse pressure gradients does not appear to keep up with that of the mean temperature. Different from the  $u'$  distributions, the  $t'$  distributions in the turbulent region for the  $K_2$  case show a region of constant value, about 10 percent of  $T_w - T_\infty$ , between  $Y^+ = 5$  and  $Y^+ = 10$ . Stronger adverse pressure gradients appear to produce more uniform and higher near-wall temperature fluctuations in the transition and turbulent regions.

**Streamwise and Cross-Stream Reynolds Heat Fluxes ( $\bar{u}t$  and  $\bar{v}t$ ).** The streamwise Reynolds heat flux,  $\bar{u}t$ , normalized by the wall heat flux, is shown in Fig. 12 for the  $K_2$  case. For

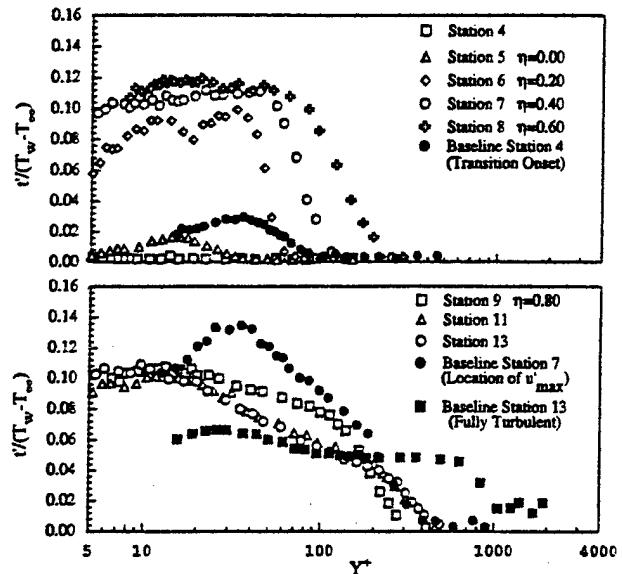


Fig. 11 RMS temperature distribution for  $K_2 = -1.05 \times 10^{-6}$  in wall units

the baseline case, the magnitude of the peak value of  $\bar{u}t$  in the transition region is approximately 17 times greater than the wall heat flux, while for favorable pressure gradients it is 20 times greater than the wall heat flux (Keller and Wang, 1996). However, for the  $K_1$  and  $K_2$  cases of this study, the peak magnitude is only five to six times greater than the wall heat flux. As can be clearly seen in Fig. 12,  $\bar{u}t$  develops twin peaks at around  $Y^+ = 15$  and 50 at station 8 for the  $K_2$  case and migrates toward the wall in late transition.

In the fully turbulent region for both the  $K_1$  and  $K_2$  cases, the maximum  $\bar{u}t$  occurs closer to the wall at  $Y^+ = 15$  with a magnitude that is about three times greater than the wall heat flux. This  $\bar{u}t$  value is larger than that of the baseline case. In comparison to the baseline case in Fig. 12, the adverse pressure gradients increase the near-wall  $\bar{u}t$  in the late-transition and turbulent regions, but their effect on the Reynolds heat fluxes is not as great in the outer boundary layer ( $Y^+ > 30$ ). The

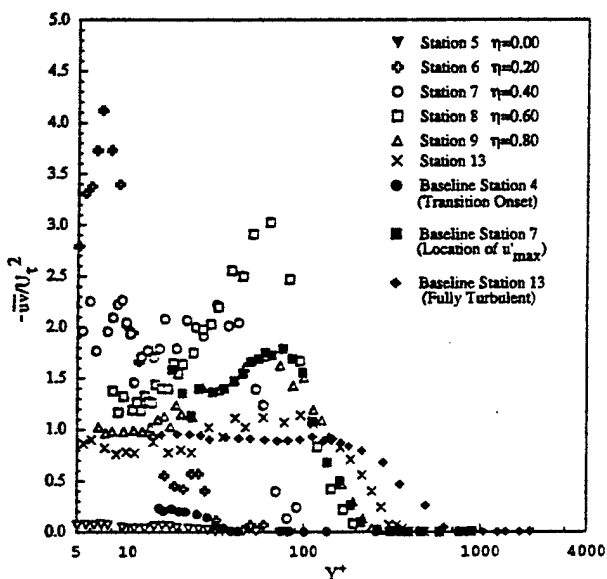


Fig. 10 Reynolds shear stress distribution for  $K_2$  case

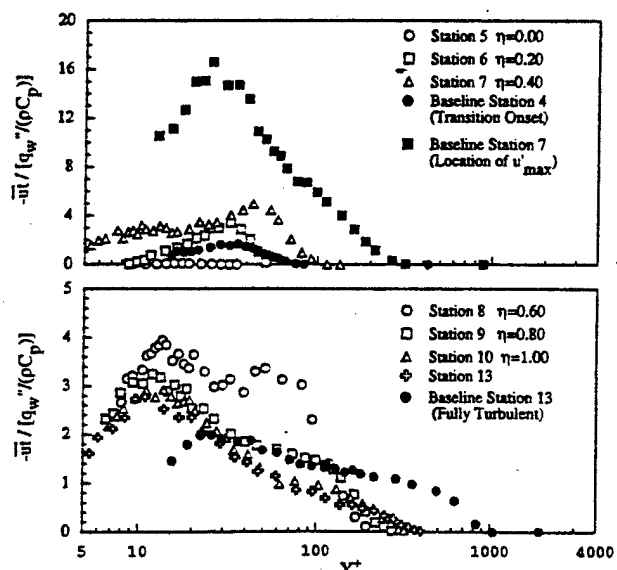


Fig. 12 Reynolds streamwise heat flux for  $K_2 = -1.05 \times 10^{-6}$  in wall units

term  $\partial u'/\partial x$  from the energy equation for a two-dimensional, incompressible, turbulent boundary layer is typically considered to be negligible in a fully developed turbulent boundary layer. However, although this term seems to be a significant contributor in the transition region for a zero-pressure-gradient flow, as was pointed out by Keller (1993), it appears to still be negligible for transitional boundary layers developing under adverse pressure gradients.

The  $\bar{w}'$  are shown in Fig. 13 for the  $K2$  case. For the adverse pressure-gradient case,  $\bar{w}'$  reaches a maximum value of 80 percent of the wall heat flux at station 8 ( $\eta = 0.60$ ). This peak value of  $\bar{w}'$  for the  $K2$  case occurs in the transition region and is about twice as large as that of the baseline case. However, in the turbulent region, the magnitude of  $\bar{w}'$  is about the same for both the  $K2$  and the baseline cases. Similar to the effect on  $u'$ , increased adverse pressure gradients increase  $\bar{w}'$  in the inner boundary layer.

**Eddy Viscosity and Turbulent Thermal Diffusivity.** The eddy viscosity,  $\epsilon_M$ , and the turbulent thermal diffusivity,  $\epsilon_H$ , normalized by their molecular counterparts, are shown in Fig. 14 for the  $K2$  case. In the transition region for the  $K2$  case, the  $\epsilon_M$  develops faster with respect to the baseline case with a peak at  $y/\delta = 0.4$  because the  $\epsilon_M/\nu$  ratios at  $\eta = 0.6$  have peak values similar to those at  $\eta = 1.0$ , whereas, for the baseline case,  $\epsilon_M/\nu$  at  $\eta = 0.57$  is still evolving toward higher values at  $\eta = 1.0$ . This peak remains fairly constant in magnitude through the turbulent region, although the  $\epsilon_M$  for the baseline continues to grow in the turbulent region and becomes higher than the  $\epsilon_M$  for  $K2$  by station 13. In the transition region, the  $\epsilon_H$  also develops faster than for the baseline case, and after reaching a maximum at  $y/\delta = 0.4$ , it remains relatively constant across the boundary layer with no distinct peak as for the  $\epsilon_M$ . In the turbulent region, as the flow moves downstream, the  $\epsilon_H$  develops a small peak between  $y/\delta = 0.4 \sim 0.5$ . Relative to the same normalized transition length-scale value,  $\eta$ , the adverse pressure gradient seems to cause an earlier and more rapid increase in the development of the  $\epsilon_M$  and the  $\epsilon_H$  throughout the transition region than does the baseline. Comparison of the  $\epsilon_M$  and the  $\epsilon_H$  for the  $K2$  case shows that the  $\epsilon_M$  increases faster to its maximum value with a distinct peak at  $y/\delta = 0.4$ .

As also seen in Fig. 14, the  $Pr_r$  for the  $K2$  case is lower than that of the baseline case in the transition region. However, in the turbulent region, the  $Pr_r$  for the  $K2$  case becomes larger and decays slower than that of the baseline case. The  $Pr_r$  for the adverse pressure-gradient case appears to exhibit a larger region of relatively constant  $Pr_r$  value than does the baseline case in both the transition and the turbulent regions. However, as men-

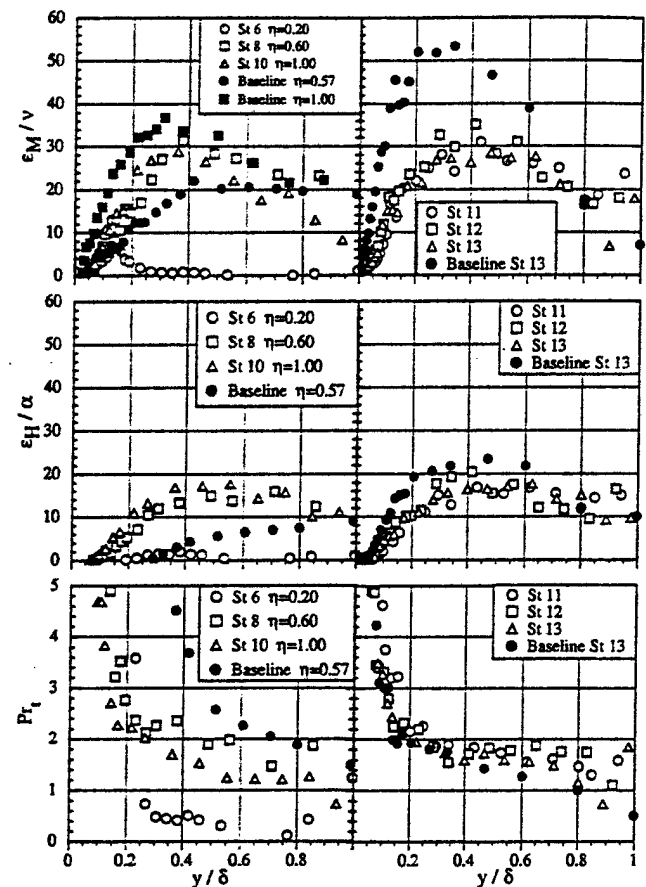


Fig. 14 Streamwise evolution of eddy viscosity, turbulent thermal diffusivity, and  $Pr_r$  for  $K2$  and the baseline cases

tioned in Part 1, Blackwell et al. (1972) showed that stronger adverse pressure gradients resulted in lower  $Pr_r$  values in the turbulent region. Also, using the slope of the present mean temperature log-linear region gives  $Pr_r = 0.71$  in Part 1. This discrepancy is likely related to the difficulty in experimentally measuring accurate  $\bar{w}'$  values. It should be noted that Blackwell et al. did not experimentally measure the  $Pr_r$ , but determined it by assuming a constant heat-flux region in the turbulent boundary layer and by assuming that the total heat flux in this region was equal to the measured wall heat flux. By subtracting the molecular heat flux from the total heat flux,  $\bar{w}'$  was obtained. A detailed discussion and comparison of this method and experimentally determined  $\bar{w}'$  values can be found in Keller (1993). Further research is required to specifically investigate the  $Pr_r$  measurements and to resolve the discrepancy.

## Conclusion

The instantaneous velocity signals taken at the  $y/\delta$  location where  $u'$  is a maximum did not show any clear turbulent/nonturbulent demarcations in the transition region. As a result, reliable intermittency values could not be obtained. It seems that stronger adverse pressure gradients affect and disguise the production of turbulent spots. In fact, even under weak adverse pressure gradients, the magnitude of the waves can be of the same order as the magnitude of the turbulent spots, making the determination of a threshold value difficult.

The  $u'$  for the  $K1$  and  $K2$  cases exhibited a broad region (from  $Y^+ \approx 10$  to 65) in which the  $u'$  value reached a virtual plateau in the transition region in contrast to a peak-production region for the zero-pressure-gradient baseline case near  $Y^+ = 20$ . The development of  $v'$  for the adverse pressure gradients

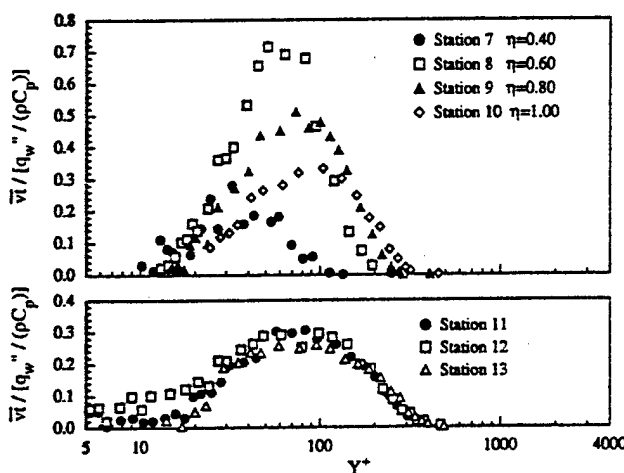


Fig. 13 Cross-stream Reynolds heat flux for  $K2 = -1.05 \times 10^{-6}$  in wall units

was more active than that of the baseline. The  $v'/U_\infty$  values for the decelerated cases increased distinctively to approximately twice the baseline value near the onset of transition and continually exceeded the baseline values throughout the transition and turbulent regions. The application of an adverse pressure gradient is apparently effective in transferring turbulence energy from the streamwise direction to the cross-stream direction in the transition region.

The Reynolds shear stress distribution in the early transition region for the stronger adverse pressure gradient ( $K2 = -1.05 \times 10^{-6}$ ) showed a near-wall region of high-turbulent shear generated at  $Y^+ = 7$ . At locations farther downstream, this near-wall shear reduced in magnitude, while a second region of high shear developed at  $Y^+ = 70$ . For the baseline case, however, the turbulent shear in the transition region was generated at  $Y^+ = 70$ , and no near-wall high-shear region was seen.

The peak magnitude of the streamwise Reynolds heat flux ( $\bar{u}t$ ) in the transition region for the decelerated cases was found to be about a third of that for the baseline case. The term  $\partial \bar{u}t / \partial x$  (from the turbulent two-dimensional energy equation) is less significant in the transition region when the boundary layer develops under decelerated conditions than under a zero-pressure gradient. However, in the late-transition and turbulent regions, the adverse pressure gradients caused an increase in the near-wall  $\bar{u}t$ . The  $\bar{v}t$  values in a decelerated transitional boundary layer are higher than those in the baseline case.

Both the  $\epsilon_M$  and the  $\epsilon_H$  developed faster in the  $K1$  and  $K2$  cases than they did in the baseline cases and reached equilibrium values in the middle of the transition region. However, the  $\epsilon_M$  and the  $\epsilon_H$  of the baseline case eventually outgrew the equilibrium values of the  $\epsilon_M$  and the  $\epsilon_H$  in the later part of the decelerated transitional flow and maintained these higher values in the zero-pressure-gradient turbulent boundary layer.

## References

Acharya, M., 1985, "Pressure Gradient and Free-Stream Turbulence Effects on Boundary Layer Transition," Brown Boveri Research Center, Baden, Switzerland, Rept. KLR 85-127C.

Arnal, D., 1984, "Description and Prediction of Transition in Two-Dimensional, Incompressible Flow," AGARD-R-709, 2-1.

Blackwell, B. F., Kays, W. M., and Moffat, R. J., 1972, "The Turbulent Boundary Layer on a Porous Plate: An Experimental Study of the Heat Transfer Behavior With Adverse Pressure Gradients," Report No. HMT-16, Thermosciences Division, Department of Mechanical Engineering, Stanford University.

Gostelow, J. P., and Blunden, A. R., 1989, "Investigations of Boundary Layer Transition in an Adverse Pressure Gradient," *ASME JOURNAL OF TURBOMACHINERY*, Vol. 111, pp. 366-375.

Gostelow, J. P., and Walker, G. J., 1991, "Similarity Behavior in Transitional Boundary Layers Over a Range of Adverse Pressure Gradients and Turbulence Levels," *ASME JOURNAL OF TURBOMACHINERY*, Vol. 113, pp. 617-625.

Gostelow, J. P., 1991, "Influence of Adverse Pressure Gradients on Chaotic Regimes Encountered During Transition," *Boundary Layer Stability and Transition to Turbulence*, ASME FED-Vol. 114, pp. 145-153.

Gostelow, J. P., Blunden, A. R., and Walker, G. J., 1994, "Effects of Free-Stream Turbulence and Adverse Pressure Gradients on Boundary Layer Transition," *ASME JOURNAL OF TURBOMACHINERY*, Vol. 116, pp. 392-404.

Hedley, T. B., and Keffler, J. F., 1974, "Turbulent/Non-Turbulent Decisions in an Intermittent Flow," *Journal of Fluid Mechanics*, Vol. 64, Part 4, pp. 625-644.

Igarashi, S., Sasaki, H., and Honda, M., 1988, "Influence of Pressure Gradient Upon Boundary Layer Stability and Transition," *Acta Mechanica*, Vol. 73, pp. 187-198.

Keller, F. J., 1993, "Flow and Thermal Structures in Heated Transitional Boundary Layers With and Without Streamwise Acceleration," Ph.D. Dissertation, Dept. of Mech. Engr., Clemson University, Clemson, SC.

Keller, F. J., and Wang, T., 1995, "Effects of Criterion Functions on Intermittency in Heated Transitional Boundary Layers With and Without Streamwise Acceleration," *ASME JOURNAL OF TURBOMACHINERY*, Vol. 117, pp. 154-165.

Keller, F. J., and Wang, T., 1996, "Flow and Heat Transfer Behavior in Transitional Boundary Layers With Streamwise Acceleration," *ASME JOURNAL OF TURBOMACHINERY*, Vol. 118, pp. 314-326.

Knapp, C. F., and Roache, P. J., 1968, "A Combined Visual and Hot-Wire Anemometer Investigation of Boundary-Layer Transition," *AIAA Journal*, Vol. 6, No. 1, pp. 29-36.

Kuan, C. L., and Wang, T., 1990, "Investigation of Intermittent Behavior of Transitional Boundary Layer Using a Conditional Averaging Technique," *Experimental Thermal and Fluid Science*, Vol. 3, pp. 157-170.

Mislevy, S. P., 1993, "The Effects of Adverse Pressure Gradients on the Momentum and Thermal Structures in Transitional Boundary Layers," M.S. Thesis, Dept. of Mech. Engr., Clemson University, Clemson, SC.

Wang, T., Keller, F. J., and Zhou, D., 1992, "Experimental Investigation of Reynolds Shear Stresses and Heat Fluxes in a Transitional Boundary Layer," *Fundamental and Applied Heat Transfer Research for Gas Turbine Engines*, ASME HTD-Vol. 226, pp. 61-70.

Wang, T., Keller, F. J., and Zhou, D., 1996, "Flow and Thermal Structures in a Transitional Boundary Layer," *Journal of Experimental Fluid and Thermal Science*, Vol. 12, pp. 352-363.

Zhou, D., 1993, "An Experimental Investigation of Transitional Flow With Elevated Levels of Free-Stream Turbulence," Ph.D. Dissertation, Dept. of Mech. Engr., Clemson University, Clemson, SC.



PII: S0017-9310(96)00336-5

# Effects of leading-edge roughness on fluid flow and heat transfer in the transitional boundary layer over a flat plate

MARK W. PINSON and TING WANG†

Department of Mechanical Engineering, Clemson University, Clemson, SC 29634-0921, U.S.A.

(Received 15 February 1996 and in final form 16 September 1996)

**Abstract**—An experimental study was undertaken to gain insight into the physical mechanisms that affect the laminar-turbulent transition process downstream of the leading-edge roughness condition. Sandpaper strips and small cylinders were attached to the leading edge of a heated test surface to simulate leading edge roughness typical of gas turbine blades. The roughness Reynolds numbers ranged from 2 to 2840. For free-stream velocities less than  $5 \text{ m s}^{-1}$ , the maximum roughness height was the primary contributor to deviations from the undisturbed case, irrespective of the roughness geometry. At higher free-stream velocities ( $5-7 \text{ m s}^{-1}$ ), three of the rough leading-edge conditions induced a dual-slope region between the laminar and turbulent Stanton number correlations. Boundary layer measurements indicated that the first segment of the dual-slope was laminar, but the wall heat transfer significantly deviates from the laminar correlation. The second segment was transitional. The dual-slope behaviour and a waviness in the Stanton number distribution observed at higher free-stream velocities are believed to have been caused by nonlinear amplification caused by the finite disturbances at the leading edge. © 1997 Elsevier Science Ltd.

## INTRODUCTION

The raising of operating temperatures to increase overall turbine efficiency has led to the need for accurate assessment of thermal loads in the turbine. Turbine blades experience significant thermal loading, and Mayle [1] and Hodson *et al.* [2] indicated that it is common for over half of the flow surrounding the turbine blades to experience laminar-turbulent transition, particularly in low pressure turbines. A better understanding of the physical mechanisms involved in the transition process is therefore desirable so that a more accurate assessment of the turbine blade temperature variations can be made possible through improved models of transitional heat transfer.

Of the many factors that can influence laminar-turbulent transition, the effect of leading-edge roughness on the process has not been clearly determined, particularly with regard to heat transfer behavior. Surface roughness can be significant to turbine vanes and blades in many ways, especially in a high pressure turbine. A study by Taylor [3] that measured the surface roughness characteristics of two used (i.e., blade surfaces had been degraded as a result of "in-service" use) turbine blades indicated the following:

- (1) Roughness is usually greatest at the leading edge of the blade.
- (2) Roughness consists of a relatively uniform distribution with a few isolated peaks, according to a statistical analysis.

The second observation made in Taylor's study was based on the large positive value of kurtosis ( $\sim 10$ ; a zero value represents a Gaussian distribution) found in the study. Such large values of kurtosis indicate that the structure of the roughness samples used in the study tended to have a few isolated peaks.

Roughness can also be significant to new turbine blades because a coating may have been added to the blade to enhance its life characteristics by increasing resistance to erosion and high temperatures. The addition of the coating to the blade can leave the surface significantly rougher than an uncoated blade. Boynton *et al.* [4] demonstrated that the overall efficiency of a turbine with new spray-coated blading ( $10.16 \mu\text{m}$  rms roughness) was 2.1 percentage points lower than when polished blading was used ( $0.76 \mu\text{m}$  rms roughness). Blair [5] also showed that increasing the surface roughness by an order of magnitude doubled the heat transfer between the flow and the blades. Also, unnecessary design constraints may be imposed as safety factors to anticipate the unknown effects of roughness. The characteristics of leading-edge roughness described by Taylor and the unknown effects of

† Author to whom correspondence should be addressed.

## NOMENCLATURE

FSTI	free-stream turbulence intensity	$x$	streamwise distance from the leading edge of the heated test surface
$K$	acceleration parameter = $\frac{v}{U_x^2} \frac{dU_x}{dx}$	$X_{UHSL}$	streamwise unheated starting length (2.5 cm for this study)
LEC	leading-edge condition	$y$	coordinate normal to test surface
$Pr$	Prandtl number	$y^+$	$yU_x/v$
$Re_1$	$Re_x$ marking the onset of dual-slope behavior in the $St$ distribution		
$Re_2$	$Re_x$ marking the onset of the second slope in the dual-slope $St$ behavior		
$Re_x$	local Reynolds number = $U_x x/v$		
$St$	local Stanton number		
$U_x$	free-stream velocity		
$U^+$	$U/u_x$		
$u'$	RMS streamwise velocity fluctuation		
$u_t$	friction velocity, $\sqrt{\tau_w/\rho}$		
$\bar{uv}$	time-averaged Reynolds shear stress	$\rho$	density
$\bar{vt}$	time-averaged Reynolds cross-stream heat flux	$\tau_w$	shear stress on the test surface
		$\nu$	kinematic viscosity.

## Greek symbols

$\delta$	boundary layer thickness at $0.995U_x$
$\delta^*$	displacement thickness
	$= \int_0^\delta \left(1 - \frac{U}{U_x}\right) dy$

gas turbine blade roughness on fluid mechanics and heat transfer suggest the need to understand the influence of leading-edge roughness on transitional heat transfer behavior.

Early work on the relationship between roughness and transition has been concerned with the location of the onset of transition, usually defined by using flow visualization or by a sudden change in the total pressure near the test surface as the maximum roughness height changes. Fage and Preston [6] reported that as roughness height increased, the transition point moved progressively closer to the physical location of the roughness element disturbing the flow. Dryden [7] suggested that roughness elements tend to destabilize the boundary layer flow and that there may be a connection between the instability induced by the roughness element and classical stability theory. Klebanoff and Tidstrom [8] examined the possible connection to stability theory. Their results indicated that the presence of roughness elements in the laminar region of the boundary layer magnified the amplitude of the Tollmien-Schlichting oscillations present in the early transitional boundary layer. However, the region of frequencies amplified were still within the range of Tollmien-Schlichting wave frequencies predicted by linear stability theory.

Many studies detailing the response of the momentum boundary layer to changes in surface roughness have been conducted, but they have been limited to the response of the fully turbulent boundary layer to surface perturbations. The study performed by Jacobs [9] indicated that while velocity profiles responded slowly to a change in surface roughness, a distinct change in velocity profile was noted. Klebanoff and Diehl [10] showed that different kinds of roughness covering the initial portion of an otherwise smooth

test surface produced different boundary layer structures on the surface downstream of the roughness. If sandpaper roughness was used, the velocity profiles gradually reattained self-similar behavior and the energy spectra indicated a boundary layer flow very close to that of a turbulent boundary layer formed due to natural transition. However, if spanwise cylinders were used to disturb the flow, the velocity profiles required a much greater streamwise distance to achieve self-similar behavior, and the energy spectra indicated a concentration of energy in the lower frequency range.

Other studies by Antonia and Luxton [11, 12] and Androopoulos and Wood [13] suggested that boundary layer flow responds to a change in the surface roughness in a gradual progression from the near-wall region that eventually expands to cover the entire thickness of the layer. The growth of the inner layer was observed through variations in normalized velocity profiles. Antonia and Luxton suggested that the presence of the inner layer made local similarity inapplicable, based on the results of a turbulent kinetic energy balance.

Studies of heat transfer behavior resulting from surface roughness characteristics have been examined, but, as before, the studies have been limited to the fully turbulent flow regime. Ligrani *et al.* [14] and Taylor *et al.* [15] obtained similar results of increasing heat transfer with increasing roughness, and a more recent study by Taylor *et al.* [16] showed that a step change from a rough surface to a smooth one causes a reduction in heat transfer. The Stanton number downstream of the change to a smooth surface initially decreases to a value below the smooth-wall value; then the values asymptotically recover the smooth wall values.

The addition of rough-surface coatings to new gas turbine blades and the observed nature of roughness on used gas turbine blades suggests the need for an investigation of surface roughness effects on turbine blade heat transfer. The significant region of transitional flow surrounding the rough turbine blades and the apparent lack of detailed information regarding heat transfer over rough surfaces also suggest that experimental work in this area will contribute to the overall effort to understand heat transfer around turbine blades.

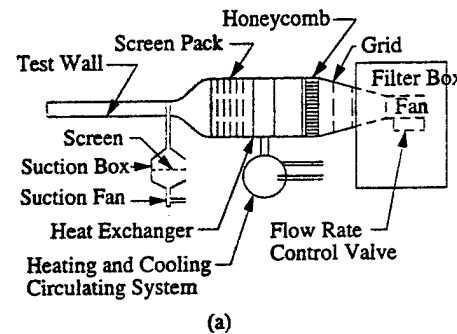
The effect of leading-edge roughness on an actual gas turbine blade is undoubtedly a function of the shape of the blade (leading-edge curvature) and the gas turbine environment (high turbulence intensity, strong acceleration, film cooling etc.). In order to fundamentally understand the leading-edge effect on flow structure and heat transfer, this study focuses on flat plate roughness. The other parameters will be considered later. Hence, this study may not be directly applicable to gas turbine design, but it has the potential for improving the understanding of the roughness effect on heat transfer in the more complicated environment of the gas turbine.

## EXPERIMENTAL PROGRAM

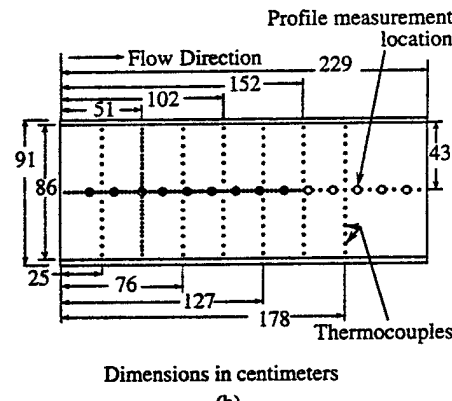
### Test facility

The test facility used is an open circuit, blowing-type wind tunnel [see Fig. 1(a)]. Air enters the system by passing through a filter designed to remove all particulate larger than  $5 \mu\text{m}$ . A honeycomb passage is used to straighten the flow and a heat exchanger which is used to control the steadiness of the free-stream air temperature to within  $0.5^\circ\text{C}$ . Suction is employed upstream of the test surface to facilitate the formation of a boundary layer from zero thickness at the elliptic leading edge. The test section is a channel that measures 2.4 m in the streamwise ( $x$ ) direction, 0.92 m in the spanwise ( $z$ ) direction (parallel to the leading edge), and 0.15 m in the cross-stream ( $y$ ) direction (moving away from the heated test surface). The spanwise to cross-stream ratio of 6 was determined to be sufficient to generate an approximately two-dimensional (2-D) boundary layer along the centerline of the 0.92 by 2.4 m test surface. Measurements made by Keller [17] with the test facility indicated that laminar and turbulent portions of the boundary layer were uniform 20 cm above and below the test surface centerline in the spanwise direction. The three-dimensionality of the transition portion reduced the spanwise uniformity to 8 cm above and below the centerline. For the purposes of the current study all measurements on the surface and within the boundary layer were made along the centerline of the test surface.

The test surface is a composite design consisting of several layers [see Fig. 1(c)]. Each of the layers shown in Fig. 1(c) is uniform and continuous over the entire area of the test surface. The foil heater, custom-



(a)



(b)

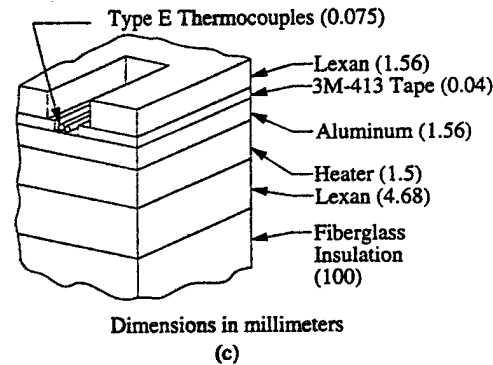


Fig. 1. (a) Wind tunnel test facility; (b) thermocouple locations on heated test wall; (c) cross-section of heated test surface.

designed by Electrofilm Inc., has heating elements covering 90% of the heater surface area. The foil heating element is covered by a silicon rubber coating with a 1.56 mm sheet of aluminum vulcanized to one side. A layer of 3M-413 tape attached to the other side of the aluminum sheet contains 184 E-type thermocouples (bead diameter: 0.076 mm) distributed over the entire test surface, as shown in Fig. 1(b). The thermocouple beads are positioned such that they are in contact with the inner side of a 1.56 mm Lexan sheet. The outer side of the Lexan forms the outer layer of the test surface, which is in contact with the free-stream air within the test section. The quality of the surface smoothness was that of the standard

smoothness for commercially available, optically clear Lexan. The other side of the foil heater is supported by a 4.68 mm Lexan sheet which, in turn, is insulated with 30 cm of R-30 fiberglass.

The 2.4 by 0.92 m channel wall opposite the heated test surface is flexible to allow for adjustment of the streamwise pressure gradient. For the purposes of this study, this "outer wall" was adjusted to accommodate the growth of the boundary layer so that the streamwise pressure coefficient varied less than 1%. In addition, the outer wall contains fourteen holes (2.54 cm in diameter) along the centerline, as shown in Fig. 1. The first hole, called station 1, is located 20 cm from the leading edge of the test surface, and subsequent holes or stations are spaced 15 cm from each other. These stations permit the structure of the boundary layer to be measured as it develops in the streamwise direction. Additional information concerning the design of the wind tunnel and the composite heated test surface is provided in Kuan [18] and Zhou [19].

#### Roughness conditions

Taylor's [3] study indicated that the leading edge of a gas turbine blade is usually the roughest area of the blade and that the rough regions contain isolated peaks. Based on these results, the present study used a sandpaper strip placed at the leading edge of the test surface to simulate the roughened leading-edge condition. The strips of sandpaper were 5 cm long in the streamwise direction and covered the entire spanwise length of the leading edge. The isolated peak nature of the roughness was investigated separately, using cylinders placed at the leading edge. Only one cylinder was attached to the leading edge at a time, and like the sandpaper strips, the cylinder length spanned the entire leading edge.

To determine the appropriate scale of the leading-edge roughness and the appropriate free-stream velocity in the test section, information concerning these parameters in gas turbine engines was obtained. Taylor's [3] measurements, using two types of turbine blades, indicated roughness heights between 1.46 and 10.7  $\mu\text{m}$ . Elovic [20] suggested a roughness range from 1.32 to 12.7  $\mu\text{m}$  and also a unit Reynolds number,  $U/v$ , of  $2.76 \times 10^7 \text{ m}^{-1}$  as being typical around a turbine blade. A detailed study involving measurements on 58 used blades (from both military and civilian aircraft) conducted by Tarada [21] indicated roughness values ranging from 2 to 161  $\mu\text{m}$ . Using the unit Reynolds number provided by Elovic and the reported roughness values, a range in roughness Reynolds number was established and is shown in Fig. 2. Also shown in Fig. 2 are the grain sizes of the sandpaper strips (in grains per linear inch—GRIT or number of grains per 25.4 mm) and the cylinder diameters (in inches i.e. 0.030 = 0.030 in = 0.762 mm) used to conduct this study. The range in roughness Reynolds number shown for the cylinders and sandpaper was determined by using the maximum ( $19.5 \text{ m s}^{-1}$ ) and

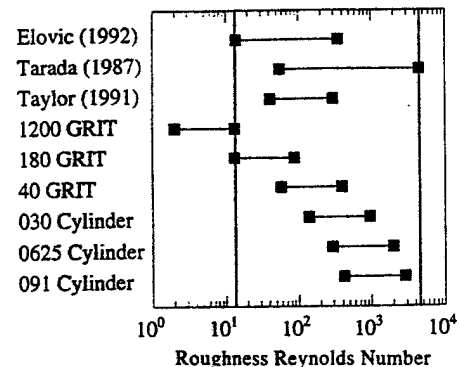


Fig. 2. Representative roughness Reynolds numbers of blades from in-service engines and the range covered by the present study.

minimum ( $2.87 \text{ m s}^{-1}$ ) free-stream velocities obtained in the test facility.

A simple model was used to estimate the average roughness height of the sandpaper. The GRIT specification was used as an indicator of roughness height. For example, the 1200 GRIT sandpaper specification suggests that each grain is approximately 21.2  $\mu\text{m}$  in length. Assuming that each grain is hemispherical and that the backing paper is completely covered with grains, the height of each particle is half the length, or 10.6  $\mu\text{m}$  in this case. This method of height estimation was used for all of the sandpaper cases shown in Fig. 2. The cylinder diameters were directly measured using a micrometer.

Elmer's all-purpose glue was used to attach the cylinders to the leading edge of the plate. The bead was evenly distributed underneath the cylinder on the side closest to the leading edge. A strip of double-sided tape was used to attach the sandpaper strips to the leading-edge of the plate. Consideration of the sandpaper/double-sided tape combination suggested that the bluff shape of the tape and the sandpaper backing might influence the results in such a way as to obscure the effect of the actual grain roughness of the sandpaper. Hence, specific tests with this bluff-body leading-edge condition were added to the test pattern by attaching a single-sided strip of tape 5 cm long in the streamwise direction with a cross-stream height of 0.5 mm. The eight leading-edge conditions are summarized in Table 1.

Table 1. List of leading edge conditions

Condition	Size
Cylinder (Diameter)	0.762 mm (0.030 in) 1.59 mm (0.0625 in) 2.31 mm (0.091 in)
Sandpaper	40 GRIT 180 GRIT 1200 GRIT
Bluff shape	Sandpaper backing ~ 0.4 mm Smooth tape (0.5 mm)

Table 2. Resultant uncertainties in experimental values

Quantity	Uncertainty	Quantity	Uncertainty
$St$	4.0%	$U$	1.6%
$T$	0.1% ( $^{\circ}$ C)	$u'$	7.1%
$uv$	11.9%	$v'$	21.0%

### Boundary layer probes

A single hot wire and a custom-made, three-sensor wire were used in this study to obtain estimates of velocity and temperature variation in the boundary layer. The single-wire boundary layer probe was a 4 micron tungsten wire configured in a standard TSI model 1218-T1.5. The three-sensor boundary layer probe consisted of two 2.5  $\mu$ m, platinum-coated hot wires in an X-array operated in constant temperature modes and a platinum 1.2  $\mu$ m cold wire operated in a constant current mode. Due to the extremely close spacing between the three sensors (0.35 mm), relatively low overheat ratios were used during probe operation to limit "cross-talk" between the sensors. The two constant temperature sensors were operated with overheat ratios of 1.43 and 1.66, and the constant current sensor was operated at 0.1 mA. The three-sensor probe was used to measure local  $u$ ,  $v$  and  $t$  variations simultaneously. The velocity and temperature signals were sampled at 2 kHz (analog low-pass filtered-cut-off frequency 1 kHz) for 20 s at each measurement location. Additional information concerning the probe design and qualification are given in Shome [22] and Wang *et al.* [23].

### Data reduction

The surface heat transfer results presented in this paper are shown in terms of the local Stanton number. The fluid properties are evaluated at free-stream conditions, with corrections made for relative humidity effects. The heat flux to the free-stream was determined by subtracting the back loss, the radiation loss and the streamwise conduction loss from the measured power input. The energy balance described above, was applied to a  $2.5 \times 2.5$  cm area of the 1.56 mm lexan layer of the test surface [see Fig. 1(c)]; then the surface temperature was calculated by correcting each measurement obtained from the thermocouples embedded in the test surface. The free-stream velocity was measured by using a micro-manometer connected to a Pitot tube. Finally, the free-stream temperature was measured by a calibrated thermocouple with corrections for recovery and compressibility effects. The methodology of heat transfer measurement outlined above and the associated uncertainty analysis was similar to those discussed in Wang and Simon [24]. A detailed uncertainty analysis was conducted by Pinson [25], using the procedure set forth by Kline and McClintock [26] and Moffat [27]. The resultant uncertainties are listed in Table 2.

The single hot wire and the X-array of hot wires in

the three-sensor probe were corrected for the effects of varying temperature as suggested by Chua and Antonia [28]. The three-sensor probe was corrected by using instantaneous temperature fluctuations, and the single-wire probe measurements were corrected by using mean free-stream temperatures. Following the method of LaRue *et al.* [29], Wang, *et al.* [23] concluded that velocity correction of the cold wire in the three-sensor probe was unnecessary. Additional details on the data reduction process and the experimental procedure for this study are documented in Pinson [25].

## RESULTS AND DISCUSSION

### Undisturbed cases

The surface heat transfer distributions (normalized in terms of the Stanton number and the local Reynolds number) of the undisturbed cases are shown in Fig. 3. The laminar and turbulent correlations, obtained from Kays and Crawford [30], presented in the figure compensate for the unheated starting length of a uniformly heated test surface, and are of the form

$$St_{\text{LAMINAR}} = 0.453 Pr^{-0.67} Re_x^{-0.5} \times \left[ 1 - \left( \frac{X_{\text{UHSL}}}{x} \right)^{0.75} \right]^{-0.333} \quad (1)$$

and

$$St_{\text{TURBULENT}} = 0.0287 Pr^{-0.4} Re_x^{-0.2} \times \left[ 1 - \left( \frac{X_{\text{UHSL}}}{x} \right)^{0.9} \right]^{-0.111} \quad (2)$$

The initial portions of all the cases shown begin with a trend that follows the laminar unheated starting-length correlation, and then they deviate from the correlation at various Reynolds numbers,  $Re_x$ , because of the laminar-turbulent transition. The minimum local Stanton number for the 2.72 m s<sup>-1</sup> case occurs at an  $Re_x$  of  $2.24 \times 10^5$ . Increasing the free-stream velocity,  $U_x$  to 4.89 m s<sup>-1</sup> delays the onset of transition to an  $Re_x$  of  $3.59 \times 10^5$ . The onset of transition for the undisturbed case is defined here as the location where  $St$  reaches a minimum and starts to deviate from the

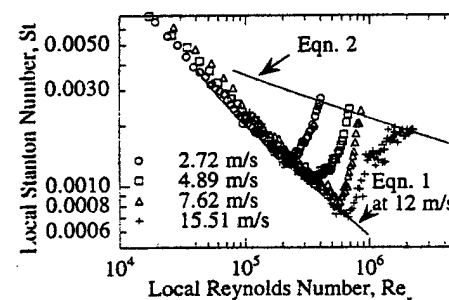


Fig. 3. Local surface heat transfer of the undisturbed case at various free-stream velocities.

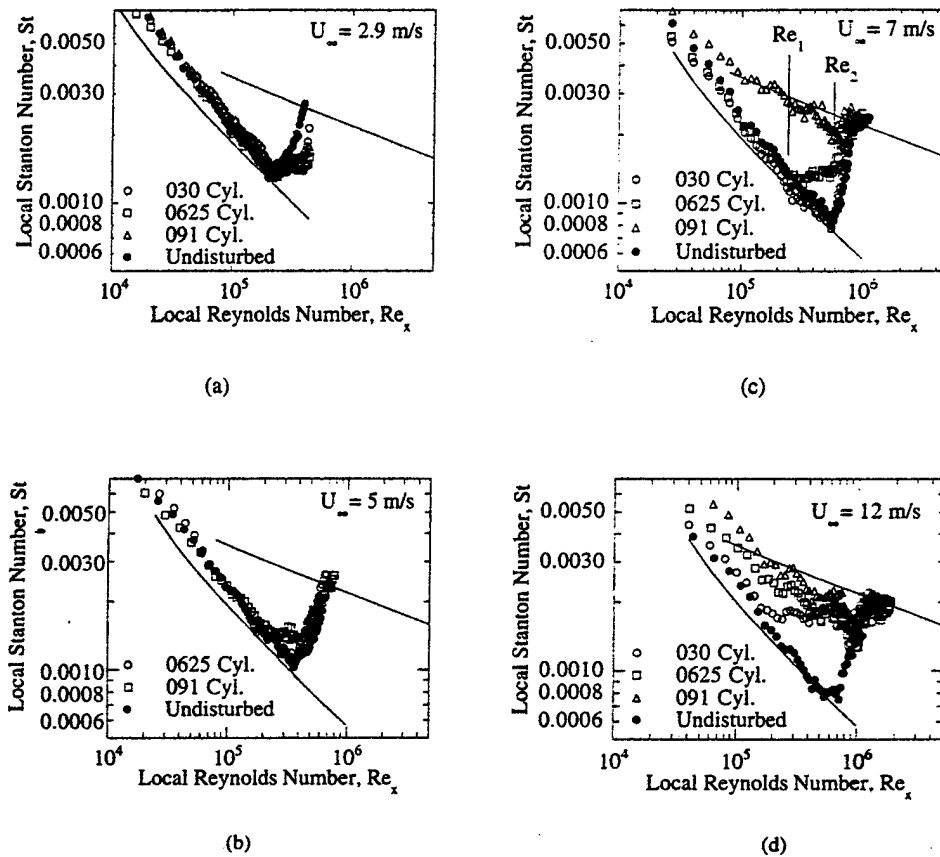


Fig. 4. Comparison of local Stanton number measurements between the undisturbed case and the cylinder leading edge conditions: (a)  $U_{\infty} = 2.9 \text{ m s}^{-1}$ ; (b)  $U_{\infty} = 5 \text{ m s}^{-1}$ ; (c)  $U_{\infty} = 7 \text{ m s}^{-1}$ ; (d)  $U_{\infty} = 12 \text{ m s}^{-1}$ .

laminar correlation. This trend of delayed transition with increased  $U_{\infty}$  continued until the free-stream velocity reached  $15.5 \text{ m s}^{-1}$ . The delay in the onset of transition between  $2.72 \text{ m s}^{-1}$  and  $15.5 \text{ m s}^{-1}$  is believed to be the result of decreasing free-stream turbulence intensity (FSTI), which was measured during the experiments. The FSTI of the  $2.72 \text{ m s}^{-1}$  case is 1.1% and the FSTI of the  $7.62 \text{ m s}^{-1}$  case is 0.4%.

Inaccuracies in the estimation of the radiant heat loss from the heated test surface could have caused the observed discrepancies between the laminar data and the laminar correlation. The emissivity (a value of 0.5 was used) of the heated test surface was the primary uncertainty in the radiant heat loss calculation. Although the deviation from the correlation is significant in the laminar region, the discrepancy does not affect the comparative nature of this study.

#### Leading-edge roughness effects on heat transfer

The surface heat transfer results from the various roughened leading-edge conditions (LECs) are shown with the undisturbed case in Figs. 4 and 5. Cylinder and sandpaper LECs do not affect the location of a transition onset at a  $U_{\infty}$  of  $2.9 \text{ m s}^{-1}$  [see Figs. 4(a) and 5(a)], but the effects of the LEC caused the slope of the  $St$  distribution in the transition region to deviate from the undisturbed case. The similar distribution of

the transitional data for the cases with sandpaper at the leading edge suggests that at this low free-stream velocity, the maximum roughness height, not the specific distribution of the roughness height, has the most significant effect on heat transfer. As the free-stream velocity increased, the  $St$  distributions for the roughened LEC cases began to deviate more and more from the undisturbed case. Inspection of the figures suggests that the greater maximum roughness height produces greater deviation from the undisturbed  $St$  distribution for a given free-stream velocity.

Several features of the Stanton number results of the cylinder LECs indicate a strong dependence on free-stream velocity. As mentioned earlier, the slowest free-stream velocity case ( $2.9 \text{ m s}^{-1}$ ) exhibited a milder slope in the transition regions of the roughened LEC cases than was seen in the transition region of the undisturbed case [Figs. 4(a) and 5(a)]. The slope of the transitional  $St$  distributions for the 030 and 0625 cases more closely resembled the undisturbed case when  $U_{\infty}$  was increased to  $5 \text{ m s}^{-1}$  [Fig. 4(b)]. In the early transition region, the 091 cylinder case exhibited an unusual deviation from the undisturbed behavior when  $U_{\infty}$  was  $5 \text{ m s}^{-1}$ . As shown in Fig. 4(b), a distinct departure from the undisturbed case began at an  $Re_x$  of  $2 \times 10^5$  until a  $Re_x$  of  $4 \times 10^5$  was reached, where the slope of  $St$  becomes steeper and more like a typical

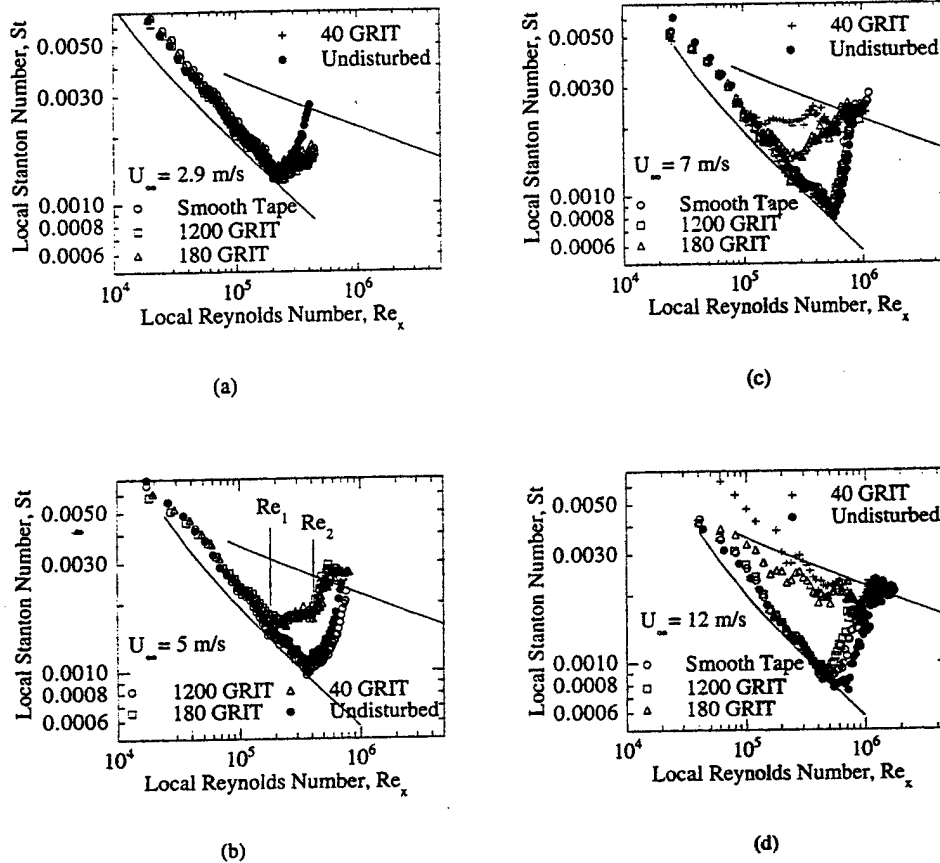


Fig. 5. Comparison of local Stanton number measurements between the undisturbed case and the sandpaper leading edge conditions: (a)  $U_{\infty} = 2.9 \text{ m s}^{-1}$ ; (b)  $U_{\infty} = 5 \text{ m s}^{-1}$ ; (c)  $U_{\infty} = 7 \text{ m s}^{-1}$ ; (d)  $U_{\infty} = 12 \text{ m s}^{-1}$ .

transition. As shown in Fig. 4(c), the  $St$  of the 091 cylinder case followed the turbulent correlation at  $U_{\infty} = 7 \text{ m s}^{-1}$ ; however, the  $St$  distribution of the 0625 cylinder case at  $7 \text{ m s}^{-1}$  [Fig. 4(c)] exhibited a dual-slope behavior similar to the behavior of the 091 case at  $5 \text{ m s}^{-1}$  [Fig. 4(b)]. Although the 091 cylinder case shown in Fig. 4(c) approximately follows the turbulent correlation, an unexpected degree of waviness in the  $St$  distribution was observed. The variation in the measured distribution was 6.4% above the correlation at an  $Re_x$  of  $1.88 \times 10^5$  and 22% below it at  $6.09 \times 10^5$ . Increasing  $U_{\infty}$  to  $12 \text{ m s}^{-1}$ , as shown in Fig. 4(d), caused all three cylinder LECs to exhibit similar waviness in  $St$ . In the upstream region ( $Re_x < 2 \times 10^5$ ), the  $St$  distribution increased and shifted upwards with little change in slope as  $U_{\infty}$  and the cylinder diameter increased. For the 091 cylinder case at  $12 \text{ m s}^{-1}$ , the magnitude of the  $St$  distribution near the leading edge was similar to that of the turbulent  $St$  correlation, but the slope was almost the same as the laminar correlation. The wavy behavior observed in the  $St$  distribution of the 091 cylinder case and the dual-slope behavior in the transitional region of the 0.0625 cylinder case are examined in greater detail in subsequent sections of this discussion.

The  $St$  behavior of the sandpaper LECs (Fig. 5) was similar to that shown by the cylinder LECs. The

40 GRIT case at a  $U_{\infty}$  of  $5 \text{ m s}^{-1}$  in Fig. 5(b) was the only sandpaper test case that exhibited the dual-slope behavior in the transitional  $St$  data that was observed in two of the cylinder LECs, but the change in slope at an  $Re_x$  of  $4 \times 10^5$  was not as distinct as the change in the 091 cylinder case [Fig. 4(b)]. At a  $U_{\infty}$  of  $7 \text{ m s}^{-1}$  [Fig. 5(c)], the 40 GRIT and 180 GRIT cases exhibited laminar behavior until an  $Re_x$  of  $1.3 \times 10^5$  and  $2 \times 10^5$  was reached, respectively. Then, both  $St$  distributions began laminar-turbulent transition with waviness similar to that observed earlier in the higher speed cylinder LEC cases.

#### Bluff leading-edge effect

Smooth tape (0.5 mm thick) was used to investigate bluff leading-edge effects on  $St$ . The results at various speeds are shown in Fig. 5, together with the sandpaper LECs. At a  $U_{\infty}$  of  $7 \text{ m s}^{-1}$ , the  $St$  distribution downstream of the bluff leading edge indicated that the onset of transition occurred at an  $Re_x$  of  $5.3 \times 10^5$  which is only 3% earlier than the onset for the undisturbed case. Increasing the  $U_{\infty}$  to  $12 \text{ m s}^{-1}$  caused the bluff leading edge condition to induce transition 15% earlier than the undisturbed case. Compared to the deviations induced by the sandpaper strips at this free-stream velocity, the bluff body effect of the sandpaper backing is relatively small.

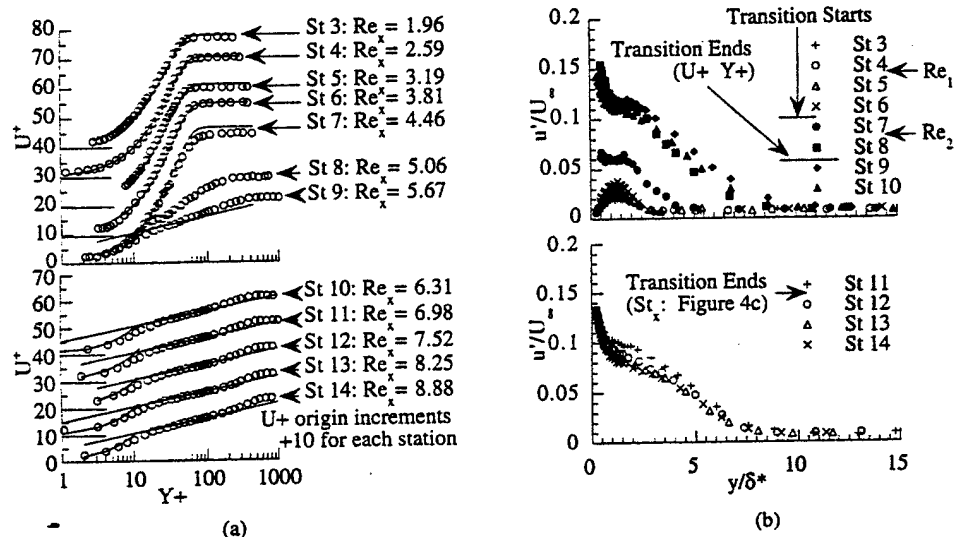


Fig. 6. Boundary layer profiles of the 0625 cylinder case ( $U_\infty = 7 \text{ m s}^{-1}$ ): (a) mean velocity profiles normalized in terms of local wall coordinates;  $U^+$  and  $Y^+$ , Reynolds numbers are  $\times 10^{-5}$ ; (b)  $u'$  distribution.

#### Dual-slope Stanton number behavior in transition region

The 091 cylinder [Fig. 4(b)], the 40 GRIT sandpaper at  $5 \text{ m s}^{-1}$  [Fig. 5(b)], and the 0625 cylinder at  $7 \text{ m s}^{-1}$  [Fig. 4(c)] all exhibited the dual-slope behavior in  $St$  between the laminar and turbulent correlations. Since this behavior was not observed in the undisturbed case and was not previously known to the authors, further study of the transport phenomena in the mean boundary layer was needed to provide insight into the physical mechanisms of the dual-slope region. Among these three similar cases, detailed measurements of the boundary layer of the 0625 cylinder case ( $U_\infty = 7 \text{ m s}^{-1}$ ) were obtained. The velocity profiles, normalized with respect to local wall coordinates, are shown in Fig. 6(a). The streamwise velocity profiles begin to significantly deviate from the Blasius correlation between an  $Re_x$  of  $4.46 \times 10^5$  and  $5.06 \times 10^5$ . During the wall heat transfer investigation, the local Stanton number began to deviate from the laminar correlation at an  $Re_x$  of  $2.88 \times 10^5$  (referred to as  $Re_1$ ) and the slope of the  $St$  distribution became steeper at an  $Re_x$  of  $4.88 \times 10^5$  (referred to as  $Re_2$ ). The mean velocity profiles suggest that the boundary layer experienced transition only after  $Re_x$  became greater than  $Re_2$ .

Further examination of the RMS quantities,  $u'$ ,  $\bar{uv}$ , and  $\bar{vt}$ , verifies the laminar and transitional status in the dual-slope region. Inspection of the  $u'$  profiles shown in Fig. 6(b) indicates that the  $u'$  variations increased in amplitude between stations 3 and 6 (the range corresponding to  $Re_1$  and  $Re_2$ ) with maximum values of  $u'/U_\infty$  ranging from 0.038 to 0.067, but the amplitude of the oscillations was still pre-transitional (typical maximum  $u'/U_\infty$  value: 0.15). At station 7, the  $u'/U_\infty$  distribution was relatively constant at 0.061 from a  $y/\delta^*$  of 0.45–0.67. This wide, relatively flat ( $\pm 5\%$  variation) region was not present in the undis-

turbed case (see Wang *et al.* [23]). Furthermore, the LEC caused the  $u'$  profiles to continue developing in the early turbulent region of the boundary layer (the maximum station-to-station variation is an average of 8% downstream of station 10), even though the mean velocity profiles indicated fully developed turbulent flow in this region [see Fig. 6(a)]. The  $\bar{uv}$  profiles depicted in Fig. 7(a) also show negligible activity in generating Reynolds shear stress between stations 4 and 6 ( $\bar{uv}/U_\infty^2$  less than 0.08), indicating pre-transitional flow in the region  $Re_1$  to  $Re_2$ . Large amplifications indicative of transitional flow were observed downstream of  $Re_2$  ( $\bar{uv}/U_\infty^2$  greater than 0.8). Similar to the  $u'$  profiles, the  $\bar{uv}$  profiles continued to develop in the early turbulent portion of the boundary layer. The  $\bar{vt}$  profiles shown in Fig. 7(b), exhibit behavior similar to  $\bar{uv}$  throughout the streamwise boundary layer development, and exhibit negligible Reynolds heat flux transport in the region between  $Re_1$  and  $Re_2$ .

The instantaneous velocity signals were inspected to provide more information about flow behavior in the dual-slope region. Representative velocity signals taken around  $Y^+ = 10$  at various stations for the 0625 cylinder case are shown in Fig. 8. The velocity signals of those stations between  $Re_1$  and  $Re_2$  (stations 5 and 6) are laminar-like with sinusoidal-like oscillations. However, the velocity traces of stations 7 and 8, which bracket  $Re_2$ , show intermittent turbulent/nonturbulent behavior, which undoubtedly indicates transitional flow. Similar behavior was observed for a low-speed 40 GRIT sandpaper case at  $U_\infty = 5 \text{ m s}^{-1}$ .

These boundary layer results suggest that a roughened leading edge may produce a pre-transitional region where the momentum and thermal transports in the boundary layer behave like laminar flow; however, the wall heat transfer significantly deviates from the laminar correlation.

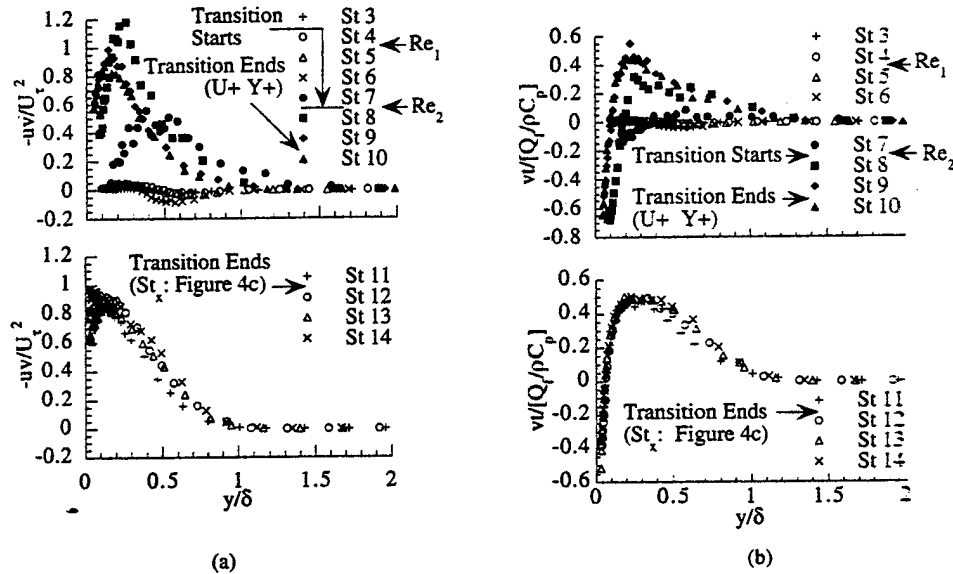


Fig. 7. Boundary layer profiles of the 0625 cylinder case ( $U_\infty = 7 \text{ m s}^{-1}$ ) continued: (a) Reynolds shear stress distribution; (b) Reynolds heat flux distribution.

#### Waviness in heat transfer data

The results of the Stanton number distributions show that waviness is present in high-speed cases with roughened leading edges. Inspection of Figs. 4 and 5 indicates that rougher leading-edge conditions cause significant wavy  $St$  behavior at lower free-stream velocities. Since the waviness was not observed in the undisturbed case, it was reasoned that the waviness was most likely induced by the flow disturbances introduced by the roughened leading edge.

The waviness could also have been caused by problems with the experimental apparatus and the test surface. Tests conducted at a fixed free-stream velocity ( $15 \text{ m s}^{-1}$ ) with varying power input levels indicate that the degree of waviness was not a function of power input. In addition, the test surface was qualified by conducting a convective heat transfer test in a laminar flow with mild acceleration of  $K \sim 4 \times 10^{-8}$ . The mild acceleration was caused by the boundary

layer growth in a constant-area channel. The  $St$  data of this qualification test matched the laminar correlation and no waviness was observed. The closeness of the match indicates that the heat flux out of the test surface was reasonably uniform and that all of the thermocouples embedded in the test surface functioned well. The energy balance used to determine the  $St$  distribution indicates that losses through the back of the heated wall were less than 1% of the flux to the free-stream. Hence, even an order of magnitude error in back-loss calculations would not have affected the magnitude of the heat flux to the free-stream to such an extent that could account for the degree of waviness present in the Stanton number data. A more detailed discussion of the waviness behaviors is presented in Pinson [25].

With the removal of the experimental apparatus and the test surface as possible culprits for the waviness, it seems possible that the observed waviness could be the result of nonlinear instabilities brought on by the finite amplitude disturbance introduced at the leading-edge. These nonlinearities in the flow condition could make the boundary layer sensitive to the minor geometrical variations present in the test section in such a way that the actual form or characteristic that causes the disturbance becomes unimportant. These minor surface disturbances, whatever they are, seem to be amplified as the free-stream velocity increases, and they significantly affect the heat transfer pattern downstream.

This study intentionally isolated the effects of leading-edge roughness on downstream flow and heat transfer behavior, so the test surface downstream of the leading-edge roughness was made smooth and flat. To better simulate the roughness condition of an in-service turbine blade, further studies are being undertaken by the authors to investigate the interactive

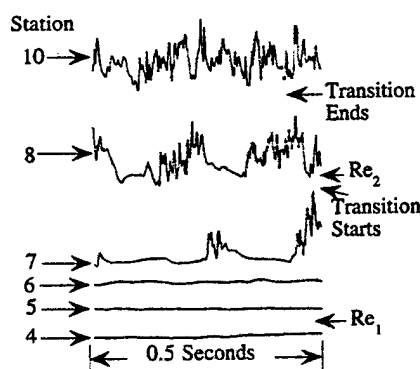


Fig. 8. Instantaneous velocity signals around  $Y^+ = 10$  at various streamwise locations for the 0625 cylinder case ( $U_\infty = 7 \text{ m s}^{-1}$ ).

effects of leading-edge roughness with the downstream roughness.

### CONCLUSIONS

A total of eight leading-edge conditions were examined to determine their effect on laminar-turbulent flow transition and downstream heat transfer flow behavior. In order to simulate the randomly distributed roughness located near the leading edge of the turbine blade, 1200, 180 and 40 GRIT sandpaper strips were adhered to the leading edge of the test surface. Similarly, 0.762, 1.59 and 2.31 mm diameter cylinders were chosen to simulate the relatively isolated peak nature of the roughness structure. Tests were also conducted by using a smooth strip of tape at the leading edge to determine the relative effects of the sandpaper backing and the actual roughness of the sandpaper. All of these leading-edge conditions were compared to the undisturbed leading edge.

Overall, greater maximum roughness height was observed to induce greater enhancement of the surface heat transfer than the undisturbed case. Depending on the free-stream velocity and the distance from the leading edge disturbance, the enhancement ranged from negligible to 200%. At low free-stream velocities ( $U_\infty = 5 \text{ m s}^{-1}$ ), the maximum roughness height was the primary contributor to deviations observed from the undisturbed case, irrespective of the roughness geometry. At higher free-stream velocities, 5–7  $\text{m s}^{-1}$ , the cases employing the 091 cylinder LEC, 0625 cylinder LEC and the 40 GRIT sandpaper exhibited a dual-slope region between the laminar and turbulent  $St$  vs  $Re$  correlations. Although the first slope was significantly different from the laminar correlation (as much as 88% higher), inspection of the mean velocity profiles, RMS fluctuations, Reynolds shear stress and instantaneous velocity signals indicated that the boundary layer was pre-transitional in this region. The second segment of the dual-slope  $St$  distribution was steeper than the first and the junction between these two segments was determined to be the approximate onset of boundary layer transition. For greater roughness, wavy  $St$  distributions were observed at higher free-stream velocities.

The presence of the dual-slope and wavy  $St$  behavior in some of the roughened leading-edge cases suggests that heat transfer is sensitive to leading-edge effects. In each situation, the behavior seems to be the result of nonlinear amplification introduced by finite disturbances at the leading edge. These nonlinear waves tend to amplify minor disturbances on the surface which propagate downstream in such a way that the wall heat transfer pattern is significantly affected. However, additional study of both of these behaviors is required before the mechanisms causing these behaviors can be understood.

**Acknowledgements**—This program was funded by the College of Engineering at Clemson University. The experiments

were performed in the test facilities sponsored by a grant from the Air Force Office of Scientific Research (Grant No. F49620-94-1-0126).

### REFERENCES

1. Mayle, R. E.. The role of laminar-turbulent transition in gas turbine engines. *Journal of Turbomachinery*, 1991, **113**, 509–537.
2. Hodson, H. P., Huntsman, I. and Steele, A. B.. An investigation of boundary layer development in a multistage LP turbine. 93-GT-310, ASME, 1993.
3. Taylor, R. P.. Surface roughness measurement on gas turbine blades. *Journal of Turbomachinery*, 1990, **112**, 175–180.
4. Boynton, J. L., Tabibzadeh, R. and Hudson, S. T.. Investigation of rotor blade roughness effects on turbine performance. *Journal of Turbomachinery*, 1993, **115**, 614–620.
5. Blair, M. F.. An experimental study of heat transfer in a large-scale turbine rotor passage. *Journal of Turbomachinery*, 1994, **116**, 1–13.
6. Fage, A. and Preston, J. H.. On transition from laminar to turbulent flow in the boundary layer. *Proceedings of the Royal Society of London*, 1941, **178**, 201–227.
7. Dryden, H. L.. Review of published data on the effect of roughness on transition from laminar to turbulent flow. *Journal of the Aeronautical Sciences*, 1953, **20**, 477–482.
8. Klebanoff, P. S. and Tidstrom, K. D.. Mechanism by which a two-dimensional roughness element induces boundary-layer transition. *Physics of Fluids*, 1972, **15**, 1173–1188.
9. Jacobs, W.. Variation in velocity profiles with change in surface roughness of boundary. Technical Memorandum 951. NACA, 1940.
10. Klebanoff, P. S. and Diehl, Z. W.. Some features of artificially thickened fully developed turbulent boundary layers with zero pressure gradient. Report 1110, NACA, 1951.
11. Antonia, R. A. and Luxton, R. E.. The response of a turbulent boundary layer to a step change in surface roughness: Part 1. Smooth to rough. *Journal of Fluid Mechanics*, 1971, **48**, 721–761.
12. Antonia, R. A. and Luxton, R. E.. The response of a turbulent boundary layer to a step change in surface roughness: Part 2. Rough to smooth. *Journal of Fluid Mechanics*, 1972, **53** (Part 4), 737–757.
13. Andreopoulos, J. and Wood, D. H.. The response of a turbulent boundary layer to a short length of surface roughness. *Journal of Fluid Mechanics*, 1982, **118**, 143–164.
14. Ligrani, P. M., Moffat, R. J. and Kays, W. M.. Artificially thickened turbulent boundary layers for studying heat transfer and skin friction on rough surfaces. *Journal of Fluids Engineering*, 1983, **105**, 146–153.
15. Taylor, R. P., Hosni, M. H. and Coleman, H. W.. Comparison of constant wall temperature and heat flux cases for the turbulent rough-wall boundary layer. *Experimental Heat Transfer*, 1990, **3**, 117–127.
16. Taylor, R. P., Taylor, J. K., Hosni, M. H. and Coleman, H. W.. Heat transfer in the turbulent boundary layer with a step change in surface roughness. 91-GT-266, ASME, 1991.
17. Keller, F. J.. Flow and thermal structures in heated transitional boundary layers with and without streamwise acceleration. Ph.D. thesis, Department of Mechanical Engineering, Clemson University, Clemson, South Carolina, 1993.
18. Kuan, C. L.. An experimental investigation of intermittent behavior in the transitional boundary layer. M.S.

thesis. Department of Mechanical Engineering. Clemson University, Clemson, South Carolina, 1987.

19. Zhou, D., Effects of elevated free-stream turbulence and streamwise acceleration on flow and thermal structures in transitional boundary layers. Ph.D. thesis. Department of Mechanical Engineering. Clemson University, Clemson, South Carolina, 1993.
20. Elovic, E., Personal Communication. General Electric Aircraft Engines, Cincinnati, OH, 1992.
21. Tarada, F. H. A., Heat transfer to rough turbine blading. Ph.D. thesis. University of Sussex, England, 1987.
22. Shome, B., Development of a three-wire probe for the measurement of Reynolds stresses and heat fluxes in transitional boundary layers. M.S. thesis, Department of Mechanical Engineering, Clemson University, Clemson, South Carolina, 1991.
23. Wang, T., Keller, F. J. and Zhou, D., Experimental investigation of Reynolds shear stresses and heat fluxes in a transitional boundary layer. *Journal of Experimental Fluid and Thermal Science*, 1992, **12**, 352-363.
24. Wang, T. and Simon, T. W., Development of a special-purpose test surface guided by uncertainty analysis. *Journal of Thermophysics*, 1989, **3**, 19-26.
25. Pinson, M., The effects of initial conditions on heat transfer in transitional boundary layers. M.S. thesis, Clemson University, Clemson, South Carolina, 1991.
26. Kline, S. J. and McClintock, Describing uncertainties in single-sample experiments. *Mechanical Engineering*, 1953, **75**, 3-8.
27. Moffat, R. J., Contributions to the theory of single-sample uncertainty analysis. *Journal of Fluids Engineering*, 1982, **104**, 250-260.
28. Chua, L. P. and Antonia, R. A., Turbulent Prandtl number in a circular jet. *International Journal of Heat and Mass Transfer*, 1990, **33**, 331-339.
29. LaRue, J. C., Deaton, T. and Gibson, C. H., Measurement of high-frequency temperature. *Review of Scientific Instruments*, 1975, **46**, 757-764.
30. Kays, W. M. and Crawford, M. E., *Convective Heat and Mass Transfer*. 3rd edn. McGraw-Hill, New York, 1993, pp. 175, 179 and 281.